New optical super-resolution imaging approaches involving DNA nanotechnology

submitted by

Tobias Lutz

to the University of Exeter as a thesis for the degree of
Doctor of Philosophy in Physics

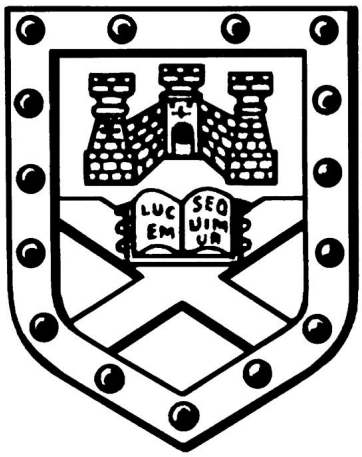

This thesis is available for Library use, on the understanding that it is copyright material and that no quotation from the thesis may be published without proper acknowledgement.

I certify that all material in this thesis which is not my own work has been identified and that no material has previously been submitted and approved for the award of a degree by this or any other University.

Tobias Lutz, April 2019

University of Exeter
Living Systems Institute
Stocker Road
EX4 4QD, Exeter

Abstract

With recent advances in optical super-resolution microscopy, biological structures can be imaged with single-nanometre resolution using visible light. One implementation thereof, DNA-PAINT (Point Accumulation for Imaging in Nanoscale Topography), is based on the highly specific and transient binding of fluorescently labelled oligonucleotides, the "imager strands", to complementary strands with which the targets are labelled, the "docking strands". The imager-docking binding events are detected as fluorescence blinking and can be localised with single-nanometre precision. From the set of localised events a super-resolution image can be assembled. DNA-PAINT has multiple advantages over other imaging methods, e.g. high photon yields resulting in high resolution, a free choice of fluorophores while being effectively free from photobleaching, straightforward implementation on a conventional fluorescence microscope and the possibility of temporally multiplexed and quantitative imaging.

In this thesis, a test sample based on functionalised microspheres is developed, which allows for optimisation of various DNA-PAINT imaging parameters and for the characterisation and testing of new variations and modifications of DNA-PAINT. One such method which was developed for this thesis, Quencher-Exchange-PAINT, facilitates temporally multiplexed imaging, which is based on the sequential exchange of imager strands targeting different docking strands. The exchange step is replaced by addition of competitive quencher-strands, allowing for rapid, low-crosstalk imager exchange even in biological samples with limited diffusion. Additionally, Proximity-Dependent PAINT is introduced, which enables the imaging of the nanoscale distribution of protein pairs by interaction of two proximity probes which activates DNA-PAINT type binding. The technique is demonstrated both on the microsphere assay as well as in biological samples. Finally, approaches for enhancing the signal-to-noise ratio are explored, based on the repetition of docking sites and on the use of imager strand complexes with multiple fluorophore-modifications.

Acknowledgements

I am very grateful to everybody who has made these last 3.5 years so enjoyable and who has supported me with the work presented in this thesis.

Firstly and especially, to Christian Soeller, for the opportunity to work with him and for being a truly excellent mentor. He left me plenty of freedom in what research I could pursue but always had his door open and provided great feedback and ideas.

Equally, I would like to thank Stefano Pagliara, Lorenzo Di Michele and Will Kaufhold, for all their support and many discussions we had.

None of the experimental work would have been possible without my team members Anna, Alex, Ruisheng and the rest. Thank you to Clara, Cecilia, Sara-Kate, Ammarah, Simona, Matthias and Carl.

A big thank you also goes to the people who endured reading this thesis and now claim my organs...Beth, Michelle and Bob.

Thank you so much to the whole Biophysics group with Dave, Fay, Skye, Michael and Uli, Siva, Ellen, Rikke, Pascaline, Seb, Richard, Nick, the ones who left: Sarah, Ryan, Claudio, Louise, Lauren, Sahand, Leanne, Jen, Sam and to our friends Ritchie, Kevin, Philomena, Cáit, Cherish, Nigella, VI Chris, Scotty and of course Mary.

At least equally important was everybody who made my life outside work so special, both in Exeter and back home. Thank you to Martin and Ana, Ben, Nicole, Julia, Connor, Jenny, Jann and Xui, Patrick and Til, Sarah, Hannah, Saskia, Feli, Wenkai, Javier and of course Connor, thank you for everything! Finally, a very special thanks goes to my family. Ganz vielen lieben Dank Mama, Papa, Abi und Anni!

Contents

List of Figures

Author's Declaration

The microscope and other imaging hardware used in this thesis were designed, set up and maintained by Christian Soeller and Ruisheng Lin. I contributed with occasional minor changes and optimisations. The corresponding software (PYME) is the work of David Baddeley and CS, and maintained and extended with help from RL. Cultured cells used in this thesis were kindly provided and fixed by Rikke Morrish, tissue sections were kindly provided by Anna Meletiou, Alexander H. Clowsley and Carl Harrison. AM, AHC, CH and Cecilia Afonso Rodrigues kindly provided conjugated antibodies. AM and AHC taught and occasionally helped me with fixation and labelling of the biological samples. New DNA nanotechnology schemes were developed with constant feedback and help from Lorenzo Di Michele, William T. Kaufhold and CS. Proof-of-principle experiments for the use of microspheres with DNA-PAINT were carried out by Simona Frustaci.

The major part of chapter 5 has been published in a peer-reviewed journal, *Nano Research* [1]. WTK, LDM and CS helped with simulation work in this chapter. All co-authors have contributed with many discussions and feedback to the technique presented in this chapter and helped with internal review of the manuscript.

Chapter 6 has been published on a pre-print server [2], submitted to a peer-reviewed journal and its contents have been filed as a patent application. The extensive modelling in chapter 6 was the work of WTK and LDM, who also provided kind help with most of the DNA sequence design. WTK, AHC, AM, LDM and CS helped with discussions, feedback and internal review of the manuscript.

Furthermore, the following publications were co-authored while working on this thesis: Jayasinghe et al. [3] and Lin et al. [4].

Abbreviations

AFM	Atomic force microscopy
bp	(DNA) base pair
CAD	Computer Aided Design
ds(DNA)	double stranded (DNA)
EDTA	Ethylenediaminetetraacetic acid
FRET	Foerster resonance energy transfer
HCR	Hybridisation Chain Reaction
HILO	Highly Inclined and Laminated Optical Sheet
ND	Neutral Density
nt	Nucleotide
PAINT	Point Accumulation for Imaging in Nanoscale Topography
(F)PALM	(Fluorescence) Photo-activated Localisation Microscopy
PBS	Phosphate Buffered Saline
PDMS	Polydimethylsiloxane
PD-PAINT	Proximity Displacement PAINT
PLA	Proximity Ligation Assay
PLL-PEG	Poly(L-lysine)-*graft*-poly(ethylene glycol) Co-polymer
PMMA	Poly(methyl methacrylate)
PYME	Python Microscopy Environment
qPAINT	Quantitative PAINT
PSF	Point Spread Function
RyR	Ryanodine Receptor
SIM	Structured Illumination Microscopy
ss(DNA)	single stranded (DNA)
STED	Stimulated Emission Depletion
(d)STORM	(Direct) Stochastic Optical Reconstruction Microscopy
TE	tris(hydroxymethyl)aminomethane-EDTA (Tris-EDTA)
TIRF	Total Internal Reflection Fluorescence

1. Introduction

This chapter gives a brief historical context and a motivation for the work presented in this thesis. Afterwards, an overview of the main aspects of each chapter is given.

1.1 Historical context and motivation

Only eight years after the first publication of a single molecule super-resolution imaging technique, the Nobel Prize in Chemistry 2014 was awarded to Eric Betzig, Stefan W. Hell and William E. Moerner for "the development of super-resolved fluorescence microscopy" [5]. The prize being awarded after such short time indicates the immense impact that the new techniques have for biological and medical research as well as the breakthrough they mean for optical microscopy.

For over a century, it was believed that the diffraction limit, first described by Ernst Abbe in 1873 [6], meant that structures with a distance of less than several hundred nanometres could not be distinguished in an optical microscope. According to Abbe, the resolution is limited to a length scale on the order of the wavelength used for imaging, thus resolving smaller structures is limited to X-ray or electron microscopy, down to picometre resolution if suitable short wavelengths are used [7, 8]. However, the high energy irradiation and complex sample preparation restrict the methods' use for biological imaging. In contrast, optical super-resolution imaging techniques maintain the advantages of (fluorescence) light microscopy, i.e. they are less invasive and, by using fluorescence markers, allow highly specific imaging of the structures of interest. For all super-resolution techniques, the diffraction limit still holds during the actual image acquisition, however, they allow sub-diffraction limited information of a sample

to be obtained by a number of schemes. An improved resolution can be achieved e.g. by confocal microscopy, (linear) structured illumination microscopy (SIM) or 4Pi-microscopy which is limited to ~100 nm for visible light [9–11]. Optical super-resolution techniques which provide theoretically unlimited resolution can be roughly divided into two groups, (1) deterministic, patterned excitation methods, e.g. nonlinear SIM [12] or stimulated emission depletion (STED, [13]), and (2) stochastic, single molecule localisation techniques, e.g. photo-activated localisation microscopy (PALM [14]) and stochastic optical reconstruction microscopy (STORM, [15]).

In both PALM and STORM, the fluorescent markers are stochastically switched between a state in which they emit fluorescence and a dark state, resulting in constantly changing subsets of active fluorescent markers which are detected as blinking events on the microscope. The single emitter events can be individually localised with a precision lower than the diffraction limit [16] and a super-resolution image can be assembled from the set of localisations.

PAINT (Point Accumulation for Imaging in Nanoscale Topography, [17]) techniques are alternative single molecule localisation methods which circumvent the need to drive fluorescence markers into photoswitching as they are based on the transient binding of fluorescently labelled markers to a target. The transient immobilisation associated with binding events are detected as fluorescent spots, mimicking the blinking by photoswitching in PALM and STORM. When not bound to the target, the fluorescent markers only appear as diffuse background in solution. In DNA-PAINT, fluorescently labelled DNA "imager" strands transiently bind to DNA "docking" strands, which are attached to the structure of interest and can be localised with single nanometre precision under suitable conditions [18]. DNA-PAINT originates from research into DNA origami, a method which allows the self-assembly of two- or three-dimensional nanostructures by folding a long single stranded DNA with the help of multiple short DNA strands [19]. The highly specific binding and the well understood kinetic and thermodynamic behaviour of DNA hybridisation make DNA a useful material for the techniques described above.

DNA-PAINT has several advantages over other single molecule imaging methods. The constant influx of new imager strands into the illuminated region due to diffusion in the sample makes the technique essentially free of photobleaching effects of the fluorophore. Additionally, apparent blinking being achieved by transient binding instead of fluorophore characteristics allows the use of a much

broader range of fluorescent dyes, and the flexibility of strand designs enables a precise control of the imaging parameters [18].

These advantages enable the versatile use of DNA-PAINT for multiple different applications, e.g. straightforward temporally multiplexed imaging (Exchange-PAINT, [20]) or quantitative imaging (qPAINT, [21]). In this thesis, several methods are developed which broaden the use of DNA-PAINT for new applications, such as simplified multiplexed imaging, multiplexing in tissue sections, an assay which shows the nanoscale distribution of protein pairs and different approaches to increase signal-to-noise and signal-to-background ratios.

Being a newer imaging method with major publications only appearing from 2014 onwards [20], compared to 2006 for PALM or STORM [14, 15], suggests that there is still room to establish the method more widely especially in biomedical research by providing improved procedures that extend or simplify the application of DNA-PAINT. A first detailed protocol covering the main aspects of DNA-PAINT was published in 2017 [22], but the described methods of testing DNA-PAINT using DNA origami pose considerable experimental difficulty and financial investments for users new to the technique. Here, different methods for assessing DNA-PAINT parameters are compared and a new, straightforward-to-implement test assay is demonstrated.

1.2 Thesis outline

Below, the thesis organisation is summarised. At the beginning of each results chapter, a short introduction and summary of its contents and a description of contributions by others are given.

- Chapter 2 provides the theoretical background for this thesis. Briefly, fluorescence microscopy and the diffraction limit are introduced. Different optical far field super-resolution techniques are described with a special focus on single molecule localisation microscopy and DNA-PAINT. Basics of the kinetics involved in DNA-PAINT are given and various adaptations of DNA-PAINT described, such as temporal multiplexed imaging (Exchange-PAINT) and quantitative imaging (qPAINT). Aspects of DNA nanotechnology which are relevant for this thesis are described and a brief overview over biological samples which were imaged is given.

- Chapter 3 is focussed on the methodologies used in this thesis. The sample preparation of biological and synthetic samples, DNA strand design, materials such as buffers and 3D printing techniques are described. Additionally, the imaging setup, image acquisition and image analysis in a Python environment are presented.

- In chapter 4, different assays for optimisation of DNA-PAINT imaging parameters are compared and a new test sample, which is based on streptavidin-coated microspheres labelled with DNA-PAINT docking strands, is introduced. Commercially assembled DNA origami slides and a customised origami design are compared to the microsphere assay. Several DNA-PAINT imaging protocol parameters are optimised, such as the illumination intensity, buffer conditions or imager concentrations.

- In chapter 5, different ways for advanced multiplexed imaging by Exchange-PAINT are demonstrated. In Exchange-PAINT, different targets are sequentially imaged using imager strands with different DNA sequences, with imager solution exchange steps separating the imaging rounds. To facilitate the solution exchange, a custom-made 3D-printed fluidic chamber is tested. Additionally, a new method for controlling the imager binding rate is introduced, which is based on the addition of competitive DNA strands. These so-called "quencher strands" enable Exchange-PAINT in simple, open top imaging chambers and allow rapid Exchange-PAINT imaging even in samples with comparatively limited diffusion, such as thick tissue sections.

- In chapter 6, Proximity-Dependent PAINT (PD-PAINT), a new super-resolution proximity assay is presented. Here, two DNA proximity probes only interact if they bind to targets that are located in close spatial proximity, typically $<10\,\mathrm{nm}$. Only if the proximity probes interact, DNA-PAINT type imaging is activated and the location of the probe pair can be detected. By imaging biotin binding sites on streptavidin and antibody pairs in cardiac tissue, it is shown that PD-PAINT detects the nanoscale distribution of target pairs with high proximity, with the proximity detection being independent of the optical resolution.

- In chapter 7, various methods aimed at increasing the signal-to-noise ratio in DNA-PAINT imaging are explored. The detected number of photons per DNA-PAINT binding event, and with it the localisation precision can

be increased if multiple fluorophores are attached to the imager strand in a suitable way. However, fluorescence quenching effects have to be taken into consideration. Additionally, DNA-PAINT imaging at higher signal-to-background levels is achieved by increasing the number of binding sites per target.

- Chapter 8 summarises the contributions made in this thesis, provides a conclusion and gives a brief outlook over potential areas for further development.

2. Theoretical Background

In this chapter, fundamentals of fluorescence microscopy and the diffraction limit are briefly described. An overview of widefield super-resolution microscopy techniques is given, with a focus on single molecule localisation microscopy. One implementation thereof, DNA-PAINT, is introduced, including a description of the involved DNA binding kinetics and options for background suppression. Advantages over other super-resolution techniques are emphasised, such as temporally multiplexed and quantitative imaging. The underlying physics and chemistry of DNA interactions is described and an overview over other applications of DNA nanotechnology of relevance for this thesis is given. Finally, biological samples, which are used for demonstration of newly developed methods in this thesis, are briefly described.

2.1 Diffraction-limited fluorescence microscopy

Fluorescence is a type of luminescence in which the absorption of a photon by a molecule, the so-called fluorophore or fluorescent dye, results in emission of another photon with lower energy. The process can be illustrated by a simplified Jablonski diagram (figure 2.1 a). The molecule is excited with a photon of energy $E_{exc} = hc \cdot \lambda_{exc}^{-1}$ from electronic ground state S_0 to an electronic singlet excited state S_1^*. Subsequent vibrational relaxation results in an excited state S_1. The lifetime of this state is typically in the range of single nanoseconds (1.8 ns for the fluorophore Atto 655 [23]). Emission of a photon with the energy $E_{em} = S_1 - S_0^* = hc \cdot \lambda_{em}^{-1}$ results in the return of the molecule to the electronic ground state. The difference in energy between the absorbed photon E_{exc} and the emitted photon E_{em} due to relaxation to the lowest electronic excited singlet

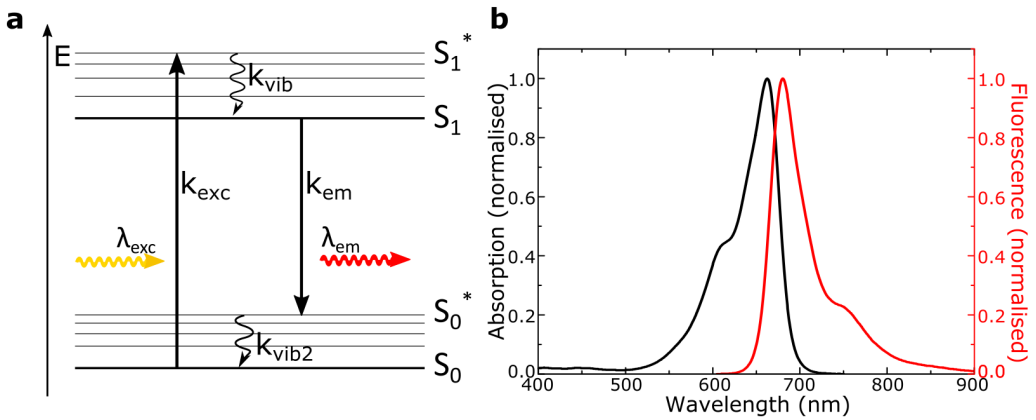

Figure 2.1: Spectra of a fluorescent dye and simplified Jablonski diagram. **(a)** Simplified Jablonski diagram of a fluorescent dye, showing excitation with wavelength λ_{exc} from electronic ground state S_0 to a higher singlet state S_1^*, subsequent vibrational relaxation to state S_1 with transition rate k_{vib}, followed by fluorescent emission of a photon with wavelength λ_{em}. **(b)** Excitation and emission spectrum of fluorescent dye Atto 655 [23].

state is reflected in a difference of wavelengths $\Delta\lambda = \lambda_{em} - \lambda_{exc}$, called the Stokes shift (figure 2.1 b).

The Stokes shift facilitates the emission to be separated from excitation by spectral filtering – the working principle of a fluorescence microscope. Selected targets of interest can be imaged if they are marked with a strong fluorescent emitter, e.g. by immunolabelling. For fluorescence excitation, a lamp or laser can be used in combination with an excitation filter, so that the spectrum of the illuminated light overlaps with the excitation spectrum of the fluorophore (see figure 2.1 b). The red-shifted fluorescence emission is separated by a dichroic mirror and emission filter. The setup of the microscope used in this thesis is described in detail in chapter 3.2.

The choice of the fluorophore does not only depend on its spectral properties. Its extinction coefficient and quantum efficiency have to be taken into consideration as they determine the brightness of the dye. The quantum efficiency, which is defined as the ratio of the number of emitted photons and the number of absorbed photons, can be reduced by a fluorescence quenching mechanism, such as collisional energy transfer or Förster resonance energy transfer (FRET) [24]. With these mechanisms, fluorescence emission can be prevented by targeted use of fluorescence quenchers. These can be regarded as fluorophores with very low

quantum efficiency, which are designed for a high energy transfer efficiency if they are located within typically single nanometre proximity of the quenched fluorescent dye.

Additionally, fluorophores generally have a limited photon budget, a term to describe the maximum number of emitted photons. The number of emitted photons can reach values up to $10^4 - 10^6$ for commonly used fluorophores [25]. The reason for the limit is typically photobleaching, the irreversible change or loss of the dye's fluorescence properties.

Diffraction-limited resolution

Fluorescence microscopy, like all other far field imaging methods, is subject to diffraction-limited resolution, first described by Ernst Abbe [6]

$$d = \frac{\lambda}{2n \sin\theta}. \tag{2.1}$$

Here, d represents the minimum distance at which two objects can be resolved, if they are imaged at wavelength λ, in a surrounding medium with refractive index n and with a lens with an acceptance angle of 2θ. The product $NA = n \sin\theta$ is known as the numerical aperture of an imaging system.

An intuitive explanation for the diffraction limit can be given for a single, infinitesimal dipole emitter, roughly following Pendry [26]. The dipole's electric field is characterised by a superposition of plane waves with spatial frequencies $k_{x/y/z}$, wavenumber k and wavelength λ

$$k = \frac{2\pi}{\lambda} = \sqrt{k_x^2 + k_y^2 + k_z^2}, \tag{2.2}$$

with k_z the component of the wave vector in propagation direction towards the detector. If the lateral spatial frequencies k_x, k_y surpass the limit

$$k_x^2 + k_y^2 > k^2, \tag{2.3}$$

then k_z becomes imaginary, the wave will not propagate and can thus not be detected. In other words, information about the position of an emitter is contained within its total radiation, but a detector in the far field can only detect its propagating component, information within the evanescent field, and thus

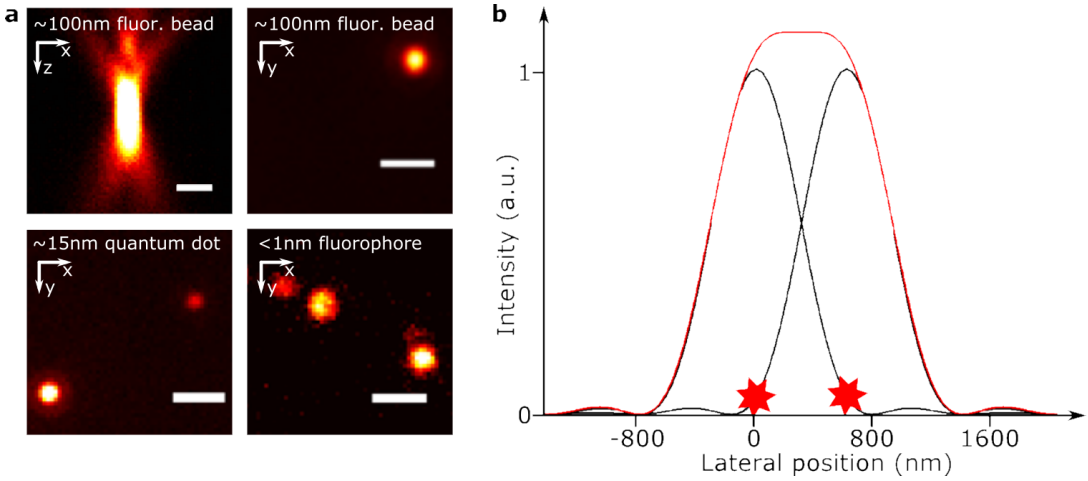

Figure 2.2: Point spread function and resolution limit. **(a)** Fluorescence emission of structures with a size below the diffraction limit (here fluorescent bead of 100 nm diameter, quantum dot of approx. 15 nm diameter and a single fluorophore of sub-nm size) can be used to estimate the point spread function (PSF) of a fluorescence microscope. **(b)** The position of two point light sources with a distance smaller than the diffraction limit cannot be detected due to the overlap of their PSFs, which results in a total photon distribution shown in the red curve. Scale bars: 1µm.

information about its exact position, is lost. From equations 2.2 and 2.3 it can be seen that this loss of information increases with increasing wavelength, consistent with Abbe's diffraction limit (equation 2.1).

In real imaging systems a limited numerical aperture further reduces the resolution, with the NA of objective lenses typically not exceeding 1.6. An imaging system can be characterised by the image of an infinitely small point light source on the detector, its point spread function (PSF). It can be estimated from the emission of a sub-diffraction fluorescent emitter, examples of which are shown in figure 2.2 a. The lateral shape of a PSF shows a so-called Airy disk, but can be distorted by aberrations of the system.

The exact characterisation of resolution of a microscope depends on the choice of the resolution criterion. The Rayleigh criterion defines the minimum resolvable distance as the distance between maximum and first minimum of the Airy disk [27], but often, the full width at half maximum (FWHM) of the PSF is given as estimated by a FWHM of a structure of sub-diffraction size [9]. Alternatively, the resolution can be defined by the system's bandwidth of detected spatial frequencies, which can be obtained from its PSF. In either case, the order of magni-

tude is similar to equation 2.1 and structures smaller than ~200 nm can typically not be resolved in an optical microscope using visible light ($\lambda \approx 400 - 750\,\text{nm}$).

2.2 Optical super-resolution imaging

Several methods have been developed which push a system's resolution below the diffraction limit defined in equation 2.1 and allow imaging with a resolution improvement up to a factor of ~2. Examples include confocal microscopy [9], structured illumination microscopy (SIM) [10, 28] or 4pi microscopy [11].

While the diffraction limit holds for any far field imaging system, there are techniques which can extract spatial information with no theoretical limit. This type of optical super-resolution imaging, i.e. resolving spatial information below the diffraction limit, can be achieved by sequential imaging of targets, such as fluorescent dyes. As demonstrated in figure 2.3 a, the position of a single point light source, can be estimated with sub-diffraction precision if no other light sources are located within a diffraction-limited distance. Recent techniques have shown sub-nanometre localisation precision of single fluorophores [29]. If light sources are located closer to each other but can be distinguished for example by sequential imaging, then the individual locations can be combined and a super-resolution image assembled. Sequential imaging can be achieved by switching only a subset of fluorophores into a detectable (ON) state, and the majority of surrounding fluorophores remain in an OFF state in which they cannot be detected [30]. Consequently, the size of the fluorophore defines in principal the resolution limit.

Super-resolution techniques can be divided into two groups [31],

(1) deterministic, targeted techniques which rely on shaping of the illumination pattern, e.g. saturated structured illumination microscopy, SSIM [12] or stimulated emission depletion (STED) [13],

(2) stochastic, single molecule localisation methods, e.g. (direct) stochastic optical reconstruction microscopy ((d)STORM) [15, 32], photo-activated localisation microscopy (PALM) [14, 33] or point accumulation for imaging in nanoscale topography (PAINT) [17].

Figure 2.3 b shows the principle of STED as an example of a deterministic method (1). STED and related techniques which are often described as RESOLFT (reversible saturable optical fluorescence transitions) methods [34], rely on reversible saturable fluorescence transitions. In STED, a conventional laser scanning confocal microscope can be used with an additional illumination beam for stimulated emission of fluorophores. Saturated depletion of the excited state S_1 is achieved if the illumination intensity is much larger than the fluorophore's characteristic saturation intensity I_S [35]. If this depletion illumination beam is applied in a pattern which contains areas of zero intensity, then fluorophores with a populated state S_1 (the detectable ON state) are confined to an area with the full-width half-maximum [30]

$$\mathrm{FWHM_{STED}} = \frac{\lambda}{2n\sin\theta} \cdot \frac{1}{\sqrt{1 + aI_{max}/I_S}}, \tag{2.4}$$

in analogy to the diffraction limit as defined by Abbe (equation 2.1). I_{max} is the peak intensity of the depletion illumination and a a correction factor for the illumination pattern [30]. As a consequence, the imaging resolution can be reduced to below the diffraction limit by increasing the intensity of the depletion beam.

A similar concept is used in saturated structured illumination microscopy. An illumination pattern, e.g. by superposition of line patterns, gives a resolution enhancement by a factor of two (structured illumination microscopy [10, 36]). Higher resolution is achieved by saturation of the electronically excited state S_1. This creates a nonlinear relationship between the excitation pattern and the emission rate per fluorophore resulting in harmonics of higher spatial frequencies than the illumination pattern, and a super-resolution image can be reconstructed by computational post-processing [12].

A disadvantage of targeted illumination approaches is that they typically require complex instrumentation to achieve a suitable illumination pattern. STED, for instance, relies on near perfect creation of a zero intensity depletion illumination in the centre of the pattern to achieve high resolutions [37]. This in turn requires accurate alignment of the illumination beams. Additionally, the high intensity of the depletion beam can damage biological samples [38].

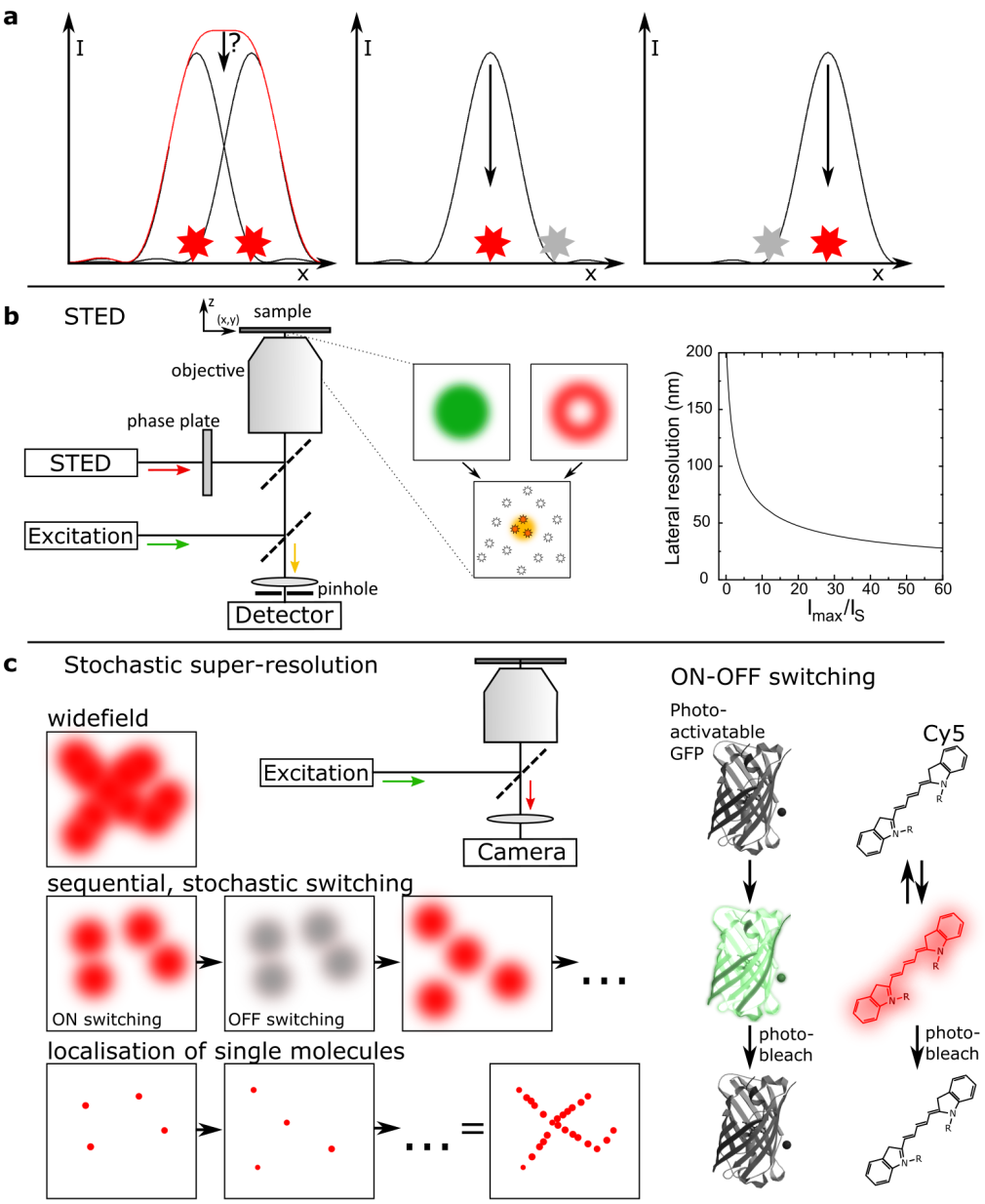

Figure 2.3: General principles of optical far field super-resolution techniques. **(a)** Super-resolution can be achieved by detection of only a subset of fluorescent markers (down to single fluorophores) within a diffraction-limited area. **(b)** STED principle, example of super-resolution by deterministic excitation. STED achieves resolution improvement over confocal microscopy by de-exciting fluorophores through stimulated emission with an additional patterned "STED"-beam, here shown as a toroid shape. **(c)** Stochastic single molecule localisation microscopy approaches (SMLM), e.g. STORM, PALM, PAINT. A stochastic subset of fluorophores is detected on a camera and single molecules can be localised. The number of photons of a single fluorophore determines the resolution of SMLM methods. Photoactivatable green fluorescent protein (GFP): Protein database 3GJ2.

2.2.1 Single molecule localisation microscopy

Single molecule localisation microscopy (figure 2.3 c) relies on localisation of fluorescent emitters with sub-diffraction precision. The localisation error Δx can be described by [16]

$$\left\langle (\Delta x)^2 \right\rangle = \frac{(\sigma^2 + a^2/12)^2}{N} \left(\frac{16}{9} + \frac{8\pi(\sigma^2 + a^2/12)^2 b^2}{N a^2} \right), \tag{2.5}$$

where σ is the standard deviation of the PSF, a^2 the detector pixel area, b describes background noise (with b^2 the number of detected background photons per pixel) and N the number of detected (signal) photons. Options to maximise N include using a fluorophore with high photostability and brightness, i.e. with high extinction coefficient and quantum efficiency, by increasing illumination intensity or extending the detection integration time. For high N compared to the number of background photons, the localisation precision becomes proportional to the square root of N,

$$\langle (\Delta x) \rangle \propto \sqrt{N}^{-1}, N \gg b^2. \tag{2.6}$$

Apart from sub-diffraction localisation, another prerequisite for super-resolution imaging is the sequential detection of the fluorophores, as described above. STORM, PALM, PAINT and similar methods all achieve this by following the steps below [31]:

(1) a stochastic subset of molecules is in a detectable *ON* state, i.e. are detected as fluorescence signals,

(2) the emission is detected by a camera, the subset of molecules localised according to equation 2.5 and the locations with sub-diffraction precision saved,

(3) the molecules are transferred to a non-emitting *OFF* state, e.g. by photobleaching or transferring them to a triplet state with long lifetime,

(4) the previous steps are repeated multiple times and the stochastically change in subsets ensure a difference in detected molecules,

(5) a super-resolution image is rendered from the set of saved molecule locations.

In practice, this protocol is implemented by the processing of a sequence of camera frames which records an apparent blinking of single fluorescence emitters. There are various software packages available to detect and localise these blinking events. Most achieve accurate localisation by fitting of a 2D Gaussian to the emission signals if 2D images are acquired, i.e. images orthogonal to the optical axis of the microscope, or by fitting of a previously detected PSF to 3D images [39].

The difference between the multiple single molecule localisation methods is typically the way by which the blinking, i.e. the stochastic choice of emitters, is achieved. Examples are shown in figure 2.3 c, right. PALM and fluorescence (F)PALM similarly rely on photoactivatable fluorescent proteins which can be switched between at least two different states, i.e. switching by activation with light of a specific wavelength and photobleaching [14, 33]. Instead, STORM uses photoswitchable organic fluorescent dyes, originally a combination of a cyanine dye and a second fluorophore in proximity which activates photoswitching [15]. Additionally, photoswitching of single dye molecules has been shown. In direct STORM (dSTORM), for instance, dyes are exposed to a redox buffer solution which stochastically transfers them to a dark, e.g. triplet, state [32, 40, 41].

The optical resolution and thus the imaging quality in post-processing free methods, such as STED, can be determined directly from the acquired image, e.g. by measuring the FWHM of imaged features [42, 43]. However, in single molecule localisation methods the imaging quality is in addition strongly dependent on the labelling density [14], which should be multiple times higher than the Nyquist criterion suggests [44]. Additionally, the rendered image can have artificially sharpened features. One method to evaluate the resolution is by Fourier ring correlation (FRC), determining the correlation of independent subsets of the acquired data [45]. But as FRC can be sensitive to systematic localisation errors [46], an alternative quality control can be provided by calibration samples, such as DNA-origami (discussed in section 2.3). With this technique, fluorophores can be placed at precisely quantified distances, e.g. 6 nm recently shown for the MINFLUX technique, a combination of STED and single molecule techniques [47].

So far, only lateral resolution, i.e. perpendicular to the optical axis of the microscope, has been explicitly discussed. Stochastic localisation techniques also allow sub-diffraction resolution in three dimensions, which can be achieved by manipulation of the PSF. Examples include introducing a slight astigmatism

[48], using spatial light modulators to create a double helical PSF [49], or by inserting a phase ramp into the detection path [50]. Alternatively, a split detection with different focal positions (bi-plane) [51] or total internal reflection illumination (TIRF) enable 3D super-resolution.

Biological questions often demand locations of not only single, but multiple targets, i.e. multiplexed, or multicolour imaging. In localisation microscopy, different targets can be labelled with spectrally different dyes. These can be distinguished either by utilising differences in the excitation spectrum and excitation at different laser wavelengths [52] or, if a single excitation laser is used, differences in the emission spectra can be detected [53].

Fluorophore characteristics, particularly photo-stability, are the major limiting factor for super-resolution techniques [54]. The techniques described above add an additional restriction on the choice of dye molecules. This holds especially for localisation microscopy methods such as STORM or PALM [37], where the blinking characteristics of fluorophores have to be optimised and the photon budget is distributed over multiple blinking cycles.

Alternatively, apparent blinking which is independent of fluorophore chemistry can be achieved by continuously renewing or exchanging the imaged fluorophores with a constant influx of emitters into the illuminated region. Thus, an imaged region of interest no longer has a limited total photon budget. A first realisation, called PAINT (Point Accumulation Imaging in Nanoscale Topography), is based on stochastic binding of freely diffusing, lipophilic fluorophores to lipid membranes. While in solution, emission of the dye is reduced and only binding of the dye to the membrane is detected as apparent blinking events [17]. However, this technique is limited to hydrophobic targets and does not provide the high specificity of immunolabelling. Instead, universal PAINT (uPAINT) presents a generalisation of the technique. It relies on fluorescently labelled, permanently binding ligands, e.g. antibodies, which continuously and successively bind to an imaged target and undergo photobleaching, which is detected as blinking events [55]. A similar variation, IRIS, is based on transient binding of protein fragment based probes [56]. DNA-PAINT, a further highly flexible and specific approach with transient binding relies on DNA strand interactions [18] and is discussed in further detail below.

2.2.2 DNA-PAINT

In DNA-PAINT, apparent blinking for single molecule localisation is achieved by transient binding of a fluorescently labelled DNA strand, the so-called *imager* (I), to a target DNA strand, the *docking strand* (D). The high specificity of DNA binding results in highly specific labelling [57]. A background on DNA and its use in nanotechnology is given in section 2.3.

Figure 2.4 demonstrates the basic principles of DNA-PAINT. Docking strands are attached to the target of interest. This is straightforward for imaging DNA structures, such as synthetic samples [18] or chromatin [58], in which case extended docking strands can be integrated into the structure by high affinity DNA binding. For other biological targets, e.g. proteins, immunolabelling is possible. Originally, docking strands were connected to antibodies via a streptavidin-biotin linker [20]. Alternatively, various methods exist which allow direct, covalent conjugation of the docking strand to an antibody, e.g. via commercially available kits [3] or NHS-ester based click chemistry [22]. For ultra-high resolution, i.e. single nanometres, the size of antibodies (approx. 150 kDa) restricts labelling density and the Nyquist criterion might not be fulfilled [56]. Thus, very recently the use of smaller labels such as aptamers (sizes below 30 kDa) has been proposed [59].

The docking strand has a DNA base sequence which is complementary to that of the imager strand. Imagers are freely diffusing in solution surrounding the sample and labelled with a fluorophore. The main criterion for the choice of the fluorophore is its brightness and photon budget. As the binding interaction between imager and docking strand is only transient, a single docking strand can be imaged multiple times if multiple imagers bind sequentially. The total photon number used for detection of the docking strand location, and consequently the localisation precision (equation 2.6), depends not only on the brightness of the fluorophore but can be increased by longer image acquisition. With average photon numbers >35,000 per localisation, calibration targets with features of 6 nm could be resolved [60]. In practice, sample drift, which increases with acquisition time, can limit the localisation correction and needs to be compensated for.

Typically, the imager-docking affinity is chosen so that the binding times are in the range of hundreds of milliseconds to seconds [22] and can be predicted from well-understood DNA binding kinetics.

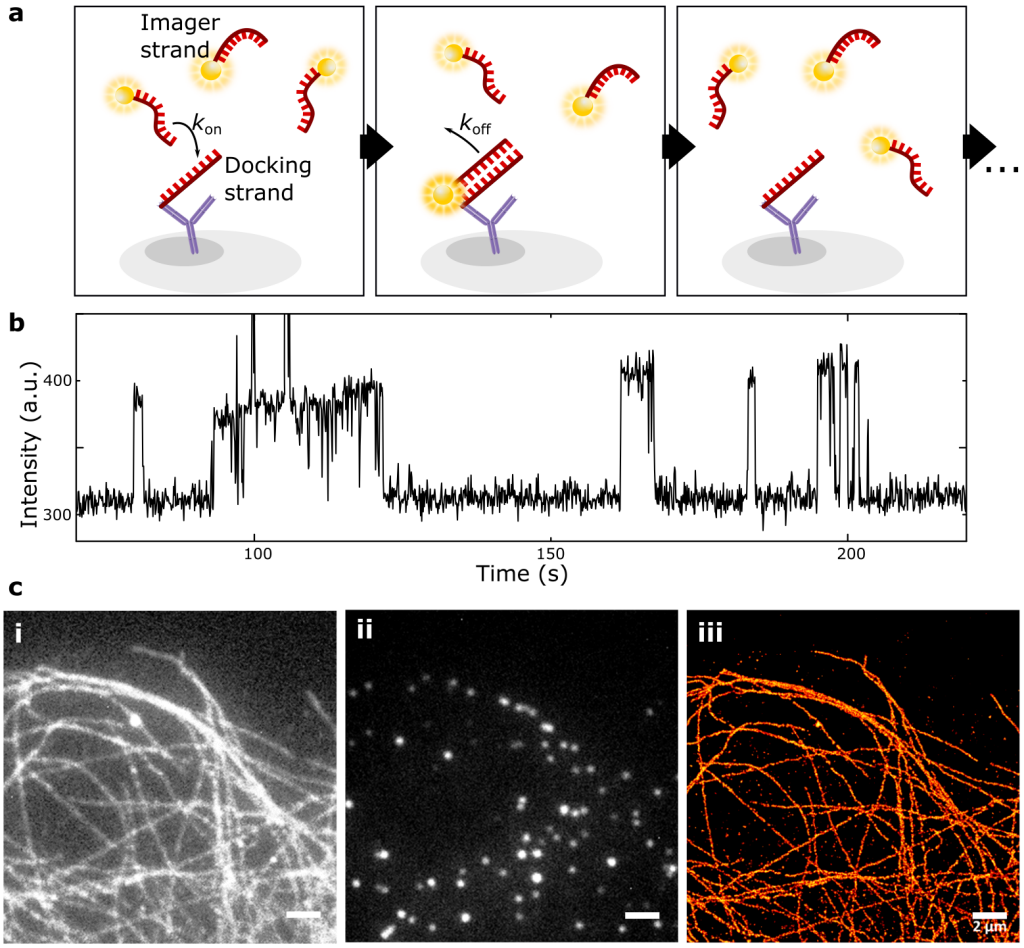

Figure 2.4: Principle of DNA-PAINT. **(a)** Schematic drawing showing a target labelled with docking strand oligonucleotides. An oligonucleotide with complementary sequence and labelled with a fluorophore (imager strand) can bind transiently to the docking strand, which results in a bright fluorescence signal and localisation of the transiently stationary fluorophore. Imager strands in solution still emit fluorescence, however, they only appear as a diffuse background due to diffusion with timescales much faster than the camera integration time. **(b)** Intensity time trace for a small (the size of the diffraction limit) region of interest. A clear distinction between bound and unbound imager strands can be seen. **(c)** (i) Microtubules imaged by wide-field fluorescence microscopy, (ii) Raw data acquired in a DNA-PAINT experiment. Typically, several 10,000 frames are detected for a single super-resolution image, (iii) Rendered super-resolution image. Scale bars: 2 µm.

Imager-Docking binding kinetics in DNA-PAINT

The transient binding interaction of an imager I to a docking strand D is a reversible reaction and can be described by

$$I + D \underset{k_{\text{off}}}{\overset{k_{\text{on}}}{\rightleftharpoons}} ID, \tag{2.7}$$

where ID represents an imager-docking complex and k_{on} and k_{off} the reaction rate constants of binding and unbinding, respectively. The corresponding rate equation is [18]

$$\frac{\mathrm{d}[ID]}{\mathrm{d}t} = -k_{\text{off}}[ID] + k_{\text{on}}[I][D]. \tag{2.8}$$

Typical imager concentrations $[I]$ used in this thesis range from 0.01 nM to 10 nM. k_{on} represents a second order reaction rate, and can be calculated via the lifetime of the single stranded (ss) state of the docking strand τ_{ss} and the concentration of imager strands $[I]$ [18]

$$k_{\text{on}} = \frac{1}{\tau_{ss} \cdot [I]}. \tag{2.9}$$

The unbinding of imager and docking strand, represented by k_{off}, is a first order reaction. It is related to the lifetime τ_{ds} of the double stranded (ds) imager-docking complex [18]

$$k_{\text{off}} = \frac{1}{\tau_{ds}}. \tag{2.10}$$

The lifetime τ_{ds} (typically hundreds of milliseconds to seconds) can be adjusted by changing the affinity of imager and docking strands, for details see section 2.3.

If photo-bleaching is negligible, i.e. if the binding time is shorter than the average time to photobleach the fluorophore, which can be adjusted by the illumination intensity, then the imager-docking complex lifetime τ_{ds} is equal to the time of observed fluorescence at a single docking site, the fluorescence time τ_F. Similarly, the single stranded lifetime τ_{ss} can be approximated by the observed dark time τ_D, at which no fluorescence is detected from a single docking strand. The straightforward and flexible way of tuning τ_F and τ_D, which is equivalent to tuning of the apparent blinking behaviour, represents one of the main advantages of the technique over other single molecule localisation methods.

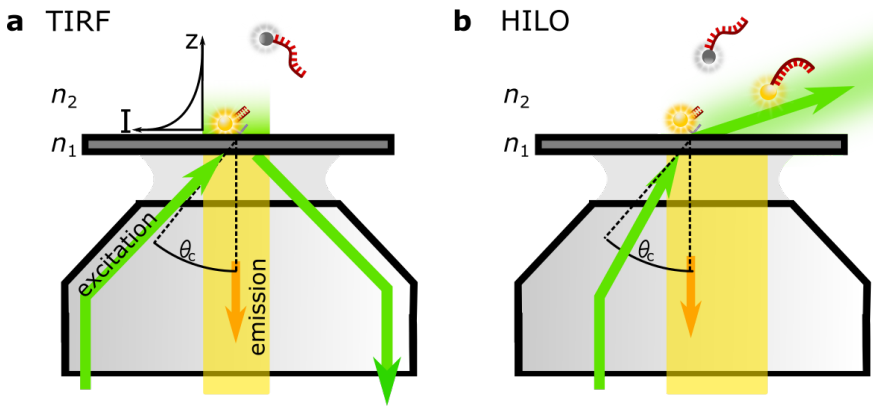

Figure 2.5: Illumination modes for background minimisation. **(a)** Total internal reflection fluorescence (TIRF) microscopy. The sample is illuminated through a high NA objective lens at an incident angle larger than the critical angle θ_c and thus by an evanescent field with exponentially decreasing intensity. **(b)** Highly inclined and laminated optical sheet (HILO) mode describes illumination near, but below the critical angle. This results in transmission of the incident light at a highly inclined angle.

However, the flexibility comes at the cost of diffuse background fluorescence emitted from unbound imager strands in solution. As this background reduces the signal-to-noise ratio, it should be minimised.

Background suppression in DNA-PAINT

The movement of a single stranded, unbound imager strand in the solution surrounding the imaged sample depends on its diffusivity. The diffusion coefficient of a double stranded, short DNA complex in an aqueous environment has been measured ($D \approx 5 \cdot 10^{-7}\,\mathrm{cm^2 s^{-1}}$ [61]), which should represent a lower limit for the imager's diffusion. During an integration time of 100 ms, the root mean square (rms) displacement of a random walk of the imager can be approximated to be larger than $rms_{min} = \sqrt{6Dt}$ (in 3 dimensions [62]), which corresponds to a value of approximately $rms_{min} = 5.5\,\mu\mathrm{m}$, roughly three orders of magnitude larger than the DNA-PAINT localisation precision. Consequently, it can be safely assumed that the fluorophore of an unbound imager cannot be detected as anything other than a diffuse background signal. While a single imager in solution will not disturb the detection of transiently binding ones, a large number of unbound imagers can add up to a high background fluores-

cence, as the following rough calculation indicates. At an imager concentration of 1 nM, the volume above an area the size of the diffraction limit (~500·500 nm^2) with 5 mm filling height of imager solution in the sample chamber, will contain $N_I \approx N_A \cdot 1\,\mathrm{nM}/1.2 \cdot 10^{-12}\,\mathrm{cm}^3 \approx 750$ free imager strands. For homogenous excitation throughout the sample, this means that fluorescence of the unbound imager would potentially outweigh the fluorescence of bound imager strands. While there have been observations that incorporation of guanine into the imager DNA base sequence can reduce the fluorescence of single stranded imager [18], such an effect will not counterbalance the difference in imager numbers.

Instead, the excitation volume can be reduced. A commonly used method in super-resolution microscopy is the use of total internal reflection for illumination (TIRF) [63]. Figure 2.5 a illustrates that by shifting the illumination beam parallel to the optical axis towards the edge of the objective lens, the beam angle in the focal plane of the microscope can be tilted by an angle θ. If this angle at the coverslip surface exceeds the critical angle θ_c

$$\theta_c = \sin^{-1}\left(\frac{n_2}{n_1}\right), \tag{2.11}$$

with the refractive indices of the coverslip n_1 and the imaging buffer n_2, then illumination light will not propagate into the sample and is fully reflected at the coverslip. Above the coverslip, the illumination intensity decreases exponentially, only an evanescent field is present. The exponential decay I_z along the optical axis can be characterised by [64]

$$I_z = I_0 e^{-z/d}, \tag{2.12}$$

where I_0 is intensity at the surface and d the penetration depth

$$d = \frac{\lambda_{exc}}{4\pi n_2 \sqrt{(\sin\theta/\sin\theta_c)^2 - 1}}, \tag{2.13}$$

with λ_{exc} the excitation wavelength (in vacuum) and θ the angle of the incident light. The penetration depth d decreases with increasing illumination angle θ, but can often be estimated to $d \approx 100\,\mathrm{nm}{-}200\,\mathrm{nm}$ for visible light [64]. The critical angle at the glass/water interface is $\theta_c \approx 61.7°$, however the maximum angle of illumination through an objective lens $\theta \leq \theta_{\max}$ is restricted by its

numerical aperture NA $= n \sin \theta_{\max}$. Consequently, only high NA objectives can be used for TIRF microscopy.

TIRF only allows excitation of targets in proximity to the coverslip surface. If targets up to several micrometres into the sample have to be excited, the illumination angle can be reduced to values slightly below the critical angle. This results in light propagation into the sample but the strongly inclined angle of the illumination beam still reduces background fluorescence from out of focus regions. The method, shown in figure 2.5 b, is known under various names, such as Highly Inclined and Laminated Optical sheet (HILO), dirty or quasi TIRF, or oblique illumination [65, 66].

Beyond 2D imaging of single targets, DNA-PAINT has been modified and combined with multiple other imaging techniques. Some examples include a combination with fluorescence correlation spectroscopy (FCS) [67], 3D imaging by PSF engineering or spinning disk microscopy [68, 69] and background was attempted to be reduced by using energy transfer (FRET) [70]. Below, two important modifications of DNA-PAINT are discussed in more detail, multiplexed imaging by Exchange-PAINT [20] and quantitative imaging by qPAINT [21].

2.2.3 Exchange-PAINT

Imaging of multiple targets in DNA-PAINT can be achieved by labelling the different populations with docking strands of non-interfering, orthogonal DNA base sequences. Imager strands will only bind to the docking strands with complementary sequences, thus the choice of imager determines which target is imaged.

Simultaneous multicolour imaging is straightforward when using imager populations with spectrally different dyes – similar to multicolour imaging in any single molecule localisation technique. This has been demonstrated with two populations of docking strands on synthetic structures which are imaged with two matching sets of imagers, labelled with fluorophores Cy3 and Cy5, respectively, and excited with different excitation wavelengths [71]. However, spectral multiplexing relies on accurate separation of the labels and can be prone to crosstalk [72]. Crosstalk can be reduced if dyes with sufficiently different emission spectra are used, but the use of a broad emission spectrum increases the influence of chromatic aberrations [73].

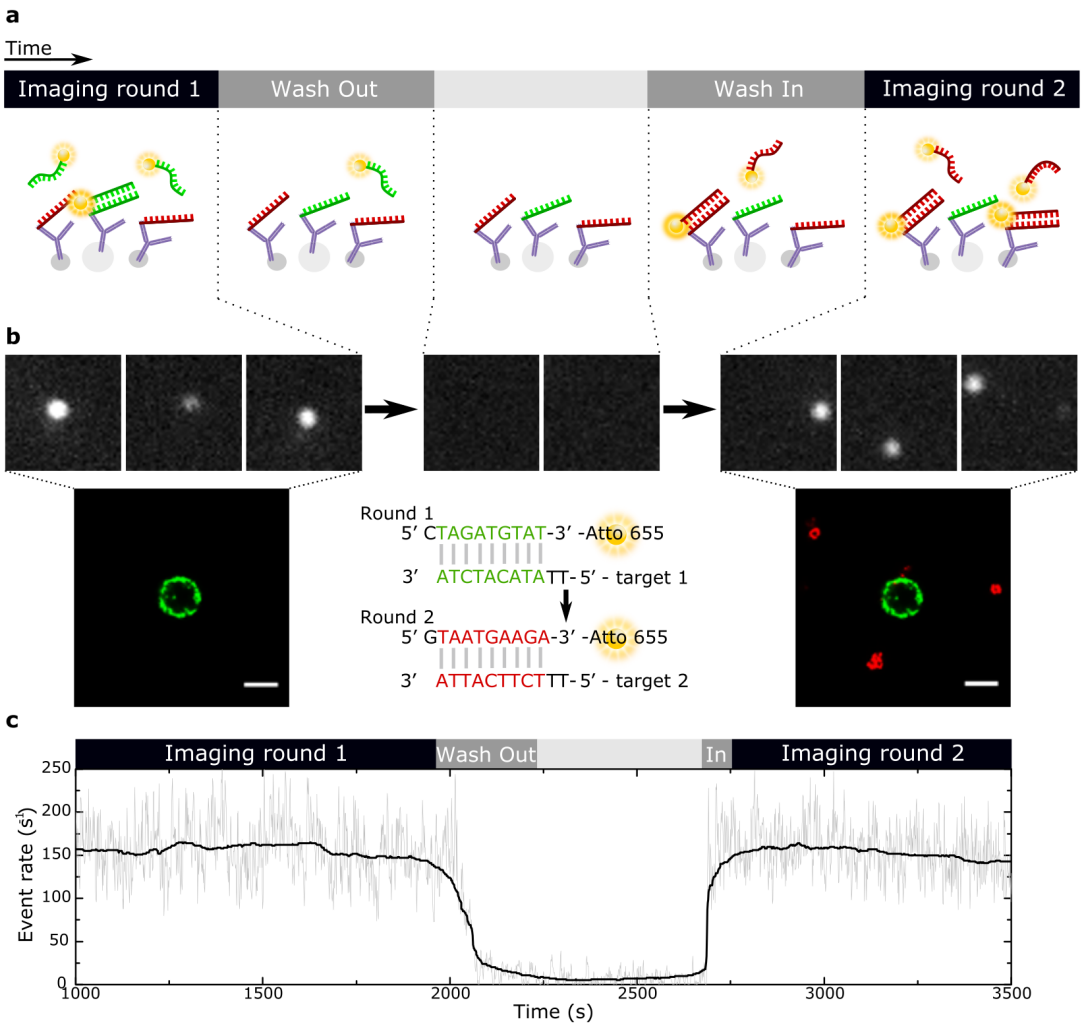

Figure 2.6: Principle of temporally multiplexed DNA-PAINT imaging by Exchange-PAINT [20]. **(a)** Different targets are labelled with docking strands of different, orthogonal DNA sequences which are imaged sequentially, interrupted by fluid exchange steps. Here, complementary imager-docking strand pairs are identified by different colours, red for imager/docking pair 1 and green for imager/docking pair 2. The scheme can be extended to a near-arbitrarily high number of different targets. **(b)** Example of raw data and corresponding rendered images of an Exchange-PAINT experiment. Different populations of colloidal particles are labelled with different docking strands and imaged sequentially, but the same fluorophore can be used. Note that typically more than 10,000 frames are recorded per imaging round. **(c)** Rate of detected imager-docking strand binding events, here called 'event rate', during an Exchange-PAINT experiment. No binding events are detected during the fluid exchange step, which separated imaging round 1 and 2. The black curve shows a 50 pt median filter. Scale bars: 500 nm.

Instead of spectral multiplexing, the imagers can be detected separately by temporal multiplexing. This so-called Exchange-PAINT scheme is illustrated in figure 2.6 [20]. A first target, labelled with docking strands of sequence 1 is imaged with the corresponding imager strand 1. After sufficient data is acquired, imager 1 is removed from the sample environment and replaced by imager 2. Imager 2 is used for detection of docking strand sequence 2, which is attached to a second target. This process can be repeated multiple times and is in principle only limited by the number of orthogonal DNA sequence combinations, in practice by the number of available markers and the available acquisition time. Exchange-PAINT on 10 targets in synthetic samples and 4 different proteins in a fixed cell sample have been published by Jungmann et al. in 2014 [20]. Figure 2.6 b demonstrates a simple two target Exchange-PAINT experiment on colloidal particles. Different populations of particles (of different sizes) are labelled with orthogonal docking strand sequences and imaged sequentially. Exchange-PAINT enables low cross-talk imaging, however, the acquisition time, and consequently the total sample drift, increases with the number of targets. Sample drift has been reported to amount up to several micrometres and has to be corrected [20].

Sequential imaging of multiple targets has been demonstrated for other super-resolution techniques, such as STORM, but it often involves complex and time-consuming additional immunolabelling steps during image acquisition [72]. As an alternative, the Exchange-PAINT principle has been generalised to allow sequential imaging in other imaging techniques, such as STED, SIM or STORM [74, 75]. In all variations, including Exchange-PAINT, the exchange of fluids during acquisition is necessary. Examples of how this is achieved are described below.

Fluidics exchange methods

A straightforward method to exchange solutions is the use of an imaging chamber, in which the imager solution is accessible for pipetting. The imager solution can be repeatedly replaced with buffer until the concentration is reduced to background levels and a new imager can be added by pipetting. As this can impact the sample stability, a fluidic handling system is typically preferred. Figure 2.7 demonstrates examples of published fluidic chambers used in super-resolution microscopy. A simple chamber can be created by sealing two glass slides with

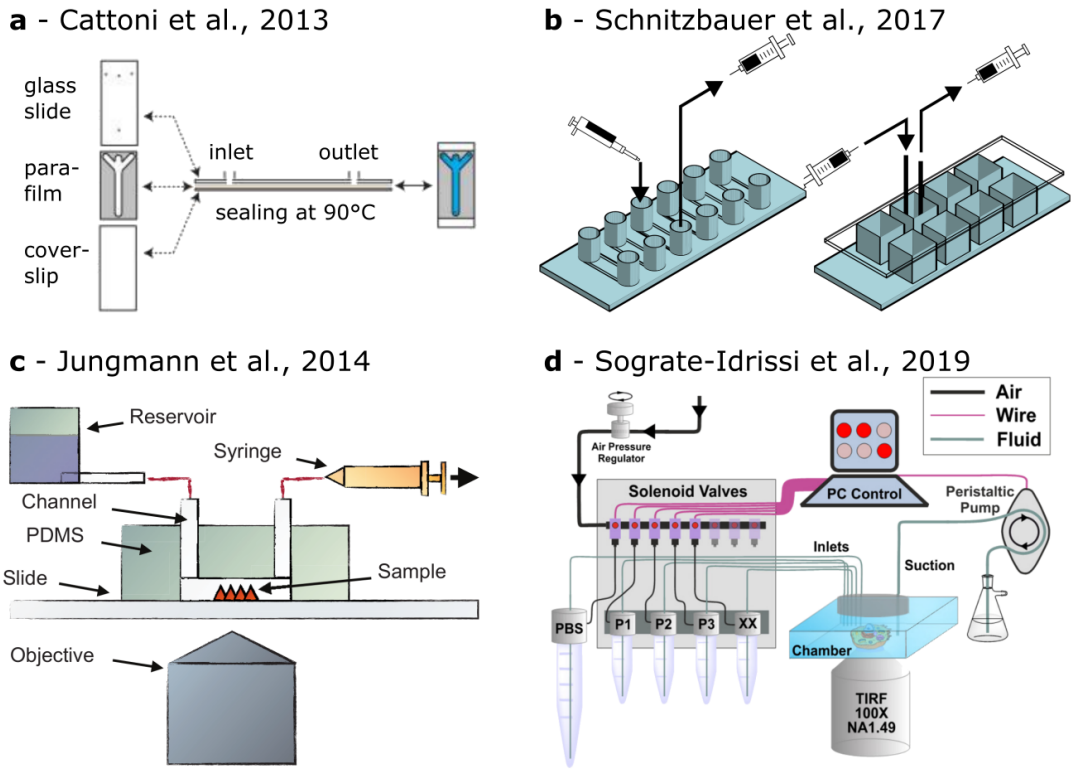

Figure 2.7: Examples of previously published methods for fluidic exchange chambers for super-resolution microscopy. **(a)** A cost-effective and basic chamber with inlet and outlet can be fabricated by sealing a coverslip and glass slide with a parafilm mask. This was used for PALM super-resolution imaging. Figure adapted from Cattoni et al. [76]. **(b)** Commercially available imaging chambers can be used with syringes, but often need adaptation, e.g. with a glass seal. Here used for Exchange-PAINT. Figure adapted from Schnitzbauer et al. [22]. **(c)** A PDMS channel, similar to a microfluidic chip, can be used for Exchange-PAINT in combination with a reservoir/syringe setup. Figure adapted from Jungmann et al. [20]. **(d)** Commercially available pump systems allow automated control of more complex microfluidic systems. Figure adapted from Sograte-Idrissi et al. [77].

parafilm or sticky tape [22, 76], or a commercially available chamber can be adapted [22].

More intricate fluid control and a lower volume consumption is possible by using microfluidic chips. Typically, micrometre sized channels are transferred by soft lithography from a mold into PDMS and subsequently sealed with a glass coverslip. Microfluidics has been shown to facilitate structured illumination microscopy, as no movement of the illumination pattern is necessary if the sample is subject to fluid flow [78]. Microfluidic chips have been used for imaging live cells, in situ fixation and correlated super-resolution imaging by STORM [79]. Furthermore, PALM and DNA-/Exchange-PAINT have been demonstrated [20, 77, 80]. A potential influence of the microfluidic environment, e.g. due to the surface roughness, increased capillary forces or chemical surface effects should be taken into account. The chambers shown in figure 2.7 a-c are all used with syringes or pipettes, which requires manual interference during imaging and can therefore often lead to a displacement of the sample. However, a fully automated microfluidic system as in figure 2.7 d is cost-intensive and requires complex and often laborious sample preparation of a microfluidic chip.

2.2.4 qPAINT

If the resolution is higher than the distance between imaged proteins, then single proteins can be detected and counted by single-molecule localisation imaging [3]. However, for higher protein densities it is not straightforward to relate the blinking event density to the number of imaged proteins, e.g. due to unknown blinking kinetics of the fluorophore or photobleaching [21, 81, 82]. In DNA-PAINT, directly counting imager-docking strand binding events can lead to under-counting of docking sites at a high site density [21].

The predictable binding kinetics and their consistency during image acquisition, i.e. negligible photobleaching, enables quantitative imaging by DNA-PAINT, so-called qPAINT [21]. As shown in figure 2.8 a, the number of imaged docking sites N_{docking} can be estimated from the mean dark time $\tau_{D,mean}$ ($\tau_{D,mean} \approx \tau_{ss,mean}$, see section 2.2.2), the concentration of imager $[I]$ and the imager-docking binding rate constant k_{on} [21],

$$N_{\text{docking}} = \frac{1}{k_{on} \cdot [I] \cdot \tau_{D,mean}}. \tag{2.14}$$

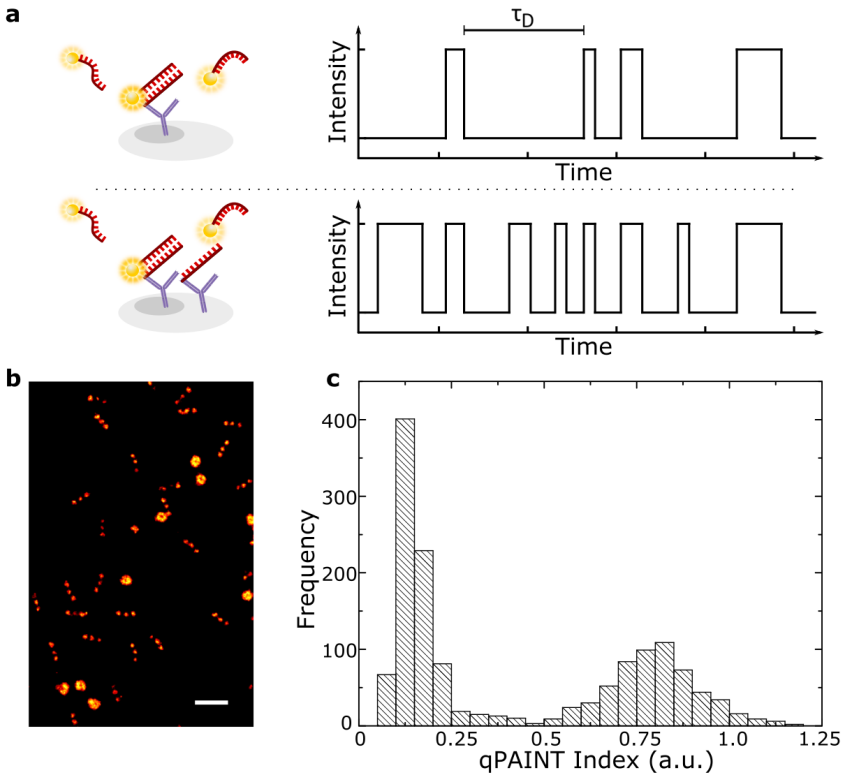

Figure 2.8: Quantitative imaging with DNA-PAINT, *qPAINT* [21]. **(a)** qPAINT estimates docking strand numbers by quantification of characteristic fluorescence off- or (dark)-times (τ_D). **(b)** Two populations of DNA origami structures with different numbers of docking strands. **(c)** Example of qPAINT analysis on structures shown in b, the qPAINT index is proportional to the inverse of the mean dark time $\tau_{D,mean}$, the two populations can clearly be distinguished. A more intricate qPAINT analysis of the sample shown here has been published by Lin et al. [4]. Scale bar: 200 nm.

The rate k_{on} can be obtained in a calibration measurement, if the number of docking sites used for calibration is known. Recently, measurements of docking strands attached to DNA nanotubes at a distance of 3 nm have shown that qPAINT provides accurate quantitative information for targets at close distances, and does not suffer e.g. from cross-reactions [83].

qPAINT has been demonstrated in synthetic samples, as shown in figure 2.8 b, and has been used to quantify protein numbers in protein clusters [3, 4]. A qPAINT index, the inverse of $\tau_{D,mean}$, has been introduced, as a measure for the quantity of proteins in relation to the calibration target.

The continuous damaging of docking sites by excited imagers has been discussed as a potential limitation for qPAINT [84], however, this has not been observed in other publications, showing constant binding rates over long durations instead [21]. More importantly, the number of imaged docking sites as obtained by qPAINT is only equal to the number of proteins, if they are labelled stoichiometrically [85].

2.3 DNA nanotechnology

The properties which make DNA the ideal material for storage of genetic information, such as its chemical stability, highly specific base pairing which allows encoding of information and the predictable and inert double-helical structure of DNA, also make it a useful material for the fabrication of nanostructures. DNA is a biopolymer, its subunits are called nucleotides (nt). Each nucleotide consists of a nucleobase, 2-deoxyribose (a pentose sugar) and a phosphate group. Alternating sugars and phosphate bonds are covalently connected via phosphodiester bonds between the third and fifth carbon of the pentose structure, forming the backbone of the resulting polymeric structure with a polarity which is typically denoted by its 5' and 3' end (by convention, the phosphate group is located on the 5' end) [86]. Attached to each sugar is one of four nucleic bases (shown in figure 2.9 a), adenine (A), thymine (T), guanine (G) and cytosine (C), which interact via hydrogen bonds to form so-called base pairs (bp).

Via these hydrogen bonds, a single chain of nucleotides, single stranded (ss)DNA, can hybridise and form a double stranded (ds)DNA. The molecular structure of double stranded DNA was first described by Watson and Crick in 1953 [90]. While there are multiple other, non-canonical base interactions, the Watson-Crick pairing of adenine-thymine (AT) and guanine-cytosine (GC) is the most common and results in a stable double strand. Additionally, the formation of a double strand requires antiparallel orientation of two strands with respect to their 5' and 3' ends. Consequently, there is only one specific sequence of bases, i.e. a specific primary DNA structure, which matches that of a single stranded DNA, a so-called complementary strand.

Figure 2.9 b shows the most common double stranded DNA confirmation, B-DNA (as opposed to other tertiary structures such as A-DNA or Z-DNA, which only occur under special conditions [62]). The double strand is not only stabilised

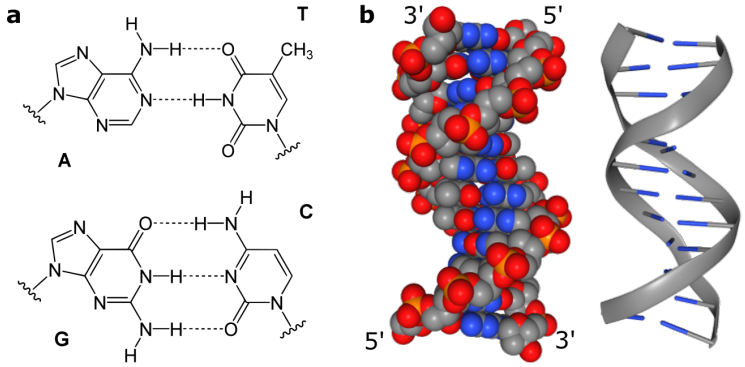

Figure 2.9: Chemical structure of nucleotides and DNA double helix. **(a)** Chemical representation of Watson-Crick base pairing, showing the four different DNA bases adenine (A), thymine (T), guanine (G) and cytosine (C) [87]. Adenine and thymine (AT) are connected via two hydrogen bonds, guanine and cytosine (GC) via three, resulting in higher stability of a GC bond. **(b)** DNA double helix of B-DNA, the predominantly naturally occurring double helix structure [88]. Image taken from RCSB PDB, Drew et al. [89]. The non-symmetrical helical structure with a major and a minor groove can be seen.

by the hydrogen bonds between the nucleic bases, but also by interactions of π-electrons in the aromatic rings of neighbouring bases, so-called base stacking [91]. B-DNA forms a right-handed double helix with a diameter of 2 nm, 10.5 base pairs per turn and a distance between nucleotides in direction of the helix of 0.34 nm. A typical imager-docking strand complex of 9 bp overlap has a length of approximately 3.1 nm, smaller than a typical antibody (~10 nm, [92]).

The stability of a double helical dsDNA depends mostly on base stacking interactions [62] but is influenced by multiple other parameters and, in the case of DNA-PAINT, affects the unbinding rate constant of the imager and docking strands k_{off}. The stability increases with the number of hydrogen bonds, either by an increasing number of base pairs or by an increased content of GC pairs, which form three hydrogen bonds, as opposed to AT base pairs which form two. For an imager-docking complex, the increased binding time with an additional base pair can be approximated to increase by one order of magnitude, e.g. from $\tau_{ds,9} = 0.625\,\text{s}$ for a 9 bp imager-docking overlap to $\tau_{ds,10} = 5\,\text{s}$ for 10 bp [18]. The association rate constant k_{on} is independent of the number of base pairs [18]. Additionally, an increase in temperature reduces the stability of dsDNA. The binary on/off model for DNA-PAINT is only a simplified view of the dissociation of dsDNA. Base pairs, especially at the end of a duplex, can stochastically

break open (fraying dsDNA). This reversible process can disrupt the stacking interaction with the neighbouring base pair, destabilising it and initiate loss of an additional base pair, stochastically leading either to re-association or dissociation of the double strand [93]. If a critical duplex length of only a few (e.g. three) base pairs is reached, the dsDNA is considered fully dissociated [18].

Thermodynamically, the stability of dsDNA can be calculated by the free energy difference between single stranded and hybridised DNA, which depends on the base pair sequence. Under normal experimental conditions, i.e. constant pressure, the standard Gibbs free energy for duplex formation ΔG^0, i.e. for 1 mole, 25°C at 1 bar, can be calculated from experimentally obtained values of the free energy of neighbouring base pairs, using the so-called nearest-neighbour model [94]. The free energy is related to the dissociation constant K_d, which describes the ratio of dissociation to association rate $k_{\text{off}}/k_{\text{on}}$ as defined in section 2.2.2

$$K_d = K_{eq}^{-1} \cdot \Gamma = \exp\left(\frac{\Delta G^0}{RT}\right) \cdot \Gamma \tag{2.15}$$

$$= \frac{k_{\text{off}}}{k_{\text{on}}}, \tag{2.16}$$

with the equilibrium constant K_{eq}, the ideal gas law constant R, the temperature T in Kelvin and $\Gamma = 1\,\text{M}$ to give K_d the dimension of molar concentration, as it is commonly used in DNA hybridisation. Another commonly used characteristic value for the duplex stability of DNA is the melting temperature T_m, the temperature at which half of the DNA strands are in duplex form, the other half having dissociated. T_m can be directly measured by detecting the ratio of ssDNA to dsDNA while increasing the temperature, e.g. in an UV absorption measurement [62]. Through experimental studies, various methods have been found that relate the melting temperature to thermodynamic properties such as ΔG^0 and equally, multiple methods allow the prediction of the melting temperature from the base sequence, using e.g. nearest neighbour methods [62, 95, 96]. For a typical DNA-PAINT imager strand (P1 base sequence = TAG ATG TAT) at 1 nM the melting temperature is $T_m \approx 4.7\,°\text{C}$ [97], indicating that an imager-docking duplex is not stable at room temperature and a majority of imager strands are unbound in solution.

Apart from its advantageous chemical properties and the predictable and controllable interactions of DNA, an important factor for the success of DNA nanotechnology is the possibility to produce arbitrary nucleotide sequences by

chemical synthesis [98]. Driven e.g. by primer development for polymerase chain reaction, the synthesis of oligonucleotides (short DNA strands of typically less than 200 nt), has been automated by solid phase synthesis and arbitrary oligonucleotides are commercially available. Additionally, oligonucleotides can be modified, for example with functional groups, fluorophores and fluorescent quenchers. Synthetic DNA crystals on the basis of branched DNA junctions such as the Holliday junction, in which two dsDNA are joined to form four branches, were the first fabricated nanoscale structures [99, 100]. Subsequently, the stability of structures was increased by avoiding branch migration, structures with dynamic properties were shown and a new assembly method for nanostructures was introduced, DNA origami [19, 101].

2.3.1 DNA origami

Figure 2.10 a shows the principle of DNA origami, as first described in 2006 [19]. A long (approximately 7000 nt) single stranded *scaffold* strand, derived from the M13mp18 phage genome, is folded by having ~200 shorter oligonucleotides, *staple strands*, bind at defined positions to the scaffold. The choice of binding positions determines the resulting desired nanostructure. The advantage of DNA origami is that a single scaffold strands folds into a single nanostructure, consequently staple strands do not have to be added stoichiometrically. Additionally, the structures are formed through self-assembly, only mixing of the strands is required with a heating and cooling protocol to achieve the structure at which the free energy is minimised [101]. For the design of DNA origami structures, software packages are available, e.g. CaDNAno [102]. Alternatively, the required staple strand sequences for multiple designs have been published [22].

DNA origami has been used to construct both 2D and 3D structures, which have been connected to form crystalline arrays, modified with dynamic functionalities or used for applications in molecular biology [101]. By extending staple strands in a DNA origami structure such that a single stranded domain containing a docking sequence is exposed to the environment, DNA origami can be imaged by DNA-PAINT. An example is shown in figure 2.10 b. DNA-PAINT was originally demonstrated on DNA origami samples [18], as were several DNA-PAINT variations such as Exchange-PAINT or qPAINT [20, 21]. Additionally, DNA-

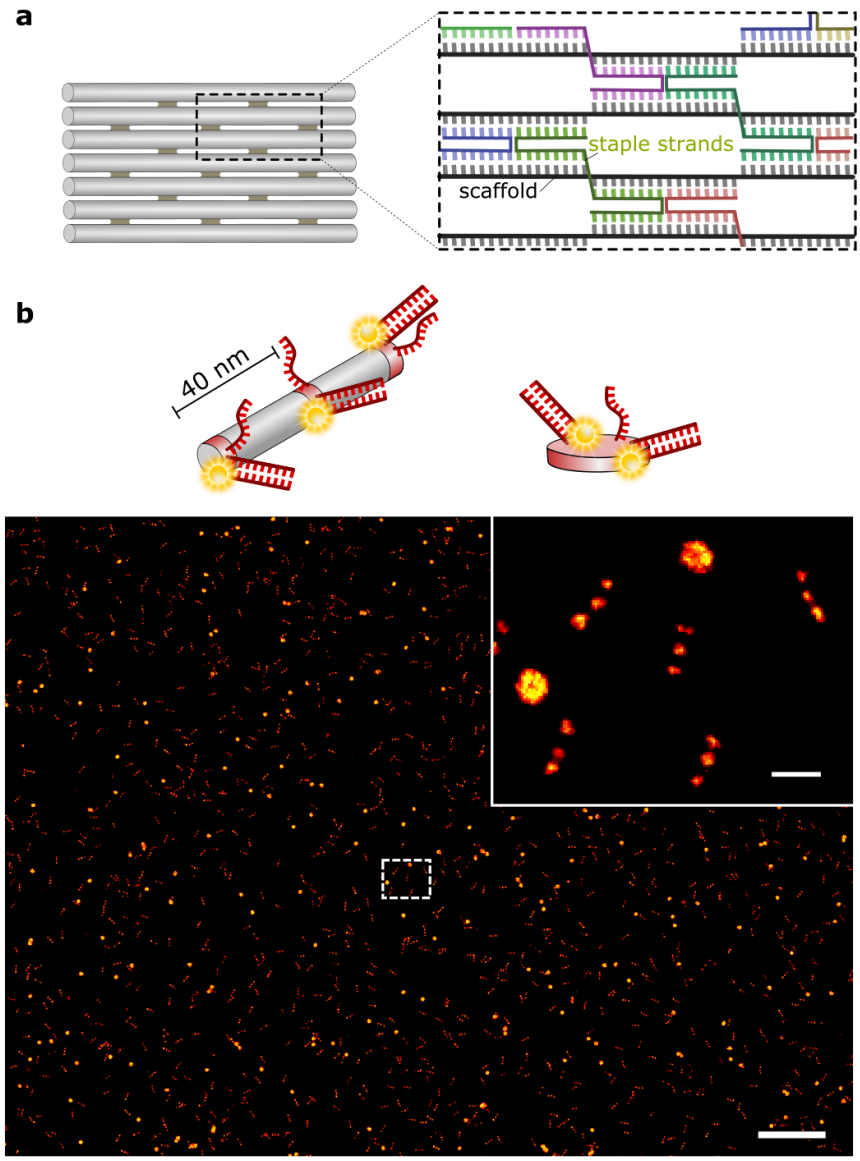

Figure 2.10: DNA origami and its use in DNA-PAINT. **(a)** DNA origami describes the assembly of a nanostructure by folding a long, single-stranded scaffold strand (grey) with multiple, short staple strands (coloured strands) [19]. Extended staple strands can be used to attach modified binding sites, e.g. DNA-PAINT docking sites, to a DNA origami structure. **(b)** DNA-PAINT imaging of DNA origami on commercially available slides with different 2D structures. Note, docking and imager strands in schematic drawing are not to scale. Scale bars: 1 µm, inset: 100 nm.

PAINT is widely used to inspect DNA origami structures, such as 3D polyhedric structures or DNA wire routing [68, 103].

2.3.2 DNA strand displacement

In order to use DNA nanostructures such as DNA origami as molecular machines, sensors or chemical reaction networks, they typically need to provide dynamic functions which are often realised by DNA strand displacement reactions [104]. For long and stable double stranded DNA with a high melting temperature, strand displacement by an invading, complementary single stranded DNA is initiated by fraying of a dsDNA base pair and formation of a branch by partial hybridisation of the invading strand. Subsequently, the branch can migrate along the dsDNA in a random walk and lead to dissociation of the original dsDNA [104, 105]. This displacement of dsDNA by stochastic branch migration is typically orders of magnitudes slower than association of ssDNA, it is slower than randomly occuring base pair fraying and the initialisation of branch migration carries a thermodynamic penalty [106]. The rate of strand displacement can primarily be influenced by the concentration of invading strands, as a higher concentration increases the chances of branch formation after fraying.

This does not necessarily relate to the total concentration of invading ssDNA, but rather to the local concentration in vicinity of the dsDNA, which can be increased by tethering the dsDNA and the invading ssDNA within close proximity to each other. The effectiveness of this so-called proximity-induced strand displacement is also influenced by the dsDNA sequences and the design of the spacers with which the strands are tethered [107]. Another option to increase the displacement rate is by using a single stranded, so-called toehold extrusion on the dsDNA, to which the invading strand can transiently bind, increasing the chance for branch migration and dissociation of the double strand before the invading strand dissociates. This toehold-mediated strand displacement can increase exchange rates by more than six orders of magnitude [108].

Parameters of these dynamic schemes, such as kinetic rates, can be predicted by numerical modelling of the random walk behaviour. Based on Monte Carlo or Molecular Dynamics simulations, some coarse grain models take into account the connectivity of DNA along its backbone, hydrogen bonds, stacking and steric effects [109].

2.3.3 Proximity assays

The strong dependence of the strand displacement rate on the proximity of the invading and dsDNA strands as described above, allows these interactions to be used as a proximity assay. Detecting proximity of targets is widely applied, e.g. for the detection of protein-protein interactions, homo- or hetero-dimer formation and enzyme or antibody interactions [114]. Additionally, proximity assays can be used for increased labelling specificity, e.g. for immunostaining, by requiring double (in proximity) labelling of different epitopes of a single target. In DNA based proximity assays, this is typically achieved by labelling the targets with proximity probes, containing DNA strands which interact if located within close distance. The interacting DNA is amplified and labelled with fluorophores.

Figure 2.11 a demonstrates the principle underlying the proximity ligation assay (PLA) [110, 112]. The DNA strands on the proximity probes hybridise to a connector ssDNA and undergo enzymatic DNA ligation, resulting in a new dsDNA present in the sample. The sequence is subsequently amplified by enzyme-based methods, e.g. by polymerase chain reaction (PCR) for *in vitro* experiments [110] or rolling circle amplification for in situ measurements [115]. However, it has been shown that PLA is often incompatible with quantitative measurements due to signal saturation at high target densities, possibly because of steric effects inhibiting the amplification [116].

The enzymatic reactions required for ligation and amplification in PLA can be replaced by simpler procedures, as demonstrated by a method called proxHCR (HCR – hybridisation chain reaction) [113], the principle is shown in figure 2.11 b. The DNA strands of the proximity probes 1 and 2 form stem loop structures which can be opened by an activator ssDNA. This allows invasion of the opened stem loop structure 1 into proximity probe 2, exposing a DNA domain in probe 2 which initiates DNA amplification by hybridisation chain reaction [113]. HCR is a purely DNA based amplification mechanism. Two populations of stem loop structures remain monomeric if mixed, but if a single stranded activation sequence is present, the stem loop structures are opened alternately by toehold mediated strand displacement and polymerise [117, 118]. If the HCR stem loop structures are labelled with fluorophores, strongly amplified fluorescence signal of the proximity assay can be achieved.

In both techniques described above, the degree of signal amplification is difficult to quantify precisely, making quantitative imaging difficult. 1000-fold amplifi-

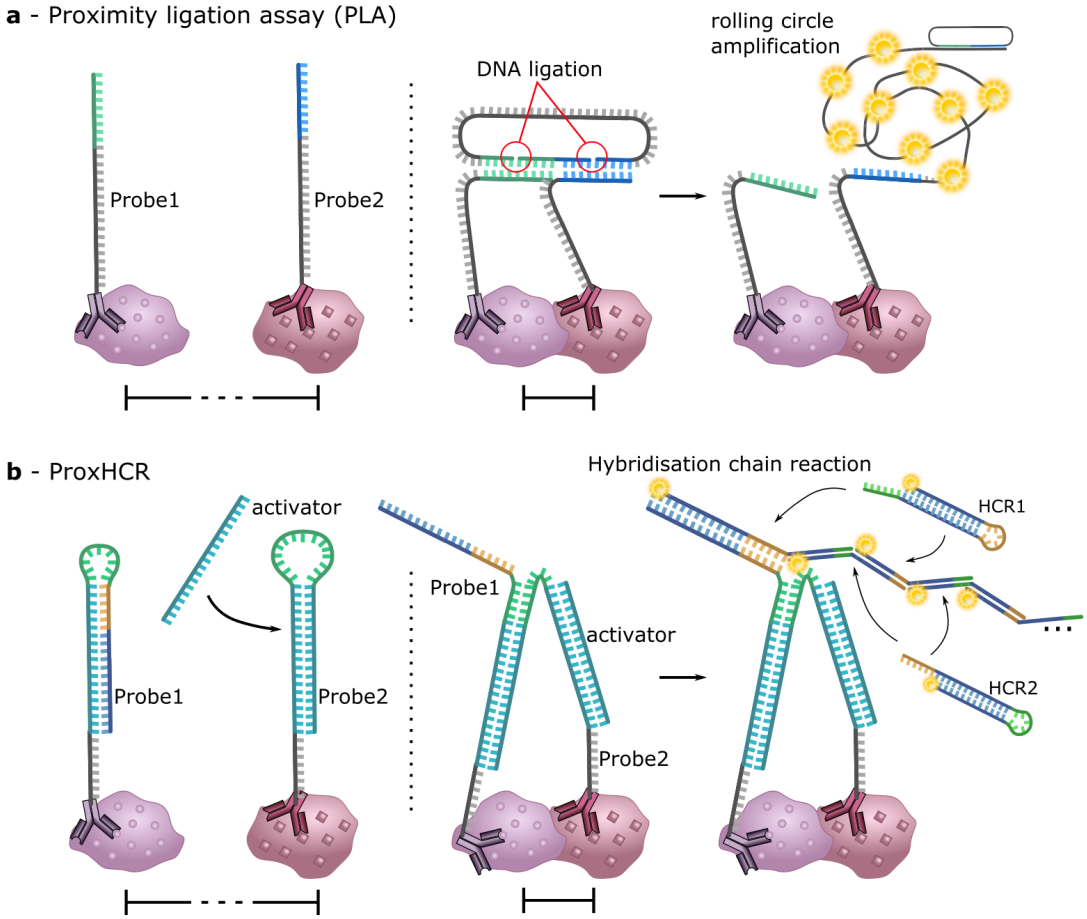

Figure 2.11: DNA-based proximity assays. **(a)** Proximity ligation assay (PLA) [110–112] on a protein-protein pair. The proteins are labelled with two probe oligonucleotides, e.g. via antibodies. Proximity of the probes allows ligation of oligonucleotides to form a new DNA strand otherwise not present in the sample, which can be detected after amplification by rolling circle synthesis and fluorescent labelling. **(b)** proxHCR [113] also uses oligonucleotide proximity probes, which initialise a hybridisation chain reaction (HCR) of fluorescently labelled strands after an activator strand is added to the sample. Note that the drawings only illustrate the underlying principles and show slight deviations from published DNA designs.

cation can be achieved [119], and while this gives strong fluorescent signals detectable in widefield mode, the strong amplification also considerably increases the size of the label and consequently makes sub-diffraction localisation of the protein interaction essentially impossible.

2.4 Biological samples for super-resolution microscopy

With advances in optical super-resolution microscopy being primarily driven by the demand of biomedical science for better imaging techniques, it is important to show the applicability of a new method *in situ*, that is by imaging of targets in a cell or tissue section. Among the most popular structures that are commonly shown are proteins of the cytoskeleton, particularly actin filaments and microtubules [20, 120–124]. The structure of actin filaments and microtubules is well studied and shows a distinct network of long biopolymer chains throughout a cell, and are thus often used as test structures for imaging techniques. Furthermore, they are present in all (eukaryotic) cells [86], antibodies are readily available, and the size of the structure is well below the diffraction limit and can show the capability of a super-resolution technique. In this thesis, microtubules in fixed cells were imaged as a model sample for different DNA-PAINT approaches.

Microtubules, which are involved in intracellular transport and influence the position of membrane-enclosed organelles, are rigid, hollow cylindrical structures with an outer diameter of 25 nm. The tubular structure is formed of 13 subunits which are oriented in a helical lattice. Each subunit consists of a heterodimer of alpha and beta tubulin, bound by strong noncovalent bonds. The position of the subunits with multiple contact points results in a stiff and straight microtubule structure [86]. With single molecule super-resolution techniques such as STORM and DNA-PAINT, a hollow tubular structure has been resolved, with apparent diameters ranging from ~20 nm to ~60 nm, where the variations of diameter can be attributed to labelling with large antibodies [125, 126]. Often however, a punctate instead of continuous and tubular structure is shown [20, 22, 70], which can originate from limited imaging resolution, insufficient labelling density or degeneration of microtubules during a fixation step.

Another well established target for super-resolution imaging are proteins and structures involved with cardiac excitation-contraction coupling [128–132], which

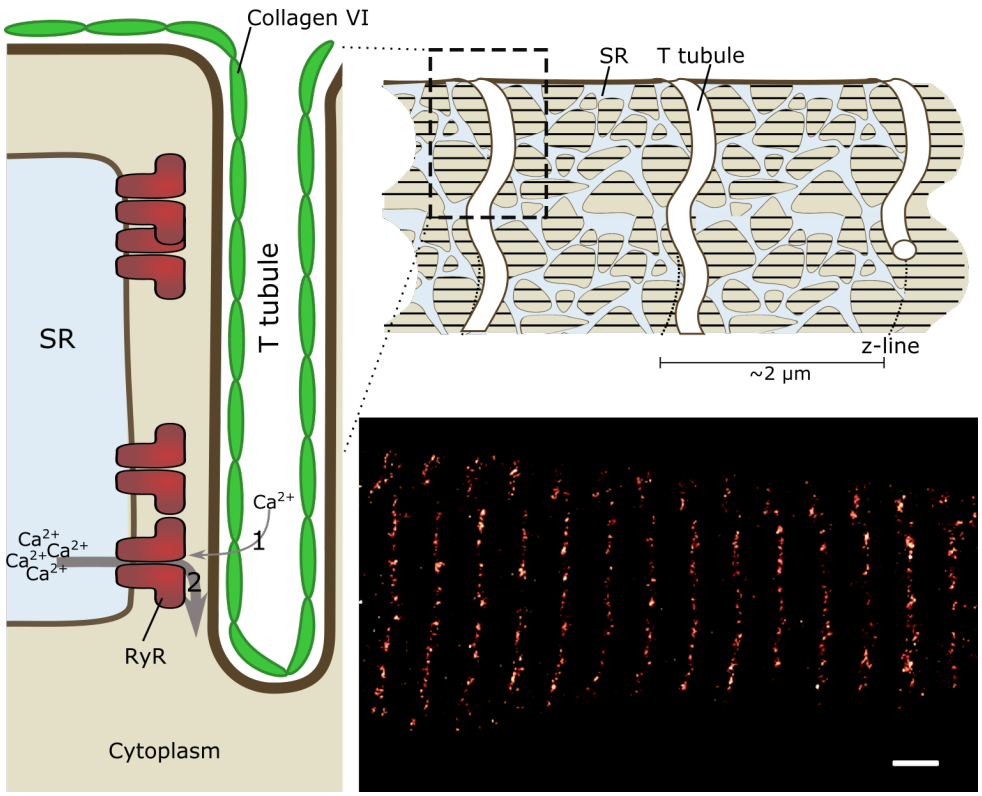

Figure 2.12: Cardiomyocyte architecture. The cell membrane extends into the cell through transverse-tubules (t-tubules) in a repetitive pattern. As the t-tubules represent an extension of extracellular space, proteins of the extracellular matrix, such as collagen, are present [127]. T-tubules are an important location for Ca^{2+} exchange. Calcium uptake into the cell via the t-tubules opens ryanodine receptors (RyR) on the sarcoplasmic reticulum (SR), which release the stored, highly concentrated Ca^{2+}, leading to contraction of the muscle cell. Bottom right: DNA-PAINT image of RyR in a fixed cardiomyocyte. Scale bar: 2µm.

is briefly described below. Figure 2.12 gives an overview of these structures in a schematic drawing of a cardiomyocyte section. A functioning, regular heart beat relies on synchronised contraction of cardiomyocytes. The contraction of each cell is initiated by an external action potential which causes the depolarisation of the cardiomyocyte. Its cell membrane, the sarcolemma, shows deep invaginations at a regular distance, so called transverse tubules (t-tubules), through which the depolarisation can spread. This activates voltage gated calcium channels in the t-tubules, and leads to a slight increase in calcium concentration in the cytosol [133]. Large reservoirs of calcium ions (Ca^{2+}) are stored within the cell in the sarcoplasmic reticulum (SR). Parts of the SR are located close to the t-tubule membranes with distances down to 12 – 15 nm [134, 135]. Ryanodine receptors (RyR) are located on the SR membrane, which get activated upon the increase of Ca^{2+} concentration during depolarisation of the cell. These receptors can exceed sizes of 2 MDa and have a size of $\sim 30 \times 30\,\mathrm{nm}^2$ [133]. The RyR is a calcium channel which, when activated, leads to Ca^{2+} influx from the sarcoplasmic reticulum into the cytosol. This calcium induced calcium release initiates the mechanical movement of actin and myosin in myofibrils, resulting in contraction of the cardiomyocyte [136]. The ryanodine receptor has been imaged with super-resolution microscopy by (d)STORM [132, 137] and DNA-PAINT [3].

3. Methods

In this chapter, materials and methods which are relevant to this thesis are described, split into three sections. First, details on sample preparation are given, followed by a description of the imaging setup and finally, image acquisition and analysis procedures of super-resolution images, widefield fluorescent and transmission images and atomic forces micrographs are described.

Preparation of biological cell and tissue samples was carried out by Alexander H. Clowsley, Anna Meletiou and Rikke Morrish (section 3.1.4). A first protocol for labelling polystyrene microspheres with oligonucleotides was tested in proof-of-principle experiments by Simona Frustaci (section 3.1.6). The optical setup described in section 3.2 and the software environment described in section 3.3.2 was the work of Christian Soeller, Ruisheng Lin and David Baddeley.

3.1 Sample preparation

This section lists DNA strands used in this thesis, including design techniques and preparation. Preparation and labelling of biological samples, i.e. fixed, isolated cells and tissue sections, is described, as well as the preparation of synthetic samples, i.e. streptavidin-coated microspheres and DNA origami.

3.1.1 Oligonucleotide design and preparation

Some DNA sequences for basic imager and docking strands were obtained from previous publications. These sequences typically have mean imager-docking binding times of several hundred milliseconds and are orthogonal with respect to their hybridisation properties for cross-talk free multiplexed imaging [18, 20, 22]. All other oligonucleotide sequences were designed using freely available on-

line applications which facilitate the prediction of thermodynamic parameters and secondary structures,

- the "DINAMelt Web Server" [138–140], which predicts the free energy difference ΔG and the melting temperature T_m for hybridisation of two single strands,
- "NUPACK" [141, 142], an application which allows both the analysis of equilibrium states of an arbitrary number of oligonucleotide sequences as well as the design of DNA (and RNA) sequences to achieve a desired secondary structure, based on the nearest neighbour model [143]. Ion concentrations, oligonucleotide concentrations, temperature and unpaired bases (dangles) are taken into account, resulting secondary structures are visualised and the probability for formation of each base pair given,
- the commercial "IDT oligo analyser tool" (Integrated DNA Technologies, Coralville) [97], which provides thermodynamic properties (e.g. T_m) of oligonucleotides, as well as information on potential self-dimer formation, hybridisation of different sequences and possible stem-loop structure (hairpin) formation.

For the design of new oligonucleotide sequences, the following aspects were considered:

- Orthogonality of the new sequence to all other DNA structures in the sample that it should not interact with. This can be achieved by minimising the number of complementary bases. For strands involved in DNA-PAINT transient binding, the overlap was kept below three consecutive base pairs.
- Affinity to other strands depending on application. Typical choices for mean binding times are $0.1-1\,\mathrm{s}$ for imager-docking interactions and $\gg 1\,\mathrm{h}$ for effectively permanently binding strands. The affinity can be tuned with the length of complementary domains and the GC ratio (amount of guanine/cytosine bonds to total base pairs), e.g. typically a 9 base pair overlap for imager-docking binding with a GC ratio of 22% for imager strands.
- Unwanted secondary structures were avoided, e.g. the formation of self-dimers or stem-loop structures with high melting temperature. In particular, a high amount of consecutive guanine (more than three) were avoided

to prevent formation of guanine quadruplexes, secondary structures which can form in guanine-rich sequences [144].

- Guanine in direct vicinity to a fluorescent dye was avoided, as fluorescence quenching by guanine has been reported [18].
- In some cases, guanine content in imager sequences was minimised or completely avoided. This criterion was adopted following experiments that suggested that increasing guanine content correlates with increased nonspecific binding in biological samples (see chapter 6).

Table 3.1 shows DNA base sequences used in this thesis. Oligonucleotides were obtained from Eurofins Scientific, Luxemburg, and IDT (Integrated DNA Technologies, Coralville). The strands were purified by high-performance liquid chromatography (HPLC) by the manufacturer and provided in lyophilised form. Upon delivery, DNA was resuspended in TE buffer or PBS (see section 3.1.3) at a concentration of 100 µM and stored at -20 °C. In order to avoid a high number of freeze-thaw cycles, regularly used oligonucleotides were split into small aliquots. Eurofins and IDT also provided modifications, such as fluorescent dyes (Atto 655, Atto 550 and Atto 700 (Atto-tec GmbH, Siegen) for DNA-PAINT imaging, Cy3, fluorescein, Cy5 for widefield labelling), chemical linkers (amino C6 modifier and azide NHS ester modifier) and fluorescence quenchers (Iowa Black RQ, Integrated DNA Technologies, Coralville). Other fluorescence quenchers, such as DABCYL, were tested but showed increased nonspecific binding in DNA-PAINT samples.

Docking strands in biological samples were labelled with fluorescent dyes (see table 3.1) to provide immediate feedback for immunolabelling and facilitate quantifying docking strand conjugation efficiency (section 3.1.5). Before DNA-PAINT imaging and if needed because of potential spectral overlap with imager fluorescence, the dyes permanently attached to the docking strand were photobleached by illumination at high laser powers of ~45 mW on an illumination spot of ~30 µm diameter. Whenever possible, dyes with low excitation at the DNA-PAINT illumination wavelength ($\lambda_{exc} = 642/647$ nm) such as Cy3 were chosen so that permanent labelling did not interfere with super-resolution imaging.

Table 3.1: Oligonucleotide sequences in 5' to 3' direction. A - adenine, T - thymine, G - guanine, C - cytosine, dye - fluorophore modification, typically Atto 655 or Atto 700, Q - quencher modification, typically Iowa Black RQ, BIO - biotin modification, AmC6 - Amino Modifier C6, AzN - Azide (NHS Ester) modification.

Name	Sequence (5'→ 3')
P1 imager [20]	CTA GAT GTA T-dye
P1e+ imager	GCG ATA GAT GTA T-dye
P1long	TTT TAG TTT TCG TTT TAC TTT TCT AGA TGT AT
2iP1	dye-ATA GAT GTA T-dye
P3 imager [20]	GTA ATG AAG A-dye
P5 imager [20]	CTT TAC CTA A-dye
P5e+ imager	GCG ATT TAC CTA A-dye
AT1	TAT ATT TTA T
Perm. imager	dye-TAT ACA TCT ATC TTC ATT ATT-BIO
I1	dye-CCA CAT ACA TCA TAT TCC CTC A
I2	CAC TTC CTC ACA ATC A-dye
Perm-i	TCA CTT CCT CAC AAT CA-dye
T-i [108]	dye-CCA CAT ACA TCA TAT TCC CTC A
P1 quencher	Q-ATA CAT CTA C
P1e+ quencher	Q-ATA CAT CTA TCG C
P3 quencher	Q-TCT TCA TTA C
Perm. quencher	TAA TGA AGA TAG ATG TAT T-Q
T-q [108]	TAT TGC CTG AGG GAA TAT GAT GTA TGT GG-Q
P1 docking-bio [20]	BIO-TTA TAC ATC TA
P1 docking-bioCy3	BIO-TTA TAC ATC TA-Cy3
P1-8 docking-bio	BIO-TAA TAC ATC T
P1 docking-Am	AmC6-TTA TAC ATC TA-Cy3
3xP1	BIO-TTA TAC ATC TAA TAC ATC TAA TAC ATC TA
6xP1	BIO-TTA TAC ATC TAA TAC ATC TAA TAC ATC TAA TAC ATC TAA TAC ATC TAA TAC ATC TA
P3 docking [20]	BIO/AmC6-TTT CTT CAT TA
P5 docking [20]	BIO/AmC6-TTT TAG GTA AA
P1P3e docking	TTA TAC ATC TAT TTT TTC TTC ATT AC
P1P3P5 docking	BIO-TTA TAC ATC TAT TTT TTT CTT CAT TAT TTT TTT TAG GTA AA

Continued from previous page.

Name	Sequence (5'→ 3')
P1stabiliser	GAA AAG TAA AAC GAA AAC TAA AA
Stabiliser	AAA AAT AAT GAA GAA AAA AAT AGA TGT ATA A
B1	TGA GGG AAT ATG ATG TAT GTG GAT GAT TGT GAG GAA GTG
B10	TGA GGG AAT ATG ATG TAT GTG GAG TAG GGT GAT GAT TGT GAG GAA GTG
B15	TGA GGG AAT ATG ATG TAT GTG GAG TAG GTT GAG GTG ATG ATT GTG AGG AAG TG
B20	TGA GGG AAT ATG ATG TAT GTG GAG TAG GTG AGG TTG AGG TGA TGA TTG TGA GGA AGT G
B30	TGA GGG AAT ATG ATG TAT GTG GAG TAG GTG AGG TGG AGT GAG GTT GAG GTG ATG ATT GTG AGG AAG TG
spacer10	TCA CCC TAC T
spacer15	TCA CCT CAA CCT ACT
spacer20	TCA CCT CAA CCT CAC CTA CT
spacer30	TCA CCT CAA CCT CAC TCC ACC TCA CCT ACT TGA TTG TGA GGA AGT GAT GAT TGT GAG GAA
3perm	GTG ATG ATT GTG AGG AAG TGA GTA ATG AAG A
1perm	TGA TTG TGA GGA AGT GAG TAA TGA AGA
T-v [108]	CCA CAT ACA TCA TAT TCC CTC ATT CAA TA
PD-PAINT S1-bio	GGA AGG AGG AGA GGA GAA TAC ATC TAT ATT CTC CTC TCC TCC TTC CTT TTT TTT TTT TTT T-BIO
PD-PAINT S2-bio	BIO-TTT TTT TTT TTT TTT GGA AGG AGG AGA GGA GAA TA
PD-PAINT S1B-bio	GGA AGG AGG AGA GGA GAT TAG GTA AAT AAT CTC CTC TCC TCC TTC CTT TTT CTT CAT TAT T-BIO
PD-PAINT S2B-bio	BIO-TTT TTA ATT GAG TAT GGA AGG AGG AGA GGA GAT TA
PD-PAINT D1	AzN-TTA TAC ATC TAT TTC TTC ATT ATT CAC TTA CTA

Continued from previous page.

Name	Sequence (5'→ 3')
PD-PAINT D5	AmC6-TTT TAG GTA AAT T-dye-TTG ATT GTG AGG AAG
PD S1 tissue	GGA AGG AGG AGA GGA GAA TAC ATC TAT ATT CTC CTC TCC TCC TTC CTT TTT TTT TTT TTT TTA GTA AGT GAA TAA TGA AGA AAT AGA TGT ATA A
PD S2 tissue	CTT CCT CAC AAT CAA AAT TTA CCT AAA ATT TTT TTT TTT TTT TGG AAG GAG GAG AGG AGA ATA

Concentrations of oligonucleotides were determined on a NanoDrop 2000 spectrophotometer (Thermo Fisher Scientific, Waltham) by measuring the absorbance at 260 nm, characteristic for DNA. For fluorophore-modified DNA, the respective correction factor was taken into account.

The degree of fluorescence quenching of imager strands, e.g. by dye self-quenching or after introduction of a fluorescence quencher, was determined in bulk fluorescence measurements. Fluorescence intensities were measured in 200 µl open-top imaging chambers (section 3.1.2) on the fluorescence microscope and 50 µm above the coverslip surface to minimise fluorescence detection of fluorophores adsorbed to the coverslip surface.

3.1.2 Cleaning and passivation of coverslips and imaging chambers

For synthetic samples, i.e. microspheres and DNA origami, $22 \times 22\,\mathrm{mm}^2$ coverslips (No 1.5 Menzel Gläser, Thermo Fisher Scientific, Waltham) were cleaned successively in acetone and isopropanol (Sigma Aldrich, St Louis) in an ultrasonic bath for 10 min each. Coverslips were rinsed in ultrapure water (Milli-Q, Merck KGaA, Darmstadt) and dried. In order to prevent nonspecific binding of imager strands when imaging microspheres, the coverslips were passivated with a PLL-g-PEG (Poly(L-lysine)-graft-poly(ethylene glycol)) co-polymer (SuSoS, Duebendorf). PLL-g-PEG was stored at -20 °C in solid form, brought to room temperature before opening and subsequently dissolved in phosphate-buffered saline (PBS, pH 7.4) at a concentration of 0.1 ml/ml. Cleaned coverslips were

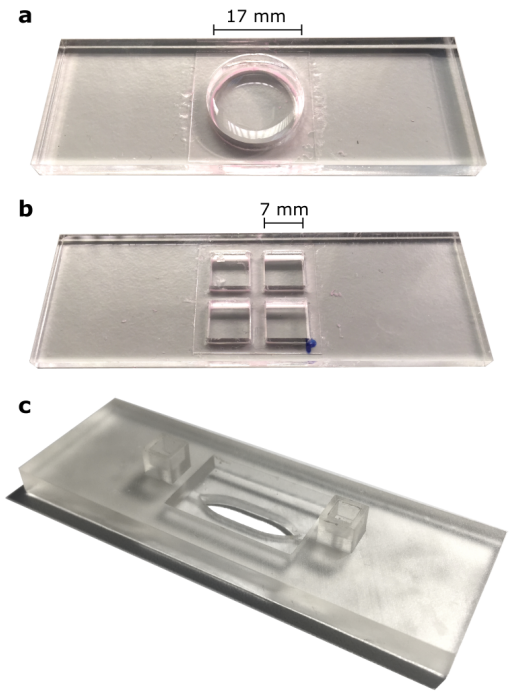

Figure 3.1: Open-top and 3D printed imaging chambers. **(a)** Imaging chamber used for biological samples. The size of the opening fits large tissue sections. **(b)** 2×2 open-top imaging chamber for synthetic samples (microspheres and DNA origami). The reduced size minimises solution consumption and increases comparability. **(c)** 3D printed macrofluidic chamber, which can be used with an external fluid handling system to enable solution exchange without manual interference during imaging.

coated with PLL-g-PEG solution, incubated for ≥ 2 h and rinsed with ultrapure water.

For mounting biological samples, coverslips were cleaned by dipping in methanol, saturated with NaOH, and subsequent multiple dipping in deionised water. Coverslips were left to air dry, before being coated with approx. 100 µl diluted 0.005% poly-L-lysine (Sigma-Aldrich, St Louis) for 15 min. Poly-L-lysine solution was removed and can be reused.

Figure 3.1 a shows imaging chambers used in this thesis for holding biological samples [145]. Coverslips were attached to a 3 mm strong perspex (PMMA) slide with a circular opening via a two component, quickly setting silicone (Pinkysil ratio 1:1, Barnes, Auckland). The chambers hold a fluid volume of ~0.5 ml

and for increased rigidity, perspex slide thickness was increased to 5 mm. For imaging of synthetic samples, perspex slides with 2 × 2 openings of smaller volume (~100 – 150 µl) were used. These chambers are shown in figure 3.1 b and reduce the consumption of solutions and cleaned coverslips, and increase comparability between different samples in adjacent wells. 3D printed chambers for fluid handling shown in figure 3.1 c are described in detail below (section 3.1.7).

3.1.3 Buffer preparation

Oligonucleotides for antibody conjugation were stored in phosphate-buffered saline (PBS, Sigma Aldrich, St Louis) at pH 7.4, all other oligonucleotides were stored in 1× TE buffer (Tris ethylenediaminetetraacetic acid, Sigma Aldrich, St Louis), diluted from 100× stock with ultrapure water and the pH adjusted to 8.0. For imaging of synthetic samples, TE buffer (pH 8.0) was diluted to 0.5× and 500 mM NaCl added (from here on called microsphere imaging buffer). For imaging of biological samples, buffer C as published by Jungmann et al. [20] was used – 1× PBS at pH 8 and with the NaCl concentration adjusted to 500 mM.

Buffer pH was measured with a pH meter (Mettler Toledo, Columbus). The pH meter was calibrated with reference solutions at pH 4 and pH 7 (Sigma-Aldrich, St Louis) in a two point calibration procedure.

3.1.4 Cell and tissue preparation

For imaging of microtubules and mitochondrial proteins of isolated cells, COS-7 cells were seeded on coverslips and left to grow overnight in DMEM (Dulbecco's Modified Eagle Medium) under 5% CO_2 at 37 °C. The medium was removed and the cells were fixed in ice-cold methanol for 15 min at -20 °C and washed three times with PBS.

The use of rat and murine tissue was approved by the University of Exeter ethics committee, the use of porcine tissue by the University of Bristol ethics committee. Tissue was fixed in 2% PFA (paraformaldehyde) in PBS for 1 hour at 4 °C. For cryoprotection, tissue samples were immersed in PBS containing stepwise increased concentrations of sucrose up tp 30%, with added 10% NaN_3. The tissue chunks were frozen with isopentane (Sigma-Aldrich, St Louis), cooled in liquid nitrogen and kept frozen for storage. Tissue sections of 10 - 15 µm thickness

were obtained by cryosectioning, deposited onto cleaned, poly-L-lysine coated coverslips (section 3.1.2) and stored at -20 °C.

3.1.5 Docking strand-antibody conjugation and immunolabelling

All azide- and amino-modified strands were conjugated to anti-rabbit and anti-mouse secondary antibodies (Jackson ImmunoResearch, West Grove). Conjugation was achieved by two techniques, either a commercial conjugation kit (Thunder-Link (Plus), Expedeon, Cambridge) or by adapting a click-chemistry protocol by Schnitzbauer et al. [22]. When the commercial kit was used, the manufacturer's protocol was followed. Briefly, 80 µM of oligonucleotides in PBS and the respective secondary antibody were activated with the respective Thunder-Link activation solutions for 1 h at RT, desalted and mixed at a volume ratio of 1:1. Purification of conjugated antibodies from unbound oligonucleotides was achieved by a precipitation and centrifugation step. Labelling efficiencies were checked by absorption spectrometry, facilitated by a fluorophore attached to the DNA strand.

For conjugation via click-chemistry, the antibody was connected to the oligonucleotide via a DBCO-sulfo-NHS ester bond. The concentration of secondary antibody stock was increased to at least 1.5 mg/ml and incubated with a cross-linker solution at 10:1 molar ratio. The antibody was purified by column centrifugation and incubated with the azide-modified oligonucleotide at a molar ratio of 1:15 for 1 h at RT. Unbound oligonucleotides were removed by spin filtration [22]. As with the Thunder-Link method, absorption measurements between every step of the procedure were carried out for quality control.

Prior to immunolabelling, fixed COS-7 cells were blocked with 1% BSA in PBS for 10 min. Primary antibodies against β-tubulin and the mitochondrial receptor protein TOM20 were diluted 1:200 in incubation solution (PBS with 1% BSA, 0.05% Triton, 0.05% NaN_3) and added for 1 h at RT. After repeated washing (3× for 5 min each) with PBS, secondary antibodies conjugated to a P1 docking strand for β-tubulin and P5 for TOM20 were added, diluted 1:100 in incubation solution. Secondary antibodies were removed by washing three times for 5 min each with PBS before imaging solution (buffer C, containing ~0.5 nM imager strands) was added.

Fixed tissue sections were rehydrated with PBS and blocked with 4 droplets of Image-iT FX signal enhancer (Thermo Fisher Scientific, Waltham) for 1 h at RT. The tissue sections were incubated with primary antibodies in incubation solution (1:200) overnight at 4 °C. Primary antibodies used were ryanodine receptor (RyR) 2-specific antibodies (MA3-916, mouse, Thermo Fisher Scientific, Waltham and HPA016697, rabbit, Sigma Aldrich, St Louis), collagen VI specific antibody (ab6588, rabbit, Abcam, Cambridge) and TOM20-specific antibody (SC-30110, Santa Cruz Biotechnology, Dallas). For staining runs involving multiple primary antibodies, labelling was carried out simultaneously. After incubation with primary antibodies, tissue sections were washed three times with PBS for 15 min each. Afterwards the appropriate secondary antibodies (Jackson ImmunoResearch, West Grove) conjugated to docking strands were added, 1:100 in incubation solution. After 2 h at RT, the tissue sections were washed four times with buffer C for 15 min each.

3.1.6 DNA origami and microsphere preparation

DNA origami structures with customised docking strands (P1P3P5 docking) were obtained readily folded in solution from Gattaquant, Hiltpoltstein. Docking strands were arranged on a flat DNA origami structure in a 3×3 grid with a nearest-neighbour distance of 30 nm. DNA origami were stored at -20 °C in small aliquots to avoid freeze-thaw cycles. The protocol for immobilisation on the coverslip was adapted from that provided by the supplier, by including an additional surface passivation step. To prevent nonspecific imager binding to the surface, the cleaned coverslip, attached to a 2×2 open chamber, was incubated with PLL-g-PEG/PEG-biotin(20%), a Poly(L-lysine)-graft-poly(ethylene glycol) and Poly(L-lysine)-graft-poly(ethylene glycol)-biotin (15-25%) mix of co-polymers (SuSoS, Duebendorf) for 2.5 h at a concentration of 0.1 mg/ml in PBS (pH 7.4). The chambers were washed three times with PBS and incubated with 50 µl BSA-biotin at 1 mg/ml (Gattaquant, Hiltpoltstein) in PBS for 5 min. BSA-Biotin was removed, the chambers washed three times with PBS and incubated with 50 µl neutravidin solution at 1 mg/ml (Gattaquant, Hiltpoltstein) in PBS for 5 min. The chambers were washed three times with PBS containing 10 mM $MgCl_2$. DNA origami were diluted in PBS with 10 mM $MgCl_2$ at 1 µl in 50 µl buffer and added to the chambers for 5 min. Red fluorescent beads of 100 nm diameter (Fluospheres carboxylate-modified microspheres F8801 (580/605), Thermo Fisher Scientific, Waltham) were added as fiducial tracers.

For imaging by atomic force microscopy (AFM), a 10 mm Mica disc (Agar Scientific Ltd, Stansted) was freshly cleaved. After incubation of the Mica sheet with 10 µl TE buffer with additional 20 mM $MgCl_2$ for 1 minute, 5 µl DNA origami in solution were added for an additional incubation time of 2 minutes. The sample was briefly dipped into a mixture of ethanol and ultrapure water (EtOH:H_2O 70:30) and transferred for several seconds into 100% ethanol. Before imaging, the samples were fully air dried.

Functionalised colloidal particles were obtained from Microparticles GmbH, Berlin. Streptavidin-coated polystyrene (PS) microspheres were obtained with a nominal diameter of 500 nm and 2 µm, streptavidin-coated poly(methyl methacrylate) (PMMA) microspheres with a diameter of 100 nm and biotin-coated PS microspheres with a diameter of 500 nm. 500 nm streptavidin-coated microspheres were provided at 10 mg/ml and a nominal biotin-binding capacity of 500 pmoles per mg, tested with biotin-fluorescein. For attachment of docking strands, streptavidin-coated microspheres were dispersed to a concentration of 0.5 mg/ml in TE buffer containing 100 mM NaCl and 1 µM of the respective biotin-modified oligonucleotide sequence. This corresponds to a 4× excess concentration of DNA. For microspheres labelled with multiple biotinylated docking strands at a fixed ratio, the oligomeres were mixed thoroughly prior to the addition of the particles to ensure a stochastic distribution of DNA strands on biotin binding sites. Microspheres with oligonucleotides were incubated on a rotor at RT overnight. Unbound DNA was removed by 4× repeated centrifugation at 13.6k rpm for 5 min each, removal of the supernatant and redispersion in TE buffer. Labelled microspheres were stored in TE buffer at 4 °C and could be used for up to several months. The same protocol was followed for microspheres of different diameters, with the oligonucleotide concentration adjusted to 4× excess of the binding capacity, as specified by the manufacturer per volume of particle stock dispersion.

Labelled microspheres were deposited on PLL-g-PEG coated coverslips, as shown in figure 3.2. The PLL-g-PEG coating of the coverslip largely prevents adsorption of the microspheres. Only a small amount (0.5 – 1 µl) of the microsphere solution was deposited onto the coverslip, so that most of the solution evaporated within 5 min. The microspheres were covered only by a thin remaining liquid film which was monitored in widefield transmission imaging (compare figure 3.2 b), drying of this film was avoided to prevent damage of the oligonucleotides. As previously observed for polystyrene microparticles, a “coffee ring” shape re-

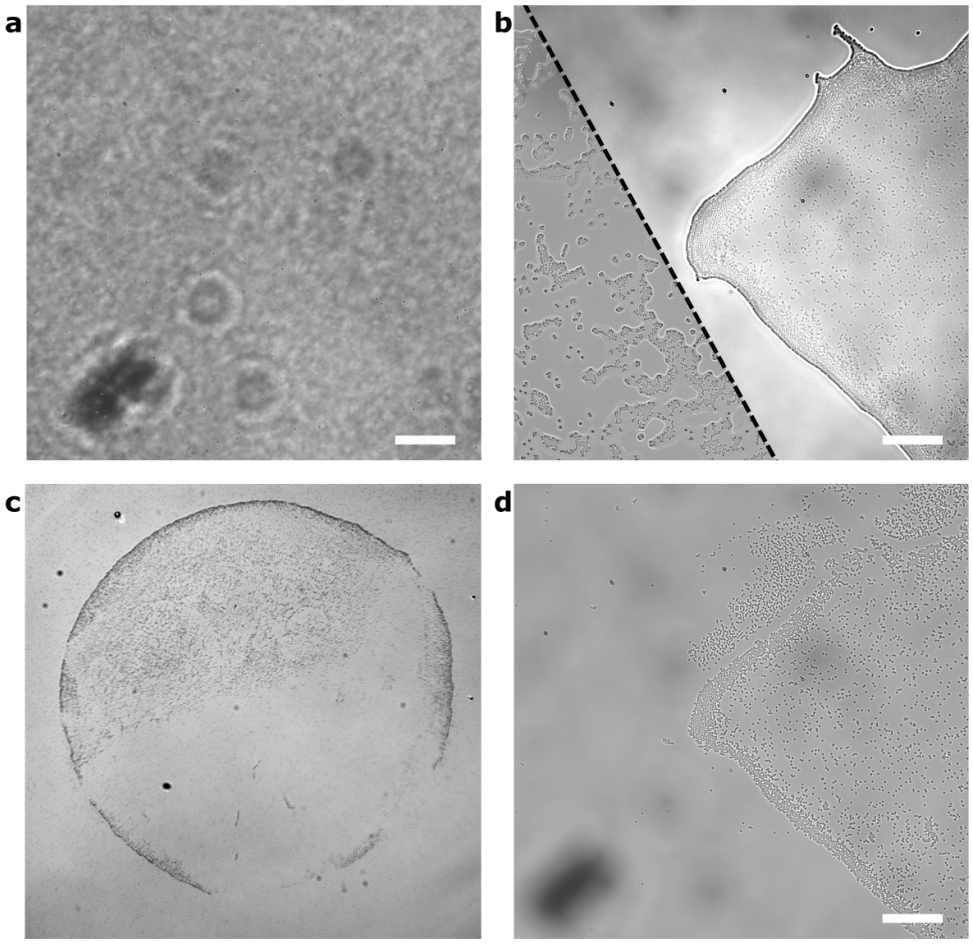

Figure 3.2: Deposition of functionalised microspheres. **(a)** Microspheres in solution on a PLL-g-PEG coated coverslip, few adsorb to the surface. **(b)** Two areas on the coverslip after partial evaporation of the solution, microspheres were fixed on the coverslip surface. A thin film of buffer surrounding the spheres can be seen. **(c)** Overview image shows "coffee-ring" structure of attached microspheres. **(d)** A high proportion of microspheres remained attached to the coverslip after imaging buffer was added, same region of interest as shown in (b), right. Scale bars: 20 µm. Diameter of "coffee-ring" approx. 1 mm.

mained [146]. The inhomogeneous distribution of microspheres was beneficial to allow a broad choice of microsphere densities for DNA-PAINT imaging. After microspheres adsorb to the surface, imaging buffer was added to the chamber, freely diffusing microspheres were removed by repeated (3×) washing of the chamber with imaging buffer.

3.1.7 3D printing of sample chambers

3D printed structures, such as fluidic imaging chambers, were designed with the commercial CAD (computer aided design) software Solidworks (Dassault Systèmes, Vélizy-Villacoublay). Structures were designed as single, connected parts and did not contain any features smaller than 0.5 mm. The models were saved in the programmes own file format (.sldprt) for further editing, and exported in a more widely used .stl file format for 3D printing.

Structures out of polylactic acid (PLA) were printed by fused filament fabrication (FFF), i.e. deposition of a continuous flow of melted, viscous PLA in lines and layers, which are solidified by rapid cooling. For printing by FFF, the .stl files were edited with the 3D printing software Simplify3D, which allows basic scaling and rotation of the printed structure, as well as arranging the position on the printing platform. Simplify3D was also used for hardware control of the MakerGear M2 3D printer (MakerGear, LLC, Beachwood). General critical printing parameters were the temperature of the extrusion nozzle of 215 °C to ensure melting of the PLA, the distance from extrusion nozzle to printing platform of ~0.3 mm and the printing platform temperature of 70 °C, to ensure adhesion of the PLA to the platform during the printing process.

Stereolithography, i.e. 3D printing by photopolymerisation of a resin, was used for printing with higher precision and of watertight structures. Structures were printed on a Form 2 printer (Formlabs Inc., Somerville), using standard clear resin (Formlabs Inc., Somerville). .stl files were edited with the corresponding software, attention was paid to having support structures only in non-critical areas. After printing, remaining liquid resin was washed off in a bath of isopropyl alcohol and the structure left to dry. For additional rigidity, the printed structures were cured under UV light for 1 h.

Figure 3.3 shows the cross-section through an assembled, 3D printed sample chamber as a schematic drawing. For microsphere imaging, a clean, PLL-g-PEG coated coverslip was attached with Pinkysil silicone (Barnes, Auckland)

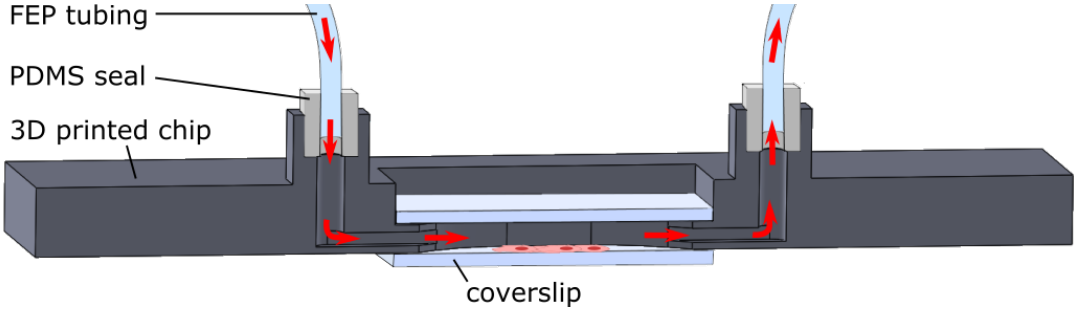

Figure 3.3: Cross-section through assembled 3D printed sample chamber. Input and output flow through 0.1" tubing, which were connected to the chamber with a PDMS seal. The imaging chamber in the centre of the structure was sealed on both sides with a coverslip. Red arrows indicate flow of solution.

to the 3D printed chamber (shown in dark grey). Microspheres were deposited by pipetting onto the sample coverslip. For imaging of biological samples, the coverslip containing the sample was dried along the edges, attached to the 3D printed chamber by Pinkysil and rehydrated by pipetting of buffer C into the chamber. The imaging chambers were subsequently sealed by attaching a second coverslip to the top of the 3D printed chamber, this results in an imaging chamber with a volume of approx. 140 µl. For input and output of solutions, 0.1" fluorinated ethylene-propylene (FEP) tubing was attached to the chamber with a PDMS seal.

3.2 Imaging setup

In this section, the optical setup is described, including methods for drift reduction and correction, and spectral multiplexing. Additionally, the fluidic setup is shown.

3.2.1 Fluorescence microscope

DNA-PAINT images were acquired on two nearly identical systems, based around Nikon Eclipse Ti-E inverted microscopes (Nikon, Tokyo). Differences between systems are described below. Figure 3.4 shows the optical layout. A continuous wave diode laser at 642 nm with a power of 140 mW (Omikron LuxX, Rodgau), using a 640/8 clean-up filter (MaxDiode), and a 561 nm laser with 200 mW maximum output Jive-200 laser (Cobalt, Solna) were used as excitation light

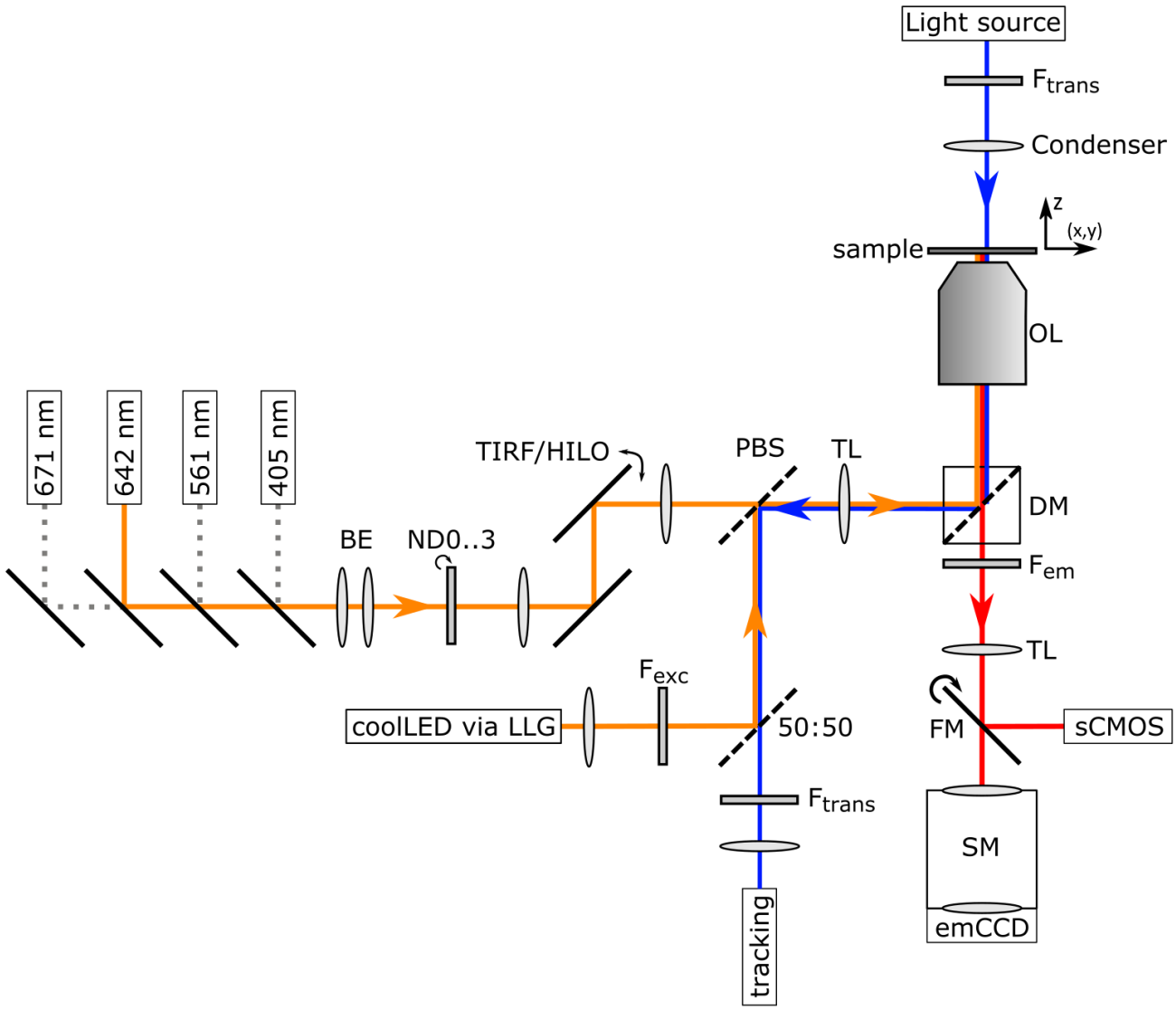

Figure 3.4: Optical setup of the fluorescent microscope. For detailed description see sections 3.2.1 - 3.2.3. Illumination path (orange): beam expander – BE, neutral density filter wheel – ND0..3, Mirror with fine adjustment screw for TIRF/HILO mode imaging – TIRF/HILO, low intensity fluorescence excitation via liquid light guide – coolLED via LLG, excitation filter – F_{exc}, polarising beam splitter – PBS, tube lens – TL, dichroic mirror – DM, TIRF oil immersion objective lens – OL. Emission path (red): emission filter – F_{em}, flip mirror for choice of camera output port – FM, Andor Zyla 4.2 sCMOS – sCMOS, splitter module – SM (see figure 3.6), iXon Ultra emCCD camera – emCCD. Transmission path for drift detection (blue): transmission filter – F_{trans}, auxiliary camera for drift detection – tracking.

sources. For coarse attenuation, a filter wheel (Thorlabs, Newton) containing a set of neutral density filters (empty, ND.5, ND1.0, ND2.0, ND3.0) in the illumination light path was used. For widefield fluorescence illumination, an LED light source was used, pE-400 (CoolLED Ltd., Andover), in combination with matching excitation filters.

The laser was focussed into the sample to an illumination area with a diameter of approx. 30 µm through a 60× APO oil immersion TIRF objective lens (Nikon, Tokyo) with a numerical aperture of 1.49. The objective lens was permanently fixed to the microscope body via a custom made aluminium holder. The focus position along the optical axis was controlled by a piezo objective lens holder, PIFOC P-725, (Physik Instrumente GmbH & Co. KG, Karlsruhe), the region of interest in lateral position by a motorised x-y stage (used with M-229-25S High-Resolution Linear Actuator, Physik Instrumente GmbH & Co. KG, Karlsruhe). The lateral position was adjusted before starting image acquisition with a manual controller, which was switched off for imaging to reduce unwanted sample movement. The illumination mode from total internal reflection (TIRF) to highly inclined illumination (HILO) was adjusted by changing the angle of illumination via a mirror in a conjugate image plane in the illumination path.

Fluorescence emission light was spectrally filtered from excitation light via interchangeable filter cubes. Figure 3.5 shows the filter settings for the commonly used fluorophore Atto 655. Because of the narrow illumination spectrum, no excitation filter was used. Cut-off of the dichroic mirror was at 660 nm, FF660-Di02 (Semrock, IDEX Health & Science LLC, Lake Forest), used in combination with an emission filter FF01-692/40-25-STR (Semrock).

For detection, an Andor Zyla 4.2 sCMOS (scientific complementary metal-oxide-semiconductor) camera (Andor, Belfast) was used. It was run in 16-bit low noise, high well-capacity mode for high dynamic range. The camera provided 560 MHz readout speed, a quantum efficiency of 82%, and had a pixel size of 6.5 µm, corresponding to 72 nm in the sample, adjusted for optimum sampling of single molecule emission.

The second system used provided images of equal quality. For excitation, a laser with 5 nm red-shifted wavelength was used, LuxX 647-140 diode laser (647 nm with a maxium output of 140 mW, Omicron-laserage Laserprodukte GmbH, Rodgau). The detection path between the microscope body and the Andor Zyla camera was extended by a 4f system of an (optional) beam splitter, used

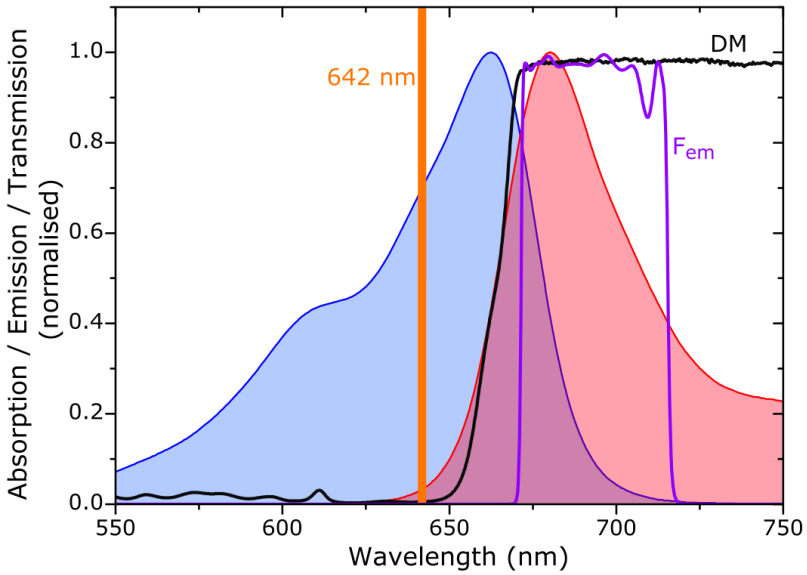

Figure 3.5: Spectral filtering for fluorophore Atto 655. Blue – absorption spectrum Atto 655 in PBS, red – emission spectrum Atto 655 in PBS, orange – excitation wavelength 642 nm, black – dichroic mirror (DM) FF660-Di02, purple – emission filter FF01-692/40.

for spectral multiplexing and biplane imaging as described below. Additionally, a second emission path enabled imaging with a smaller, low-cost machine vision camera, UI-3060CP-M-GL uEye (IDS Imaging Development Systems GmbH, Obersulm).

3.2.2 Drift correction

Thermal drift in the sample was reduced by imaging in an air-conditioned room at constant temperature and additionally, by reducing objective lens movement with a custom made solid aluminium holder. Sample drift along the optical axis was actively compensated for using a negative feedback loop. Sample movement was tracked by an auxiliary camera (UI-3060CP Rev. 2, IDS Imaging Development Systems GmbH, Obersulm) in transmission illumination mode. A wavelength was used that did not interfere with fluorescence emission and excitation, by filtering the tracking illumination and detection with a set of matching bandpass filters FB450-40 (Thorlabs, Newton). Before image acquisition, a stack of reference tracking images along the optical axis was recorded. Cross-correlation and interpolation of the tracking data with the calibration measurements en-

abled determination of both lateral displacement and defocus [147]. Whenever drift along the optical axis of greater than ~50 nm was detected, then the defocus was actively set to zero using the PIFOC piezo holder. Thus, defocus was constrained to approx. ±50 nm.

However, sample drift in lateral direction during long acquisition times (>1 h) typically still added up to several hundred nanometres, requiring correction in post processing. Information on lateral sample drift was obtained by cross-correlation of data from the auxiliary tracking camera with the calibration information, with position information saved to acquired imaging files. Alternatively, fiducial tracers were used and detected in the same channel as the fluorescence emission of super-resolution data.

3.2.3 Spectral multiplexing and biplane 3D imaging

Figure 3.6 a shows the detection path setup for spectral multiplexing, using the second output port of the microscope. The dichroic mirror remained unchanged (FF660-Di02, Semrock, IDEX Health & Science LLC, Lake Forest), the emission filter was replaced by a long pass BLP01-647R-25 (Semrock, IDEX Health & Science LLC, Lake Forest). Fluorescence emission was separated in a splitter module OptoSplit II (Cairn research, Faversham), containing a dichroic mirror with a cut-off wavelength of 710 nm, DC/T710 LPXXR-UF3 (Chroma Technology Corporation, Bellows Falls). For background reduction in the long wavelength channel, an additional low pass was used (SP01-785R-25, Semrock, Lake Forest). Both channels were imaged simultaneously on one half each of a camera chip, using an iXon Ultra emCCD camera (DU-897U, Andor, Belfast). The working principle in the second imaging system was equal, with a excitation/emission dichroic FF650 (Semrock, Lake Forest), an emission filter LP02-647RU (Semrock, Lake Forest), and without the additional shortpass filter in the long wavelength channel. The same camera as in single-colour detection was used (Andor Zyla 4.2 sCMOS, Andor, Belfast).

Figure 3.6 b shows the emission spectra of Atto 655 and Atto 700, with the filters used in the spectral multiplexing setup. Both emission spectra pass through the emission filter in the microscope, but get split by the dichroic mirror in the splitter module. The intensity ratio between both colour channels determined the assignment to Atto 655 vs Atto 700 for each detected single molecule event, as shown for both fluorophores in figure 3.7 b.

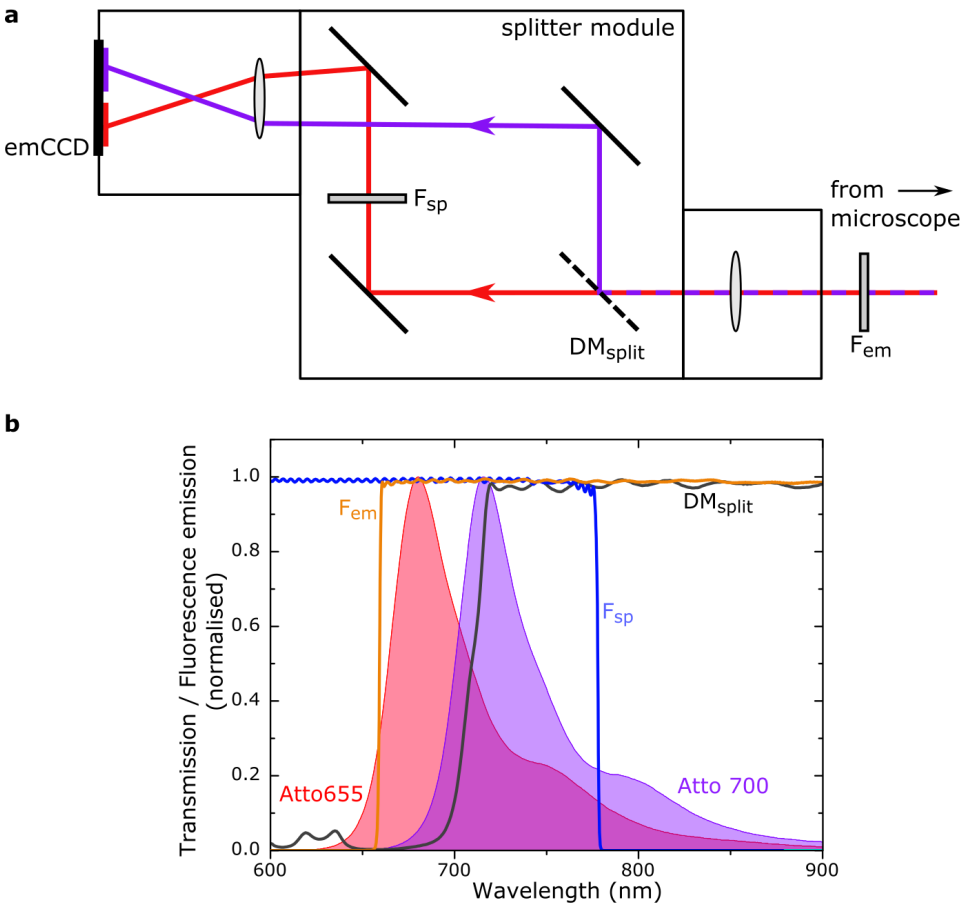

Figure 3.6: Spectral multiplexing. **(a)** Setup of the detection path, using a long-pass emitter filter F_{em}, a splitter module containing a splitter dichroic mirror DM_{split} and an additional short-pass emission filter for background suppression in the long wavelength channel F_{sp}. The two spectral channels were imaged simultaneously by two halves of the same camera chip (emCCD). **(b)** Emission spectra of Atto 655 (red) and Atto 700 (purple) and filters used for spectral multiplexing as described in (a).

Coarse adjustment of any shift between the two channels, e.g. due to chromatic aberrations, was done by adjusting the mirrors in the splitter module manually. Residual, potentially non-uniform, shift was reduced to $\leq$10 nm by calibration with a sample of sparsely distributed fluorescent beads (Dark red fluorescent, diameter of nominally 200 nm, Fluospheres carboxylate-modified microspheres F8807 (660/680), Thermo Fisher Scientific, Waltham), mounted on a sealed coverslip in ProLong Gold antifade mountant (P36930, Thermo Fisher Scientific, Waltham). As shown in figure 3.7 a, bead fluorescence was detected in both

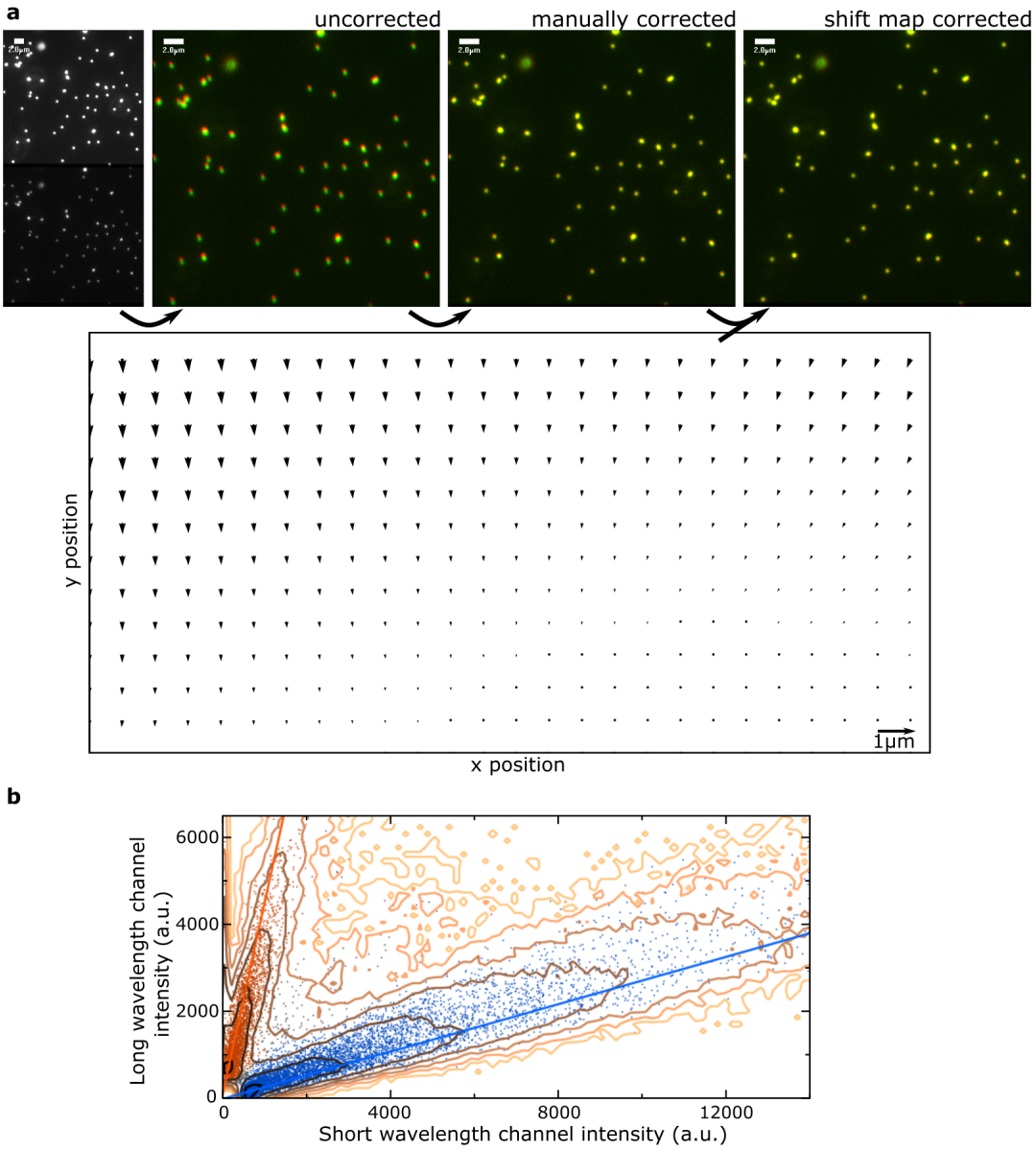

Figure 3.7: Shift correction and colour assignment for spectral multiplexing. **(a)** Steps for compensation of shift between channels using a slide with dark red fluorescent beads. Left to right: Both channels were imaged on a single chip, the long wavelength channel at the bottom. Both channels were overlaid, red – long wavelength, green – short wavelength, colocalisation was manually adjusted by adjusting the mirror angles in the splitter module, fine adjustment was done by applying a calibration shift vector map (shown below). **(b)** Colour assignment to single molecule events depending on the ratio between the two spectral channels. y-axis: long wavelength channel, x-axis: short wavelength channel, shown on a sample with Atto 700 and Atto 655 fluorophores.

colour channels. The bead sample was moved stepwise, e.g. with 4 µm steps in x and y direction to cover an area of $60 \times 60\,\mu m^2$. From the localisation data a vector field of lateral shift was calculated and used to constrain multi-channel fits, as described by Baddeley et al. [53].

For 3D imaging using the biplane method [51], the emission signal was split using the splitter module described above, but with a 50:50 non-polarising beam splitter. In one channel, a lens of focal length $f = 4\,m$ was inserted, resulting in a focal shift between the channels of $\Delta z \approx 350\,nm$, i.e. about half of the axial extent of the point spread function. Any shift between the different channels was corrected as described above. For fitting of event data, calibration point spread functions PSF(z) and PSF($z + \Delta z$) are recorded prior to image acquisition and detected events are assigned a value z which matches the calibration data the best.

3.2.4 Fluidics control

The fluidics control setup used in combination with microfluidic chips and 3D printed imaging chambers is shown in figure 3.8. A 15 ml falcon tube held plain imaging buffer, other solutions were in 2 ml microcentrifuge tubes (Fluigent SA, Le Kremlin-Bicêtre). The fluid reservoirs were connected via 0.1" fluorinated ethylene-propylene (FEP) tubing to a 10-way multiplexer ESS M-switch (Fluigent SA, Le Kremlin-Bicêtre). The output was connected via FEP tubing to the input of the sample chamber, as shown in figure 3.3. The sample output was connected to tubing leading to a fluid waste beaker. Solutions were pumped from the fluid reservoirs by applying air pressure using a MFCS-EZ flow control system (Fluigent SA, Le Kremlin-Bicêtre). Both flow control system and multiplexer were PC controlled by a commercial software (Fluigent SA, Le Kremlin-Bicêtre).

3.3 Image acquisition and analysis

In this section, imaging protocols are described, as well as the detection, analysis, post-processing and visualisation of DNA-PAINT binding events. Quantitative analysis of DNA-PAINT data (qPAINT) on microspheres is described, as well as AFM imaging of DNA origami structures.

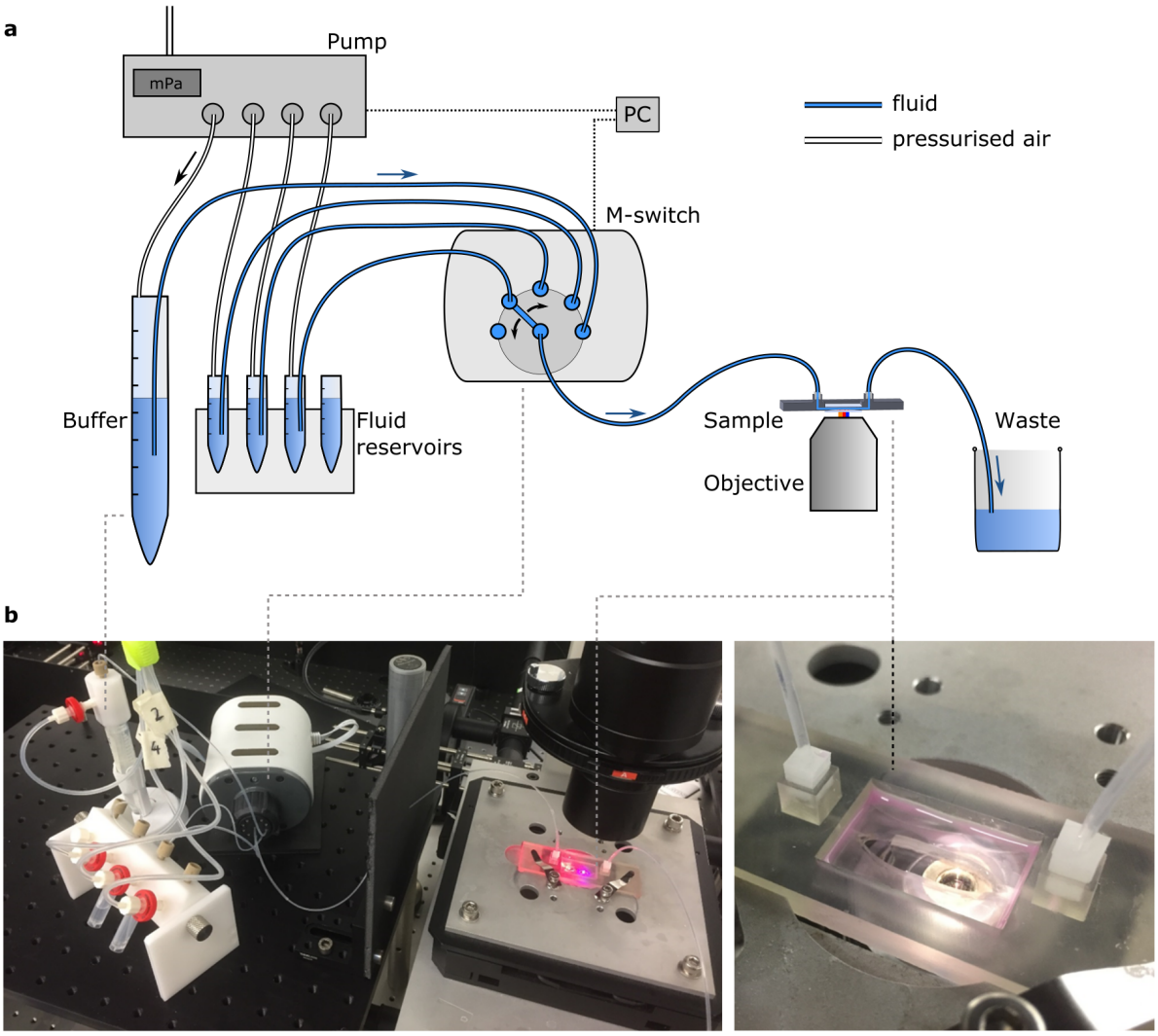

Figure 3.8: Fluidics setup for use of microfluidic chips and 3D printed macrofluidic sample chambers. For detailed description, see main text. **(a)** Schematic drawing of the setup. Solutions were pumped from the respective reservoir through the imaging chamber, a multiplexing device (M-switch) was used for input selection. Waste solutions were collected below the sample stage in a waste beaker. **(b)** Photographs of the fluidics setup and a 3D printed sample chamber in use.

3.3.1 DNA-PAINT protocols

For DNA-PAINT imaging, the laser power directed into the microscope was attenuated to approx. 15 mW and the region of interest was constrained to the size of the laser spot, approx. $20 \times 20\,\mu m^2$. Images were acquired with an integration time of 100 ms, unless specified otherwise. For imaging of microspheres, an imager concentration of $0.05 - 0.1$ nM in microsphere imaging buffer was used, imaging was done in TIRF mode. DNA origami structures were imaged with microsphere imaging buffer and imager concentrations of $2 - 5$ nM in TIRF. Fixed cells were imaged with buffer C containing 0.5 nM imager strands in TIRF mode, fixed tissue sections with $1 - 2$ nM imager in HILO mode. Tissue sections were imaged 5 µm, 3 µm and 1 µm above the coverslip surface for figures 5.14, 5.15 and in chapter 6, respectively. Prior to super-resolution imaging of biological samples, the labelling was checked in widefield fluorescence, detecting the fluorophores directly conjugated to the docking strands. These fluorophores were typically photobleached before a DNA-PAINT image was acquired, see also section 3.1.1.

For imager exchange steps as part of Exchange-PAINT acquisition runs by pipetting, the active compensation of defocus detected via drift tracking in transmission mode (section 3.2.2) was disabled. When imager exchange was carried out by pipetting, the sample washed with plain buffer for at least 3 times, after which the new imager strand was added and the focus lock reactivated. For imager exchange by Quencher-Exchange-PAINT (chapter 5), a small amount ($< 10\,\mu l$) of quencher strands were added to the sample and the imaging solution lightly mixed.

For imaging of Proximity-Dependent PAINT (PD-PAINT, chapter 6), the proximity probes Tissue-S1 and S2 were added at 100 nM during acquisition, and (Biotin-) S1 and S2 were added at 500 nM for labelling of microspheres, both concentrations at which interaction of the probes in solution is negligible (see chapter 6, figure 6.2).

3.3.2 Event detection and post-processing in PYME

A custom-made software package, Python Microscopy Environment (PYME) was used for hardware control of the microscope, illumination and cameras,

for image acquisition and analysis. Its main components are freely available at `https://bitbucket.org/christian_soeller/python-microscopy-exeter-test`.

Event detection

The acquisition and analysis protocols in PYME are customisable, e.g. for multi-colour or 3D imaging. Figure 3.9 shows the analysis workflow for regular DNA-PAINT imaging of microspheres. During acquisition of camera data (raw data shown in figure 3.9 a), single molecule events were detected (figure 3.9 b). The threshold for detection was tested prior to data analysis on a single frame. To each detected DNA-PAINT binding event, a 2D Gaussian least-squares fit was applied, taking into account any corrections for sCMOS chip inhomogeneities, such as pixel specific read-noise, offset and sensitivity variation [149]. This real-time analysis enabled the display of the localisation data, i.e. the centres of the Gaussian fits, during imaging. Localisation data points, colour coded by time of detection, are shown in figure 3.9 c.

Post-processing and visualisation

In post-processing, sample drift was corrected for by using drift data obtained from fiducial markers or the auxiliary camera in the transmitted light path, shown in figure 3.9 d. Binding events which were detected for more than a single frame (100 ms) were generally coalesced into single events. Post-processing filters could be applied for different parameters of the fits, e.g. filtering for the amplitude, sigma, localisation error or photon numbers. Unless specified otherwise, the min/max filter settings applied were an amplitude of 5/20k ADU, a sigma of 95/200 nm and lateral localisation errors of 0/30 nm. Localisation data was visualised into 16-bit greyscale images with a pixel size of typically 5 nm by jittered triangulation [148], where the greyscale value represents the local density of localisation events.

3.3.3 Comparison of methods for drift correction

The resolution of a single-molecule localisation image not only depends on the localisation precision, but also on (amongst other factors) the sample drift, often caused by thermal drift. Especially for long acquisition times, e.g. for

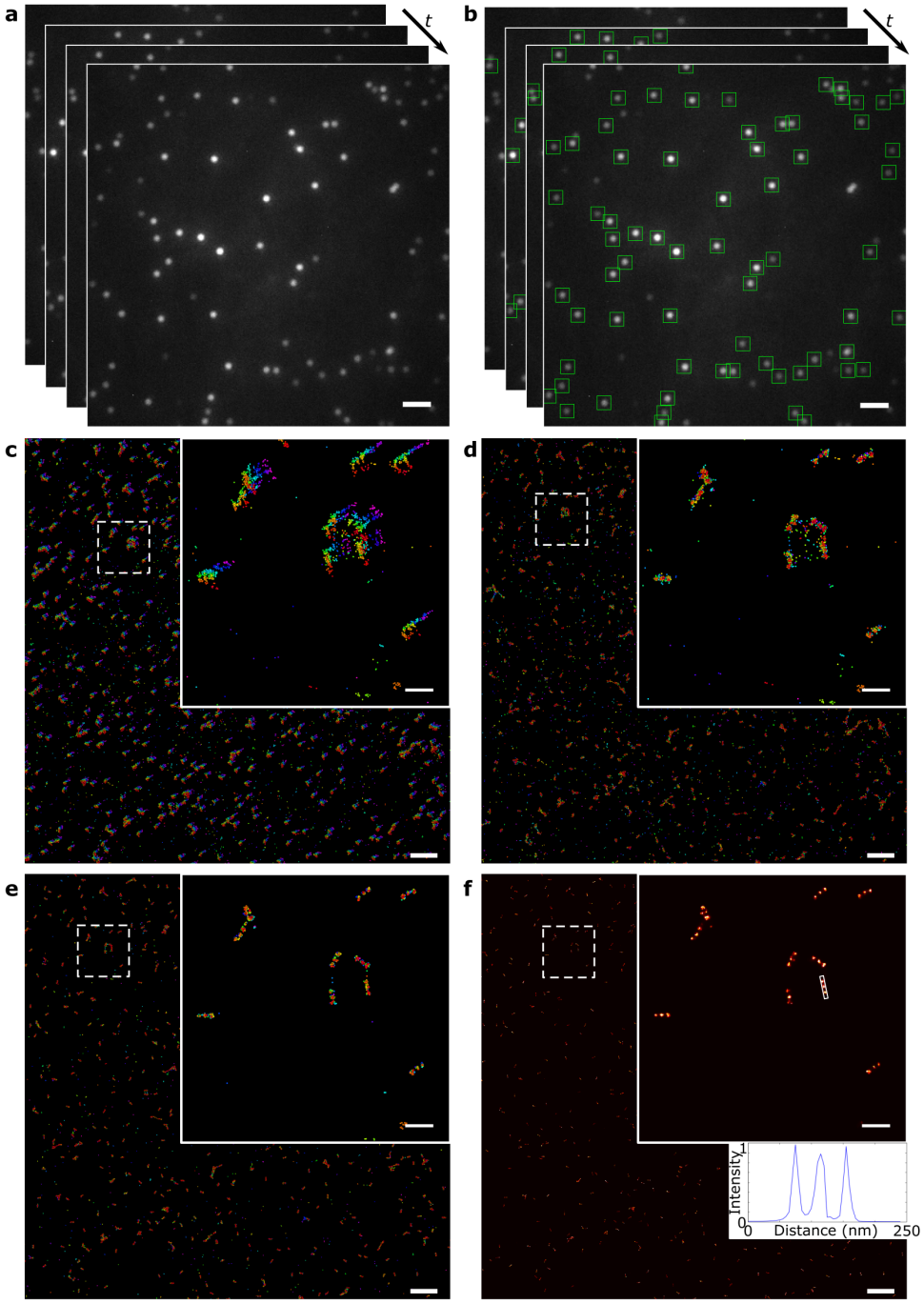

Figure 3.9: Typical DNA-PAINT imaging workflow, demonstrated using a commercially available DNA origami sample. **(a)** Several thousand frames of raw data were acquired. **(b)** Single imager-docking binding events were detected, based on a customisable, signal-to-noise based threshold. **(c)** Localisation data was visualised, the colour coding represents the time of occurrence for each event. **(d)** Drift was corrected, see main text for details. **(e)** Post-processing filters were applied, here filtered for a localisation error $< 5\,\mathrm{nm}$. **(f)** A super-resolution image was rendered by jittered triangulation [148]. Scale bars: $2\,\mu\mathrm{m}$(a,b), $1\,\mu\mathrm{m}$(c-f), $200\,\mathrm{nm}$ (insets).

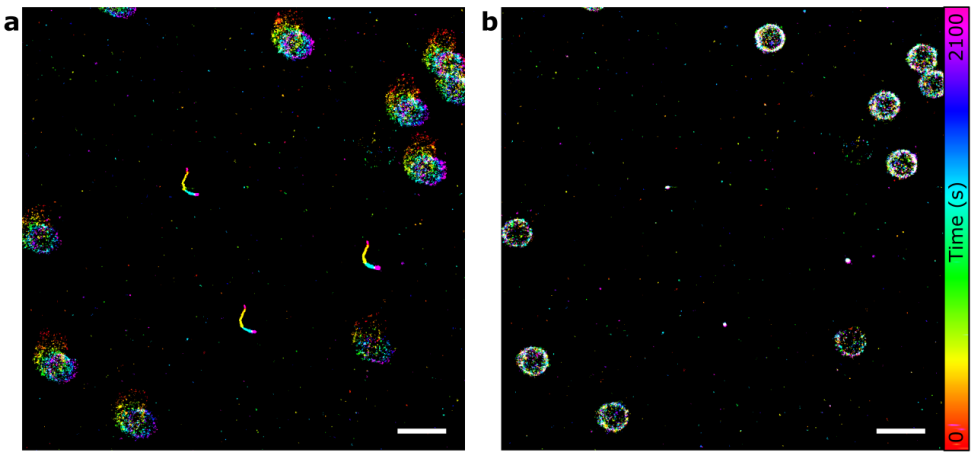

Figure 3.10: Localisation data showing drift correction. **(a)** Uncorrected localisation data. The colour represents the acquisition time for each event, between 0 and 2100 s. Larger areas show DNA-PAINT data of microspheres, event traces in the centre show localisation data from fiducial markers (200 nm red fluorescent beads). **(b)** Drift is determined from detection of fiducial markers and the drift correction applied to DNA-PAINT data. Scale bars: 1 µm.

multiplexed imaging as discussed in chapter 5, it is crucial that sample drift is compensated for. Here, different methods for drift correction are compared on a microsphere sample.

Figure 3.10 a shows a DNA-PAINT image of microspheres imaged with high localisation precision, but without drift correction. The smaller structures in the centre of the image show time traces of fiducial markers, here red fluorescent beads, which do not show blinking behaviour and are detected in each frame. The time traces of all structures follow the same path, indicating that sample drift is homogeneous throughout the imaged field of view, as can be assumed for structures which are fixed onto the coverslip. In post-processing, the sample drift can be extracted from the localisation data and the localisation data displayed with compensation of sample drift (figure 3.10 b).

Different methods for extraction of sample drift information are shown in figure 3.11. As fiducial markers, gold nanoparticles (Au-NP) were compared to red fluorescent beads of 100 nm and 200 nm diameter. As stated by the manufacturer, red fluorescent beads have an excitation peak at 580 nm with a reduced excitation to <5% at the laser wavelength used for DNA-PAINT (642 nm). Due to their low excitation even at high laser powers of that wavelength, photo-

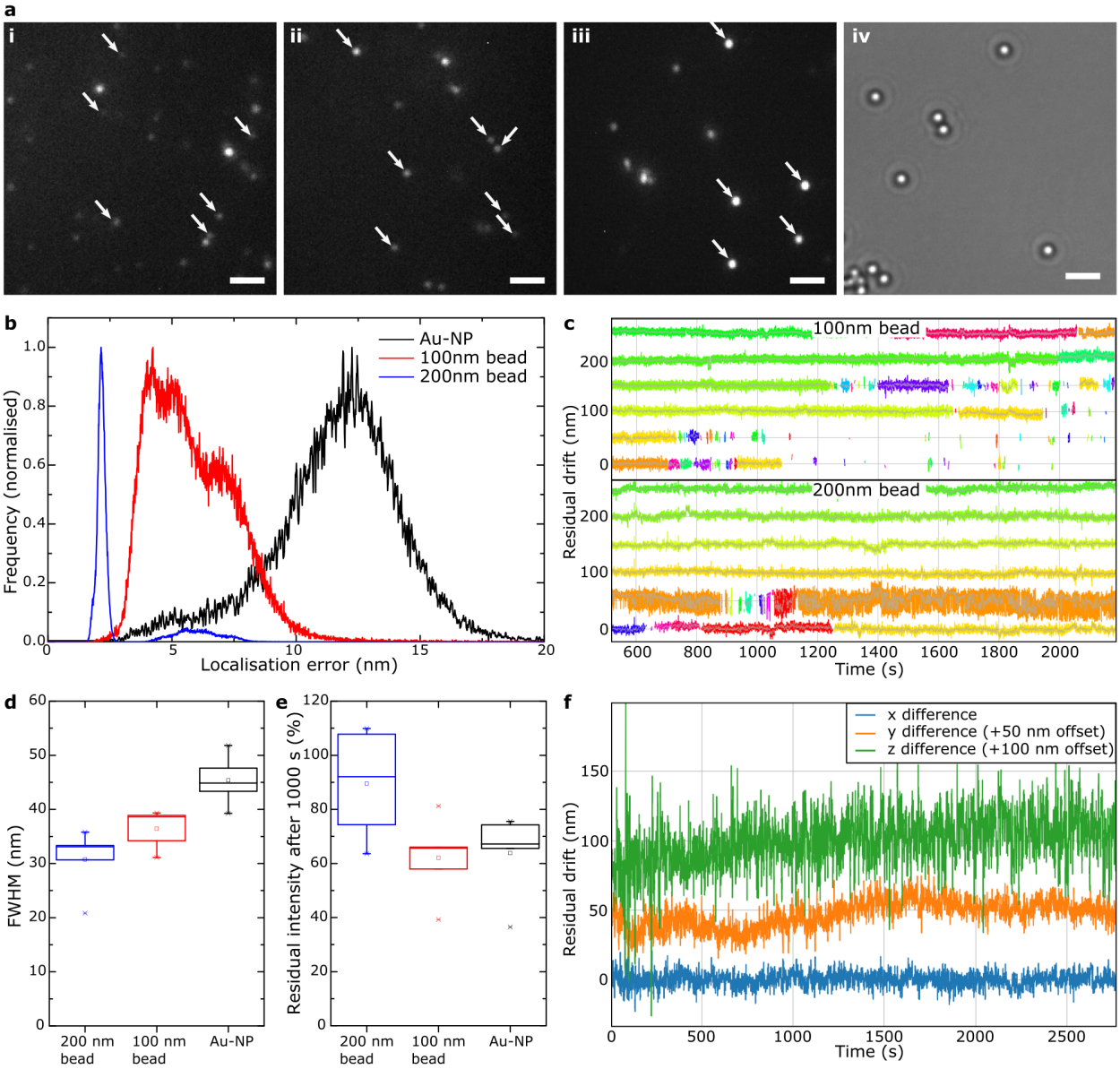

Figure 3.11: Comparison of methods for drift correction. **(a)** Raw data showing of drift markers. White arrows: fiducial markers, other bright areas are DNA-PAINT blinking events. (i) Gold nanoparticles (Au-NP), (ii) 100 nm and (iii) 200 nm fluorescent beads, (iv) widefield transmission of microspheres. **(b)** Localisation error of fiducial markers gold nanoparticles (black), 100 nm (red) and 200 nm (blue) fluorescent beads ($n = 5$). **(c)** Time traces showing residual drift of fluorescent bead fiducial markers after drift corrections. Markers are shown with an offset of 50 nm for improved visualisation. **(d)** Full-width at half maximum (FWHM) of rendered image after drift correction with respective fiducial marker. **(e)** Residual intensity of fiducial marker reduced by photobleaching after 1000 s. **(f)** Time traces showing residual difference between drift correction by transmission tracking and by 200 nm fluorescent beads. Scale bars 2 µm.

bleaching was expected to be reduced and the fluorescence emission did not lead to saturation of the detector. Additionally, drift was tracked in transmission mode at 430 – 470 nm, detecting changes in high-contrast transmission data of the microspheres. Raw data of the drift tracking methods is shown in figure 3.11 a, with white arrows pointing to fiducial markers. Other fluorescent events were DNA-PAINT imager binding events, which could be distinguished by their apparent blinking. While Au-NP showed lower emission intensities than the mean DNA-PAINT binding event, 100 nm fluorescent beads were in a comparable range to DNA-PAINT events and 200 nm beads were significantly brighter. This was reflected in the localisation error of the fiducial markers (figure 3.11 b), with the localisation error of 200 nm beads the lowest (blue), and of Au-NP the largest (black). The distribution of localisation precision was further reflected when rendering a super-resolution image from drift-corrected data. Shown in figure 3.11 d is the full width at half-maximum (FWHM) of a Gaussian fit to the event density data of fiducial markers. Due to higher localisation precision of 200 nm fiducial beads (blue), the binding events formed a smaller cluster and a tighter event distribution than the 100 nm beads (red) or the Au-NP (black).

Figure 3.11 c shows exemplary residual deviation from the extracted drift correction track for 100 nm (top) and 200 nm (bottom) fiducial beads. Five fiducial markers are shown each, separated by a relative offset of 50 nm for illustration purposes. Detection of a continuous fluorescence time trace is shown in a single colour, a colour change indicates interruptions between otherwise continuous signals detected from the position of the marker. Except for one outlier of the 200 nm beads, the residual drift of different 200 nm beads was smaller than the residual drift of 100 nm beads. Additionally, the 200 nm beads were detected during the full experiment, while several time traces of 100 nm beads ended, probably due to photobleaching reducing their intensity to values below the detection threshold. The photobleaching is further shown in figure 3.11 e, comparing the residual mean intensity of the fiducial markers after 1,000 s (10,000 frames). The residual intensity of 100 nm beads (red) and Au-NP (black) was approx. 60 – 70%, the residual intensity of 200 nm beads (blue) slightly higher. Note, that the initial intensity of 200 nm beads was considerably higher than that of 100 nm beads.

In figure 3.11 f, fiducial drift correction with 200 nm beads is compared to correction by using the transmission image data acquired with the auxiliary camera and cross-correlation to a calibration image, as described in section 3.2.2. Here,

the time traces obtained in transmission mode are fitted to the mean trace of the fiducial markers. The plot shows the residual difference between the tracking and fiducial time traces in lateral direction (blue, orange) and along the optical axis (green). While it is difficult to determine whether the fiducial marker or the transmission tracking represent the actual sample drift, the separate optical path makes errors in the transmission path more likely.

A comparison of fiducial markers for single-molecule localisation microscopy has been published very recently by Balinovic et al. [150], coming to a similar conclusion, i.e. fluorescent beads with a de-tuned excitation and emission spectrum provide better drift detection than other options, e.g. gold nanoparticles.

qPAINT

The qPAINT analysis follows Jungmann et al. [21], as described in chapter 2.2.4 and was implemented using a PYME plugin for qPAINT, available at `http://bitbucket.org/christian_soeller/pyme-extra`. Intensity time traces allow the extraction of dark times, i.e. time intervals between detected fluorescence. Attention was paid that the binding event rate during acquisition remained constant. Dark times of single-frame duration were omitted to avoid thresholding artefacts arising from event detection, for details see chapter 4.3. The mean dark time $\tau_{\mathrm{D,mean}}$ was calculated by fitting the dark time distribution, which is assumed to follow an exponential distribution, in the form of a cumulative distribution function $\mathrm{CDF}(t) = 1 - \exp(-t/\tau_{\mathrm{D,mean}})$ [21]. The number of available binding sites was estimated as $N_{\mathrm{bind}} = k_{\mathrm{on}} \cdot [I] \cdot \tau_{\mathrm{D,mean}}$, where k_{on} is the imager-docking association rate constant, $[I]$ is the imager concentration (see equation 2.14). By applying an intensity threshold to a rendered image, microsphere structures were identified and labelled in PYME (for an example see figure 3.12 c), however, microspheres in close proximity were assigned to a single cluster. The number of microspheres per cluster could be estimated from its total area, as seen in the stepwise area distribution of microspheres clusters shown in figure 3.12 d. In order to detect the number of binding sites per single microsphere, the number of binding sites per cluster was divided by the number of microspheres in the cluster.

k_{on} was estimated from a calibration measurement performed on a bead featuring a single binding site as $k_{\mathrm{on}} = (\tau^{\mathrm{single}}_{\mathrm{D,mean}} \cdot [I])^{-1}$ (Figure 3.12 e) [21]. $\tau^{\mathrm{single}}_{\mathrm{D,mean}} = 57.1\,\mathrm{s}$ (Figure 3.12 f) and $k_{\mathrm{on}} = 3.5 \cdot 10^6\,\mathrm{M^{-1}s^{-1}}$ was obtained when using $[I] = 5\,\mathrm{nM}$,

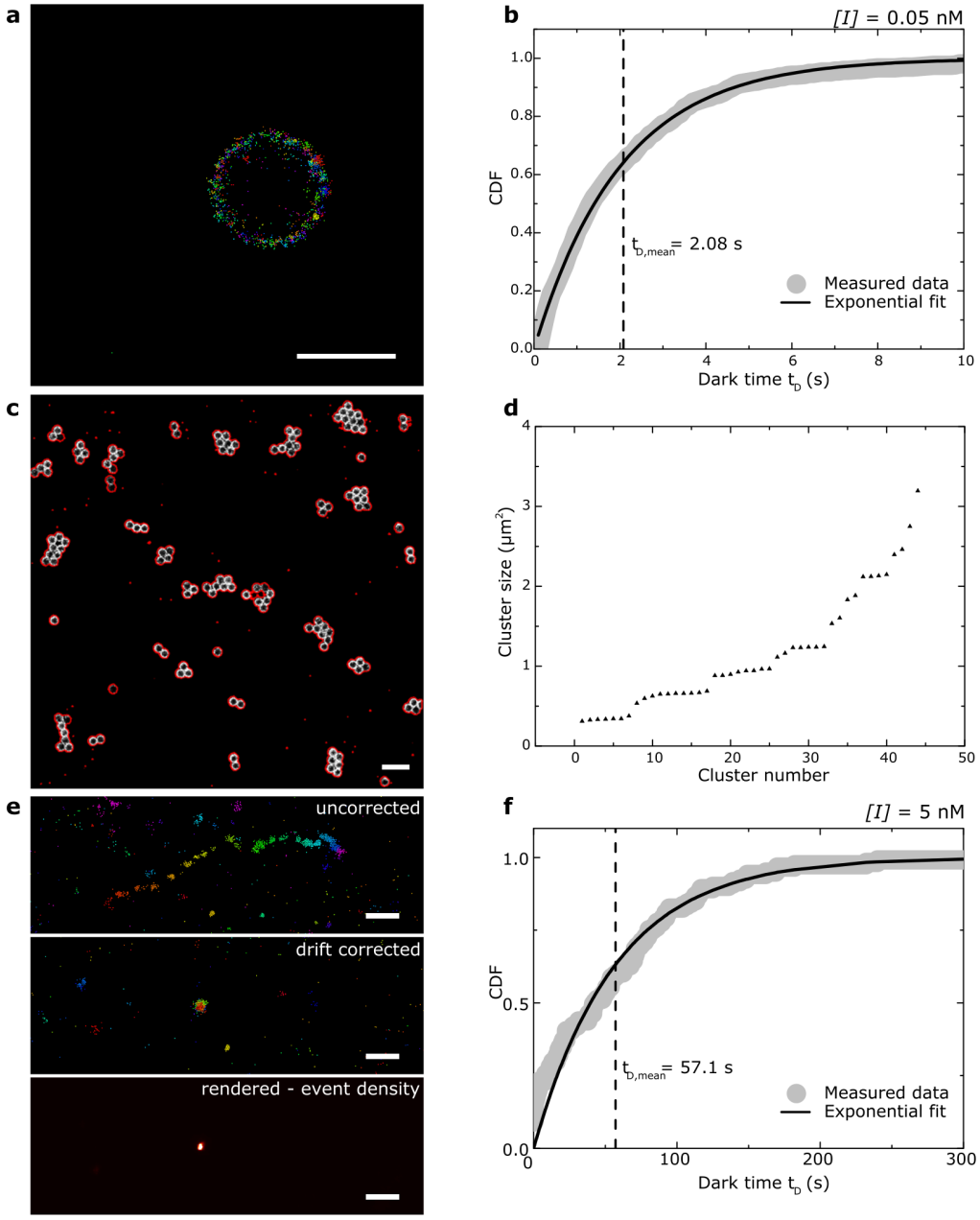

Figure 3.12: qPAINT of microspheres. **(a)** Localisation data of a single microsphere **(b)** Cumulative dark time distribution fitted by an exponential distribution, showing $\tau_{\mathrm{D,mean}}$. **(c)** Outline detection of imaged microspheres. **(d)** Area for each structure found in **c**, showing a stepwise increase in area depending on the number of microspheres in a cluster. **(e)** Localisation data of the calibration sample, top: not drift corrected, showing sequential occurrence of binding events. Middle: drift corrected. Bottom: Rendered image. Imaged over 3 h / 108k frames. **(f)** Cumulative distribution function fitted to dark time distribution of a single binding site. Scale bars: 500 nm (a), 2 µm (c), 200 nm (e).

in broad agreement with previously reported values [21, 151]. Binding of a single docking strand on a particle was achieved by functionalising the particles with a very dilute solution of docking strands (0.5 nM, see also Delcanale et al. [151]).

3.3.4 Atomic Force Microscopy

Dried DNA origami samples on freshly cleaved Mica sheets, as described in section 3.1.6, were imaged on a NaioAFM atomic force microscope (Nanosurf, Liestal). The AFM includes a granite slab and was placed on an optical bench for oscillation compensation. Samples were held in place by a magnet. A region of interest of $1 \times 1\,\mu m^2$ was imaged in dynamic force (tapping) mode.

4. Test Samples for DNA-PAINT Imaging Parameter Optimisation

Single molecule super-resolution microscopy and DNA-PAINT in particular are of interest for a wide range of researchers, and new variations of the techniques are continuously developed, for example the techniques described in chapters 5 – 7. To facilitate the implementation of a new method, test samples can be used, i.e. samples in which the underlying imaged structure is known a priori and which can be used under similar conditions as the actual application. Furthermore, test samples enable quantification and continuously checking the system performance, e.g. the imaging resolution, and allow for optimisation of various parameters which influence the performance. Ideally, a test sample responds to changes in imaging parameters similarly to the application of interest, is cost- and time-efficient to fabricate, remains stable over a long period of time and shows highly reproducible results under defined conditions.

To determine the resolution of single molecule super-resolution systems in both 2D and 3D, DNA origami structures have been used previously [152, 153]. In so-called DNA nanorulers, several DNA-PAINT docking sites are attached to a DNA origami structure with defined distances, which can be used to estimate the system's imaging resolution. These structures are commercially available in sealed imaging chambers and can be used for up to several months [4, 154]. However, in these sealed samples the imaged structures are not directly accessible and buffer composition and DNA sequences are not disclosed by the manufacturer. Thus, for DNA-PAINT they provide only limited use for comparison of different sample conditions, such as variations of the imaging buffer, labelling density and concentration of DNA-PAINT imager strands, or variations in DNA sequences

and structures. Instead, DNA origami are typically fabricated and deposited by the user [18, 20, 22].

In this chapter, issues related to the fabrication of DNA origami samples as test samples for optimisation of DNA-PAINT imaging parameters are shown. An alternative test assay, based on streptavidin-functionalised polymer microspheres which are labelled with biotinylated docking strands, is described and characterised. The new method provides a test sample which is considerably more cost- and time-efficient to fabricate. The influence of several DNA-PAINT parameters on imaging performance is characterised, such as the concentration of imager strands, the illumination intensity, buffer conditions and changes to the imager and docking strand sequences. Additionally, the use of microspheres for testing of advanced imaging modalities, e.g. 3D and quantitative imaging, is shown. Finally, the limitations of the microsphere test samples are described.

Customised DNA origami structures were obtained from Gattaquant, Hiltpoltstein, and DNA origami structures according to Schnitzbauer et al. [22] were fabricated by Dr Ana Cecilia Afonso Rodrigues. A basic labelling protocol for the microparticles was originally provided by Dr Lorenzo Di Michele and first proof-of-principle experiments were carried out by Simona Frustaci. Anna Meletiou provided help with the acquisition of 3D DNA-PAINT data.

4.1 DNA origami and microparticles as test samples

In this section, customised DNA origami as test samples for DNA-PAINT are compared to an assay based on functionalised, labelled microspheres.

4.1.1 DNA origami

To design a customised DNA origami test sample, the sequences for several hundred staple oligonucleotide have to be determined in order to achieve the desired folding of the scaffold DNA strand, a process which can be facilitated by software design tools [102]. However, if a defined arrangement of docking strands on a 2D grid is sufficient, previously published staple strand sequences can be used [22]. Alternatively, customised DNA origami structures can be obtained commercially.

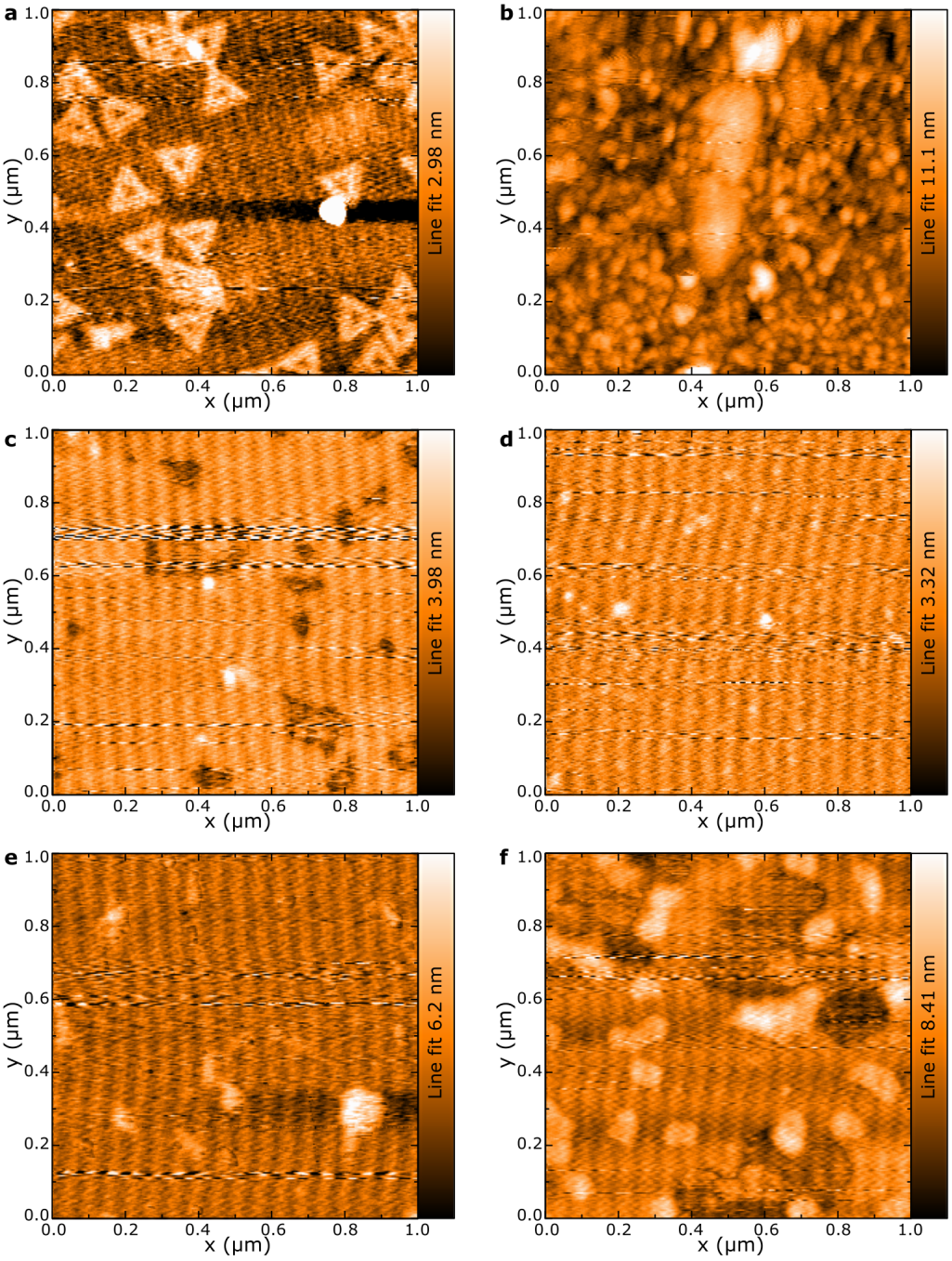

Figure 4.1: Atomic force microscopy (AFM) images of DNA origami. **(a)** Commercial AFM sample of triangular DNA origami structures, pre-prepared on mica surface. **(b)** Cleaned glass coverslip. **(c)** Freshly cleaved mica sheet. **(d)** Freshly cleaved mica sheet treated treated as if depositing DNA origami. **(e)** Mica sheet treated as in d, with DNA origami fabricated following a protocol by Schnitzbauer et al. [22]. **(f)** Deposition of commercially obtained square-shaped DNA origami in solution onto freshly cleaved mica sheet.

With flat origami structures only having a thickness of a single DNA double helix (<3 nm) and DNA giving a low contrast in widefield microscopy, it is difficult to obtain feedback on an optical microscope whether DNA origami have been deposited onto a coverslip. Alternatively, a first quality control can be achieved by atomic force microscopy (AFM). Figure 4.1 shows the imaging of DNA origami using an AFM. The ability of the microscope to resolve DNA origami structures was tested by using a commercial test sample, consisting of triangular DNA origami structures fixed on a mica surface. As shown in figure 4.1 a, they appear similar to the structures published originally by Rothemund et al. [19]. Ideally, the DNA origami would be imaged under similar conditions as used in DNA-PAINT in order to provide control for both fabrication and deposition steps, but the roughness of glass coverslips with peak sizes of up to 10 nm prevent detection of flat DNA origami structures, if the glass is left untreated [155] (figure 4.1 b). Freshly cleaved mica sheets provide a smooth surface (sub-nanometre roughness [155]), shown in figure 4.1 c. A negative control by treating a mica sheet with the necessary steps for deposition of DNA origami, i.e. washing with buffer and rinsing with ethanol, but without using DNA origami, shows that the treatment does not result in visible structures on the sample (figure 4.1 d). Figures 4.1 e and 4.1 f show examples of DNA origami made following a published protocol [22], and DNA origami which were obtained readily folded, respectively. Only few structures can be seen in figure 4.1 e, and features do not appear well defined. This indicates that either only a low number of DNA origami were folded or other issues might have occurred during the DNA origami fabrication process – a process which is time intensive (>10 h [22]) and contains multiple critical steps, e.g. during DNA origami purification. Instead, the deposition of readily folded commercial DNA origami confirms the presence of approximately square-shaped structures (figure 4.1 f).

DNA origami shown in figure 4.1 f were designed with single DNA-PAINT docking sites arranged in a 3×3 grid with a nearest-neighbour distance of 30 nm. Figure 4.2 a shows a DNA-PAINT image of the structures, with insets of magnified areas on the right. The sample was imaged for ~100,000 frames (approx. 3 h), and the colour in the insets represents data acquired during the first 50,000 frames (green) and the last 50,000 frames (red). Sample drift was corrected by using 200 nm red fluorescent beads as fiducial markers. The repeated binding of imager strands to the same docking strands results in the colocalisation of red and green areas acquired in the first and second half of the acquisition, as

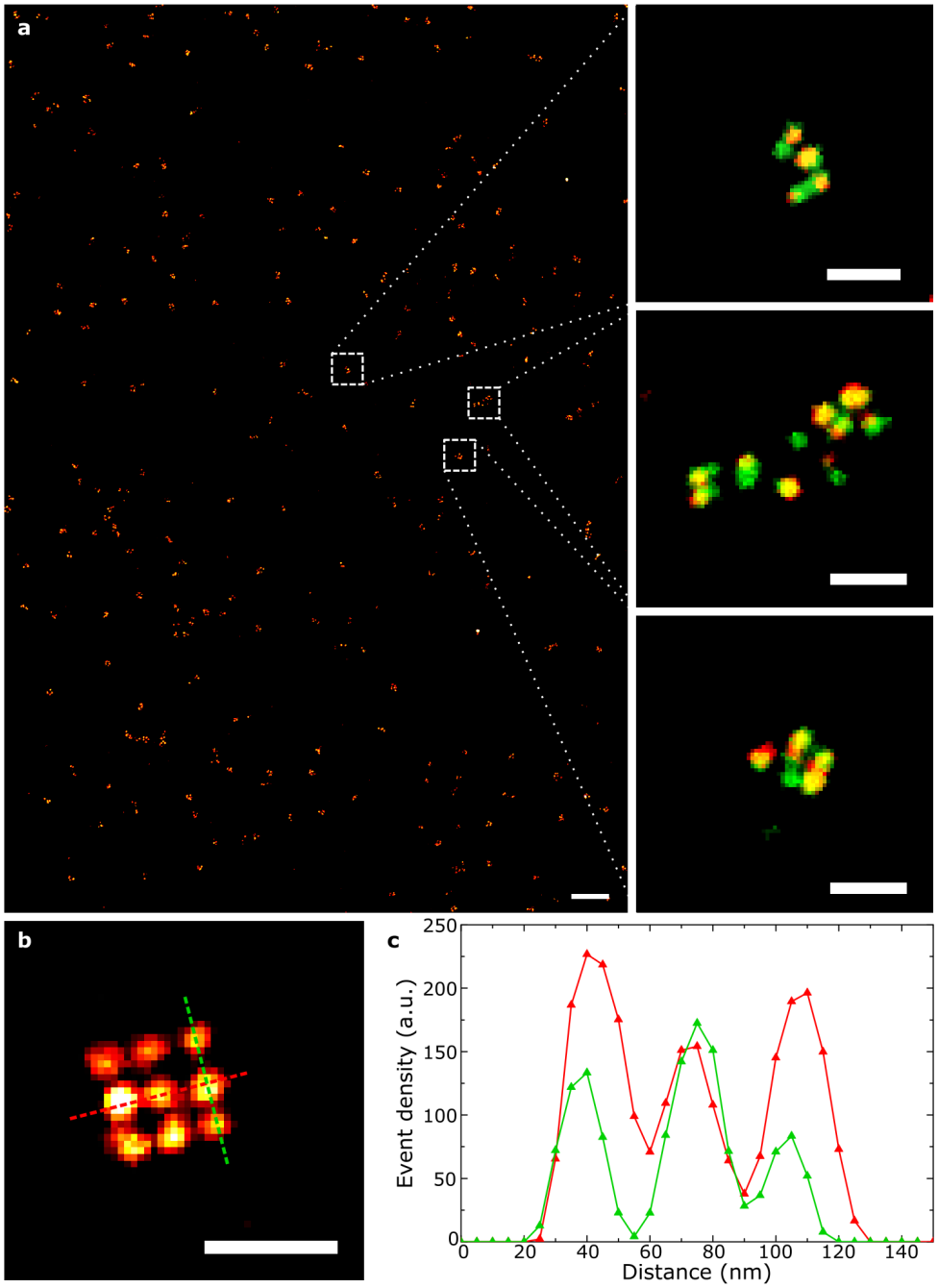

Figure 4.2: DNA-PAINT of DNA origami. **(a)** Overview of total field of view, showing fragments of 3 x 3 DNA origami grid structures. Insets: Dataset split into events detected in the first 50k frames (green) and last 50k frames (red). The strong overlap indicates a high imaging resolution. **(b)** Manual overlay of 10 randomly chosen DNA origami fragments (rotation adjusted), showing the expected grid structure. **(c)** Cross section of event density data shown in dashed lines in b. Scale bars: 1 µm, insets: 100 nm.

shown in the figure 4.2 a insets, with the size of the data points indicating at an imaging resolution of few tens of nanometres.

However, only incomplete grid structures were observed, possibly due to degradation of docking sites during storage of DNA origami solution. The high number of degraded docking sites on the commercial DNA origami grid might stem from the extended storage. The manufacturer only states stability for 6 months at -20 °C, but the structures shown in figure 4.2 were imaged after more than 12 months. Even with only a subset of expected docking sites visible, the distribution of docking sites matches the grid structure. In figure 4.2 b, a randomly chosen subset of 10 imaged structures were overlaid and manually adjusted by rotating each structure to achieve maximum overlap, a process commonly used for DNA-PAINT imaging of DNA origami [22, 70, 156]. Cross-sections of the sum image show the expected modulation with 30 nm spacing between neighbouring binding sites (figure 4.2 c, with colours indicating direction of cross-section as indicated in figure 4.2 b). Both commercial DNA origami structures as well as the purchase of individual staple strands is cost-intensive (GBP600+ for commercial structures, up to several thousand GBP for self-made samples), which, in combination with the limited sample stability, motivates the use of alternative DNA-PAINT test samples.

4.1.2 Development of a streptavidin-coated microsphere assay

Spherical microparticles can be fabricated with a high degree of monodispersity (coefficient of variation of <5% [157]), which is a prerequisite for achieving reproducible results when imaging the particles and of advantage when used as test samples. Microspheres based on polystyrene (PS) or polymethyl-methacrylate (PMMA) are biocompatible, insoluble across a wide range of pH and do not show swelling in aqueous environments [157]. For use as a DNA-PAINT test sample, microparticles were obtained with a streptavidin coating, which allows for high-affinity binding of biotin-modified oligonucleotides.

With a refractive index of polystyrene microspheres of 1.59, particles with a diameter of 500 nm show high contrast in aqueous medium and the deposition of microspheres on the coverslip can be directly observed (see figure 3.2 in chapter 3). Fluorescent blinking events originating from locations where no particles are deposited can thus be distinguished as nonspecific adsorption of imager strands

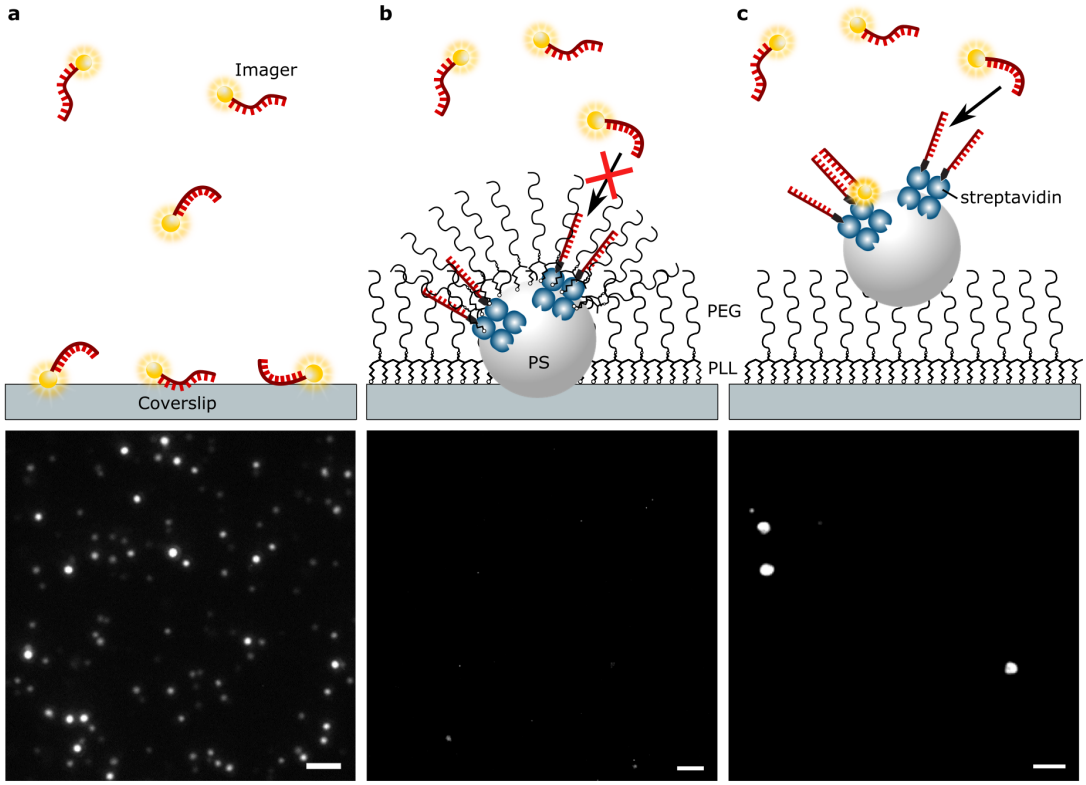

Figure 4.3: Coverslip passivation with PLL-g-PEG. **(a)** Cleaned, uncoated coverslip with imager in buffer, showing nonspecific adsorption of the imager to the glass surface. Bottom: raw data of single frame **(b)** Coating of coverslip with PLL-g-PEG after deposition of streptavidin-functionalised polystyrene (PS) microspheres prevents nonspecific binding of imager to coverslip, but also prevents binding of imagers to docking sites on microspheres. **(c)** Deposition of microspheres onto PLL-g-PEG pre-coated coverslips makes docking sites accessible to imager strands but maintains low background adsorption. High concentration (5 nM) of imagers results in saturated intensity at location of microspheres (bottom). Scale bars: 2 µm.

to the coverslip surface – a type of binding event that needs to be minimised if the sample is used to study DNA-PAINT binding.

Figure 4.3 a shows a single frame of fluorescence raw data where imaging buffer with imager strands at a concentration of 0.1 nM, typical for DNA-PAINT, was addressed on a cleaned, but otherwise untreated coverslip. Nonspecific adsorption appears as blinking events, terminated presumably by photobleaching or unbinding of the imager. These events are difficult to distinguish from DNA-PAINT binding events. Adsorption to the coverslip can be minimised by passivation of the coverslip with a polymer coating of polyethylene glycol (PEG), attached to the coverslip via a poly-L-lysine (PLL) linker. Figure 4.3 b demonstrates the lack of fluorescence if the coverslip is passivated with PLL-g-PEG, and the same imager concentration as in 4.3 a is used. However, the PLL-g-PEG coating equally inhibits DNA-PAINT binding of imagers to docking strands on microparticles if it is applied after deposition of the particles. Instead, the microspheres have to be deposited onto the precoated coverslip, resulting in highly specific binding of imager strands to docking strands (figure 4.3 c).

The increase in sensitivity is characterised in figure 4.4. Rendered images, showing the local density of observed fluorescence blinking events, of microspheres imaged by DNA-PAINT on a PLL-g-PEG passivated coverslip and on an untreated coverslip are shown in figure 4.4 a and b, respectively. While specific binding to the microspheres can be observed in both cases, the untreated coverslip gives rise to a higher number of fluorescent events uniformly distributed across the region of interest. Here, the number of detected events originating from the locations of microspheres was assumed to be specific DNA-PAINT binding in large majority, any binding events from other areas was assumed to be nonspecific background events. The mean number of events normalised to an area of 1 μm^2 is shown in figure 4.4 c for data shown in figure 4.4 a and b. The coating with PLL-g-PEG increases the signal-to-background-event ratio from 74.51 to 235.33, i.e. shows a >3-fold suppression of nonspecific binding.

This strongly sample-dependent factor can be multiple times higher, as the amount of nonspecific adsorption can vary considerably. Figure 4.4 d demonstrates a second example of DNA-PAINT of microspheres on an untreated coverslip, with the number of background events strongly outweighing the specific binding. The location of microspheres is shown in the transmission image in the inset.

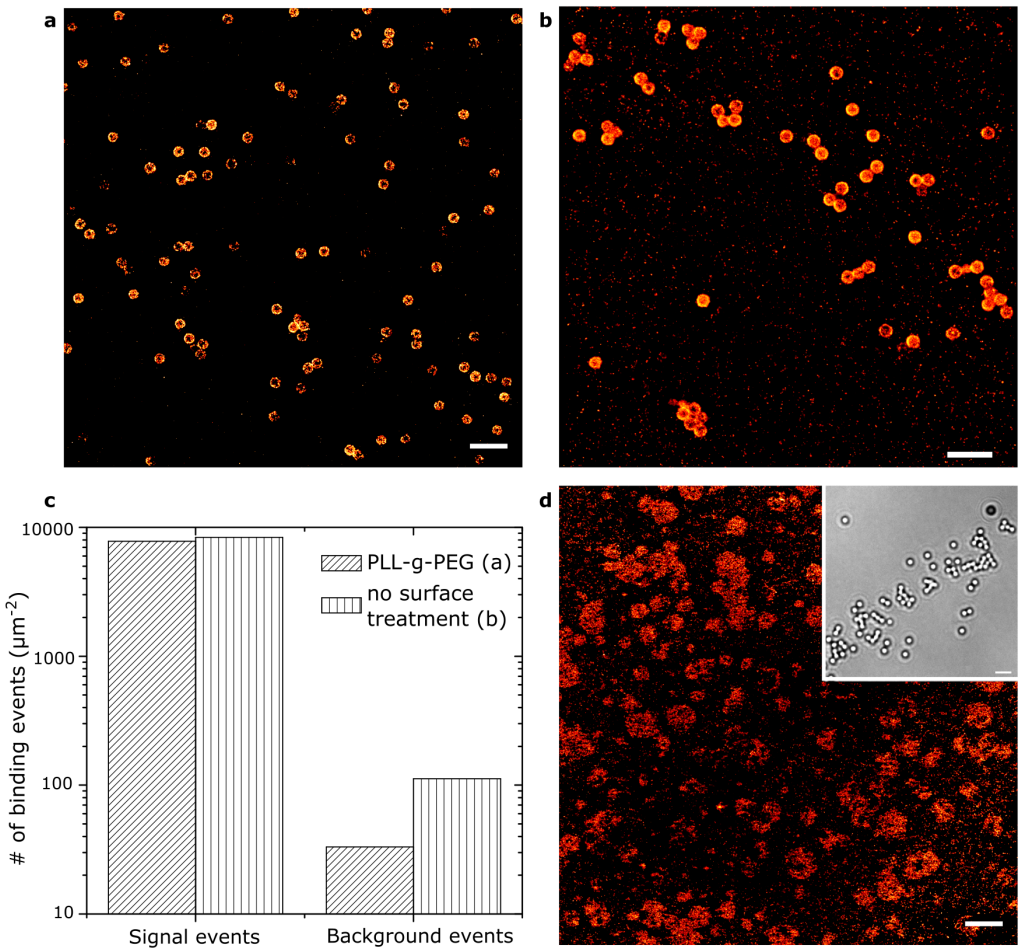

Figure 4.4: DNA-PAINT of microspheres on passivated coverslips. **(a)** Rendered DNA-PAINT image on PLL-g-PEG pre-coated coverslip of microspheres, showing a high signal-to-background ratio. **(b)** Example of DNA-PAINT of microspheres on cleaned, but uncoated coverslip, resulting in an increased amount of random nonspecific binding events to the coverslip. **(c)** Mean density of binding events at location of microspheres "signal events", compared to background events. Here, the PLL-g-PEG coateing reduces background by almost an order of magnitude. Note logarithmic scaling. **(d)** Further example of DNA-PAINT on uncoated coverslip, showing background events outweighing signal events. Inset: transmission images showing location of microspheres. Scale bars: 2 µm.

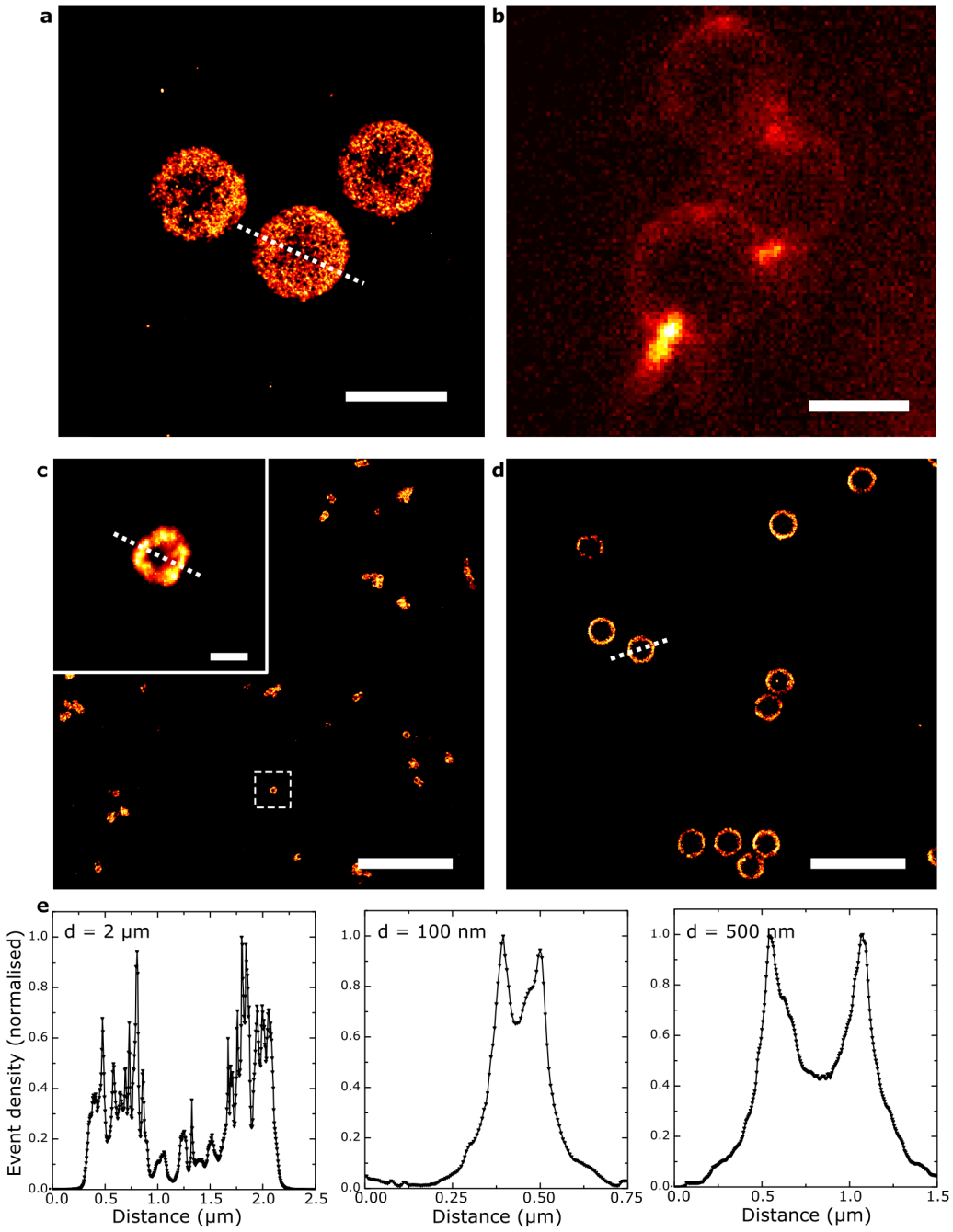

Figure 4.5: Rendered DNA-PAINT images of streptavidin-functionalised microspheres of different sizes. **(a)** Polystyrene microspheres with nominal diameter of 2 µm, imaged near the coverslip surface. **(b)** Intensity raw data of 2 µm microspheres imaged ~1 µm above the coverslip showing single imager strands binding. The lensing effect of the microspheres leads to a strong distortion of the PSF. **(c)** Streptavidin-functionalised poly-methyl-methacrylate (PMMA) spheres with a nominal diameter of 100 nm. **(d)** Polystyrene microspheres with 500 nm diameter. **(e)** Cross-sections along dashed lines for spheres shown in a (left), c (middle) and d (right). Scale bars: 2 µm, inset: 100 nm.

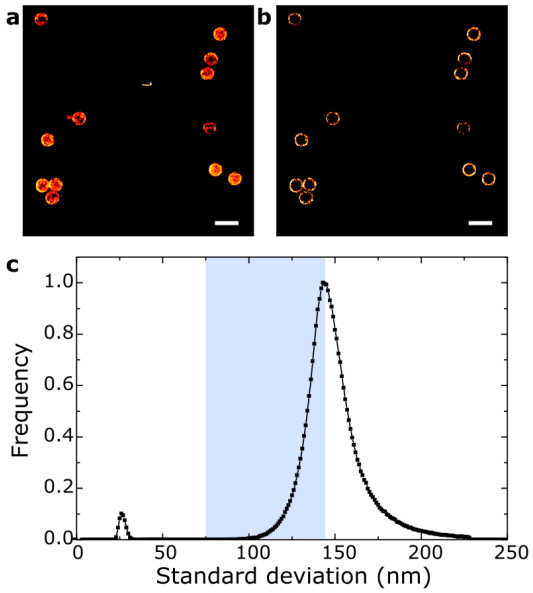

Figure 4.6: Effect of post-processing filters on rendered image. **(a)** Rendered DNA-PAINT image of 500 nm microspheres without filters applied in post-processing step. **(b)** Ring-shape structure resulting from sectioning by applying a strong filter on the event width by filtering the standard deviation of the Gaussian fit to DNA-PAINT events. **(c)** Standard deviation (σ) distribution of Gaussian fits to events detected in image shown in a,b. Blue area shows accepted events rendered in b. Scale bars: 1 µm.

Polymer microparticles are available in a range of particle diameters from 100 nm up to several micrometres [157], offering flexibility in choice for DNA-PAINT test samples. Figure 4.5 shows DNA-PAINT images of microspheres of different sizes, ranging from nominally 2 µm in figure 4.5 a and 500 nm PS spheres (figure 4.5 d) down to 100 nm PMMA spheres in figure 4.5 c. For all particles, a high degree of monodispersity was observed. While the refractive index of polystyrene is useful for observation in transmission mode, it can also distort the PSF. As shown in figure 4.5 b for 2 µm spheres, the particle acts like a micro-lens if the focal plane ranges far into the sample (here 1 µm). Consequently, regular fitting algorithms will no longer localise the binding event precisely. Unless specified otherwise, only the lower half of 500 nm and 2 µm microspheres was imaged in this thesis by adjusting the focal plane accordingly. Figure 4.5 e shows cross-sections through the microspheres shown in figure 4.5 a, c and d.

Particularly the microspheres in figure 4.5 c and d appear as thin ring structures, rather than filled-out circles, which allows a precise measurement of their sizes.

The ring-shape appearance of microspheres when imaged in 2D can result from several factors,

- docking sites are only located on the outside of the particles, thus the image is an orthographic projection of a hollow sphere, which results in a cosine-like modulation in intensity,
- the immobilisation of the microspheres on the coverslip/PLL-g-PEG can result in the docking sites at the bottom of the sphere not being accessible to imager strands,
- imaging in TIRF and HILO modes leads to optical sectioning and thus a reduced imaging of binding events to the top surface of the 500 nm microspheres, and
- filtering in post-processing steps allows for increased sectioning of the imaging data.

Figure 4.6 a and b show the effect of filtering for the standard deviation of the Gaussian fit. The fits to the individual localisation events show a distribution of standard deviations as shown in figure 4.6 c. Filtering for low σ acts effectively like a reduction of the pinhole size in a confocal microscope, resulting in increased optical sectioning as shown in figure 4.6 b.

4.2 Optimisation of DNA-PAINT imaging parameters

In this section, several parameters which impact the performance of DNA-PAINT imaging are characterised by using the microsphere assay described above. Optimisation of these parameters is not only relevant for regular DNA-PAINT, but equally for advanced DNA-PAINT variations described in the following chapters.

4.2.1 Imager concentration

A straightforward method to adjust the imager-docking binding rate is the tuning of imager concentration, as shown in the original DNA-PAINT publication by Jungmann et al. [18]. Figure 4.7 a illustrates the importance of an optimum

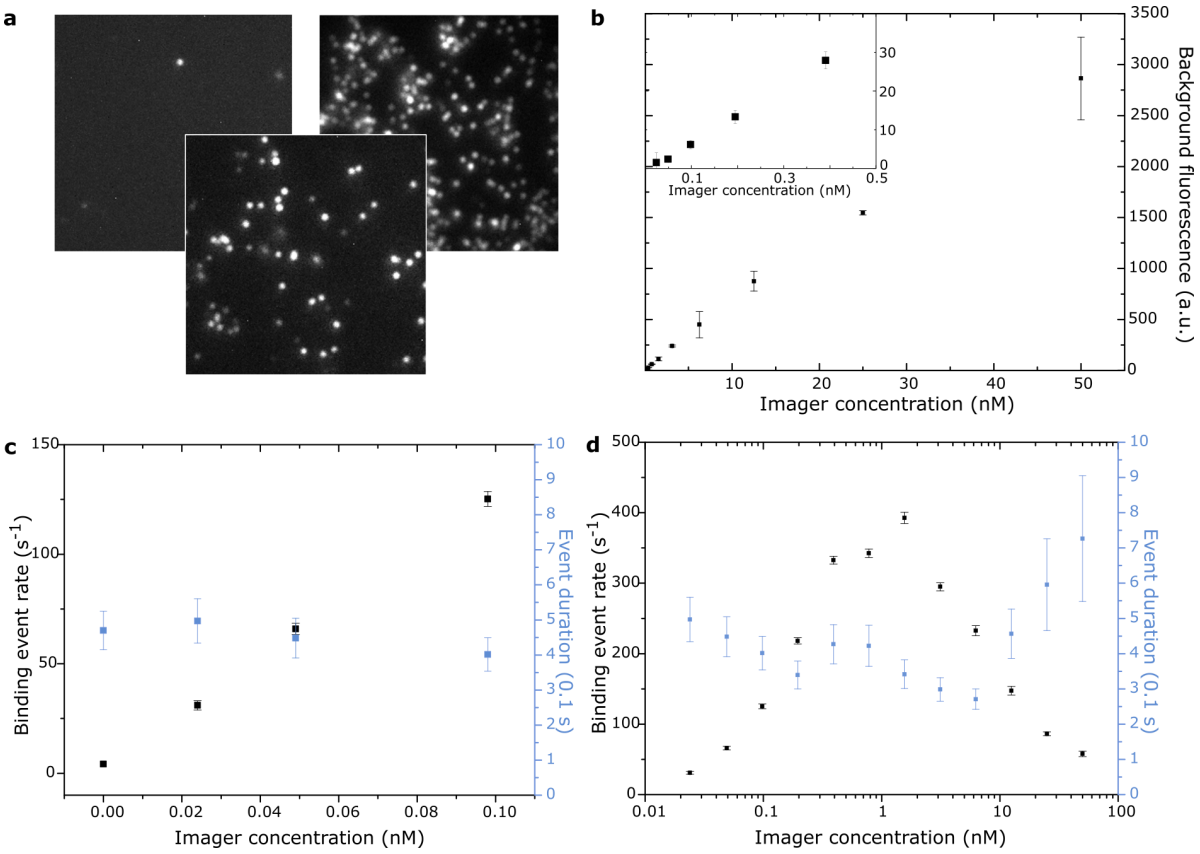

Figure 4.7: Influence of imager concentration on DNA-PAINT. **(a)** Examples of intensity raw data for low imager concentration (left), resulting in long acquisition times, high concentration (right), resulting in a high probability of overlapping events, and imager concentration giving a typical event density used in this thesis (middle). **(b)** The diffuse fluorescent background scales linearly with the imager concentration. Inset shows data at low imager concentrations, not resolved in main plot. **(c)** For imager concentrations at which overlapping events are unlikely (here <0.1 nM), the number of detected binding events scales proportional to the imager concentration and the binding time τ_{ds} (measured as the event duration τ_F) is independent of the concentration. **(d)** At higher imager concentrations, overlapping events result in a decrease in observed binding events and the measurement of event duration shows large error values. Error bars: standard deviation of events (black) or mean event duration (blue) per second.

binding rate. The acquisition time necessary for a sufficient number of detected binding events is proportional to the inverse of the binding rate, and with a higher acquisition time sample drift increasingly reduces imaging quality. However, if the binding rate is too high, the number of overlapping binding events increases. Even advanced fitting methods can extract localisation data out of overlapping events only to a certain limit [46]. Note that the optimum imager concentration depends on the local density of docking strands.

Figure 4.7 b demonstrates that the diffuse fluorescent background signal, here measured in an area without docking strands present, is proportional to the imager concentration over the range of concentrations relevant for DNA-PAINT. The inset shows a magnified view of data points not resolved in the main plot. Consequently, background fluorescence measurements provide a direct measurement of the imager concentration.

As shown by Jungmann et al. [18], figure 4.7 c confirms that the observed binding rate is proportional to the imager concentration, here between 0 and 0.1 nM. The mean binding time, approximated by the mean lifetime per fluorescent blinking event τ_F is independent of the imager concentration (figure 4.7 c, blue). However, the previously published linear relationship between observed rate of detected binding events and imager concentration only holds for a limited range of imager concentrations. At concentrations higher than ~0.1 nM, a non-linear relationship between the imager concentration and the fluorescent event rate was observed (figure 4.7 d, black). These imager concentrations correspond to the values at which overlapping events become non-negligible and event detection becomes problematic. If binding events are assumed to scale proportionally with the imager concentration, then the increasing number of overlapping blinking events which cannot be localised can explain the reduction in apparent binding event rate at concentrations >1 nM. Additionally, the event duration cannot be determined reliably at high concentrations, resulting in large error values.

4.2.2 Illumination intensity

Often, DNA-PAINT is portrayed as virtually unaffected by photobleaching, due to the constant influx of new, unbleached imager strands [3, 20, 22]. Imager-docking binding events are considered to be terminated by unbinding of the imager [18]. However, at sufficiently high illumination intensities, the mean lifetime of fluorescence emission by a fluorophore which is limited by photobleaching

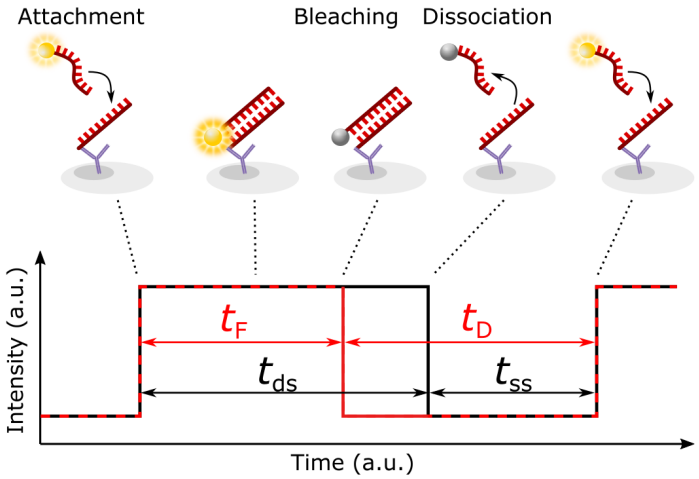

Figure 4.8: Life times relevant for DNA-PAINT in case of premature event termination due to photobleaching. The imager binds to the docking strand for t_{ds}, with a mean double stranded lifetime τ_{ds}. After dissociation, the docking strand remains single stranded for t_{ds}, with a mean single stranded lifetime τ_{ds}. Observed on the fluorescence microscope is the fluorescence time t_F, with a mean τ_F, followed by a dark time t_D, with a mean τ_D.

can reach values similar to the mean binding lifetime of the imager τ_{ds}, in which case the detected fluorescence emission from an imager binding event can be terminated prematurely due to its photobleaching. This case is illustrated in figure 4.8. Detected blinking events are characterised by observed fluorescence and dark times τ_F and τ_D. Only if the time to photobleaching is larger than the imager binding time, it can be assumed that $\tau_F = \tau_{ds}$. In case of photobleaching of the fluorophore while the imager is still bound to the docking strand, this leads to reduced fluorescence on-times $\tau_F < \tau_{ds}$.

In principle, the dependence of DNA-PAINT on different illumination intensities can be characterised by sequentially illuminating a sample with varying laser powers. As this can lead to varying experimental conditions over the course of the experiment, here, different illumination intensities are compared simultaneously by detecting signals from a densely labelled, but homogeneous sample over a large field of view, using the non-uniform laser profile. Figure 4.9 a shows a microsphere sample at the edge of the "coffee ring" structure as seen in figure 3.2. The imaged structure showed a high density of docking strands, but still provided feedback to ensure only specific binding is observed.

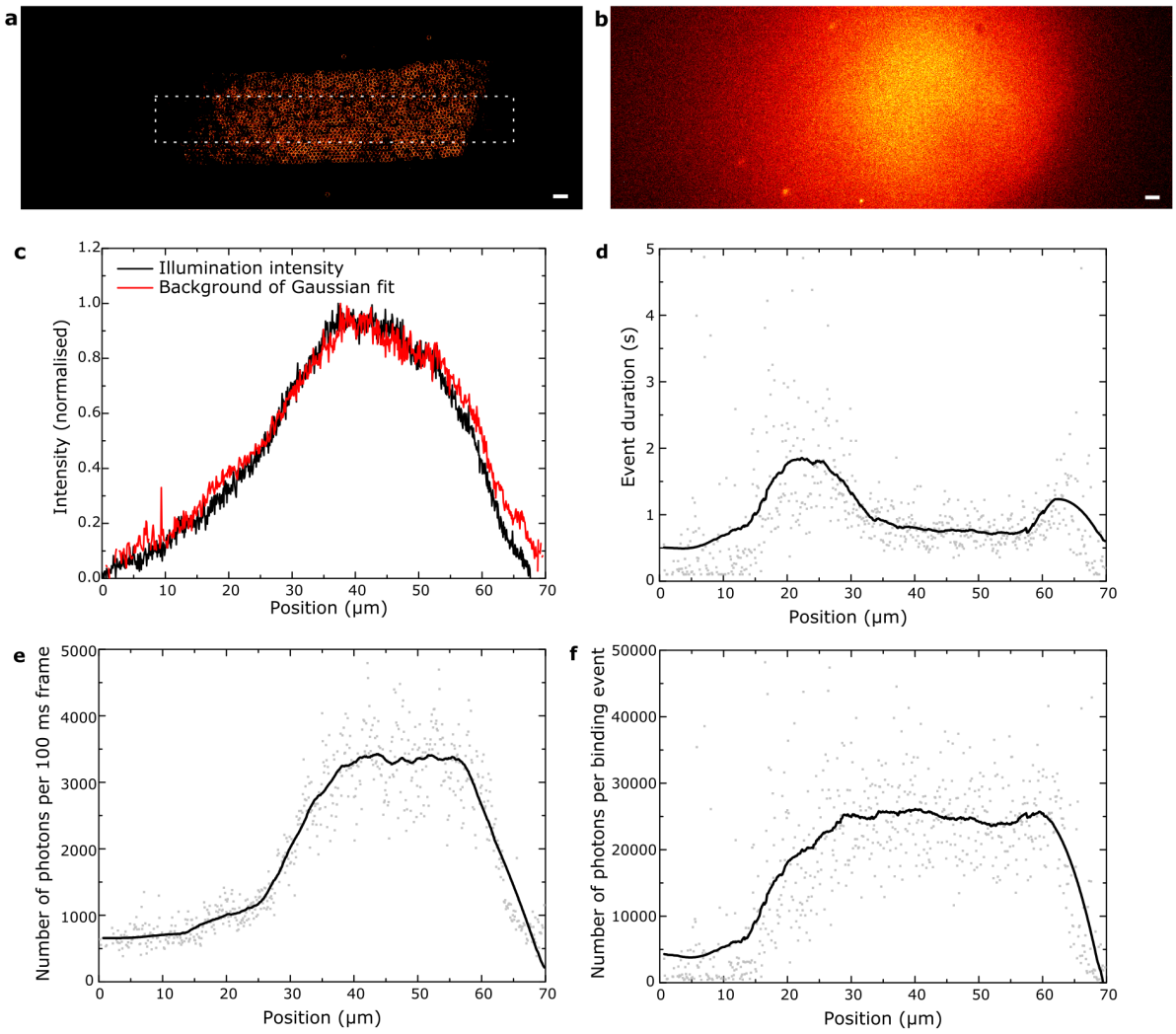

Figure 4.9: Influence of illumination intensity on DNA-PAINT. **(a)** Rendered image of dense area of microspheres, white dashed line indicates area used for intensity-dependent measurements. **(b)** Laser illumination profile on empty glass coverslip. **(c)** Normalised illumination intensity (black) depending on horizontal position of region of interest shown in a, in comparison to the mean offset (background) of the Gaussian fits to events detected at the respective locations. **(d)** Event duration for the positions used in c, limited by the detection threshold for low intensities and by photobleaching for high intensities. **(e)** Photon flux, i.e. the number of photons detected per 100 ms frame and per event, depending on position used in c, roughly proportional to the illumination intensity. **(f)** Total number of photons per binding event as a function of position, limited by photobleaching in areas of high illumination intensity. Lines: 100 pt moving-average filter. Scale bars: 2 µm.

The structure was illuminated with a laser profile shown in figure 4.9 b. Here, only the coverslip in absence of microspheres and imager was imaged. The detected intensity was assumed to represent the intensity profile of the laser beam. Its origin was not analysed, but it might stem from fluorescence or Raman scattering of the glass itself or impurities within, and the profile was independent of the position of the sample. A cross-section through the illumination profile along the horizontal axis of the area indicated by the dashed white box in figure 4.9 a is shown in figure 4.9 c, black curve. From 0 to ~40 µm, the intensity increases almost linearly, which allowed for acquisition of sufficient data for the characterisation of DNA-PAINT at different intensities. Alternatively, the illumination intensity can be directly estimated from the localisation data. Each binding event was fitted with a 2D Gaussian, with an offset- or background-parameter. If the density of events is sufficiently low, the offset is only dependent on the local diffuse fluorescence background and thus proportional to the local illumination intensity in the likely absence of saturation of excitation (compare figure 4.7 b). The red curve in figure 4.9 c shows mean offset values of the Gaussian fits, binned over areas 100 nm in width, and is in good agreement with the directly measured illumination profile.

Figure 4.9 d shows the average event duration depending on the position used in figure 4.9 c. Here, a 10 bp overlap of imager and docking strands was used. The event duration increased with increasing illumination intensity, presumably because events were increasingly likely to exceed the detection threshold. However, at a location where approx. 50 % of the maximum laser intensity is reached, the event duration started to decrease. At this stage, photobleaching outweighed the binding lifetime of the imager (here approx. 2 s).

The mean photon number per binding event and per frame (100 ms integration time), i.e. the photon flux, depending on the position in the sample is shown in figure 4.9 e. For illumination intensities between ~20% and ~80%, the photon flux broadly followed the illumination profile. The SNR-based threshold which determines which fluorescence events are detected effectively sets a minimum value for the photon flux of detected events. This leads to fewer events being detected at low intensities (<20%) and the mean photon flux of detected events not falling below a mean value of ~500 photons per frame. At high illumination intensities (>80%), the photon flux is saturated, possibly because the photobleaching lifetime approached the camera integration time.

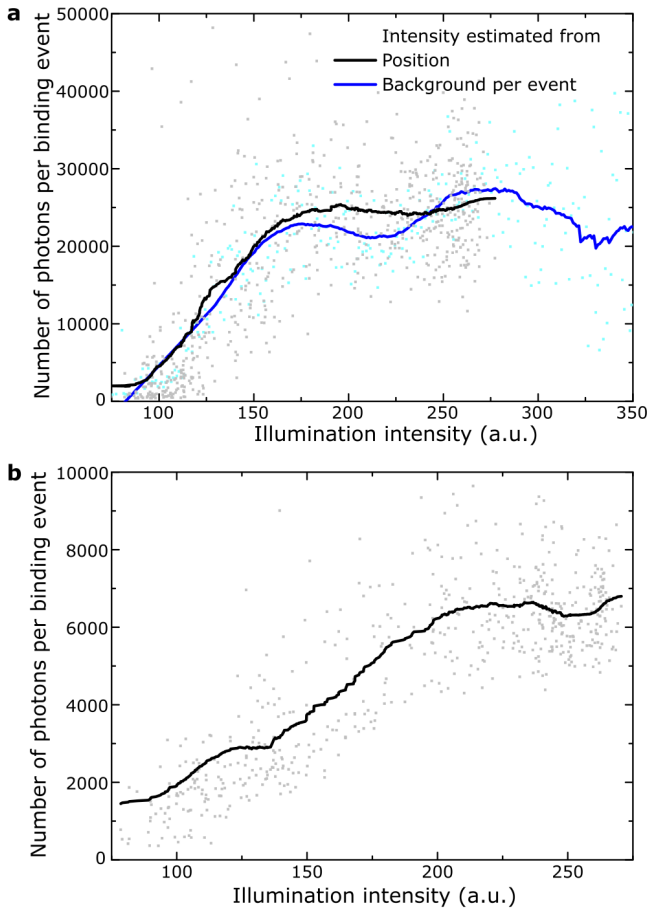

Figure 4.10: Influence of illumination intensity on number of photons per binding event. **(a)** Imager-docking strand overlap of 10 base pairs (bp). Black: illumination intensity estimated from the position, as shown in fig 4.9 c. Blue: Intensity estimated directly from the offset/background of the Gaussian fit to each event. **(b)** Photons per event depending on illumination intensity estimated from position, for an imager-docking strand overlap of 9 bp. Lines: 100 pt moving-average filter.

Of more relevance than the binding event photon flux is the total number of photons per event, as this determines its localisation precision. The total number of photons per binding event depending on the location is shown in figure 4.9 f. It is proportional to both the mean photon flux of an event as well as the event duration, which are discussed above and shown in figures 4.9 d and e.

Figure 4.10 a illustrates the total number of photons per binding event depending on the illumination intensity, for the data used in figure 4.9. For data shown in black, each location in the sample was assigned an illumination intensity

value as shown in figure 4.9 c (black). The mean total photon number per event was calculated for each of the locations and plotted against the respective illumination intensity. A similar distribution of events can be seen in blue. Here, the background values, i.e. values of illumination intensity, are taken directly from the offset of the Gaussian fit for each event. Values exceeding the intensity maximum obtained in the data shown in black can occur from neighbouring binding events which additionally increase the individual local background.

A similar distribution can be seen for imager strands with lower docking strand affinity (9 bp overlap, figure 4.10 b). The saturation intensity was slightly higher than that of imager strands with 10 bp overlap. This was expected as the mean photobleaching time of the fluorophores would remain the same but the mean imager-docking binding time, which can also end a blinking event, is shorter for lower imager-docking affinities. In conclusion, the illumination intensity is an important factor to be optimised for increasing the number of detected photons per binding event and the optimum illumination intensity is strongly imager/docking affinity dependent – illumination at higher intensities results generally in higher photon numbers and thus an increased localisation precision. However, if the illumination intensity exceeds the saturation point, the photon number no longer increases and the signal-to-noise ratio will decrease.

4.2.3 Buffer conditions

Imaging of microspheres in open-top chambers allows for changes of the buffer conditions, e.g. the buffering agent, ion concentrations or additional components during an experiment and thus the direct observation of their influence on DNA-PAINT parameters. One example is shown in figure 4.11. Due to the phosphate group in its backbone, DNA is negatively charged which results in Coulombic repulsion of two single strands. The repulsion can be compensated for by sufficient ion concentrations (e.g. Na^+ or Mg^{2+}), with the affinity of DNA strands being nonlinearly dependent on the ion concentration [158]. A Na^+-dependent change in affinity of imager and docking strands is shown in figure 4.11. Here, the number of binding events per frame (event rate, black) increases for concentrations of Na^+ <600 mM. Interestingly, the stability of the double strand, measured by the event duration at illumination intensities low enough for negligible photobleaching, remains constant over the measured range of Na^+ concentrations (blue). Consequently, changing the NaCl concentration

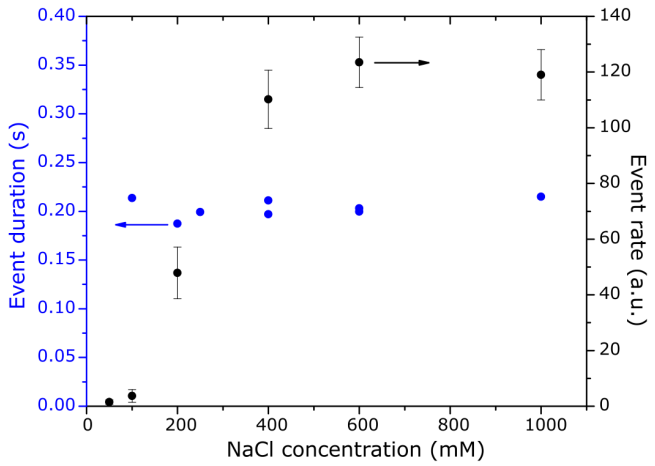

Figure 4.11: Event rate and event duration depending on NaCl concentration. Blue: Event duration, using 9 base pair imager-docking strand overlap and reduced illumination intensity so that the event duration approximately corresponds to the imager-docking strand binding lifetime. Black: Number of detected binding events per frame (100 ms). Error bars: standard deviation of events per frame.

between 100 mM and 600 mM was found to represent an alternative method for tuning the event density.

A range of different buffer compositions is compared in figure 4.12. Two buffering agents were compared, Tris (tris(hydroxymethyl)aminomethane) used in an Tris-EDTA (TE) buffer (blue, cyan), and phosphate buffered saline (PBS, red, pink), both previously used in DNA-PAINT [22]. Additionally, different pH levels were compared as well as the influence of additionally added Mg^{2+} (dashed lines), as often used for DNA origami [19, 22]. All buffers contained 500 mM NaCl. The imager-docking binding event rate remained within the same order of magnitude for all buffer conditions, with slightly higher binding rates observed for TE buffer with added $MgCl_2$ at 10 mM (figure 4.12 a). As shown in figures 4.12 b and c, both the event duration and the mean number of photons per binding event appear to be independent of the tested buffer conditions, indicating that DNA-PAINT interactions are stable over the range of typically used buffer parameters. Figure 4.12 d shows the distribution of photon numbers per event corresponding to the data shown in figure 4.12 c.

As implied by the results shown in figure 4.10, higher localisation precisions per binding event could be achieved by reducing the degree of photobleaching. Pho-

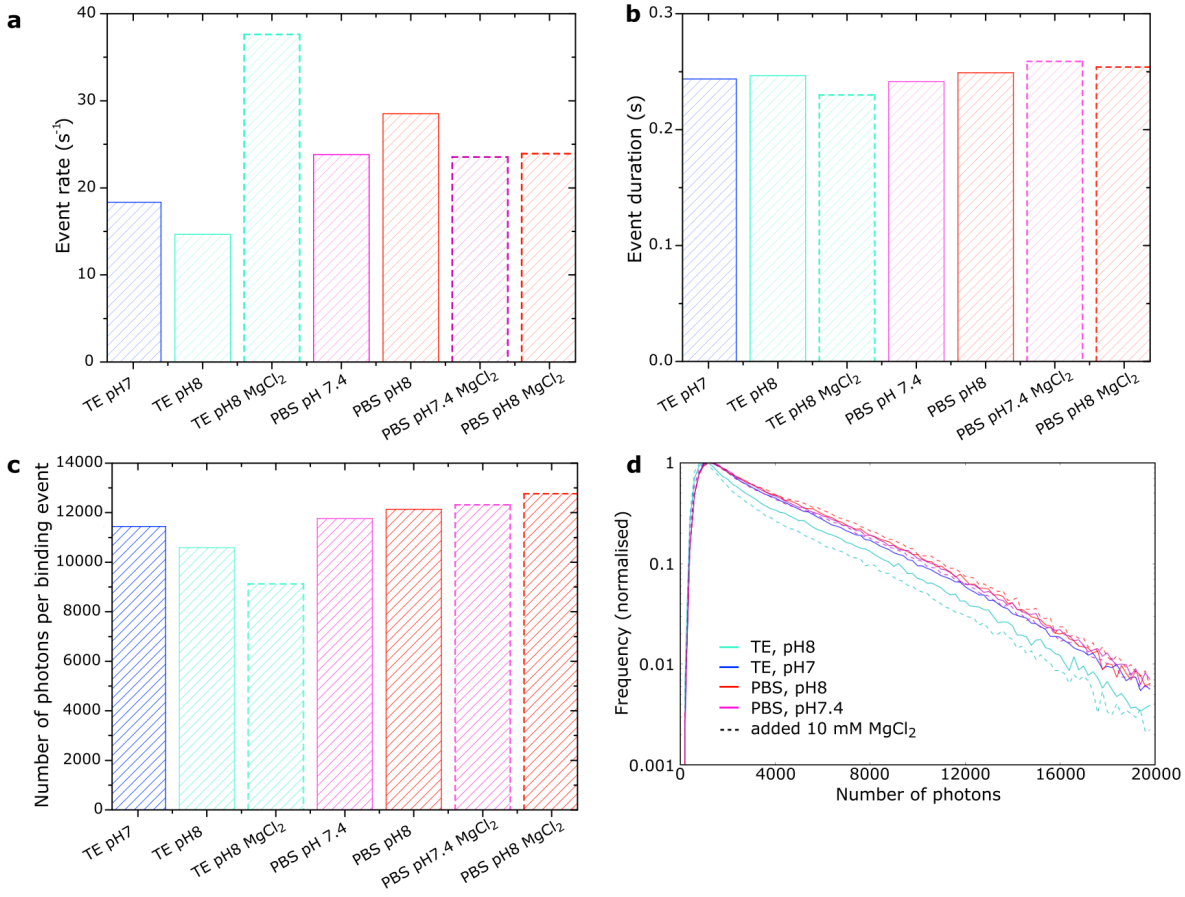

Figure 4.12: Influence of buffer properties on DNA-PAINT parameters, comparing Tris-EDTA (TE) buffer (blue, cyan) to phosphate buffered saline (PBS, pink, red), pH 7 (blue), pH 7.4 (pink) and pH 8 (cyan, red), and added $MgCl_2$ (dashed outlines). **(a)** Comparison of event rates. Note that the event rate directly depends on the imager concentration which can vary considerably at low values. **(b)** Event durations, estimating the mean binding lifetime. **(c)** Number of photons per binding events. **(d)** Distribution of number of photons per binding event for values shown in c. As shown here, the number of photons for DNA-PAINT events was typically linearly distributed in a logarithmic plot, with a detection cut-off near the peak of the histogram, which strongly depends on the chosen detection threshold.

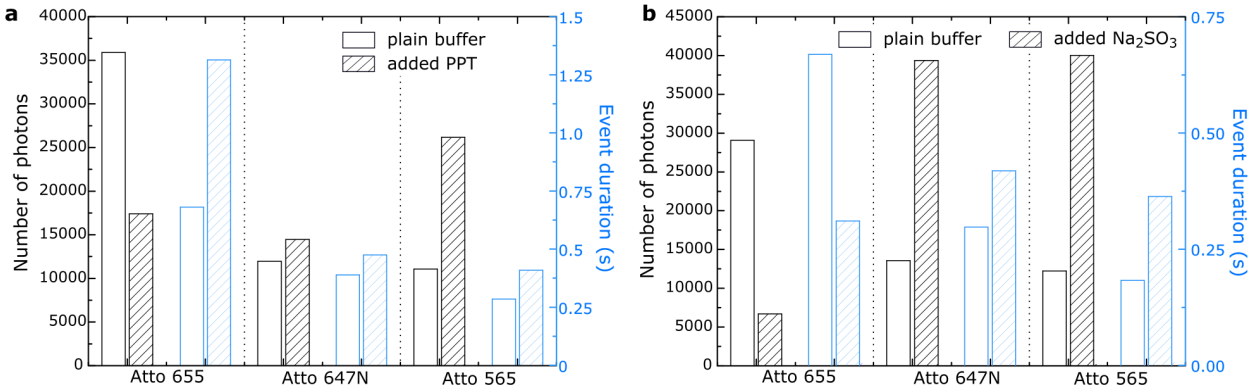

Figure 4.13: Influence of oxygen scavenging solutions on photon number per binding event (black) and event duration (blue) for different dyes used in DNA-PAINT. Comparison of Atto 655, Atto 647N and Atto 565. **(a)** Comparison of plain buffer (TE buffer + 500 mM NaCl, empty bars) and buffer with added oxygen scavenging system PCA/PCD/Trolox (PPT, filled bars). **(b)** Comparison of plain buffer with oxygen scavenger agent sodium sulfite Na_2SO_3.

tobleaching often occurs due to the presence of oxygen in the sample, and can be reduced by using oxygen scavenger systems, e.g. a mixture of PCA (Protocatechuic acid), PCD (Protocatechuate 3,4-dioxygenase) and trolox (as mixture: PPT) [159], as previously used in DNA-PAINT [22, 160]. An alternative oxygen scavenger is sodium sulfite (Na_2SO_3), which has been used in single molecule imaging [161, 162].

The effect of addition of the oxygen scavenger systems is compared to the use of plain buffer in figure 4.13 for different fluorophore-modifications of the imager. An imager with increased affinity (10 bp overlap) was used at high illumination intensities (~70 % of maximum value in figure 4.10), in order to see an effect on the photobleaching lifetime of the fluorophore while attached to the docking strand. While the event duration for the fluorophore Atto 655 almost doubled when adding the PPT system (figure 4.13 a, blue), the photon flux decreased considerably, and the total number of photons per binding event was reduced to approx 50 % (black). Slight increases in photon number and event duration were observed for Atto 647N and a strong increase in photon flux, resulting in a >2× increase in photons per binding event, was observed for Atto 565. As shown in figure 4.13 b, a 50 % decrease in event duration was observed for Atto 655 when using Na_2SO_3, resulting in a ~75 % decrease in the number of photons per binding event. Strong increases in photon numbers were observed for Atto 647N

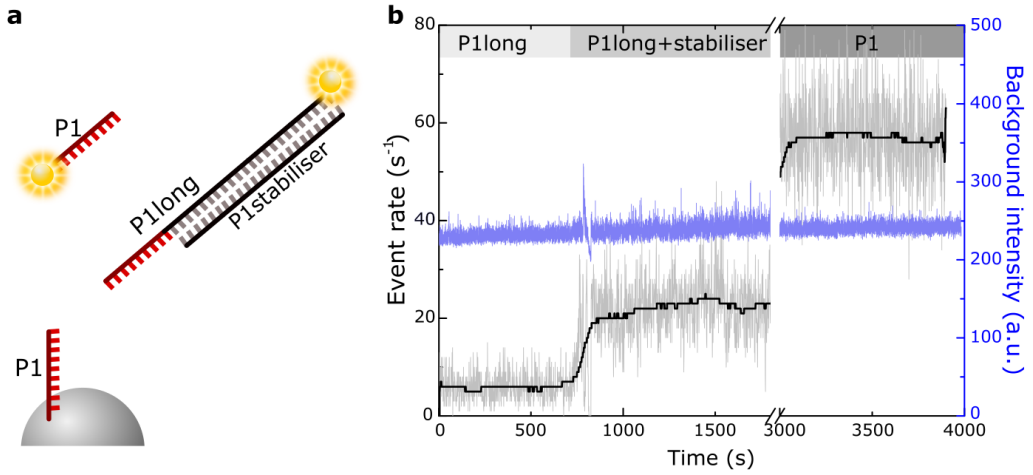

Figure 4.14: Influence of additional bases at the imager on imager-docking binding event rate. **(a)** Schematic drawing comparing regular P1 imager (10 bases, 9 bases complementary to docking sequence) to P1long (9 bases complementary to docking sequence and additional 23 noncomplementary bases), with an optional P1stabiliser to render noncomplementary section of P1long double-stranded. **(b)** Event rate (black) of P1long without stabiliser, followed by addition of P1stabiliser in excess to P1long, in comparison to regular P1 imager. A constant background intensity (blue) indicates that the imager concentrations remain constant.

and Atto 565 when adding Na_2SO_3. A potential reason for reduced number of photons per event of Atto 655 by the tested oxygen scavenging systems could be its strong quenching by electron donors, as stated by the manufacturer [23].

4.2.4 Imager affinities

The flexibility of the microsphere assay also allows for testing of alternative DNA interactions schemes, beyond conventional 9- or 10 bp imager-docking interactions. Here, the influence of extensions of the imager or docking strands are studied. Some examples from literature which could be characterised directly with the test assay is Foerster resonance energy transfer (FRET)-based DNA-PAINT [70] or the extension of imager strands by additional, double stranded domains to prevent photodamage [84]. The influence of extended imager or docking strands is relevant later in this thesis when schemes for increasing the signal-to-noise ratio are examined, as described in chapter 7. There, an extended imager complex enabled addition of multiple fluorophores to a single imager, in-

creasing the photon flux, and an extension of the docking strands with repeated docking domains was tested for an increased binding rate at constant background levels.

Figure 4.14 shows the influence of the addition of noncomplementary bases to the imager on apparent imager-docking affinity. The imager sequence of "P1long" contains the same domain complementary to the docking strand as regular DNA-PAINT imager P1, but is extended by an additional, noncomplementary domain of 23 nt. The background intensity is controlled to be constant for a comparison of both regular P1 imager and P1long imager, indicating that imager concentrations are the same (figure 4.14 b, blue, background levels at approx. 150 a.u.). The observed rate of binding events (black) for P1long is approx. an order of magnitude smaller than for conventional P1. The effect of the additional sequence extension on the binding rate can be compensated partially by addition of a stabilising strand (P1stabiliser), rendering the extended sequence double-stranded and thus more rigid.

A similar effect was observed for extensions of the docking strand structure, as shown in figure 4.15. Microparticles were functionalised with extended docking strands, containing three orthogonal docking domains (P1, P3, P5), separated by 6 thymines. As a Nupack [142] analysis shows, the strand remains largely single stranded and accessible for imager binding, only the P5 docking domain has a ~10 % probability of forming a secondary structure. Imagers P3, P5 and P1 were imaged sequentially, the binding event rate is shown in figure 4.15 b. While imager P1 and P3 show comparable binding rates, P5 binding is considerably reduced. The event rate can be increased 5-fold if the rigidity of the docking strand is increased by hybridisation of a stabiliser (figure 4.15 b, $t > 700$ s). The remaining difference between P1 and P5 binding event rates could occur due to the formation of secondary structures of the P5 docking domain as shown in figure 4.15 a. The decrease of the P1 imager binding rate in figure 4.15 d after addition of the stabiliser strands shows the high rate of hybridisation to the docking strand, making the P1 docking site inaccessible to the P1 imager. Figure 4.15 c compares mean binding event rates for the cases shown in figure 4.15 b and d.

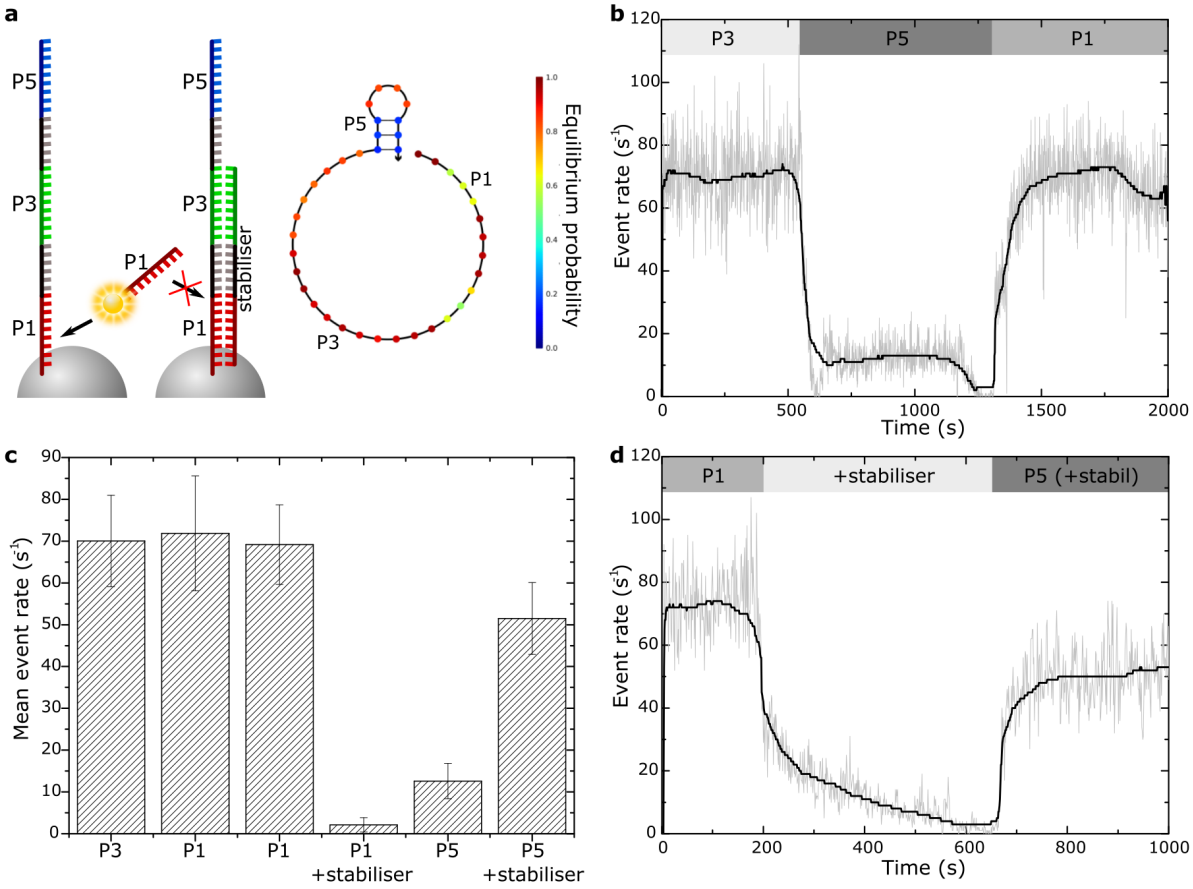

Figure 4.15: Effect of increased docking strand lengths on imager-docking binding rate. **(a)** Schematic drawing showing extended docking strand, containing a P1, P3 and P5 docking domain, separated by poly(T) spacer sequences. A stabiliser can be added to permanently hybridise to the P1/P3 domains of the docking strand. A Nupack analysis [142] shows a high probability of the docking strand being in fully single stranded state. **(b)** Binding event rate for P3- P5- and P1-imager subsequently imaged with the same imager concentration. **(c)** Mean binding event rates for different modes shown in b and d. Error bars: standard deviation of events per second. **(d)** Binding event rate of P1 imager without and after adding the stabiliser. P5 binding event rate after addition of stabiliser.

4.3 Use of the microsphere assay for optimised qPAINT analysis

The effective circumvention of photobleaching and the well characterised binding and unbinding behaviour of imager strands enable quantitative imaging by DNA-PAINT, i.e. a quantification of the number of labelled targets. While the number of binding sites can be estimated by directly measuring the binding frequency [163], it is preferable to use the distribution of times between events (dark times) in order to avoid under-counting of binding sites [21]. This so-called qPAINT approach can be applied to different DNA-PAINT variations, e.g. as described in chapter 6 and is used for quantification of docking sites throughout this thesis.

For qPAINT, it is assumed that detection of a fluorescent event ends with the unbinding of the imager from the docking site. However, as shown in figure 4.16, the absence of detectable binding events can have multiple reasons. Here, three examples resulting in detection of a short, single-frame dark time are shown. Figure 4.16 a shows the generally assumed case, with an imager detaching from the docking site and, subsequently, another imager strand binding to a docking site on the same complex of interest. Here, the second imager hybridised to a different docking strand, seen by a clear spatial shift between the two events.

A single-frame dark time can also originate from events detected near the detection threshold (figure 4.16 b). A single binding event was observed throughout the sequence, but a slight modulation in brightness results in the event not being detected in the second frame. A third example of a short dark time is shown in figure 4.16 c. Here, a strong intensity modulation was seen without a spatial shift between the events. This can result from either blinking of the fluorophore or subsequent binding of the same, or different imagers to the same docking strand. The ratio of short dark frames resulting from near-threshold detection as shown in figure 4.16 b can be estimated from the photon distribution as shown in figure 4.16 d. Here, detected events which occur just before or after a single dark frame are shown in black, as a subset of the total events in grey. Events just after or before short dark times showed a reduced mean photon number. As low photon numbers are characteristic for near/threshold detection, this indicates that a considerable fraction of short dark times originate from detection of events near the threshold.

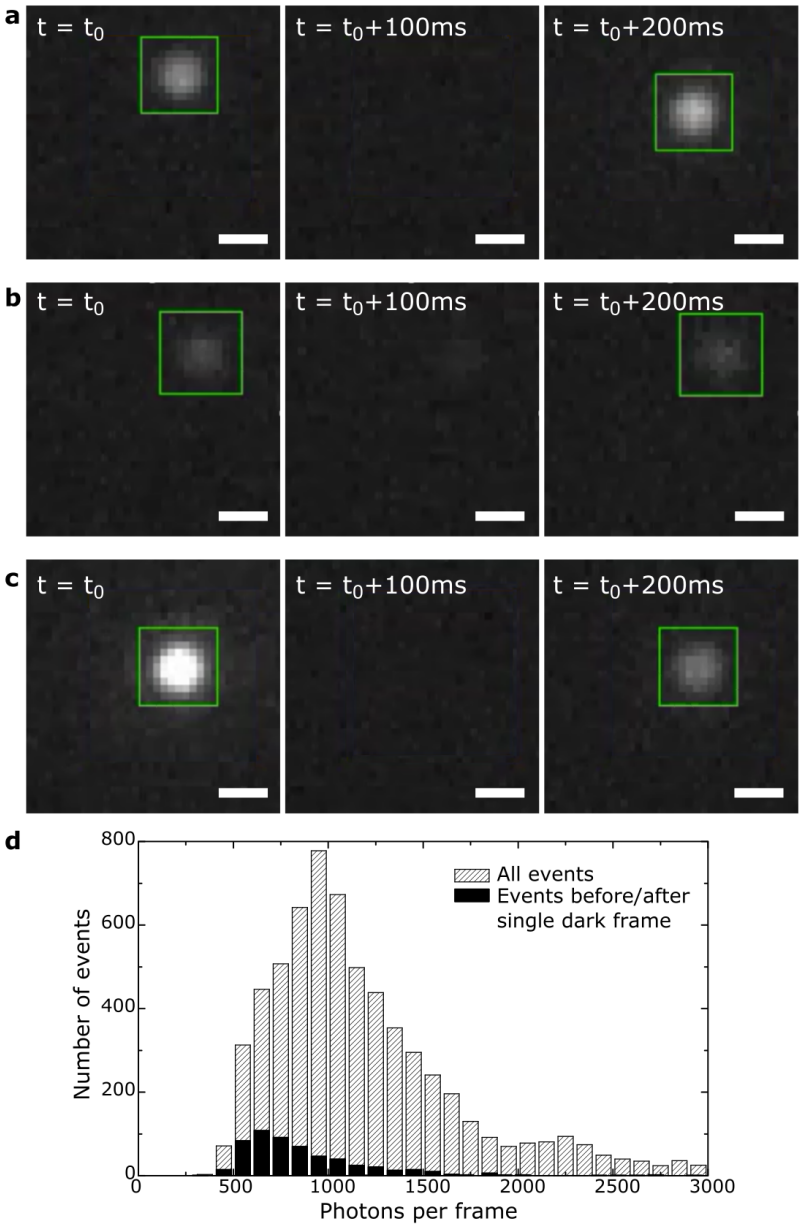

Figure 4.16: Examples of raw data resulting in short dark times, relevant for quantitative imaging. Green squares indicate an event detected by the analysis software. **(a)** Three consecutive frames showing two different imager strands binding to nearby, but different docking strands, resulting in a single-frame dark time. **(b)** Imager binding event near detection threshold, a slight reduction in intensity results in a single-frame dark time. **(c)** Single-frame dark time resulting from strongly modulated imager intensity at a single location. This can either be due to blinking or subsequent binding and unbinding of imagers to the same docking strand. **(d)** Distribution of photons per event and frame shows an increased number of low photon events just after or before single-frame dark times, indicating a strong influence of the case shown in b. Scale bars: 500 nm.

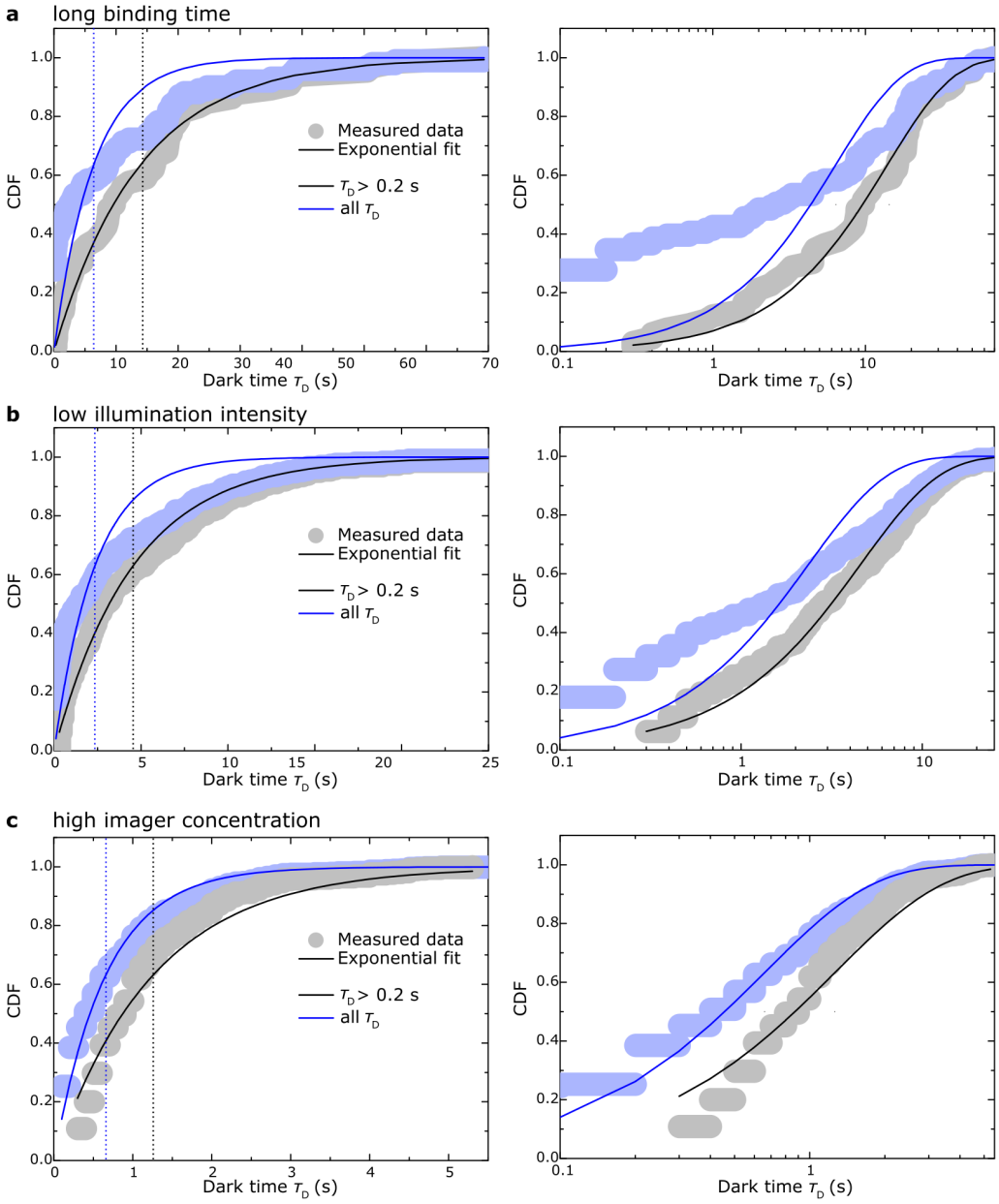

Figure 4.17: Cumulative distribution function (CDF) of dark times for different cases of DNA-PAINT. Measured data is shown in light grey/blue, the exponential fit as a line. Blue curves: total measured dark times, black: dark times of single and double frame length omitted. Right column: Plots shown on left with logarithmic x-axis scaling. **(a)** Imager with imager-docking sequence overlap of 10 base pairs, resulting in longer imager-docking binding time than the usually use 9 base pair overlap. **(b)** Illumination intensity reduced to 1/3 of typically used intensity, resulting in decreased mean photon numbers. **(c)** High imager concentration (0.1 nM on 500 nm microspheres) used, resulting in a shorter average dark time between binding events.

The effect of dye blinking and near-threshold detection on the dark time distribution is shown in figure 4.17. In qPAINT, the mean dark time, from which the number of binding sites is calculated, is obtained from an exponential fit to the cumulative distribution function of dark times. In figure 4.17 a, imagers with increased binding time (10 bp overlap with the docking strand) were used, which was expected to increase the number of short dark times due to near threshold detection. As shown in particular at logarithmic scaling of the x-axis (right), an exponential fit to the dark time distribution (blue) shows strong distortions at low dark times. However, an exponential fit shows a considerably improved overlap if single- and double-frame dark times are omitted in the distribution (grey). A similar effect was observed when using low illumination intensity (figure 4.17 b), with the total dark time distribution (blue) not being fitted by an exponential distribution as well as when short dark times are omitted (black).

However, the opposite effect can be seen in cases of high event densities, e.g. due to a high density of docking sites or an increased imager concentration (figure 4.17 c). Here, the average dark time was considerably shorter than in the cases described above, so that the influence of near-detection threshold dark times or of imager blinking becomes negligible. As a result, an exponential fit matches the total dark time distribution (blue) better than when short dark times were omitted (black).

Omission of short dark times strongly affects the calculated mean dark time $\tau_{\mathrm{D,mean}}$, and consequently the calculated number of binding sites. Mean dark times are shown as dashed lines in figure 4.17, changing by a factor of 2.23, 1.94 and 1.91 for figures 4.17 a, b, c, respectively. The influence of different factors on the dark time distribution was mentioned in a recent publication by Baker et al. [83], in which dark times below 300 ms were attributed to blinking of the imager while bound and were omitted. To conclude, qPAINT requires careful observation of the fit quality. Either the fit should be adjusted for optimum match to the dark time distribution by omitting a certain number of dark frames, or an omission value proportional to the calculated mean dark time should be chosen (e.g. omitting dark times $\tau_{\mathrm{D}} < 0.1 \cdot \tau_{\mathrm{D,mean}}$ would result in good exponential fits for all cases shown here).

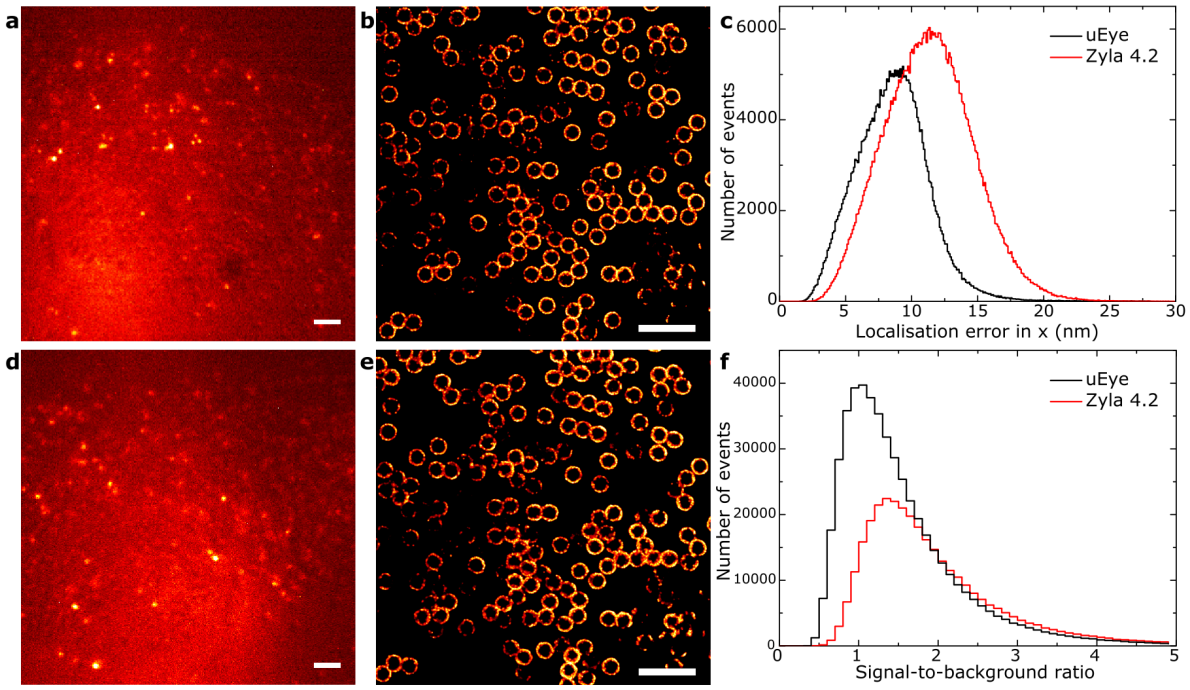

Figure 4.18: Comparison of different cameras for DNA-PAINT imaging, using an imager modified with Atto 488. **(a)** Raw data and **(b)** rendered DNA-PAINT image of 500 nm microspheres taken with a uEye camera (IDS, Obersulm). **(d)** Raw data and **(e)** rendered data for an Andor Zyla 4.2 sCMOS camera. **(c)** Localisation error for the camera data shown in a,b (black) and d,e (red). **(f)** Signal-to-noise ratio for the data detected by both cameras. Scale bars: 2 µm.

4.4 Other uses of the microsphere test assay

Apart from analysing the characteristics of DNA-PAINT interactions, the microsphere assay can also be used to test the general performance of the imaging setup and analysis modules, either when introducing new modalities or as a regular quality control measurement. While the uses shown here were not central to the results shown later in this thesis, they illustrate other uses of the assay preparation and further demonstrate its utility as a flexible test preparation.

4.4.1 Comparison of different cameras

One example is the comparison of different cameras for single molecule localisation microscopy, as shown in figure 4.18. The same, homogeneous sample of microspheres was sequentially imaged using different output ports of the microscope, coupled to an Andor Zyla 4.2 sCMOS and an IDS uEye camera. The uEye camera is considerably cheaper than a Zyla sCMOS, and shows the highest quantum efficiency below 650 nm. Consequently, imager strands modified with Atto 488 were used instead of Atto 655. Figure 4.18 a and d show raw data for the uEye (a) and Zyla (d), with the colour-scaling artificially increased to show regions of low intensity with higher contrast. Here, a faint striped pattern can be seen for the uEye camera, which might potentially affect DNA-PAINT localisation. Imaging of microspheres, however, yields high resolution in both cases (figure 4.18 b, e) and both the localisation error and the signal-to-background ratio are slightly higher for the uEye camera. However, using this blue-shifted excitation wavelength (here: 488 nm) can be problematic in biological samples and often leads to increased background blinking. Here, background fluorescent events were reduced by extensive bleaching of the imaged region at high laser intensities before imaging, which should be avoided in biological samples.

4.4.2 Biplane 3D imaging

The monodisperse appearance of the microspheres provide a useful test sample for 3D imaging. In figure 4.19, microspheres of 500 nm and 2 µm diameter were imaged in biplane 3D mode. The emission path was split using a 50:50 beam splitter and imaged on one half of the camera chip each, as described in chapter 3.2.3. A lens with long focal length (4 m) was inserted into one path, leading to a focal shift along the optical axis of approx. 350 nm. By taking a calibration PSF with fluorescent beads, the axial position for each DNA-PAINT event can be determined, when comparing appearance in both focal channels.

The localisation data when imaging 500 nm microspheres is shown in figure 4.19 a, with a cross section along the plane indicated in light grey shown in figure 4.19 c. The colour scaling corresponds to the z-position of the detected events. The imaged particles do not appear spherical, which can have multiple reasons: (1) the refractive index mismatch between the aqueous buffer medium and the coverslip leads to a foreshortening of the apparent focal plane, which

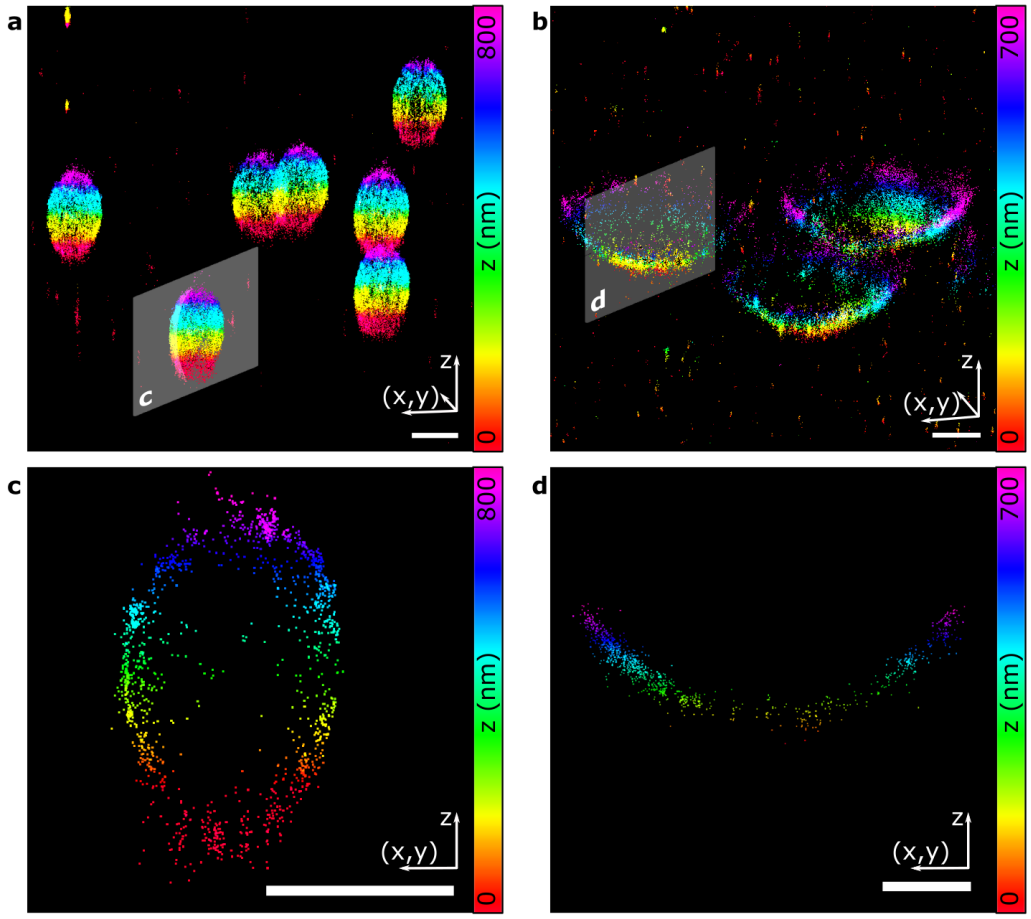

Figure 4.19: Biplane 3D imaging of microspheres of different sizes. Colour coding illustrates position along the optical axis. **(a)** 3D localisation data of imagers binding to the surface of microspheres with a diameter of 500 nm. Along the optical axis z, the spheres appear distorted due to a refrective index mismatch between the aqueous buffer solution and the coverslip and oil immersion, possibly also due to a lensing effect of the microspheres. **(b)** 3D localisation data for microspheres of a nominal diameter of 2 µm. **(c)**, **(d)** Cross sections along the optical axis for spheres shown in a and b. Scale bars: 500 nm.

would have to be compensated in post-processing. This effect would lead to a roughly elliptical representation of localisation data as shown in figure 4.19 c, (2) the refractive index mismatch of polystyrene (1.59) and the imaging buffer can lead to a change of the degree of foreshortening and additionally to a lensing effect, making the exact determination of binding events from the top half of the microsphere difficult. However, localisation events from the bottom half of the microspheres should only be minimally distorted due to a lensing effect originating from the refractive index mismatch of the particle and its surrounding, which allows for the use of microspheres for characterisation of foreshortening in aqueous samples. As shown in Lin et al. [4], an ellipsoidal model can be fitted to the localisation data and information about foreshortening and additional non-linear effects extracted.

Figure 4.19 b shows 3D imaging of microspheres with a nominal diameter of 2 µm, and a cross-section in figure 4.19 d. Due to the optical sectioning by TIRF-illumination, only a limited area near the bottom of the microsphere is imaged.

4.5 Limitations of the microsphere test sample

In this section, limitations of the microsphere assay for DNA-PAINT analysis are discussed. Limitation can occur due to two reasons,

(1) the simplified microsphere assay cannot be used to reproduce effects unique to the application of DNA-PAINT, e.g. in biological samples. Examples relevant for the following chapters are the limited diffusion of imager strands in thick tissue sections compared to microspheres or isolated cells which are directly exposed to changes in the imaging buffer, and the influence of nonspecific binding to biological samples on the signal-to-background-event ratio. Other test samples might simulate these conditions in a better way, such as the development of cell lines giving reproducible biological samples [164]. However, such samples usually involve considerably more complex preparation steps. New methods presented in the following chapters were tested in biological samples after initial testing on the microsphere assay,

(2) the microsphere assay does not always provide high quality data, e.g. due to a low signal-to-noise ratio. An exemplary case of reduced SNR due to excitation at short wavelengths is discussed below.

4.5.1 Autofluorescence of microparticles

During synthesis and functionalisation of the microspheres, the synthesis of oligonucleotides and during labelling of microspheres with docking strands, there are chances of impurifications building up in the sample which can show an increase of background fluorescence. While background fluorescence is negligible for DNA-PAINT using a 647 nm laser after brief photobleaching of the sample at high intensities, higher background was observed at shorter wavelengths, e.g. at 488 nm as shown in figure 4.20.

In figure 4.20 a, an area containing a high density of microspheres was imaged near a region without any particles, as seen in the transmission image (top). When no imager was added, excitation at 488 nm resulted in higher fluorescent background from locations of the microspheres (centre), while no increased fluorescence was observed at 647 nm (bottom). While similar increased background was observed when adding Atto 488-modified imager strands (figure 4.20 b, right), increased background was not observed in biological samples, e.g. imaging microtubules in fixed cells (figure 4.20 b, left). Arrows in the microsphere sample point at imager binding events, which are of comparable intensity to the fluorescent background. Figure 4.20 c shows rendered images of the sample used above, when imaged without imager strands first (green), and after addition of the imager (red). Considerably higher background fluorescence results in detection of events for microspheres (right), distorting the DNA-PAINT data. The ratio of detected fluorescent events before and after addition of the imager strands is shown in figure 4.20 d, giving an approximate signal-to-background-event ratio of 458.7 for the biological sample and a reduced signal-to-background-event ratio of 5.03 for microspheres.

While non-uniform fluorescent background is routinely corrected for in other single molecule localisation methods, e.g. in STORM [53], most methods cannot be applied if background fluorescence shows blinking behaviour, as observed for the microspheres. Only strong photobleaching could reduce its intensity, as well as careful comparisons of variations between different batches of labelled microspheres.

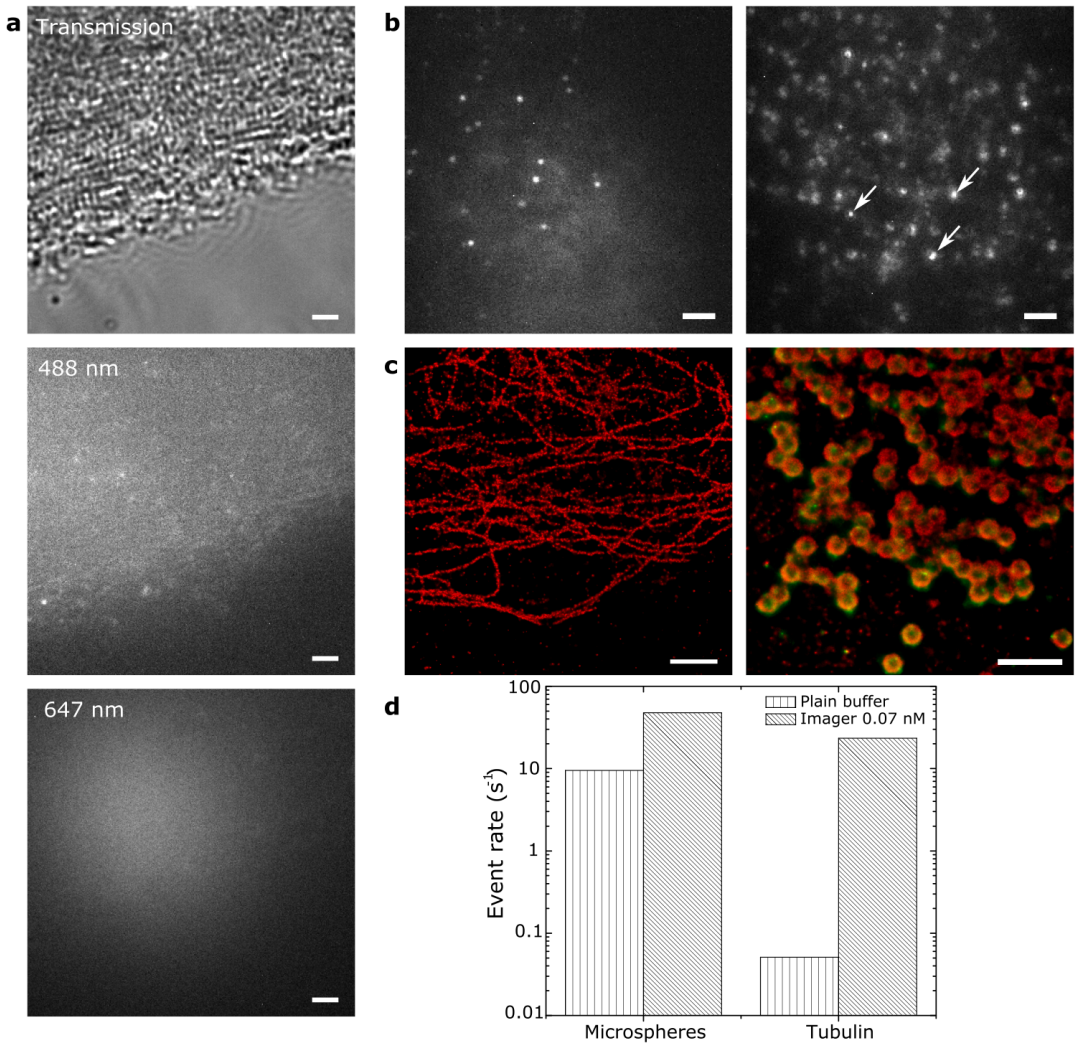

Figure 4.20: Autofluorescence of microspheres at 488 nm excitation. **(a)** Top to bottom: Transmission image of area with high density of microspheres and clear coverslip. Same region of interest excited at 488 nm, showing background fluorescence without presence of imagers. Excitation at 647 nm does not show increased fluorescence of microspheres. **(b)** Left: DNA-PAINT raw data using an imager modified with fluorophore Atto 488, excited at 488 nm, on microtubules. Right: Atto 488-imager on microspheres, showing several imager binding events (arrows) against a strong background. **(c)** Rendered DNA-PAINT data corresponding to data in b. Red: data acquired with added imager, green: data acquired when plain buffer is added. **(d)** Mean event rates of data shown in c, comparing detected events using plain buffer and added Atto 488 imager. Scale bars: 2 µm.

4.6 Discussion

In this chapter, a test sample for DNA-PAINT imaging based on functionalised polymer microparticles is characterised and several examples for optimisation of DNA-PAINT imaging parameters are shown. In contrast to commonly used DNA origami-based test samples [19, 22], which are here shown to suffer from the difficulty for positive feedback during sample preparation and the limited stability of the samples at relatively high cost, microsphere-based test samples are quick and cost-efficient to prepare and allow high flexibility if use in an open-top imaging chamber. Presumably, they provide the same advantages over biological test samples currently in development by other researchers [164]. After publication of the microsphere assay [1], its use as a test sample has been recognised by other researchers, e.g. for quantitative or 3D imaging [151, 156]. In this thesis, it is additionally shown that the passivation of the coverslip guarantees highly specific observation of DNA-PAINT binding.

Several parameters relevant for DNA-PAINT imaging are characterised beyond previously available literature [18, 22], i.e. the choice of imager concentration, illumination intensity, imaging buffer composition and extensions to imager or docking sequences. In the following chapters, these parameters were used at optimised values. Specifically, the imager concentration was set to being just below the values at which overlapping events become non-negligible, the illumination intensity was set to values corresponding to the transition point of the photon number into saturation stage and no additional oxygen-scavenging systems were used in combination with Atto 655.

The microsphere assay is used for optimisation and analysis of different imaging modalities, such as 3D imaging and quantitative imaging by qPAINT. The highly reproducible results of the test assay allowed for identification of problems with conventional qPAINT analysis, where short dark times originating from dye blinking or near-threshold detection are not compensated.

However, there are several limitations of the microsphere-based assay. Compared to biological samples, the excitation at blue/green wavelengths is shown to increase fluorescent background. Furthermore, the microsphere assay does not allow for precise placement of single docking strands with single-nanometre precision, as can be achieved for DNA origami [22], which reduces the use of microspheres for quantification of imaging resolution. In order to approach a size of the imaged structure comparable to DNA origami targets, the use of func-

tionalised polymer spheres smaller than 100 nm could be tested. Furthermore, the number of accessible docking sites on microspheres cannot be adjusted as it depends on the density of the streptavidin coating and it can vary e.g. due to steric effects or the adhesion of the particles to the cover slip. However, varying numbers of docking sites have also been observed for DNA origami [84].

In conclusion, the microsphere-based test sample has been shown to provide sufficient robustness for multiple applications and optimisations of DNA-PAINT imaging with a relatively straightforward preparation and imaging procedure. In the following chapters, the microsphere assay presented here is used to analyse further modifications of DNA-PAINT, followed by validation in biological samples.

5. Advanced Exchange-PAINT

Several major advantages of DNA-PAINT over other single molecule super-resolution techniques are based on the fluorescent markers not being directly fixed to the target structure. This includes the effective absence of photobleaching effects, the ability for quantitative imaging and the ability to successively alter experimental conditions during image acquisition, as demonstrated for example for different imager concentrations in the previous chapter. Similarly, multiplexed imaging can be achieved by exchanging imager solutions with different sequences, known as Exchange-PAINT [20, 22, 120]. This imaging of multiple targets with Exchange-PAINT using the same fluorescent dye gives an image free of chromatic aberrations. However, current Exchange-PAINT protocols require lengthy washing steps and potentially complex fluidic systems. Especially in samples with limited diffusion, e.g. tissue sections, the switching time between different imagers can take up a considerable amount of time due to slow diffusional removal of imagers. The washing steps are critical since a full removal of imagers between exchange rounds is crucial for crosstalk free imaging.

Here, a new version of a simple fluidic system for optimised imager exchange is developed and assessed, based on custom-designed 3D-printed fluidic handling chambers for Exchange-PAINT (Here called macrofluidic chambers, in analogy to smaller scale microfluidic chips which can be used in the same lab setup). 3D-printing allows high flexibility of design with high reproducibility at modest costs. The evaluation of the chambers is shown in comparison to conventional imager exchange by pipetting in open-top chambers. The macrofluidic chambers still require an increased complexity while suffering from problems such as increased sample drift.

As an alternative, a revised and simplified procedure for imager switching is demonstrated, called Quencher-Exchange-PAINT. Instead of washing off and replacing imager strands, so-called "quencher strands" are added which hybridise

to, and thus passivate, the imager. This rapidly reduces the effective concentration of free, single-stranded imagers available for binding with docking strands. In order to maintain a low fluorescent background, a fluorescence quencher is conjugated to the quencher strand, with minimum intramolecular distance to the imager dye. The use of quencher strands allows easier sequential target imaging without the need for washing steps or specialised chambers. Quencher-Exchange-PAINT imaging can be performed in a conventional open-top imaging chamber, and imager binding to the docking strand is rapidly stopped by adding a small volume of quencher strands at a sufficiently high concentration to the imaging chamber.

It is shown that a suitably designed quencher-imager pair with high affinity allows rapid switching times up to an order of magnitude faster than conventional Exchange-PAINT while yielding the same imaging quality. Furthermore, imagining of nanostructures in tissue sections with rapid imager switching is demonstrated. Switching is decoupled from the slow, diffusion limited imager removal from the sample when imaging a tissue section, because the concentration of quencher strands rises to a required level for inhibition more rapidly than the diffusional removal of imagers in a washing step with buffer solution.

Sections 5.3 to 5.7 of this chapter have been published in a peer-reviewed journal [1]. An illustration of Quencher-Exchange-PAINT was used as a cover figure and is shown in Appendix B. Some alterations to the publication have been made, e.g. the inclusion of supplementary materials and newer results into the main text and additions to tie in the sections on macrofluidic chambers. All co-authors, Alexander H. Clowsley, Ruisheng Lin, Stefano Pagliara, Lorenzo Di Michele and Christian Soeller, have contributed with multiple discussions and feedback to the development of the technique and to the writing of the manuscript.

5.1 Macrofluidic chamber design for solution exchange

A straightforward and effective method for imager exchange in an Exchange-PAINT experiment is the use of open-top chambers (see methods chapter 3.1.2), with solution exchange by pipetting on the microscope stage. Repeatedly replacing the imager solution with plain buffer by pipetting reduces the imager concentration to background levels, typically after at least three of these wash-

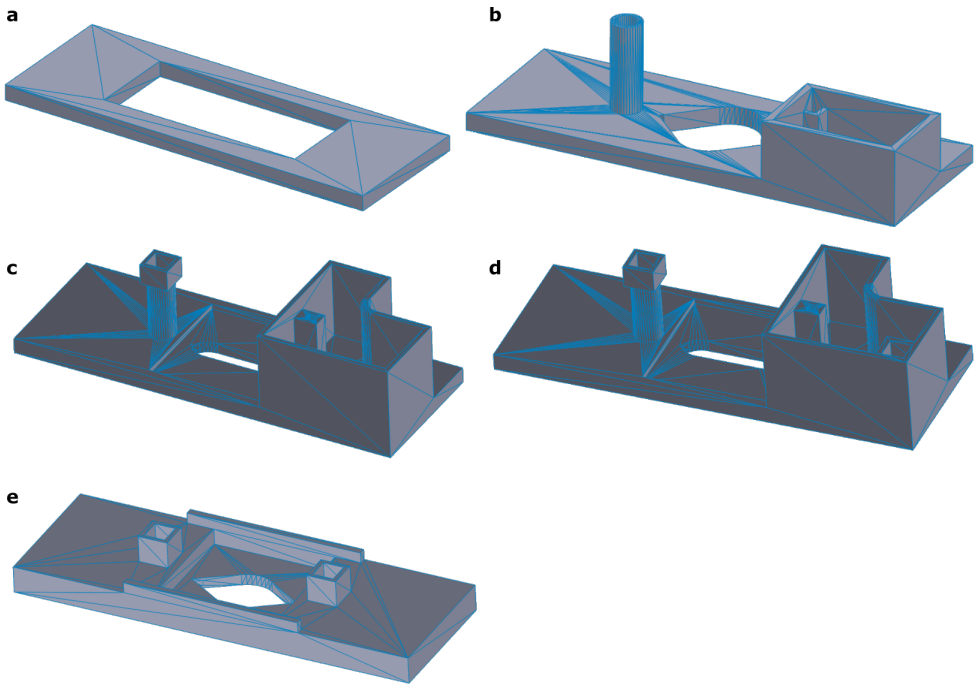

Figure 5.1: Computer-aided design drawings showing different generations of 3D printed macrofluidics chambers. **(a)** Holder allowing a microfluidic chip to be used in a stage designed for standard microscope slides. **(b)** First generation fully 3D-printed macrofluidic chip with input (left), imaging area (middle) and waste reservoir (right). **(c)** Second generation macrofluidic chip with leak-proof input and maximised waste reservoir. **(d)** Third generation, same design as (c) with optional waste output of the reservoir (bottom right). **(e)** Forth generation, the waste reservoir is replaced by a directly coupled waste output and sample drift is reduced by a sturdier design.

ing steps. However, the manual removal of solution during an experiment can drastically affect the stability of the sample, can result in drying of the sample and, due to its manual nature, it can be difficult to achieve reproducible results.

Instead, fluidic handling systems based on PDMS are commonly used, e.g. custom fluidics channels [20], commercially available imaging chambers adapted with PDMS seals [77] or microfluidic chips [165]. Figure 5.1 a shows a CAD (computer aided design) drawing of a microscope slide holder, which allows the use of microfluidic chips on a microscope stage designed for microscope glass slides. The chip, which is attached to a regular cover slip, is glued onto the bottom of the 3D-printed holder. However, the fabrication of PDMS-based chips, including curing steps, typically requires a preparation time of multiple hours and can only be used for a single experiment.

For samples attached to a coverslip surface, DNA-PAINT experiments do not require a chamber design with µm precision. Instead, 3D printing can be used to construct reusable "macrofluidic" chambers. Figure 5.1 b-e shows CAD drawings of different generations of such devices, all of them comprising of an input for tubing (column-like structure on the left), an opening which can be sealed on both sides with coverslips and allows epifluorescence and transmission imaging (centre of the structure), and a form of waste/output handling. In the original design (figure 5.1 b), the tubing is inserted straight into the input column and waste fluids are collected in a reservoir. The input was improved to allow the addition of a square-shaped PDMS seal (see chapter 3.1.7 for details) and the imaging chamber volume reduced for minimisation of fluid use (figure 5.1 c). To avoid any overflow of the waste reservoir, the third design included an optional attachment inside the reservoir for output tubing (figure 5.1 d, bottom right). A final design, shown in figure 5.1 e, removed the waste reservoir for a fully sealed design and thus presents no danger of damaging the microscope with overflow of fluids. Additionally, the slide thickness was increased to 5 mm and walls with increased thickness added, in order to ensure a maximum rigidity of the device and reduce sample drift.

In addition to testing the chamber designs, different 3D printing methods were compared, for detailed descriptions see methods chapter 3.1.7. A cost-efficient and among the methods tested least time-consuming printing method is *fused filament fabrication* (FFF), printing by extrusion of a thermoplastic, e.g. polylactic acid (PLA). However, the limited printing resolution of > 0.3 mm and the extrusion of filament lines lead to inhomogeneous surfaces with channels and

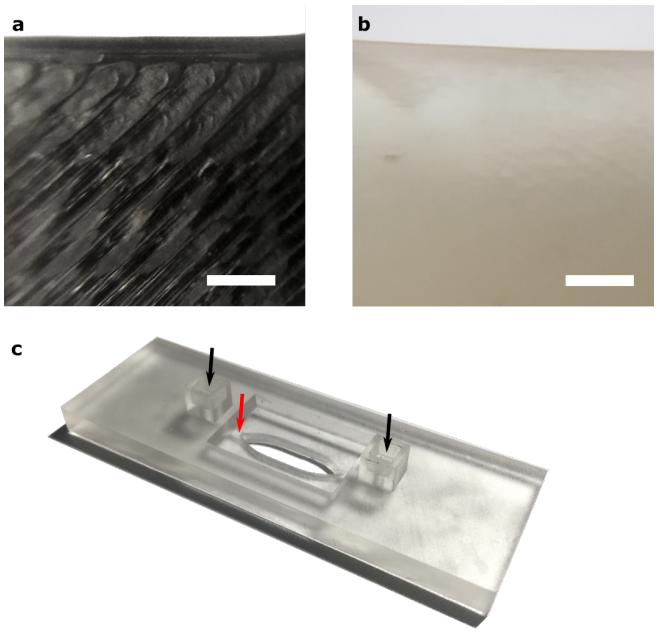

Figure 5.2: Comparison of 3D print quality of different printing methods and 3D printed macrofluidic chip (generation 4). **(a)** Close-up view of a chip printed by *fused filament fabrication*, i.e. polymer extrusion of polylactic acid (PLA). Gaps and inhomogeneities of the print are clearly visible. **(b)** Chip printed by *stereolithography* of a commercial resin which allows photo-polymerisation, achieving a smoother sample finish. Scale bars: 2 mm. **(c)** Forth generation macrofluidic chip printed by stereolithography. Black arrows indicate the input and output openings, the red arrow shows the channel inside the polymer opening into the imaging chamber.

gaps throughout the whole structure, as can be seen in a close-up view of the surface in figure 5.2 a. First tests of macrofluidic devices printed this way regularly resulted in leakages. Instead, chambers were 3D printed by resin-based *stereolithography* (SLA), which is based on photopolymerisation of the resin. Cross-linking by formation of covalent bonds within but also between different printing layers, in contrast to FFF techniques, results in isotropic physical properties and prevents any liquid from leaking out of the device. Figure 5.2 b shows a close-up view of a device printed by SLA. In figure 5.2 c, a full macrofluidic chip of the 4th generation, printed by SLA, is shown. The transparent polymerised resin allows fluid flow through the input to be observed (left black arrow), into a small channel within the chip (red arrow) and into the imaging chamber. The right black arrow indicates the output channel, symmetric to the input.

5.2 Exchange-PAINT in macrofluidic chips

A full Exchange-PAINT experiment using a macrofluidic chip in comparison to Exchange-PAINT by pipette-washing in an open-top chamber is demonstrated in figure 5.3. In both experiments, two populations of streptavidin-coated particles were labelled with different biotinylated docking strand sequences, P1 and P5, and attached to PLL-PEG coated coverslips (For details see chapter 3.1.6). For Exchange-PAINT by pipetting, first imager P1 was added to the imaging chamber at a concentration of 0.05 nM. Figure 5.3 a shows the detected binding event rate of combined P1 and P5 imager binding over the duration of the experiment. Starting from $t = 1400$ s, the buffer solution in the chamber, containing imager P1, was repeatedly (3×) fully removed by pipetting, and replaced with plain buffer. At $t = 1600$ s, buffer containing 0.05 nM P5 imager was added and the P5 labelled particle population imaged. The reduction of the binding event rate to near zero during the washing step indicates a near complete removal of P1 imager strands. Note that the difference between P1 and P5 event rates can depend on multiple parameters such as docking strand density, differences in actual and nominal imager concentration or differing binding times and thus a difference is not unexpected.

In figure 5.3 b, the imager binding rate of an equivalent Exchange-PAINT experiment to figure 5.3 a, but using a macrofluidic chip, is shown. Imagers and washing buffers are exchanged by washing using the fluidic system described in chapter 3.2. Tubing paths of several tens of cm, a large imaging chamber volume of several hundreds of µl and the additional internal volume of the fluidic switch module result in a response time of the system of several minutes (i.e. an observed change in imaging condition after changing the input flow behaviour), considerably slower than the fluid exchange by pipetting. This results in a slower reduction of the binding event rate. Here, washing of plain buffer into the system is started at $t = 1100$ s. First changes in the binding event rate are observed at $t \approx 1200$ s. With buffer containing 0.05 nM P5 imager being washed into the system at $t \approx 1300$ s, the event rate does not drop to the low levels observed for pipette washing, before imager P5 binding events increase the rate again. From $t = 1600$ s, fluid flow through the chamber is stopped again and P5 labelled microparticles imaged. However, a full removal of P1 imager for both pipette washing and exchange in a macrofluidic chamber can be assumed from low cross-talk in figure 5.3 c and d, showing the rendered images

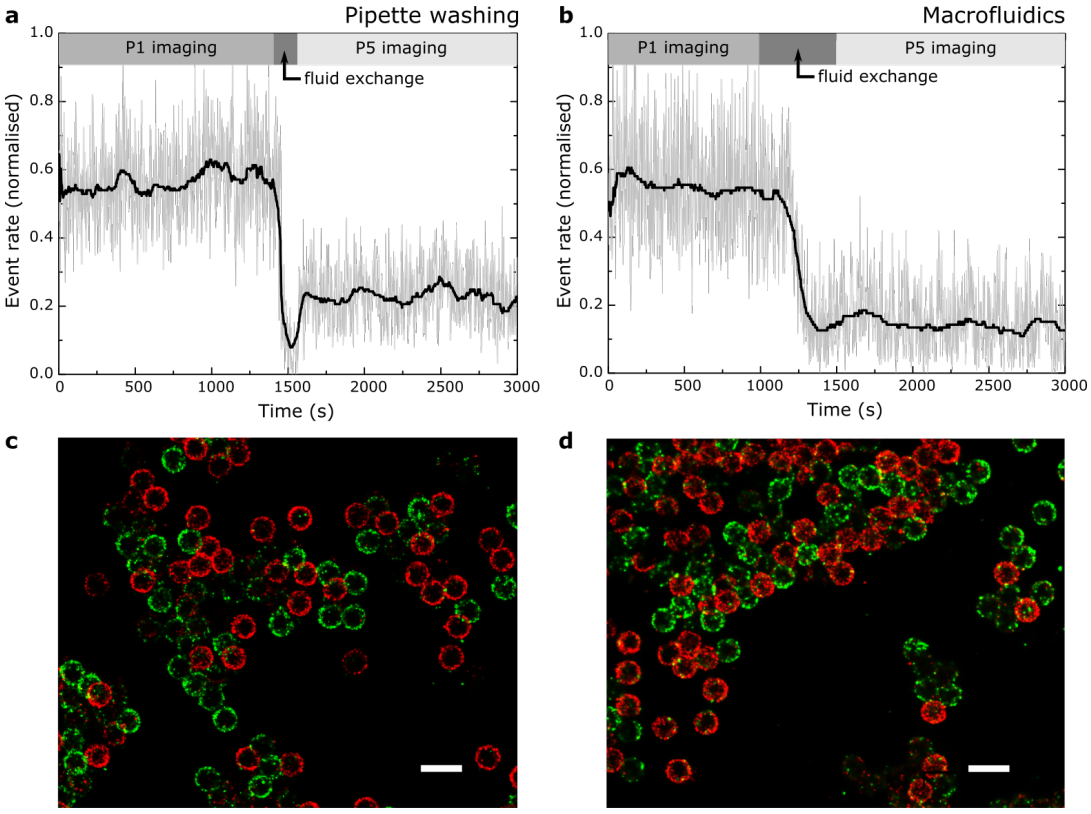

Figure 5.3: Exchange-PAINT by pipetting in an open-top imaging chamber in comparison to a macrofluidic chip. Two populations of streptavidin-coated colloidal particles were imaged, one labelled with biotinylated P1 docking strands, the second with orthogonal P5 docking strands. **(a)** Normalised rate of observed DNA-PAINT binding events including a fluid exchange step. Imaging with P1 imager until $t = 1400\,\mathrm{s}$, subsequent removal of imaging buffer by pipetting and wash with pure buffer. $t = 1600\,\mathrm{s}$: Addition of P5 imager. The drop of the binding rate during the washing step to near zero indicates that P1 imager has been completely removed. **(b)** An Exchange-PAINT experiment using a macrofluidic chip, with imaging samples and protocol equivalent to (a). Imagers and washing buffers are pumped through the chip instead of exchanged by pipetting. The longer duration of the fluid exchange and slower drop of the binding rate indicates the longer time scales needed for a fluid exchange in these chips. **(c, d)** Rendered images corresponding to (a) and (b), respectively. Clear colour separation between green (P1) and red (P5) indicates a cross-talk free imaging for both implementations and thus a good separation of imager buffers. Scale bars: 1 µm.

of Exchange-PAINT by pipette and macrofluidic washing, respectively. Events detected before the washing step, i.e. P1 binding events, are shown in green and events detected after the washing step (P5 binding) in red. If a non-negligible amount of P1 imager were still present after the fluid exchange step, binding of P1 imager to P1 labelled particles would be misassigned as P5 binding and visible in the rendered images as red areas on the P1 labelled beads (shown in green).

The sample drift during the Exchange-PAINT experiments shown in figure 5.3 is compared in figure 5.4. As described in chapter 3.2, drift is detected by correlation of a transmitted light image with a calibration image taken before the start of the experiment. A stack of calibration images along the optical axis allows drift detection in the axial, as well as the lateral direction. Because the axial drift is corrected in real-time by a feedback system, figure 5.4 a and b only show drift in lateral direction. Drift along the x-axis is shown in blue, along the y-axis in green. The drift was measured in units of pixels of the tracking camera, and then converted into actual sample drift in nanometre by correlation with the imaging data.

For Exchange-PAINT by pipette washing, shown in figure 5.4 a, low, commonly occurring sample drift (e.g. due to thermal changes) is observed during imaging with imager P1. However, sample drift drastically increases during the washing step, $t = 1400 - 1600\,\mathrm{s}$. The lateral sample position after the washing step is considerably different to before washing, and does not recover while imaging with imager P5. Figure 5.4 c shows the localisation data before any lateral drift correction, with colours indicating the detection time (from the start of the experiment - red, orange, yellow, to the end - blue, purple). The arrow shows an area where particles imaged before fluid exchange (yellow/red) seemingly overlap with particles imaged after the exchange (blue/purple), even though they are positioned next to each other on the coverslip, due to the change of sample position during washing.

In a macrofluidic chamber (figure 5.4 b), these sudden changes do not occur. However, an increased drift can be observed during the exchange step (e.g. $t = 1100 - 1400\,\mathrm{s}$), as compared to the periods without fluidic flow, which indicates an influence of the change in pressure applied and the coupling of the sample chamber to the fluidic system via tubing on the sample drift. In some cases, e.g. drift in x-direction after $t = 1500\,\mathrm{s}$, the drift seems to be decreased once pressure is reduced again and fluid flow stopped. Similarly to

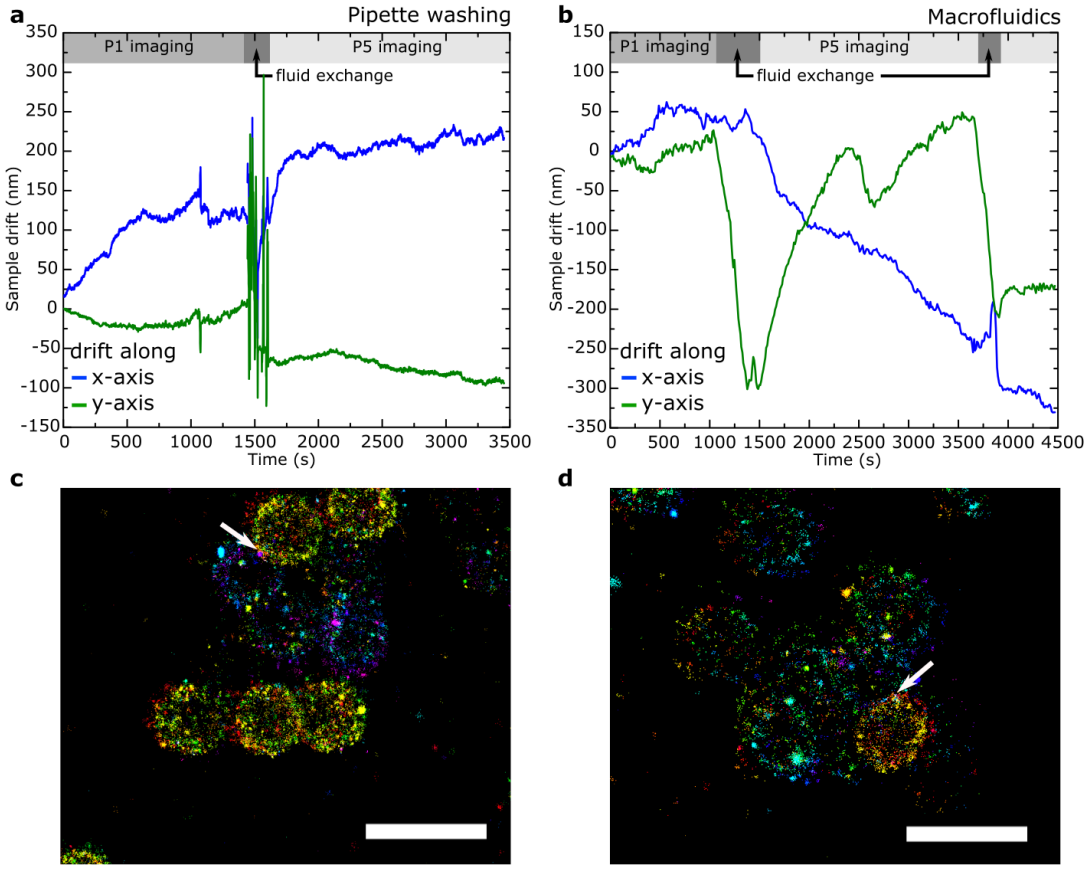

Figure 5.4: Comparison of sample drift during Exchange-PAINT experiments while using macrofluidic chips with conventional open chamber-wash out. Sample drift is measured by an auxiliary camera detecting transmitted light for drift correction. **(a)** Drift during Exchange-PAINT by pipetting along x- (blue) and y-axis (green) in pixels, with 5 pixels corresponding to ~100 nm sample drift. Sample drift during washing steps ($t = 1400 - 1600$ s) is considerably higher than during imaging, and does not recover after pipetting. **(b)** Drift during Exchange-PAINT in a macrofluidic chip. While total drift is considerably lower than during pipetting, it is still higher during fluid flow through the chip (e.g. $t = 1100 - 1400$ s), than if no flow is applied. Partial recovery after pressure is reduced. **(c, d)** Localisation data before drift correction corresponding to (a, b), with the colour corresponding to detection time. Particles are located next to each other, not overlapping, however, white arrows show apparent overlap of particles detected at different time points due to sample drift. Scale bars: 1 µm.

pipette washing, figure 5.4 d shows overlap of spheres as an example that the drift introduced during the washing step can lead to misinterpretation of the location of different targets in Exchange-PAINT.

In conclusion, the macrofluidic chamber design allows Exchange-PAINT imaging without manual intervention during the experiment, which increases reproducibility of experiments and allows an increased automation of DNA-PAINT imaging. However, sample drift issues introduced by pipette exchange cannot fully be resolved when using macrofluidic chambers. In addition, the fluidic system adds to the complexity of the experiment and buffer exchange durations (and thus experiment length) can be increased. As an alternative, the following sections discuss an approach for controlling the imager binding rate in DNA- and Exchange-PAINT that circumvents the need for large volume fluid exchange..

5.3 Tuning of DNA-PAINT event rate with competitive strands

Binding event rate optimisation is crucial for efficient DNA-PAINT imaging [18, 22]. If too many binding events per frame are observed, the risk of overlapping events increases, reducing the localisation precision. If the rate is too low, the imaging takes an unnecessarily long time. Exchange-PAINT represents an extreme case, in which the event rate has to be reduced to background levels before switching to a new round of imagers to allow crosstalk-free imaging. The most obvious way to tune the binding event rate during image acquisition is by changing the concentration of free imager strands. Usually, this is achieved by diluting or concentrating the imager strands in a microscope chamber (Figure 5.5, top) during a sequence of washing steps, which directly changes the event rate. Here, Quencher-Exchange-PAINT is proposed, a scheme in which the free imager concentration can be reduced by simply adding a DNA strand complementary to the imager. The added complementary strand competes with the docking strand for binding to the imager. Fluorescence quenchers are conjugated to the competitive strand (which is therefore call a 'quencher strand', see Figure 5.5, bottom) to reduce background fluorescence and maintain a high signal-to-background ratio.

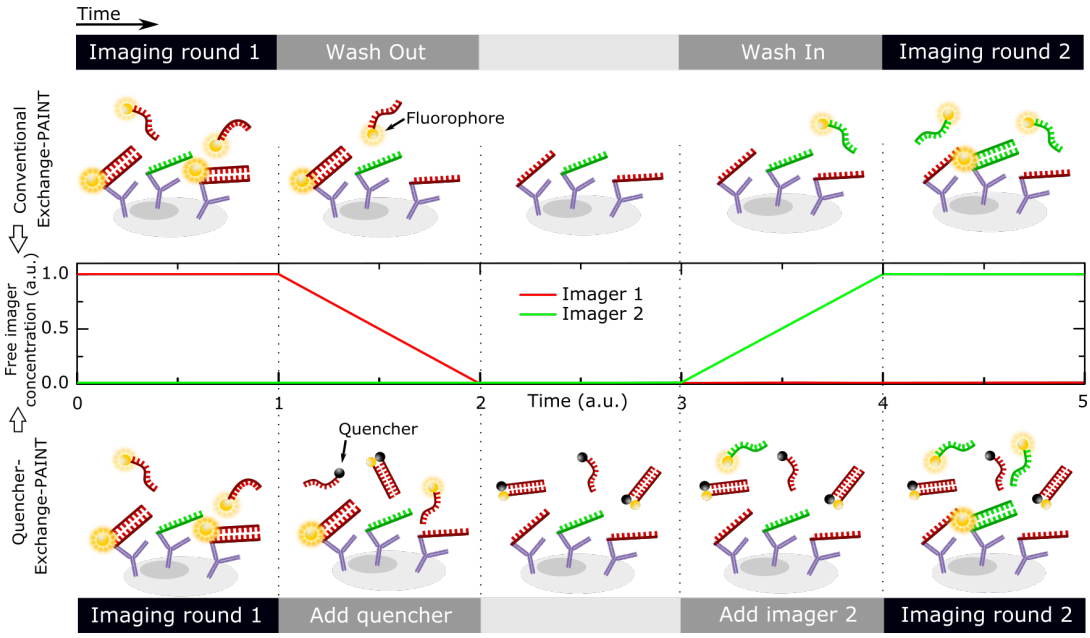

Figure 5.5: Sketch demonstrating conventional tuning of DNA-PAINT imager/docking binding event rate vs. proposed tuning via quencher strands, which are complementary to the imager and thus compete with docking strands for binding to the imager. In DNA-PAINT, the event rate is proportional to the concentration of free imager strands. The concentration of free imager strands can either be tuned by the absolute concentration of imager ("Conventional", top), or by adding a competitive complementary strand ("Quencher", bottom). The fluorescent quencher, conjugated to the competitive strand, reduces background fluorescence levels thus enhancing signal-to-background ratio. In the schematic, the colour of DNA strands identifies corresponding complementary strands, docking and imager strands 1 – red, docking and imager strands 2 – green.

5.4 Design of efficient imager and quenching strand pairs

It is desirable to minimise the concentration of competing binding strands required to significantly reduce free imager concentrations. The reasons are twofold,

(1) it makes it practical to add just small amounts of quencher strand solution to achieve fast and complete termination of docking-imager binding events, and

(2) it reduces the concentration of quencher strand in solution required to achieve essentially complete removal of free imagers.

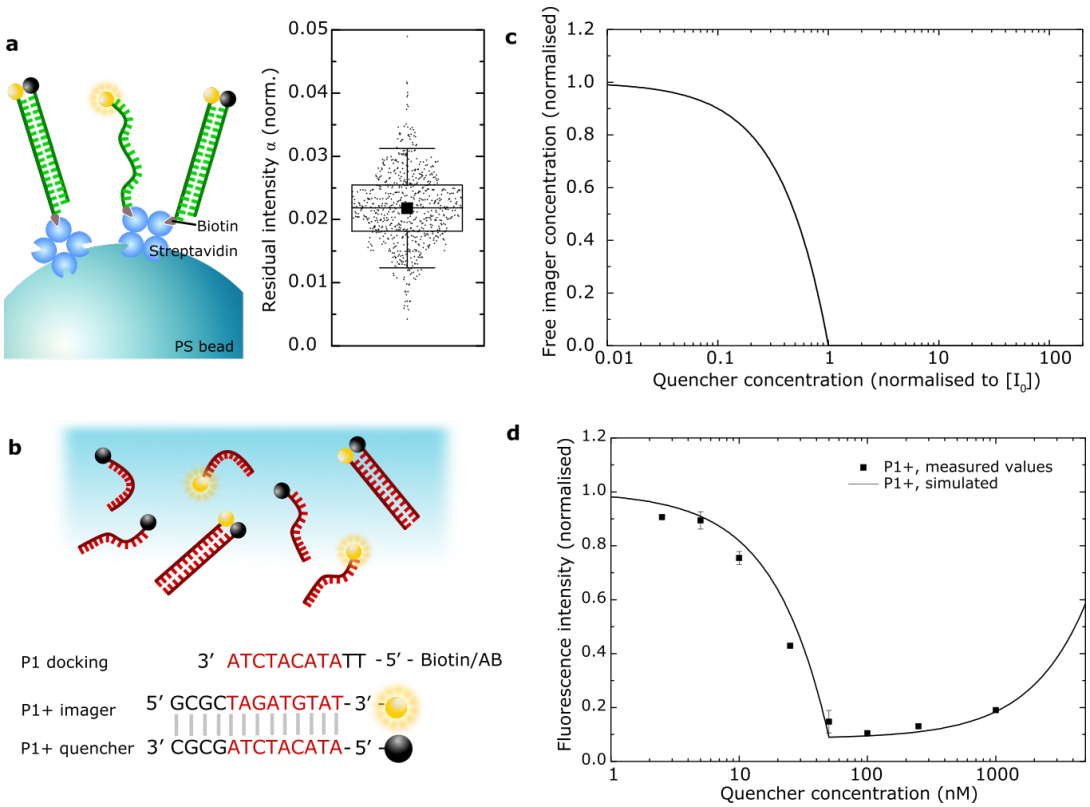

Figure 5.6: Quenching efficiency of quencher coupled to complementary oligonucleotides. **(a)** Dye-labelled, biotinylated oligonucleotides are linked to a streptavidin-coated polystyrene bead (bottom). Complementary quencher-modified strands (17 bp) will permanently bind and unbound quencher in solution is removed by washing. The residual fluorescence intensity per bead after saturated, permanent binding of quencher strands is $2.1 \pm 0.6\%$. **(b)** Imager-quencher pair P1+ and complementary P1 docking strand used in (c) and (d). Sketch shows P1+ pairs bound and unbound in solution. **(c)** Modelled free imager concentration $[I]$ for an imager-quencher pair with high binding affinity (P1+). **(d)** Experimental data of bulk fluorescence intensity for the imager-quencher pair, using an imager concentration of 50 nM. Line: Modelled bulk fluorescence intensity. Rise of intensity for higher concentrations of quencher due to fluorescence of quencher. Simulated fluorescence intensities with parameters $\alpha = 0.02, \beta = 5 \cdot 10^{-3}, \gamma = 0.07, K_d = 3.8 \cdot 10^{-5}$ nM at equilibrium. K_d has been calculated with an estimated $G = -18.0$ kcal/mol (DINAmelt webserver [139, 140]).

With respect to the latter consideration, tuning of the binding event rate would be possible with a competitive complementary strand lacking a conjugated quencher. However, this would come at the cost of significant background fluorescence from imagers that do not contribute to the super-resolution image, which in turn negatively affects localisation precision [166]. This can be effectively avoided by adding a quencher dye that quenches the fluorescence of competitively bound imagers, thereby maintaining a high signal to background ratio and high localisation precision. On the other hand, extremely high quencher concentrations ($> 10\,\mu M$) give rise to their own backgrounds as shown below, which motivates the design of a quencher-imager pair with high mutual affinity.

An efficient extinction of the imager dye fluorescence by the quencher is highly desirable. This was tested with long complementary strands that bind permanently and are labelled with a dye-quencher pair (Atto 655 and Iowa Black RQ, Figure 5.6a). Streptavidin coated polystyrene beads were attached to a coverslip to act as anchors for biotinylated single stranded DNA with a conjugated dye molecule. Complementary quencher strands with an overlap of 17 base pairs were added to the solution surrounding the beads, hybridised to the dye-labelled strands attached to the beads and remaining free quencher and imager strands were washed out with plain buffer (see methods chapter 3.3.1). The bulk fluorescence measurements indicated that fluorescence of the Atto 655 dye was reduced by approximately 98% upon hybridisation with a quencher strand.

Criteria (1) and (2) above can be optimally fulfilled when quencher and imager strands have high affinity for binding to each other but the design must also ensure a comparatively low affinity for transient binding between docking and imager strands, which is the basis of DNA-PAINT super-resolution.

Based on these considerations an imager-quencher pair is designed, using a DNA sequence termed P1+ (Figure 5.6b), which is based on a previously published P1 design [20] but with a higher binding affinity compared to P1 imager and P1 docking binding due to an increased number of 13 complementary bases between P1+ imager and P1+ quencher. For this design, $G = -18.0\,\text{kcal/mol}$ (in typical DNA-PAINT imaging buffer conditions, calculated with DINAmelt [139, 140] for 500 mM NaCl, $T = 293.15\,\text{K}$), so that the dissociation constant $K_{d,q}$ becomes small enough (38.1 fM) to ensure near permanent binding of the imager-quencher complex. The modelled curve based on equilibrium binding in Figure 5.6c (for details see equation 5.3) indicates that the free imager concentration can be reduced to negligible levels once quencher strand concentration exceeds imager

concentration. The imaging quality is not expected to change compared to conventional DNA-PAINT because the transient low-affinity binding between P1+-imager and P1-docking strand involves only 9 complementary base pairs.

To estimate the background fluorescence intensity F, the residual fluorescence of a hybridised imager-quencher complex (IQ) as well as the fluorescence from the free quencher strand itself (Q) have to be taken into account. The background fluorescence should be proportional to the concentration of these species

$$F \propto [I] + \alpha [IQ] + \beta [Q] + \gamma. \tag{5.1}$$

where α and β are parameters that denote the ratio of fluorescence from quencher-imager complexes and quencher strands, respectively, versus a free imager strand, γ quantifies additional, nonspecific constant background fluorescence that tends to be present in experiments, e.g. from free dye molecules or dyes attached to non-complementary oligonucleotides.

With $[I_0]$ the total concentration of imager strands, free or in IQ complex and $[Q_0]$ the total concentration of quencher strands, free or in IQ complex,

$$\begin{aligned} [I_0] &= [I] + [IQ] \\ [Q_0] &= [Q] + [IQ], \end{aligned} \tag{5.2}$$

the concentration of the imager-quencher complex $[IQ]$ can be calculated as a function of $[I_0], [Q_0]$ and the dissociation constant K_d,

$$\begin{aligned} K_d &= \frac{[I] \cdot [Q]}{[IQ]} \\ &= \frac{([I_0] - [IQ])\,([Q_0] - [IQ])}{[IQ]} \\ [IQ]_{1,2} &= \frac{[I_0] + [Q_0] + K_d}{2} \pm \sqrt{\frac{([I_0] + [Q_0] + K_d)^2}{4} - [I_0]\,[Q_0]}, \end{aligned} \tag{5.3}$$

with only $[IQ] = \cdots - \sqrt{\ldots}$ giving non-negative concentrations.

Equations 5.1-5.3 allow to calculate the fluorescence intensity from known concentrations I_0 and Q_0,

$$\begin{aligned} F \propto\ & [I] + \alpha\,[IQ] + \beta\,[Q] + \gamma \\ =\ & [I_0] - [IQ] + \alpha\,[IQ] + \beta\,([Q_0] - [IQ]) + \gamma \\ =\ & [I_0] + (\alpha - \beta - 1)\left(\frac{[I_0] + [Q_0] + K_d}{2} - \sqrt{\frac{([I_0] + [Q_0] + K_d)^2}{4} - [I_0]\,[Q_0]}\right) \\ & + \beta\,[Q_0] + \gamma. \end{aligned} \tag{5.4}$$

A curve calculated from equation 5.4 is shown in Figure 5.6d as a function of quencher strand concentration. Once the quencher concentration is much higher than the total imager concentration $[I_0]$, the very small fluorescence of the quencher itself becomes non-negligible and the total measured fluorescence increases.

The predicted dependence of fluorescence intensity based on the model eq 5.1 was confirmed experimentally (Figure 5.6d, squares). Increasing concentrations of P1+ quencher strands were added to imager present at a fixed concentration of $I_0 = 50\,\text{nM}$ and bulk fluorescence F was recorded. The data shows that efficient quenching is possible with the quasi permanently binding quencher strands and overcomes the limitations of a standard DNA-PAINT experiment. Notably, the measured fluorescence remains low from a quencher concentration of 50 nM up to several hundred nM, i.e. the fluorescence of the quencher is still negligible even at 10× higher concentration of quencher strands compared to the imager concentration.

5.5 Tuning of binding rate and background by quencher strands

The benefit of a competitive strand with high affinity is demonstrated in figure 5.7. Streptavidin-coated colloidal particles, labelled with biotinylated docking strands were imaged at a constant imager concentration of 0.05 nM. Subsequently, competitive strands with increasing concentrations were added and the resulting reduction in DNA-PAINT binding events of imager to docking strands observed. The binding event rate is assumed to be proportional to the concen-

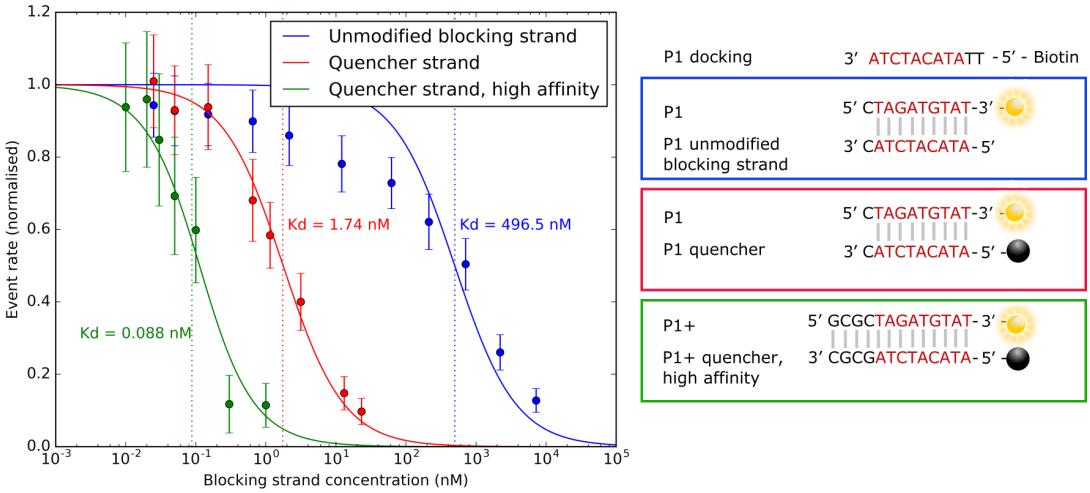

Figure 5.7: Influence of the affinity between imager and competitive strands on reduction of binding event rate. Three competitive strand designs - an unmodified complementary strand "blocking strand", a complementary strand with conjugated fluorescence quencher "quencher strand" and a strand with increased affinity - are added to imager of constant concentration while conducting a DNA-PAINT experiment on streptavidin-coated colloidal particles. Sequences of competitive strands are shown on the right. Data shown as points, the curves show a fit based on eq. 5.5. The observed imager-docking strand binding event rate drops with increased concentration of competitive strands. While high-affinity quencher strands reduce the event rate the most efficiently, there is also a noticeable difference between quencher-modified and unmodified competitive strands, indicating a strong effect of the modification on the affinity. Note that especially in very low concentration regimes ($< 1\,\mathrm{nM}$) the concentrations cannot be given with high precision, which can lead to strong overestimations of K_d for the high affinity strand. Error bars: standard deviation of events per second.

tration of single-stranded, free imager $[I]$, which in equilibrium depends on the total imager concentration $[I_0]$ and total competitive strand concentration $[Q_0]$,

$$\begin{aligned}[I] &= [I_0] - [IQ] \\ &= [I_0] - \left(\frac{[I_0] + [Q_0] + K_d}{2} - \sqrt{\frac{([I_0] + [Q_0] + K_d)^2}{4} - [I_0]\,[Q_0]} \right) \\ &= \frac{[I_0] - [Q_0] - K_d}{2} + \sqrt{\frac{([I_0] + [Q_0] + K_d)^2}{4} - [I_0]\,[Q_0]},\end{aligned} \tag{5.5}$$

derived from equation 5.3.

Three competitive strand sequences were compared, an unmodified complementary strand "blocking strand" (figure 5.7, blue), a complementary strand with conjugated fluorescence quencher "quencher strand" (figure 5.7, red) and a quencher strand with increased affinity (figure 5.7, green), as described above. The curves in figure 5.7 show a fit for the normalised experimental data based on equation 5.5, with the unknown parameter K_d determined by a least-squares fit. As expected, a quencher strand with increased affinity due to additional overlap between quencher and imager strands shows an efficient reduction of the event rate, i.e. only a small concentration of quencher strand is needed to reduce the imager binding to background levels. A lack of the additional overlap reduces the affinity, but interestingly, using a competitive strand without a conjugated quencher shows an even lower affinity than the quencher-modified strand. This indicates that the interaction of the fluorescence quencher with the imager strand strongly affects the affinity, an increase similar to the effects of conjugated fluorescent dyes on DNA affinity which have been observed previously [167] (also compare chapter 7).

The anticipated reduction in background fluorescence by an imager-quencher pair with high binding affinity compared to the imager-docking binding affinity was tested in a Quencher-DNA-PAINT experiment as shown in Figure 5.8. The extended imager sequence P1+ shows – just as the conventional imager P1 – a comparatively low affinity for transient binding between docking and imager strands as it contains the 9 base sequence of P1 to allow for transient binding to a P1 docking strand. Adding the quasi permanently binding P1+ quencher strand to a solution containing the P1+ imager in DNA-PAINT tuned the effective concentration of free imager. Again, 500 nm streptavidin-coated polystyrene beads were imaged, which are labelled with biotinylated P1 docking strands, and compare both the binding event rate and the fluorescence background as a function of the effective free imager concentration $[I]$. If no quencher was added, then the free imager equals the total imager concentration $[I] = [I_0]$ and the binding event rate increases proportionally to an increase in $[I]$ (Figure 5.8 c black filled squares). A similar proportionality of the event rate with the effective free imager concentration is observed with added high affinity P1+ quencher strands (Figure 5.8 c black empty squares), where $[I]$ (see equation 5.5) can be approximated by

$$[I] \approx [I_0] - [Q_0], (K_d \ll [I_0], [Q_0]) \tag{5.6}$$

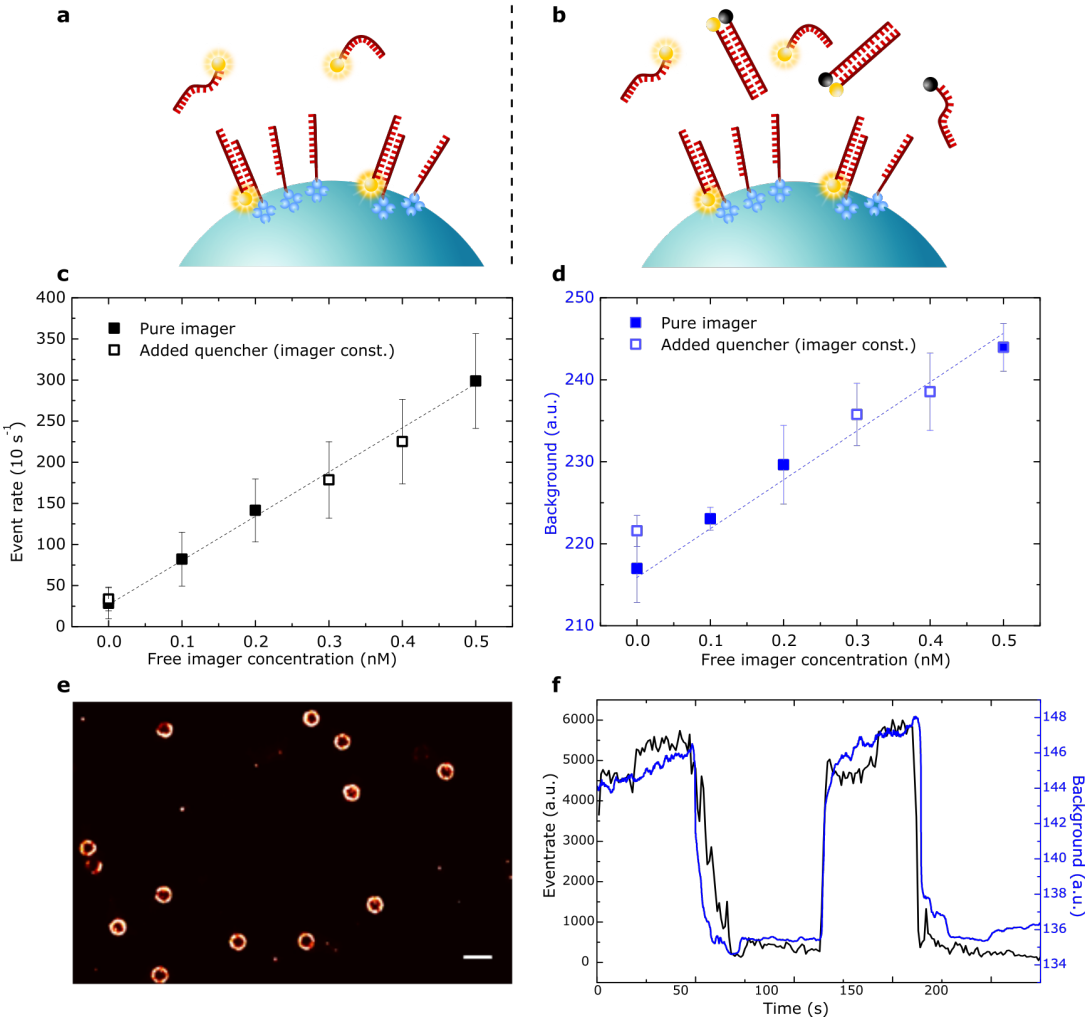

Figure 5.8: Effect of increasing imager and quencher concentration on DNA-PAINT event rate and fluorescence background. **(a)** The binding event rate of imager strands to docking strands attached to polystyrene beads is proportional to the concentration of unbound, free imager strands. **(b)** The same effective free imager concentration, i.e. event rate, as in a can be achieved with a higher concentration of imager, if the additional imager strands are bound to complementary quencher strands. **(c)** Event rate is proportional to the effective free imager concentration both without quencher (filled symbols) and as the quencher concentration is varied with a fixed total imager concentration of 1 nM (empty symbols). The free imager concentration is estimated from equilibrium binding and a K_d of $3.8 \cdot 10^{-14}$ M. Error bars: standard deviation per second. **(d)** Fluorescent background intensity after subtraction of non-imager related offset increases linearly with the free imager concentration. **(e)** Rendered image of DNA-PAINT data for e+f. Scale bar 1 µm. **(f)** Time trace of binding event rate (black) in comparison with the fluorescence background (blue) during an Exchange-PAINT cycle while using a full wash ($t = 50$ s) and addition of quencher strands ($t = 170$ s) to reduce event rate and background.

due to quencher-imager binding with high affinity, i.e. $K_d \ll [I_0], [Q_0]$.

As expected, the measured fluorescence background shows an approximately linear increase with increasing total imager concentration in the absence of quencher strands (Figure 5.8 d blue filled squares). If quencher is added, and the measured background fluorescence is plotted against remaining free imager concentration (calculated as $[I] = [I_0] - [Q_0]$) a similar dependence is observed, although the background is slightly higher (Figure 5.8 d blue empty squares). This is compatible with residual fluorescence of the imager-quencher complex and free quencher itself (i.e. $\alpha, \beta > 0$ in eq 5.1). Taken overall, Figure 5.8 c,d demonstrates that the effective free imager concentration can be reduced both by adding the high affinity P1+ quencher strand or by reducing the absolute imager concentration, resulting in a similar behaviour of both the fluorescence background as well as the binding event rate. Figure 5.8 f shows this effect in a qualitative way. Here, the appropriately normalised time traces of both binding event rate and background show a virtually identical behaviour, independent of dilution of the imager solution with plain buffer or addition of quencher strands.

The experiments above show that the use of the high affinity quencher strands work as desired, namely that the addition of the quencher strands in solution has an effect almost exactly equivalent to physically removing imagers from the solution. This holds for both the reduced pool of free imagers that can bind to docking strands and thus a reduction in the binding event rate by competitive binding, as well as for the reduction of bulk fluorescence by adding a fluorescence quencher modification to the quencher strand.

These findings also demonstrate that the use of quenchers are not suitable to increase the signal-to-background ratio in DNA-PAINT, at least using simple competitive binding strategies. The concomitant reduction in event rate at best matches the reduction in fluorescence background. In other words, one cannot do better in terms of signal-to-background ratio for DNA-PAINT than adjusting imager concentrations to achieve the desired event rate, at least not by simple competitive quencher binding schemes. This includes the quencher strand designs shown in this manuscript and also extends to the potential use of molecular beacon imagers [168]. Nevertheless, the use of quenchers shown here is a practical alternative to actually removing imagers from the solution as is further demonstrated below in experiments with biological samples.

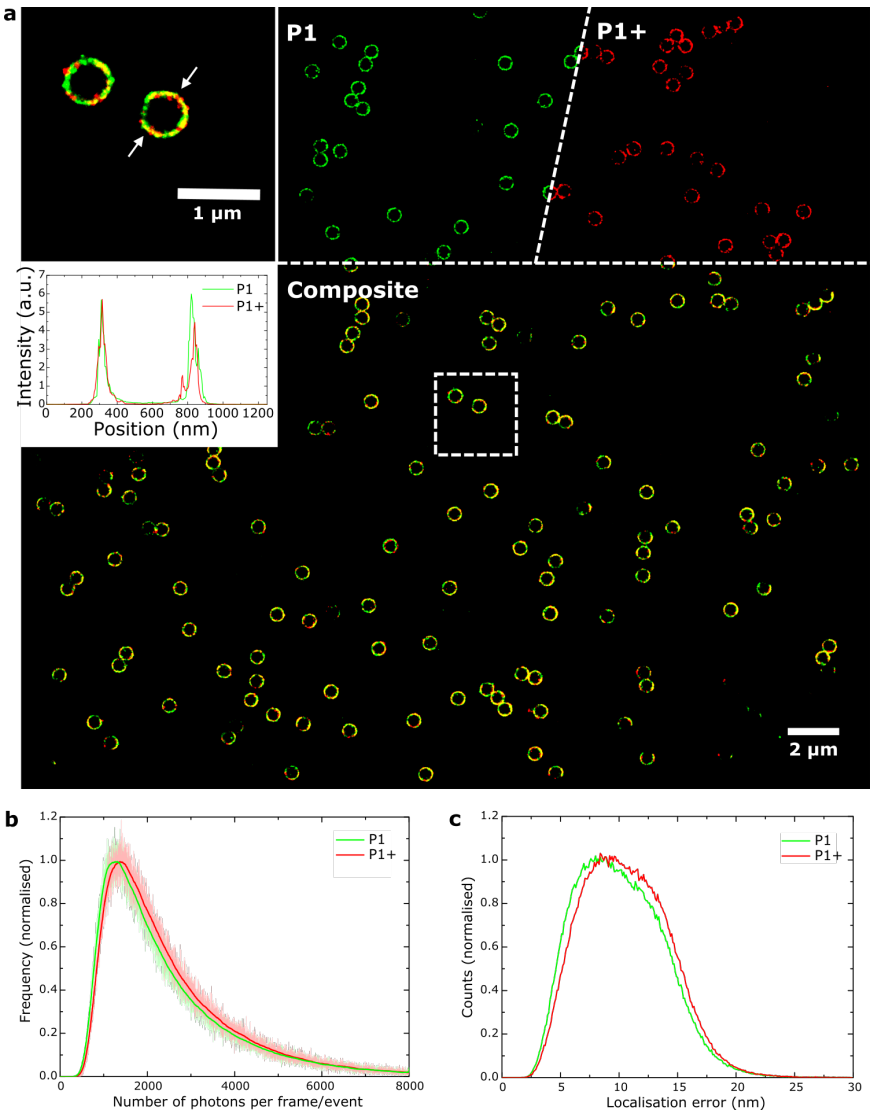

Figure 5.9: Comparison of extended Imager P1+ with P1 by Exchange-PAINT imaging of ø = 500 nm polystyrene beads. **(a)** Composite Exchange-PAINT image using imager P1 (green) and P1+ (red). Top left: Magnified view of the boxed region. Inset: Cross section of an individual bead indicated by the arrows. **(b)** Histogram showing the number of detected photons per frame and binding event. **(c)** Histogram of the localisation error for imagers P1 and P1+.

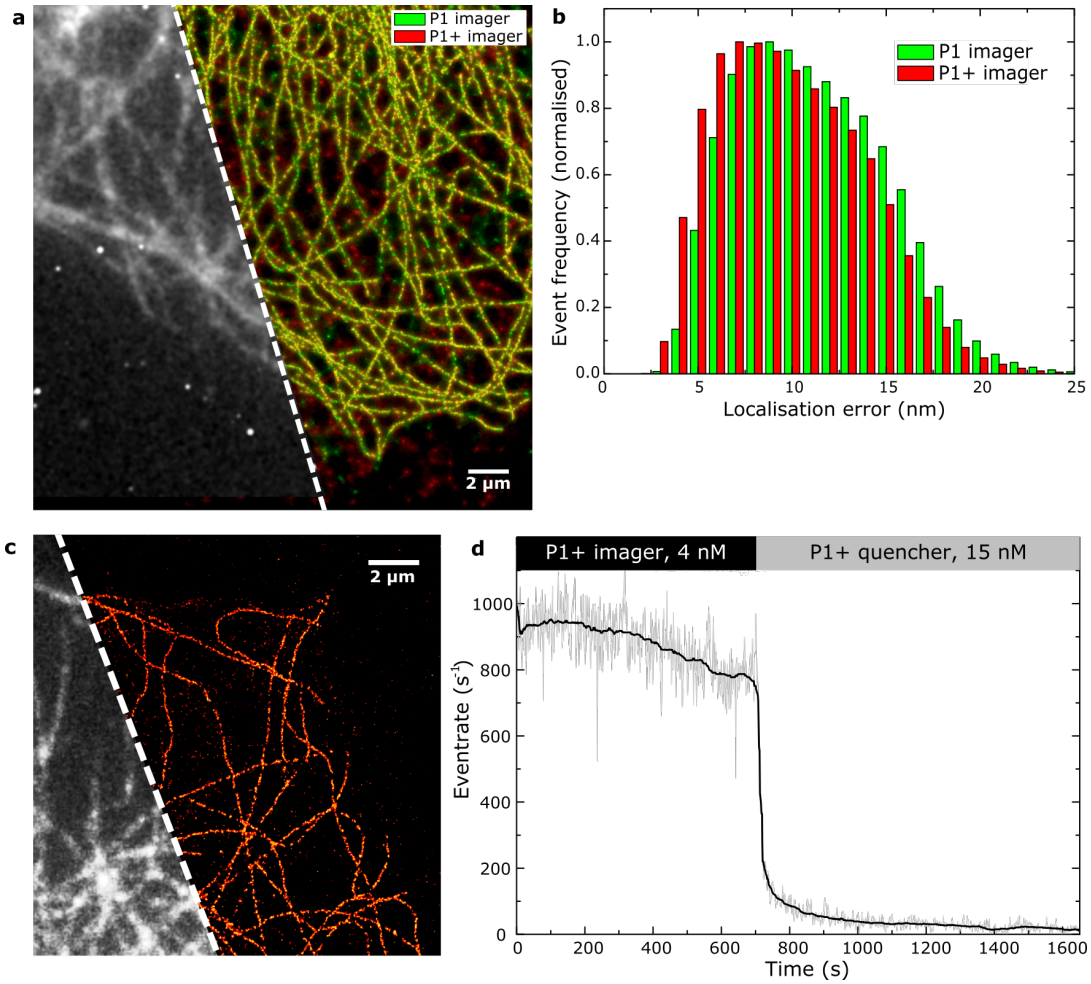

Figure 5.10: Efficient quenching of a modified imager strand with a quasi-permanently binding quencher shown on tubulin in fixed COS-7 cells. **(a)** DNA-PAINT imaging with a 10 base P1 imager (green) gives a similar imaging quality as an extended 13 base P1+ imager (red). Grey: Fluorescent widefield image. **(b)** Similar localisation errors for P1 and P1+ imager confirm a similar binding behaviour. Image shown in a rendered only localisation events with an error $< 8\,\mathrm{nm}$. **(c)** Tubulin imaged for data shown in d; grey: Fluorescent widefield image. **(d)** Localisation event rate of tubulin imaged with P1+ imager at 4 nM in an open chamber. At t = 710 s, 7.5 µl of P1+ quencher is added to the 500 µl chamber to achieve a total quencher concentration of 15 nM. Efficient suppression of the binding event rate can be achieved without washing or fluid exchange steps and without using a high concentration of quencher.

5.6 Quencher-Exchange-PAINT without the need for solution exchange

The presented high affinity quencher/imager tuning scheme (as illustrated with the P1+ design) can be used to implement Exchange-PAINT, that is imaging serially with different imagers, without solution exchange. DNA-PAINT imaging of polystyrene beads (Figure 5.9) and microtubules in fixed COS-7 cells (Figure 5.10a, b) confirm that the additional three bases of the P1+ imager sequence beyond those complementary to the P1 imager do not interfere with the imaging performance, as the docking-imager binding site is left unchanged. In rendered images, the localisation error and the photon number per binding event show similar results with P1+ and P1 imagers.

To demonstrate Quencher-Exchange-PAINT without the need for exchanging solutions, microtubules were imaged in an open top chamber with P1+ imager. A small amount of concentrated complementary quencher strands was then added into the imaging chamber, here 7.5 µl of 1 µM P1+ quencher strand into a 500 µl volume open top imaging chamber containing imager at 4 nM. This yielded a total quencher strand concentration of ~15 nM in the chamber and ensured saturated quenching of imager strands. The diffusional distribution of quencher strands in a sample chamber containing fixed cells is fairly rapid and achieved efficient quenching after approx. 5 min (Figure 5.10c, d). As has been shown before, the nonspecific adsorption of imagers is very low in biological samples [20], and as a result the super-resolution images (e.g. Fig. 5.10c) have very high contrast.

Conventional Exchange-PAINT requires full fluid exchanges from one imager to washing buffer and next imagers. This is typically achieved either with specially designed chambers [22], or as described above, which can require complex preparation, or with multiple washing steps in an open top chamber. A drawback when working with an open chamber is that accidental full draining can deteriorate the sample quality or dislodge the sample.

Here, a full Quencher-Exchange-PAINT cycle is demonstrated in fixed cells using an open top imaging chamber by imaging microtubules and the mitochondrial import receptor subunit TOM20 (Figure 5.11a, b). With 1× excess of quencher strands to imager concentration, efficient suppression of P1+ binding is achieved

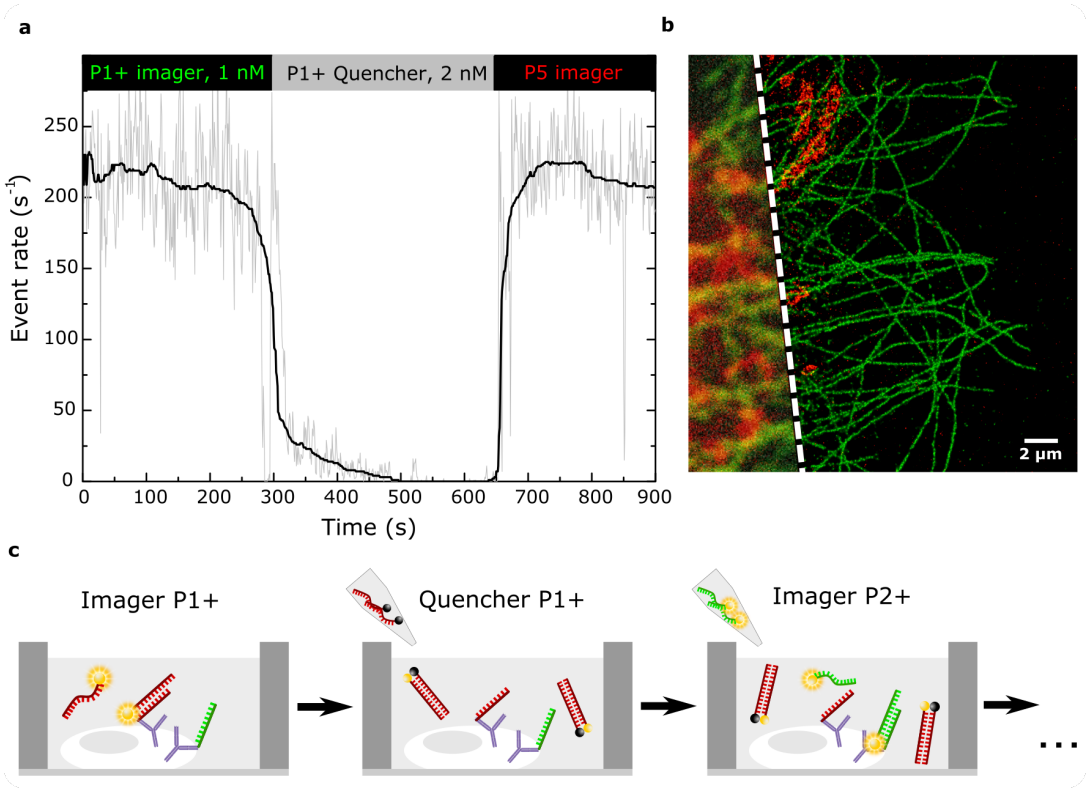

Figure 5.11: Quencher-Exchange-PAINT concept using a simple open top microscopy chamber. **(a)** Full Exchange-PAINT cycle using P1+ imager and quencher for β-tubulin and P5 imager for TOM20 in fixed COS-7 cells. Low crosstalk is achieved without any washing steps by adding a small amount of quencher and subsequently P5 imager to an open chamber. **(b)** Widefield and rendered Exchange-PAINT image corresponding to data shown in a, red: TOM20, green: β-tubulin. **(c)** Left to right: Transient binding of imager P1+ to a partially complementary (9 bp) docking strand allows imaging of first target. A small volume of highly concentrated complementary (13 bp) quencher strands is added. The concentration is chosen so that the resulting concentration in the chamber is at least equal to the imager concentration. Depending on diffusion, but typically after several minutes, the binding event rate of P1+ imager drops to negligible levels and the imager matching the next target can be added to the sample. In principle, these steps can be repeated with an arbitrary number of orthogonal imager/quencher pairs.

after 3 minutes, comparable to the suppression speed shown at 4× excess above (Figure 5.10c, d).

The main benefits of conventional Exchange-PAINT, such as negligible crosstalk and independence of chromatic aberrations, are maintained. Figure 5.12 shows that imaging quality, e.g. specificity and sensitivity of DNA-PAINT do not suffer if a quencher strand is added in a washing step. Localisation errors of a a second imager round (Figure 5.12 a, here imager strand P5) do not seem to be affected by the presence of an orthogonal imager-quencher pair (here P1+ imager and quencher). Equally, the binding event rate of imager P5 remains within the region of binding event rates in conventional Exchange-PAINT (Figure 5.12 b). Figure 5.12 c allows a rough comparison of the sensitivity and specificity of the second imager round (P5) for conventional Exchange-PAINT (left) and Quencher-Exchange-PAINT (right). Here, a mask was applied to the localisation data which distinguishes between true positive event detection, i.e. imagers binding within to the surface of a streptavidin-coated particle, and false positive events, i.e. event detection from areas where no particles are present. The values in the plot are normalised for time and area. The P5 imaging round of both Quencher-Exchange-PAINT and conventional Exchange-PAINT show a similar number of detected events per bead, which indicates a similar imaging sensitivity. The similarly low number of false positive events indicate the high specificity of DNA-PAINT, independent of the use of quencher strands. Note this is a case of DNA-PAINT with a high concentration of docking strands on the particles and a passivated coverslip surface to ensure minimum nonspecific imager binding.

A generalised Quencher-Exchange-PAINT protocol (Figure 5.11c) implements multiple rounds of Exchange-PAINT without the need of fluid exchange. Here, the sample is imaged in an open top microscopy chamber and full suppression of imager binding events can be achieved with a small amount of concentrated complementary quencher added by pipetting, for example, 1 µl of 500 nM Quencher into a 500 µl volume chamber. This would result in a final quencher strand concentration of ~1 nM, sufficient to reduce the binding event rate as well as the background fluorescence to negligible levels. Adding excess quencher strand concentration will speed up the suppression and thus allows faster switching. Additionally, it guarantees full suppression even in the case of local concentration variations. Note that adding the quencher strand complementary to the previous imager (here P1+) and the subsequent imager (here P2+) at different

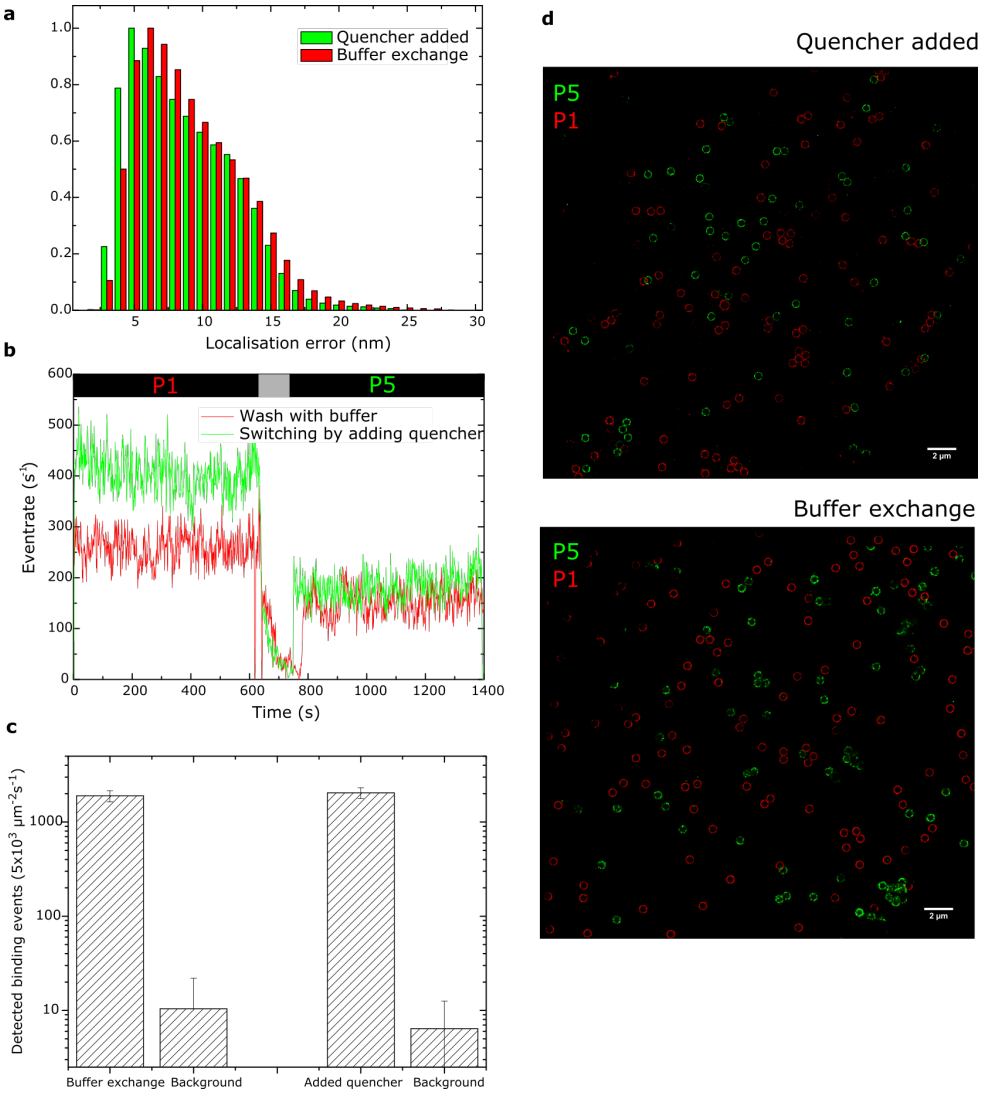

Figure 5.12: Comparison of imaging sensitivity and specificity of Quencher-Exchange PAINT and conventional Exchange-PAINT on streptavidin-coated particles. **(a)** The localisation error of P5 imager binding events does not change noticeably in the presence of bound P1 imager-quencher pairs. **(b)** The time course of the binding event rate demonstrates a slightly faster drop by adding quencher due to multiple washing steps required in buffer exchange. Please note that different absolute values of the event rate depend on multiple parameters such as different imager concentrations or a different number of imaged beads. **(c)** The imaging sensitivity can be estimated by comparing the number of detected events on a single bead between conventional Exchange-PAINT (left) to the Quencher-based approach (right), the specificity by comparing detection of false positive events, here called "Background". These values show the number of detected events in equally sized areas without beads present. Please note the logarithmic scaling. **(d)** Rendered images of Quencher-Exchange-PAINT (top) and buffer-exchange based Exchange-PAINT (bottom).

times is proposed for quality control, i.e. to check that event rates drop to negligible levels before adding imager complementary to a different docking strand. P1+, P2+,... are orthogonal imagers that follow a similar scheme as the P1+ design shown in Fig 5.6, i.e. high affinity between imager and quencher strands, but relatively low affinity between imager and docking strands. This can be achieved by generalising the scheme underlying the P1+/P1 strands and adapting it to orthogonal DNA-PAINT strands, such as those evaluated by Jungmann et. al [20]. Even faster and less invasive Quencher-Exchange-PAINT could be achieved by adding the P1+ quencher strand and P2+ imager simultaneously as a mixture in a single pipetting step and the localisation events of a suitably chosen transition time are discarded to avoid crosstalk between the P1+ and P2+ channels.

In principle, Quencher-Exchange-PAINT with orthogonal quencher-imager pairs allows multiplexed imaging of an arbitrary number of targets labelled with orthogonal docking strand sequences. Subsequent imager binding (P2+, P3+,...) can be suppressed with respective complementary quencher strands (P2+ quencher, P3+ quencher,...). Repeated imaging and quenching of the same target is possible as well. The free imager concentration $[I] \approx [I_0] - [Q_0]$, which determines the binding event rate, has to be adjusted by adding sufficient imager, to compensate for an excess quencher strand concentration.

5.7 Rapid imager exchange in Quencher-Exchange-PAINT of tissue samples

In addition to the use of Quencher-Exchange-PAINT for simplified multiplexed super-resolution imaging I also investigated its use to accelerate imager switching in multiplexed tissue imaging. If the imager solution surrounding the sample is fully replaced by buffer during a conventional wash-out, the drop of the event rate depends on the diffusion of imager strands out of the sample. While these time scales are negligible with DNA origami samples in free solution and with thin fixed cells, diffusion of imager strands in tissue sections is much more varied and can result in an imager washing step requiring regularly more than 15 minutes. In our experiments, time scales of 50% removal were as large as 10 minutes, although in some tissue locations in our experiments with mouse, rat and pig cardiac tissue samples removal was considerably faster. Notably, there were no

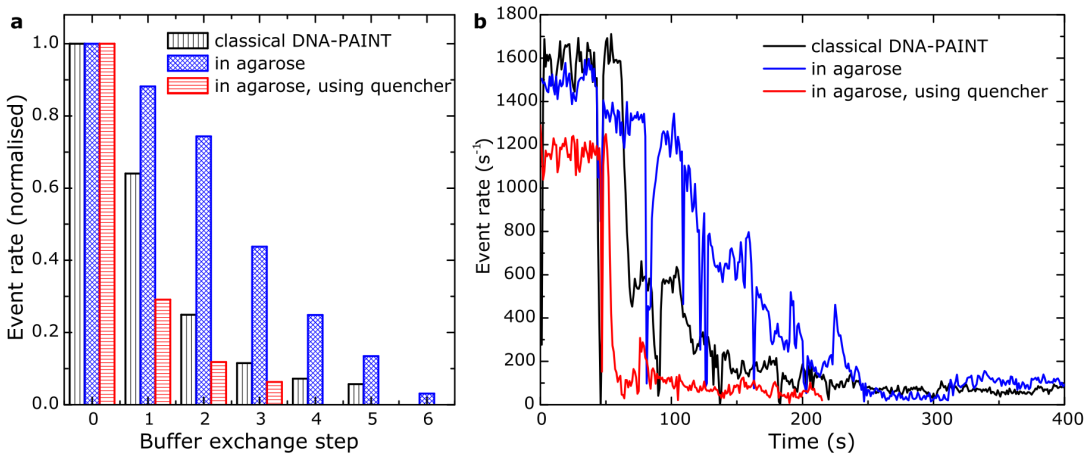

Figure 5.13: Rapid event rate suppression in microsphere sample with an imitation of reduced diffusion in tissue sections by embedding microspheres in agarose. **(a)** Mean imager docking binding event rate reduction during multiple washing steps by replacing buffer by pipetting in an open top chamber. For classical DNA-PAINT (black) of microspheres, the event rate is reduced to below 10% after 3 washing steps, a reduction which is only achieved after 6 washing steps when microspheres are embedded in agarose (blue). If quencher strands are added during washing step (red), the event rate is reduced even faster than if no agarose embedding is used. **(b)** Time trace of event rate data shown in a. Brief reductions of event rates indicate washing steps.

obvious criteria to predict imager removal time which precluded selecting tissue portions for fast exchange.

Quencher-Exchange-PAINT presents a way to decouple the binding event rate from the absolute imager concentration and thus from imager diffusion itself. To reduce the event rate, quencher strands at a concentration multiple times higher than the imager concentration can be added to the solution surrounding the diffusion-limited sample. This concentration gradient will lead to an increase of quencher strand concentration to a sufficient level throughout the tissue much faster than the diffusion of imager out of the tissue, resulting in a rapid reduction of the binding event rate.

The effect was first studied in a microsphere test sample, with limited diffusion of imagers imitated by embedding the microspheres in agarose gel (figure 5.13). While a full buffer exchange by pipetting with plain buffer reduces imager binding rates to a background level after approx. 3 washing steps for regular microspheres (event rates shown in black), twice the number of washing steps

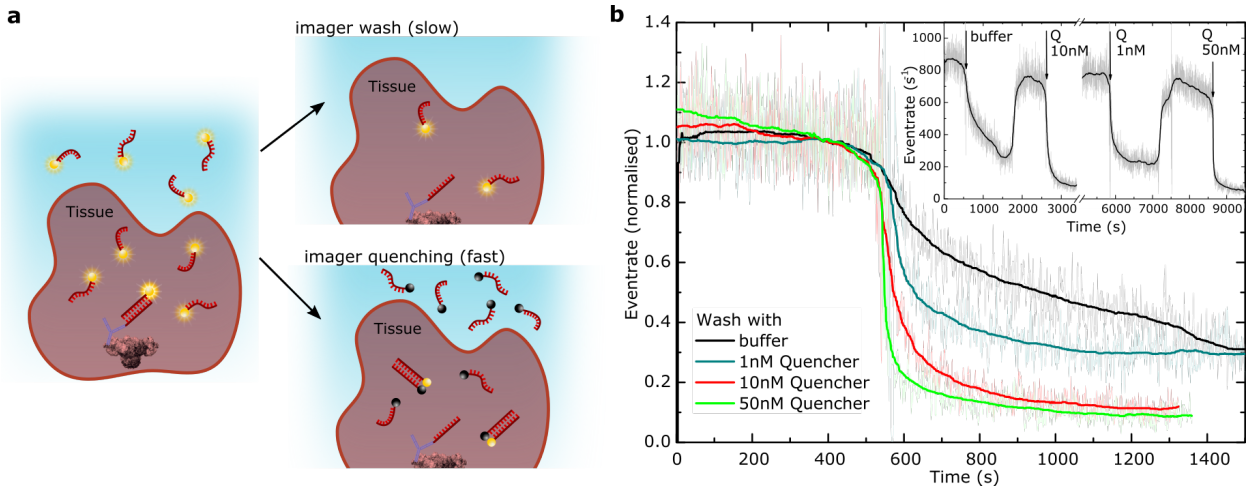

Figure 5.14: Influence of fluorescence quencher on washing steps in Exchange-PAINT imaging of cardiac tissue samples. **(a)** After imaging one target in Exchange-PAINT (left), the imager has to be removed efficiently for subsequent imaging steps. This is achieved by replacing the imager with plain buffer (top), but can take several minutes in samples with limited diffusion. Quenching remaining imager with complementary quencher-conjugated strands will reduce the event rate much more rapidly (bottom). **(b)** A cardiac tissue sample is washed with plain buffer (black) and increasing quencher concentrations (blue, red, green), which reduces the event rate more efficiently. Inset shows the absolute event rate of the washes, the free imager concentration was re-adjusted by adding more imager after each wash.

are required in agarose (blue), similar to observations made in tissue sections. However, if quencher strands at a concentration 50× higher than the imager concentration are added during a washing step on an agarose embedded sample, the washing is considerably faster, with 2 washing steps sufficient for suppression of 90% of the imager binding event rate.

Rapid washing by Quencher-Exchange-PAINT was confirmed in cardiac tissue samples, which showed limited imager diffusion (Figure 5.14a). The effect of the quencher strand concentration on the event rate reduction was characterised. Figure 5.14b demonstrates an increasingly rapid event rate suppression with increasing quencher strand concentrations. Ryanodine receptors in a cardiac mouse tissue section were imaged and the event rate modulated sequentially by washing with plain buffer and different concentration of complementary quencher strands (1, 10, 50 nM with an initial imager concentration of 1 nM), while the field of view and imaging sequence remained the same for comparability. In the

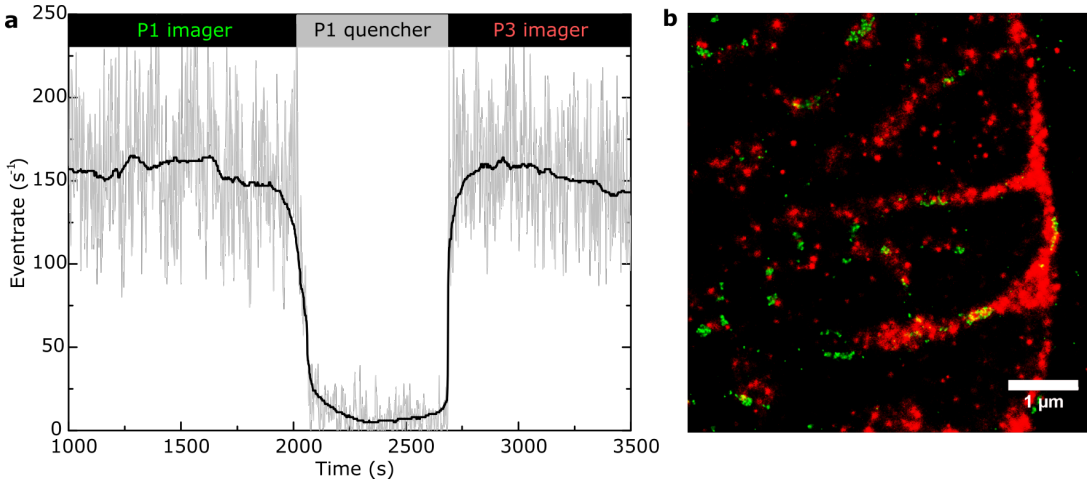

Figure 5.15: Exchange-PAINT facilitated by wash with additional quencher. **(a)** DNA-PAINT event rate for P1 imager drops to background levels after wash with a complementary quencher strand. Subsequently, P3 imager is added. **(b)** Superimposed image of P1 and P3 channel. Green: Ryanodine receptors imaged with 1 nM P1, washed with 10 nM P1 Quencher. Red: TOM20 imaged with P3 at 1 nM. The tissue section was imaged 3 µmabove the coverslip in HILO mode.

shown case, washing with plain buffer did not decrease the event rate to levels necessary for Exchange-PAINT for over 10 minutes. Washing with quencher strands $10 - 50\times$ more concentrated than the imager concentration within the tissue reduced the event rate to background levels within less than 5 minutes.

Due to the washing steps involved in the presented tissue Quencher-Exchange-PAINT, a high quencher-imager binding affinity is no longer crucial, because a high fraction of the imager-quencher pairs will be washed out in the process. Therefore, a shorter quencher strand, binding to a conventional P1 imager with 9 bp overlap, could be used here as well. Nevertheless, the P1+ type approach without explicit solution exchange should also work for tissues, with the alteration that a larger excess of P1+-Quencher should be added, as the acceleration of the suppression of imager-docking binding relies on the saturation of binding between quencher and imager strands. This rapid saturation steepens the time course of reduction of free imager relative to the diffusional time course of quencher concentration increase.

To demonstrate a full Quencher-Exchange-PAINT cycle in tissue, rat and pig cardiac tissue sections were imaged, targeting ryanodine receptors (Imager P1)

and TOM20 (Imager P3) (Figure 5.15). The binding event rate drops to negligible levels in less than a minute (Figure 5.15 a). Here, the washing step was maintained longer than strictly necessary to demonstrate a constantly low event rate, similar to the background event rate in tissue, after quencher has been added. Subsequent addition of an orthogonal P3 imager allowed crosstalk-free multiplexed imaging of the next target, here TOM20 (Figure 5.15 b).

5.8 Combination of Quencher-Exchange with other multiplexing techniques

Both methods presented in this chapter, i.e. the use of macrofluidic chips for Exchange-PAINT and Quencher-Exchange-PAINT, can easily be combined. Figure 5.16 shows, from data taken in a macrofluidic chip, a comparison of the reduction of the imager event rate in a cardiac tissue sample by wash with plain buffer and with quencher strands, in analogy to figure 5.14, where this was done in an open-top chamber. The same target (RyR, labelled with a P1 docking strand) in the tissue section inside the fluidic device is imaged in two rounds, interrupted by a washing step with plain buffer. The second imaging round is ended by wash-in of buffer containing 65 nM P1 quencher. Figure 5.16 a shows a high overlap of RyR imaged in the first round (red) and second round (green), which indicates good sample stability in the fluidic chamber. The combination of slower buffer exchange in the fluidic chamber and slow imager wash-out in tissue sections results in a slow reduction when washed with plain buffer (figure 5.16 d, black curve). The washing speed can be greatly increased if quencher strands are used (figure 5.16 d, green curve). The combination of Quencher-Exchange-PAINT and fluidic devices is beneficial if a higher degree of automation of DNA-PAINT experiments is desired, e.g. for high content imaging or correlative live cell and DNA-PAINT imaging [77, 169].

Furthermore, Quencher-Exchange-PAINT can be combined with spectrally multiplexed imaging. Figure 5.17 shows a proof-of-principle experiment, in which streptavidin-coated microspheres are imaged simultaneously by imagers which share the same sequence but are labelled with different fluorophores, Atto 655 and Atto 700. The two colour channels were separated with a dichroic mirror and imaged on either half of an EMCCD camera chip. Due to a clear difference in their emission spectra, the two fluorescent dyes can be cleary separated (figure 5.17 a). The binding event rate is suppressed by the quencher strand,

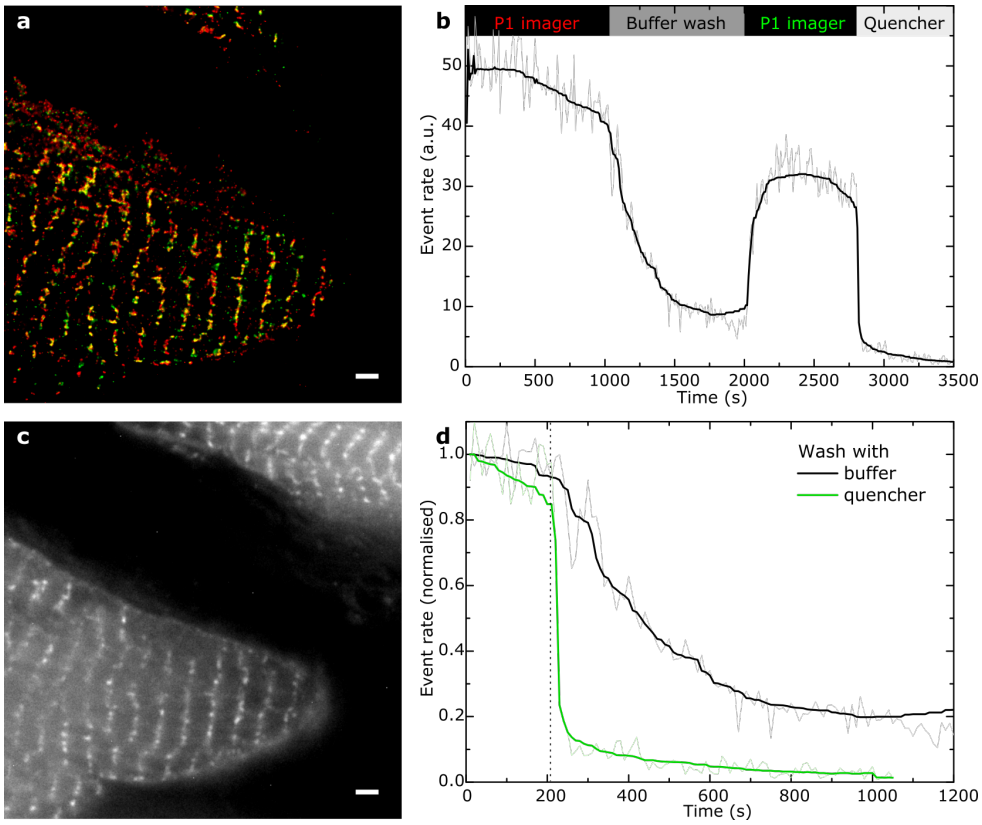

Figure 5.16: Comparison of event rate reduction by washing with pure buffer and by using quencher strands in a macrofluidic chip. A cardiac tissue sample inside a macrofluidic chip was exposed to P1 imaging buffer, washing buffer and quencher strands. **(a)** Rendered image of RyR, imaged in two rounds of P1 imager (red/green). **(b)** Imager binding event rate showing P1 imager, wash with buffer, repeated P1 imager round and wash with quencher, subsequently. **(c)** Fluorescent wide field image. **(d)** Comparison of buffer and quencher wash with normalised data shown in (b) demonstrating a slow reduction in events during buffer wash and a faster reduction during wash with quencher strands. Scale bars: 2 µm.

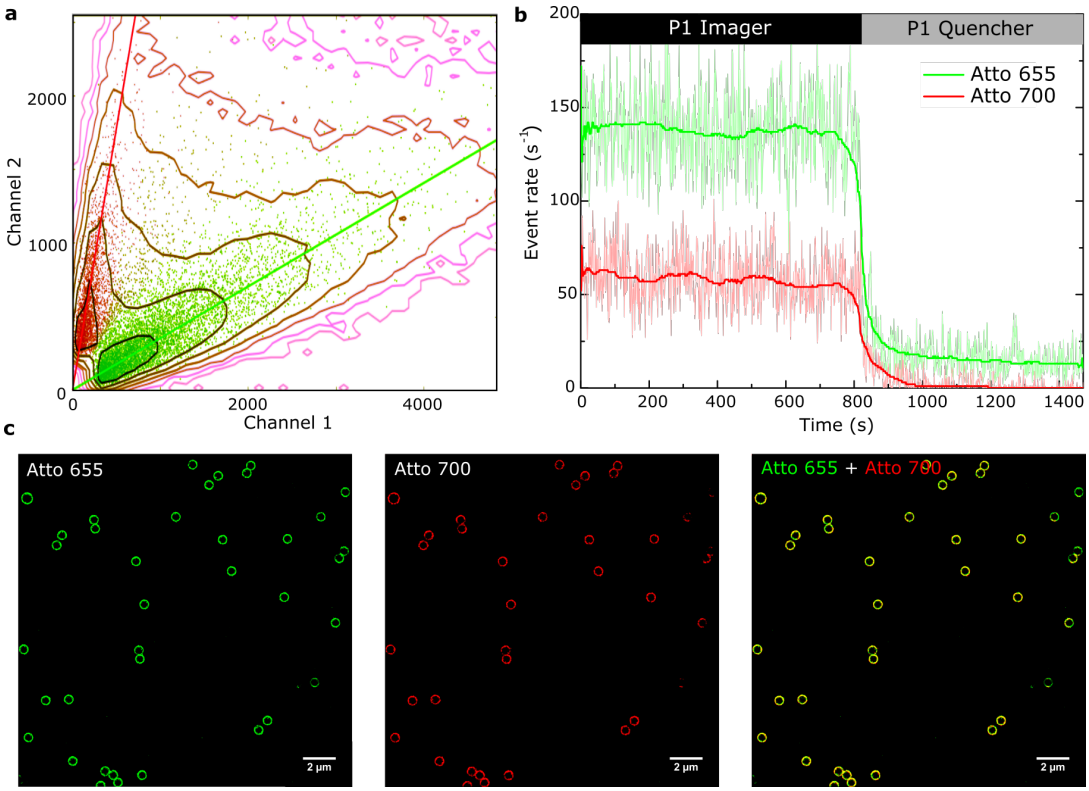

Figure 5.17: Spectrally multiplexed DNA-PAINT in combination with quencher strands demonstrating the possibility of a combination of multi-colour imaging with Quencher-Exchange-PAINT. Streptavidin-coated polystyrene beads labelled with P1 docking strands were imaged simultaneously by two types of P1 imagers modified with Atto 655 and Atto 700, respectively. **(a)** The intensity plot of both channels shows that the emission of Atto 655 (green) and Atto 700 (red) can be clearly separated. **(b)** The complementary quencher strand hybridises to the P1 imagers independently of the dye modification and thus reduces the detection event rate in both channels. In principle, different imager/quencher sequence pairs could be used and additional, orthogonal imager strands could be added after a quenching step to increase the number of detected targets. **(c)** Rendered images of the Atto 655 channel (green), the Atto 700 channel (red) and an overlay, which demonstrates a strong correlation between the two channels.

independent of the dye modification. The fluorescence quencher modification used in this experiment covers a large part of both emission of Atto 655 and Atto 700. In principle, the combination of spectrally multiplexed imaging and Quencher-Exchange-PAINT allows a higher throughput in multiplexed imaging. For example, two targets could be imaged simultaneously by spectral multiplexing, the respective imagers subsequently quenched and two further targets imaged in a following Exchange-PAINT imaging round. The total number of targets imaged would be the product of the number of Quencher-Exchange-PAINT imaging rounds with the number of spectrally different fluorophores used.

5.9 Discussion

In this chapter, different approaches for improved Exchange-PAINT protocols are demonstrated. The implementation and evaluation of a fluidic system is described, which offers simplified sample handling and preparation compared to conventional microfluidic schemes and allows for more sample stability compared to pipette washing. However, it suffers from increased complexity compared to a simple open-top imaging chamber, increased imaging duration due to slow buffer exchange and can still exhibit increased sample drift during washing steps.

As an alternative, Quencher-Exchange-PAINT is introduced, which allows rapid, low crosstalk Exchange-PAINT imaging of protein clusters and membrane structures in cell and tissue samples. The addition of fluorescence quenchers conjugated to oligonucleotides and complementary to imager strands is equivalent to a decrease of imager concentration, reducing both fluorescence background as well as the binding event rate. Thus, exchanging imager solutions in Quencher-Exchange-PAINT can be decoupled from slow diffusional wash-out of residual imager, accelerating the process considerably. The same approach using quencher coupled strands can be used for straightforward Quencher-Exchange-PAINT imaging without the need for washes and full fluid exchange chambers. The free imager concentration and therefore the imager-docking strand binding event rate can be easily tuned by adding a small volume of complementary quencher strands at high concentration to an open top imaging chamber.

Importantly, the flexibility of the synthetic DNA design is shown, using an imager and quencher strand pair with slightly extended length that achieves the desired high affinity while not affecting the super-resolution imaging quality.

Quencher-Exchange-PAINT can be combined with the presented fluidic systems and the throughput of Quencher-Exchange-PAINT can in principle be increased by combination with spectrally multiplexed imaging. Furthermore, the concept of Quencher-Exchange-PAINT could be used to facilitate other related techniques such as the generalisation of Exchange-PAINT to confocal imaging and other super-resolution techniques such as STORM or STED [74, 75, 170]. In these methods, a tuning or reduction of the imager binding rate is also essential and can be facilitated by adding complementary quencher strands.

6. Proximity-Dependent PAINT (PD-PAINT)

Characterising protein interactions by detection of protein-protein complexes is the basis of understanding many processes in biology [114]. Often, these are detected by in vitro methods such as co-immunoprecipitation, cross-linking or affinity blotting [171, 172]. It is increasingly evident that besides detecting the mere presence of protein-protein interactions, it is important to determine where these occur within a cell or tissue, since the nanoscale organisation of signalling complexes directly controls cell function [3, 112]. To this end, methods have been developed that are based on labelling the features of interest with synthetic DNA oligonucleotides, conjugated to antibodies or other molecular markers. The oligonucleotides act as proximity probes, and a subsequent amplification step is implemented to produce a fluorescent signal detectable by a conventional microscope. In an (in situ) proximity ligation assay (PLA), enzymatic amplification occurs via the rolling circle method [110–112, 115], while in the ProxHCR scheme amplification is non-enzymatic and relies on a hybridisation chain reaction [113, 117]. However, the high fluorescent amplification in both methods also effectively restricts them to diffraction-limited imaging. This implies that the presence of protein pairs can be located to within a certain region, but generally precludes accurate quantification and visualisation of their distribution at the nanometre scale [119].

Fluorescent super-resolution techniques can be used to acquire multi-target images which, in principle, allow for estimating the proximity of protein targets by fluorescence colocalisation. DNA-PAINT offers several options for super-resolution multiplexed imaging, i.e. by spectral multiplexing or via (Quencher-)Exchange-PAINT [1, 20], as described in the previous chapter. However, unequivocal identification of protein-protein pairs is complicated by the fact that

colocalisation can be prone to false positive signals, as the precision of colocalisation is directly dependent on the local imaging resolution. Resolution can vary considerably, especially in optically complex samples such as thick cells or tissue sections. Often, there is limited resolution along the optical axis (several hundreds of nanometres in 2D super-resolution techniques, >40 nm in 3D methods [124]) which can lead to additional false positives. Furthermore, registration errors between multiple channels, e.g. due to chromatic aberrations or sample drift, can lead to incorrect colocalisation estimates.

Here, a proximity-sensitive super-resolution imaging method is introduced which allows detection of the presence and characterisation of the local density and nanoscale distribution of protein-protein complexes, determining the detailed structure and morphology of possible clusters. Importantly, the proximity detection is fully decoupled from local imaging resolution and optical multi-channel registration is not required. In this approach, two proteins of interest are labelled with DNA constructs which are designed to interact if in molecular proximity and, as a result, allow for a DNA-PAINT signal to be detected. One construct however, includes the DNA-PAINT docking sequence which is protected by a stable DNA stem loop structure, rendering the docking site effectively inaccessible. If the second target is within a distance of approximately 10 nm, the second DNA construct associated with it can displace the stem of the hairpin, thereby unfolding the loop, fully exposing the docking site, and enabling DNA-PAINT imaging of the structure. This new approach is termed Proximity-Dependent PAINT (PD-PAINT) and demonstrated by means of coarse-grained molecular simulations and experimentally by imaging high-proximity biotin binding sites on streptavidin and epitopes on cardiac ion channels. PD-PAINT combines proximity detection with all the advantages of DNA-PAINT. These include high specificity, straightforward implementation on a conventional fluorescence microscope, freedom in the choice of dye and wavelength, and importantly the possibility of readily achieving high photon yields, resulting in very high resolution [22, 173]. In addition, by exploiting the principle of quantitative PAINT (qPAINT), PD-PAINT enables accurate determination of the local density of protein pairs in the sample [21, 22]. Finally, PD-PAINT is fully compatible with multi-colour imaging and can be implemented in addition to conventional DNA-PAINT of multiple other channels, essentially without performance penalty. This is demonstrated here by following an Exchange-PAINT protocol to image the protein complex as well as the individual protein epitopes in separate channels.

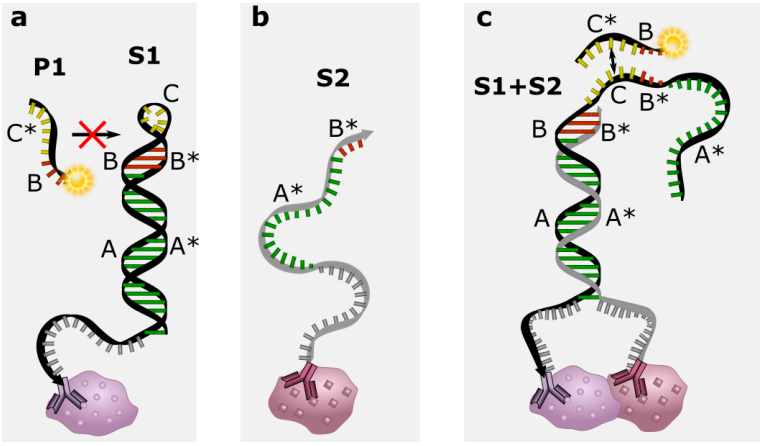

Figure 6.1: Principle of Proximity-Dependent PAINT (PD-PAINT). **(a)** Strand S1 forms a stem loop structure which prevents imagers (P1) binding to the docking domain (B*C), due to a high curvature of domain S1-C and hybridisation of domain S1-B* to S1-B. **(b)** Strand S2 contains domains A* and B* which are complementary to A and B of the S1 stem. **(c)** Close proximity of S1 and S2 allows the S2-A* domain to displace S1-A*, opening up the loop. The equilibrium probability and kinetics of the displacement is highly dependent on the distance between S1 and S2. The exposed docking domain in the open loop allows the transient binding of an imager to the S1-S2 complex so that a super-resolution image can be obtained by DNA-PAINT.

This chapter has been published on the pre-print server bioRxiv [2] and has been submitted to a peer-reviewed journal for further publication. Here, only minor alterations have been made, e.g. the integration of supplementary figures into the main text and the addition of data showing sequence-dependent nonspecific imager binding in biological samples. All co-authors, William T. Kaufhold, Alexander H. Clowsley, Anna Meletiou, Lorenzo Di Michele and Christian Soeller, have contributed to the manuscript through multiple rounds of revisions. WTK and LDM wrote section 6.2 and appendix A, designed DNA sequences S1 and S2 and did the molecular simulations used for figure 6.2. AHC and AM provided biological samples and helped with immunolabelling, as described in chapter 3.

6.1 PD-PAINT principle

Figure 6.1 demonstrates the principle of PD-PAINT, where fluorescence signals are only detected if two epitopes of interest are within close distance to

each other. To implement PD-PAINT the two targets are labelled with oligonucleotides S1 and S2, e.g. via two types of antibody to which S1 and S2 are respectively conjugated. As shown in figure 6.1 a, S1 contains the 9 nt docking sequence consisting of domains B* (3 nt) and C (6 nt). When S1 is isolated, the docking site is protected by a closed stem-loop motif in which B* is hybridised to the complementary domain B, and C is wrapped to form a short loop. The loop is further stabilised by the complementary domains A and A* (17 bp). In the closed-loop configuration of S1 the docking site has negligible affinity for imagers of sequence C*-B (figure 6.1 a), as previously determined in the context of catalytic DNA reactions [117] and further demonstrated by means of coarse-grained computer simulations discussed below. The second target is labelled with strand S2, which contains sequence A*-B* (figure 6.1 b). This sequence is complementary to B-A in the S1 stem, making the S1-S2 dimerisation reaction and the consequent opening of the stem loop on S1 thermodynamically only feasible for sufficiently high concentrations of the constructs. If the local concentration of S1 and S2 is too low, e.g. ~500 nM as used for sample labelling steps, the closed-loop configuration remains favourable. Furthermore, owing to the stability of the S1 stem, the dimerisation reaction is kinetically highly unlikely unless the two species are kept in close proximity.

If S1 and S2 are attached to stationary epitopes located within close distance to each other, their dimerisation can proceed through the process of proximity-mediated strand displacement (PMSD) [107, 174]. Here, the occasional fraying taking place at either end of the S1 stem duplex enables the formation of transient base-pairing bonds with either the A* or the B* domains on S2, which then have a chance of progressing until S1 and S2 are fully hybridised through a stochastic branch-migration process [106]. The likelihood for the branch-migration to initiate, and thus the overall S1-S2 hybridisation rate, is proportional to the local concentration of S1 and S2 and, as such, strongly proximity dependent [107, 174]. Likewise, the equilibrium probability of the S1-S2 complex being formed is expected to depend on the distance between the tethered constructs. When S1 and S2 are fully hybridised the open loop exposes the docking sequence B*-C of S1, allowing transient binding of the complementary imager P1, which results in frequent detection of these binding events as fluorescent blinks, i.e. a DNA-PAINT signal (figure 6.1 c).

6.2 Simulation of thermodynamic properties

To explore the functionality of the proposed PD-PAINT scheme its thermodynamic properties were investigated by means of Monte Carlo (MC) simulations using the oxDNA coarse-grained model of nucleic acids, as described in detail in appendix A [175, 176]. For PD-PAINT to elucidate the presence of dimers, it must obey two thermodynamic design criteria. First, the S1 loop must be opened if S2 is nearby. Second, binding of the imager to the closed loop must be inhibited to prevent false positives, i.e. binding should only be possible when the loop is open.

We implemented free-energy calculations to determine the likelihood of the formation of S1-S2 dimers, resulting in the opening of the S1 loop, as a function of the distance between their anchoring points (figure 6.2 a). The standard free energy for S1-S2 dimerisation and loop opening, with the strands tethered at distance x from each other, can be expressed as

$$\Delta G_{\mathrm{tet}}(x) = \Delta G^0_{\mathrm{sol}} - \phi^0(x) \tag{6.1}$$

where $\Delta G^0_{\mathrm{sol}}$ is the standard free energy for dimerisation of untethered S1 and S2, which can be estimated via nearest-neighbour thermodynamic rules for known S1 and S2 sequences [142], and $\phi^0(x)$ is a correction that encodes the free-energy cost of mutual confinement of the constructs following dimerisation [178, 179]. The latter is obtained from MC simulations and accounts for the polymer elasticity of the ssDNA segments (here 15 nt) connecting the active domains of S1 and S2 to their tethering points, as well as excluded volume and electrostatic interactions between the constructs. As expected, both $\Delta G_{\mathrm{tet}}(x)$ and the loop-opening probability, $p_{\mathrm{dim}}(x)$, display a strong dependence on x, and $p_{\mathrm{dim}}(x)$ effectively becomes negligible for distances exceeding ~10 nm (figure 6.2 a). At small x, the loop-opening probability saturates at ~0.6, reflecting the fact that in conditions of high proximity a significant fraction of neighbouring S1-S2 pairs will produce available docking sites. Note that once an ensemble of constructs is brought to a certain level of proximity, relaxation of the dimerisation probability to the predicted distribution is not instantaneous, but will occur at a finite and separation-dependent rate, as well characterised for analogous PMSD processes [107, 174]. It is therefore critical in experiments to allow sufficient time for the S1-S2 pairs to reach equilibrium. The dimerisation probability for untethered constructs at a concentration of 500 nM, which was the maximal concentration

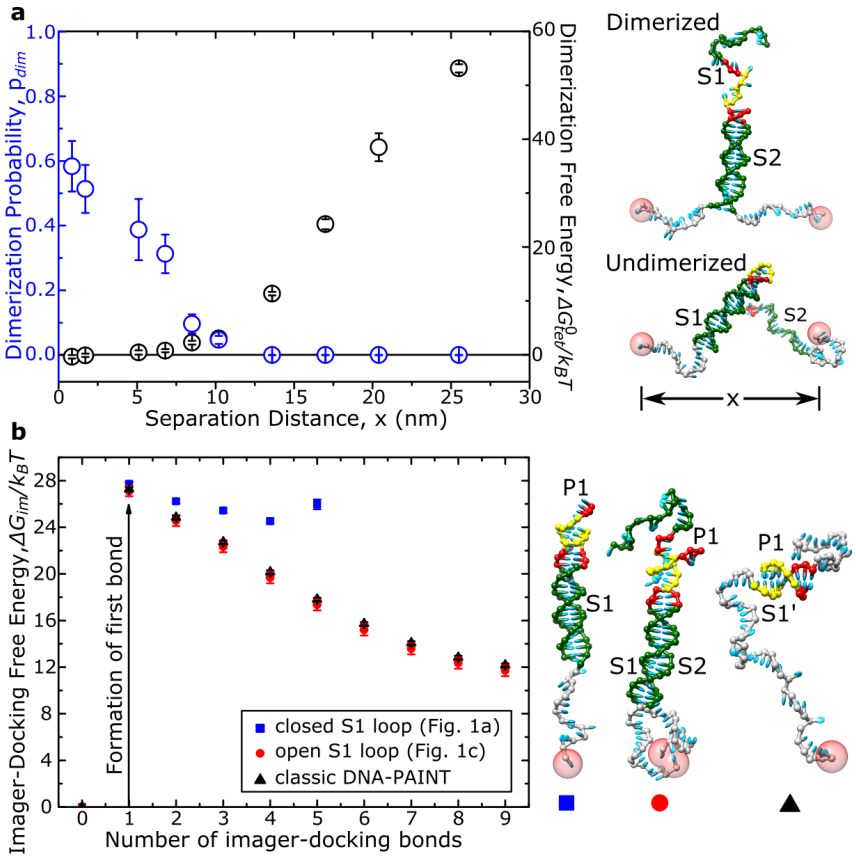

Figure 6.2: Thermodynamic properties of PD-PAINT. **(a)** The dimerisation probability of S1 and S2 is highly sensitive to the separation distance between tethers, x. Left: dimerisation probabilities (blue) and the free energy change of dimerisation (black) are calculated from coarse-grained Monte Carlo (MC) simulations based on the oxDNA model [175, 176]. When the tethers are separated by short distances (1 nm), S1 and S2 dimerise with probability 0.6, forming a complex that can be imaged by DNA-PAINT. As separation distances increase the dimerisation probability falls until dimerisation is negligible at separation distances exceeding 10 nm. Right: simulation snapshots of the dimerised and undimerised configurations. **(b)** Hybridisation of the imager to S1 as a closed loop is inhibited in the absence of S2 and restored by the presence of S2. Left: free energy profiles for formation of Watson-Crick bonds between the imager and S1, relative to the unhybridised state. Compared are the closed loop state of S1 (blue squares), the open state after hybridisation of S2 (red circles) and conventional DNA-PAINT binding (black crosses). Note that closed loop states with > 5 bonds resulted in large free energies whose contribution to the overall hybridisation free energy is negligible. Right: simulation snapshots for the three cases. Snapshots from the simulation are visualised with UCSF Chimera [177]. All errorbars are given as one standard error.

used during sample functionalisation steps, is $\sim 5.6 \times 10^{-4}$, implying that false positive signals resulting from the dimerisation of untethered S1 and S2 should be negligible. The likelihood of this occurring on experimental timescales is further suppressed by the slow initiation kinetics of the branch migration process for freely diffusing constructs [107, 174].

For the presence and location of S1-S2 dimers to be positively identified via DNA-PAINT binding of the imager to closed S1 loops must be inhibited, yet the imager must have a sufficient affinity for the exposed docking site. We verify this by estimating the interaction free-energy $\Delta G_{\mathrm{S1-P1}}$ between the P1 imager and S1 in its closed and open loop states, shown in figure 6.2 b as a function of the number of formed base-pairing bonds. The free energy barrier for the formation of the first bond is similar between the open and closed loop configurations but, while in the former case further base pairing does not result in a significant drop in free energy, a steep monotonic decrease is observed for the open-loop configuration. As a result, we estimate imager binding times to the closed S1 loop as $\sim 1.4\,\mu$s, well below the detection threshold for a typical DNA-PAINT experiment (see appendix A and table A.3). In turn, for the open loop configuration we predict a binding time of ~ 0.2 s, ideal for DNA-PAINT at typical frame integration times of $50 - 300$ ms (Table A.3). For comparison figure 6.2 b also features the $\Delta G_{\mathrm{S1-P1}}$ profile for a conventional DNA-PAINT docking strand that matches, within statistical errors, with the one determined for the open S1 construct.

6.3 Imaging of biotin-binding sites by PD-PAINT

To experimentally validate the PD-PAINT concept, the biotin-binding sites of streptavidin were used as a well-studied model system that is expected to yield a positive PD-PAINT signal (figure 6.3). Streptavidin binds up to four biotin molecules, with two sites each located on either side of the protein tetramer at a distance of ~ 2 nm from each other [180]. The very high affinity of biotin ensures an effectively permanent attachment of biotinylated S1 and S2 constructs. Streptavidin was attached to the surface of polystyrene colloidal particles, to provide a convenient imaging geometry as previously used in the context of DNA-PAINT (compare chapter 4 and [1, 151]). Biotinylated S1 and S2 constructs were mixed thoroughly before streptavidin-coated particles were dispersed on the coverslip to ensure a stochastic attachment of S1 and S2 to the biotin-binding

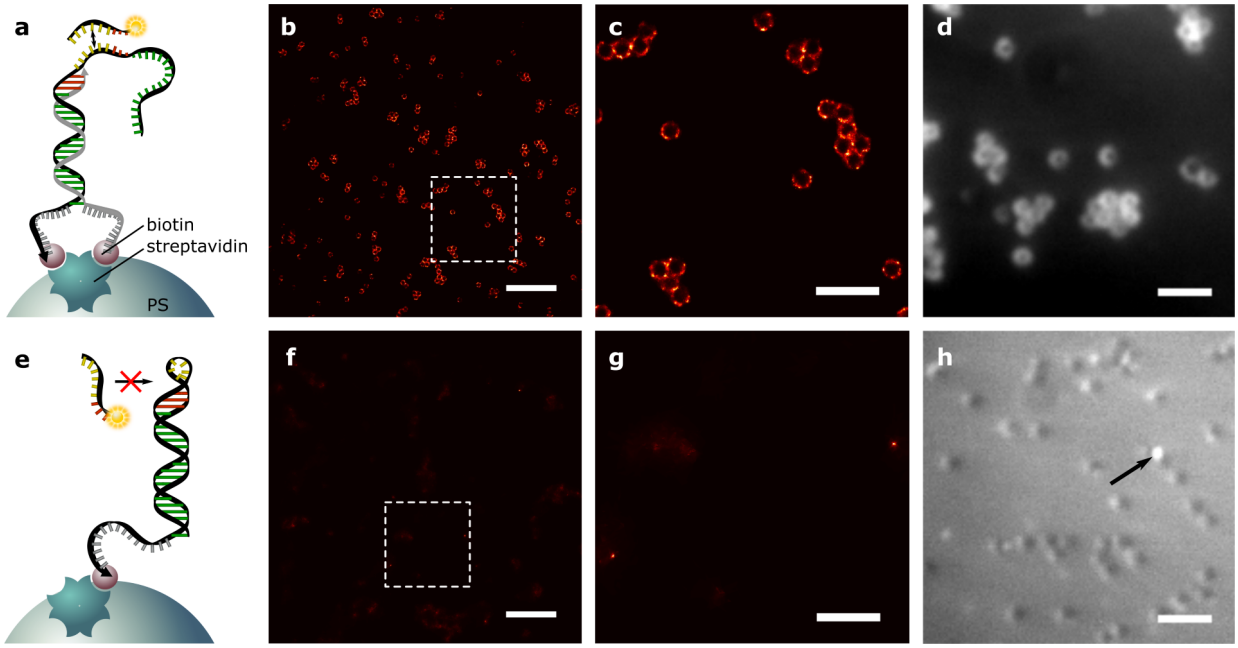

Figure 6.3: PD-PAINT to detect proximity of biotin binding sites on streptavidin. **(a)** Biotinylated strands S1 and S2 were allowed to attach in equal amounts to the surface of streptavidin-coated 500 nm polystyrene spheres, which allows a considerable fraction of S2 to open up the S1 stem loop structure, whenever S1 and S2 attach to adjacent binding sites on the same protein. **(b)** Rendered image of the resulting DNA-PAINT signal, the box indicates area of magnified inset in c. **(d)** Widefield fluorescence image at high imager concentrations (5 nM), with many of the accessible docking domains occupied by imagers. **(e)** If only S1 is used, the loop remains closed and does not allow imagers to bind. **(f, g)** Rendered images, analogous to b and c, but displaying little signal. **(h)** Widefield fluorescence image showing only a diffuse background fluorescence signal from comparatively high concentration of imagers (10 nM) in solution, outlining shadows of particles against the fluorescent background and very rare binding of single imagers (arrow). Note that the gray scale in h is different from d. Scale bars: 6 µm (b,f), 2 µm (c,d,g,h).

sites. The prominent ring structure observed in an optical section through the particles, shown in figures 6.3 b,c, arises from a distinct PD-PAINT signal, providing positive confirmation that binding of DNA-PAINT imagers is observed as expected. Assuming a distance of ~2 nm between the anchoring points of S1 and S2, at equilibrium approximately 50% of these site-pairs should feature dimerised strands with an open S1 loop, as discussed above (figure 6.2 a). DNA-PAINT imaging resulting in the super-resolved micrographs in figures 6.3 b,c, is performed at very low imager concentration (~0.05 nM) to reduce the likelihood of simultaneous binding events that would prevent single-molecule localisation [22]. When imagers are added at a much higher concentration (5 nM), as shown in figure 6.3 d, multiple docking sites within a diffraction-limited area are occupied, resulting in a fluorescence signal clearly visible in widefield fluorescence mode, consistent with a large fraction of all S1 loops being open and available for imager binding.

To confirm that there is negligible interaction between imagers and isolated S1 constructs with a closed loop, beads functionalised with S1 but lacking S2 were imaged (figure 6.3 e-h). No DNA-PAINT signal is observed, consistent with the simulation results which indicated that binding events of imagers to the closed loop on S1 are extremely brief and thus undetectable (figure 6.2 b and table A.3). Indeed, hardly any binding is observed, even at high imager concentrations (figure 6.3 h).

6.4 PD-PAINT in fixed tissue samples

Figure 6.4 demonstrates the applicability of PD-PAINT to biological samples, using fixed cardiac muscle tissue. In these experiments, binding sites for S1 and S2 are generated by means of a primary antibody (AB), of mouse origin, targeted against the cardiac ryanodine receptor (RyR2, a large ion channel). This primary AB has been previously used for DNA-PAINT imaging of RyRs [3]. Constructs S1 and S2 were hosted by two different populations of secondary ABs, targeting the mouse primary AB. By simultaneously applying equal concentrations of S1- and S2-conjugated secondary ABs to samples labelled with the primary, a high proportion of primary ABs featuring S1-S2 pairs was achieved. With the epitopes on the same primary antibody providing proximal binding sites, this scenario resembles the one validated in figure 6.3 with streptavidin, albeit now in a complex biological tissue. In order to allow the sequential imag-

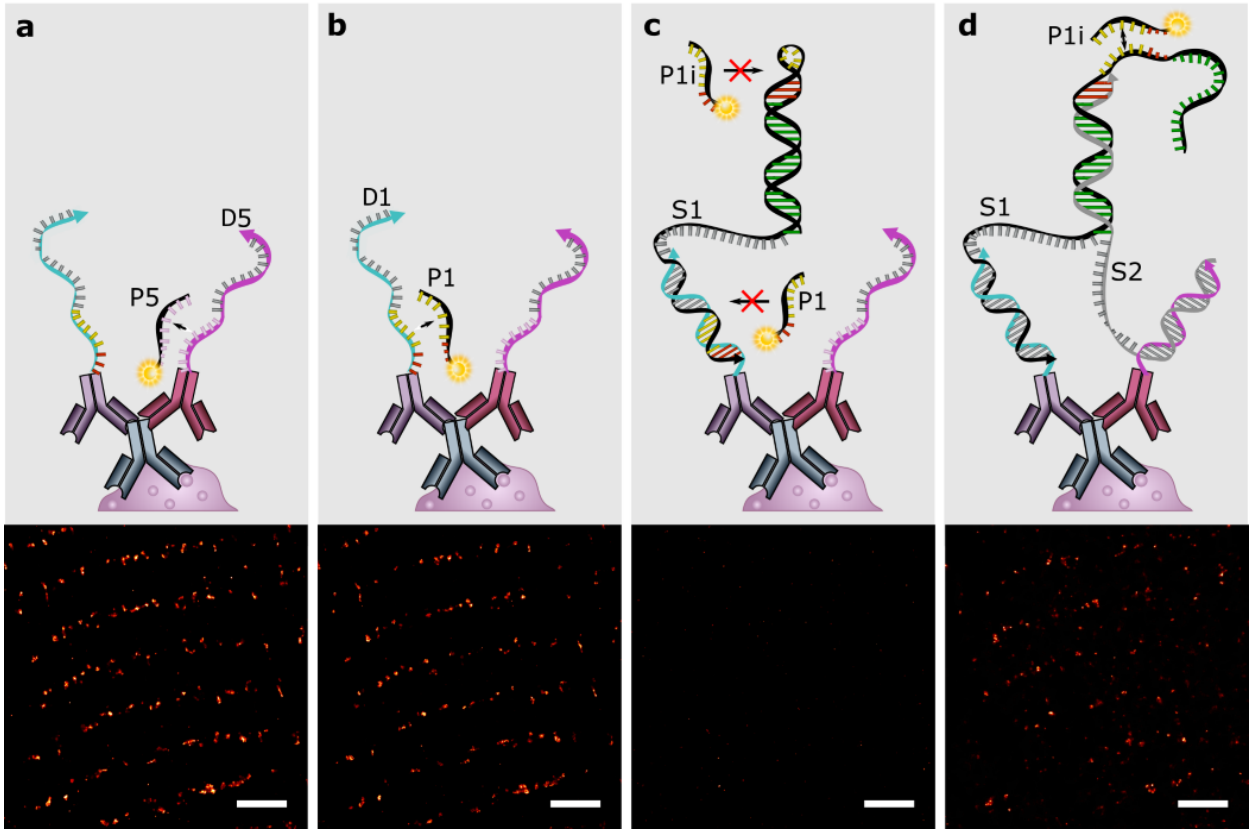

Figure 6.4: PD-PAINT with multiple antibodies binding to ryanodine receptors (RyR) in cardiac tissue sections. Two populations of secondary antibodies, labelled with extended docking sequences D1 and D5 containing P1 and P5 docking motifs, respectively, bind to single primary antibodies. **(a), (b)** Exchange-PAINT imaging steps with imagers P1 and P5. **(c)** A strand S1 binds to the extended docking sequence D1, preventing imagers from binding. **(d)** Strand S2 binds to docking sequence D5 and if in close proximity opens up the S1 loop. This allows imager P1 binding to the S1 docking domain. Bottom: rendered DNA-PAINT images of the respective steps. Scale bars: 2 um.

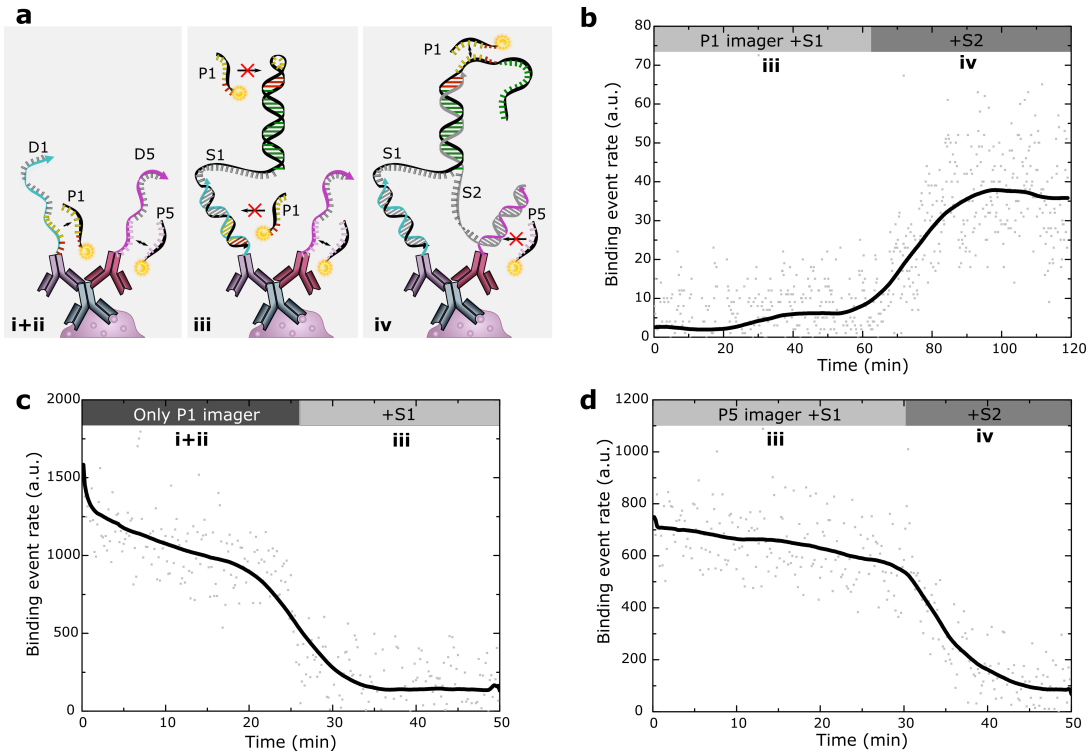

Figure 6.5: Equilibration time of PD-PAINT targeting antibodies in cardiac tissue sections. **(a)** Schematic drawing similar to figure 6.4, showing stepwise addition of PD-PAINT strands S1 and S2 to antibody-conjugated strands D1 and D5, respectively. Subsequent panels refer to the phases shown (a+b, c, d) above the kinetic responses. **(b)** Equilibration time of PD-PAINT, measured with imager P1. Imager P1 cannot bind if only strand S1 is present in the sample and in closed loop configuration. When strand S2 is added to the sample, equilibrium is reached after ~30 mins. **(c), (d)** Reduction of imager binding rates to D1 and D5 after addition of S1 and S2, respectively. If strands S1 or S2 are added to the sample, the imager binding to D1 or D5 is reduced to background levels within ~10 mins. Note that data in c and d is taken in a different sample, a control experiment shown in figure 6.8. Data of P1 and P5 were obtained simultaneously by spectral multiplexing (see figure 6.10) using different imager fluorochromes. Consequently, absolute values of binding event rates differ between figures.

ing of all targets involved and to also study the equilibration time of PD-PAINT while imaging, S1 and S2 were not directly conjugated to the secondary ABs. Instead, extended docking sequences D1 and D5, that would later anchor the S1 and S2 strands, respectively, were attached to the secondary ABs. D1 and D5 were designed to respectively bind the modified S1 and S2 constructs with high affinity, resulting in effectively irreversible attachment. The two secondary antibodies were initially imaged (figures 6.4 a,b) in conventional Exchange-PAINT mode [20], with P1 and P5 imagers binding transiently to D1 and D5, respectively, which host docking domains for these imagers. The good overlap between D1 and D5 images (figures 6.4 a,b bottom panels) suggests that a high proportion of primary ABs were labelled with both types of secondary ABs. When strand S1 was added (100 nM), while imager P1 was still present, the binding rate for imager P1 was eventually reduced to background levels (figure 6.5 c), because S1 permanently hybridises with D1, blocking the docking site (figure 6.4 c). Notably, during this step the P1 docking site of S1 remained inaccessible due to the closed stem loop structure. The suppression of DNA-PAINT binding occurred rapidly, within 10 min, which indicates quickly saturating binding of S1 strands to D1 (figure 6.5 c). When added in solution, S2 attached with a similarly high rate to D5 (monitored with imager P5, figure 6.5 d). Since pairs of ABs labelled with D1 and D5 are located within close distance of each other, once S1 and S2 constructs are both present the stem loop structure on S1 is expected to open with significant probability, enabling the detection of a DNA-PAINT signal by means of imager P1. This is indeed confirmed in figure 6.5 d. After addition of S1 and S2, a stationary DNA-PAINT binding rate was reached after ~30 min, indicating that an equilibrium state of S1-S2 complex formation was reached (see also figure 6.5 a,b).

Comparison of the three channels representing the localisation of ABs carrying S1, ABs carrying S2 and the PD-PAINT signal, shows that PD-PAINT signal is only observed in areas of colocalisation of the two conventional DNA-PAINT channels, as shown by the overlaid images in figure 6.6. Note that the limited resolution of conventional DNA-PAINT in complex tissue samples such as the one utilised here, especially along the optical axis (several 100 nm in regular 2D SMLM imaging), is expected to lead to a non-negligible number of false positive colocalisation signals. PD-PAINT offers a route to rule out false positives while retaining super-resolved spatial information on the distribution of proximity pairs.

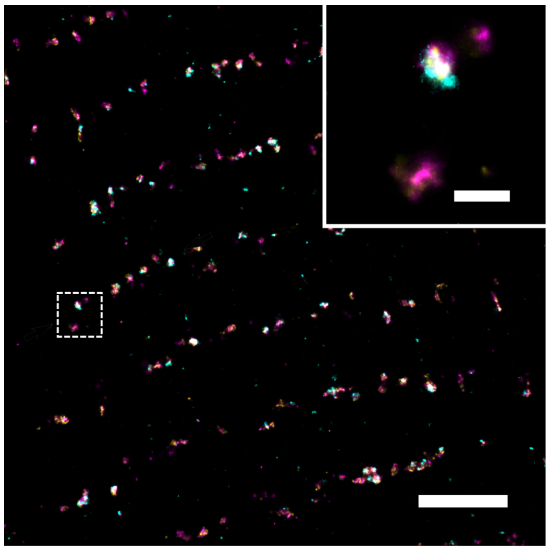

Figure 6.6: Overlay of PD-PAINT with multiple antibodies binding to ryanodine receptors (RyR) in cardiac tissue sections. Overlay of the DNA-PAINT images described in figure 6.4 (P5 yellow, P1 magenta, PD-PAINT cyan). PD-PAINT signal typically only appears where P1 and P5 signals show colocalisation (inset). Scale bars: 2 µm, inset: 500 nm.

Figure 6.7 demonstrates the application of PD-PAINT to detect the proximity of two different epitopes on RyRs in a tissue section. The two epitopes were first targeted by two distinct primary ABs, one rabbit-raised and the other mouse-raised. Secondary ABs conjugated to the D1 and D5 strands were then applied, targeting the two different primary ABs, before adding the constructs S1 and S2 to implement PD-PAINT.

The results of PD-PAINT experiments were broadly consistent with those where S1 and S2 carrying secondary ABs were attached to the same primary antibody (figure 6.4 and 6.6), however, here a lower rate of imager binding was detected after equilibration. With the binding rate being proportional to the number of available docking sites [21], the reduced rate indicates a lower number of S1-S2 dimerised pairs. This is consistent with the labelling system used in this approach where S1 and S2 are linked via two sets of antibodies to the protein of interest resulting in an increased average separation, as compared to the situation in figure 6.4. As supported by MC simulations (figure 6.2), a greater separation reduces the dimerisation probability and thus the fraction of open S1 loops and available docking sites.

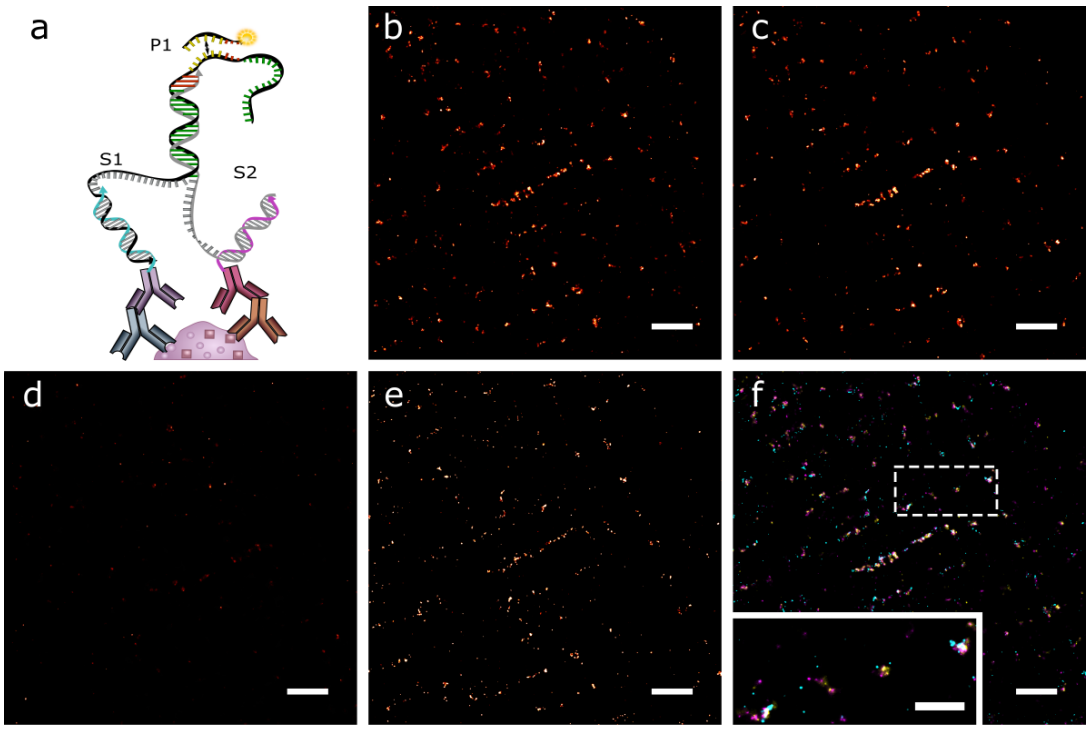

Figure 6.7: PD-PAINT with two primary antibodies against RyR. **(a)** Schematic drawing, showing PD-PAINT strands S1 and S2 binding to two different oligo-labelled secondary antibodies which in turn bind two populations of primary anti-RyR antibodies. **(b), (c)** Classical Exchange-PAINT image of the two populations of secondary antibodies with P1 image (b), (compare figure 6.4 b) and P5 image (c), (compare figure 6.4 a), **(d)** only S1 added, compare figure 6.4 c, **(e)**: both S1 and S2 added – PD-PAINT image, compare figure 6.4 d, **(f)** overlay, yellow – P5, magenta – P1, cyan – PD-PAINT. Scale bars: 2 µm, inset 1 µm.

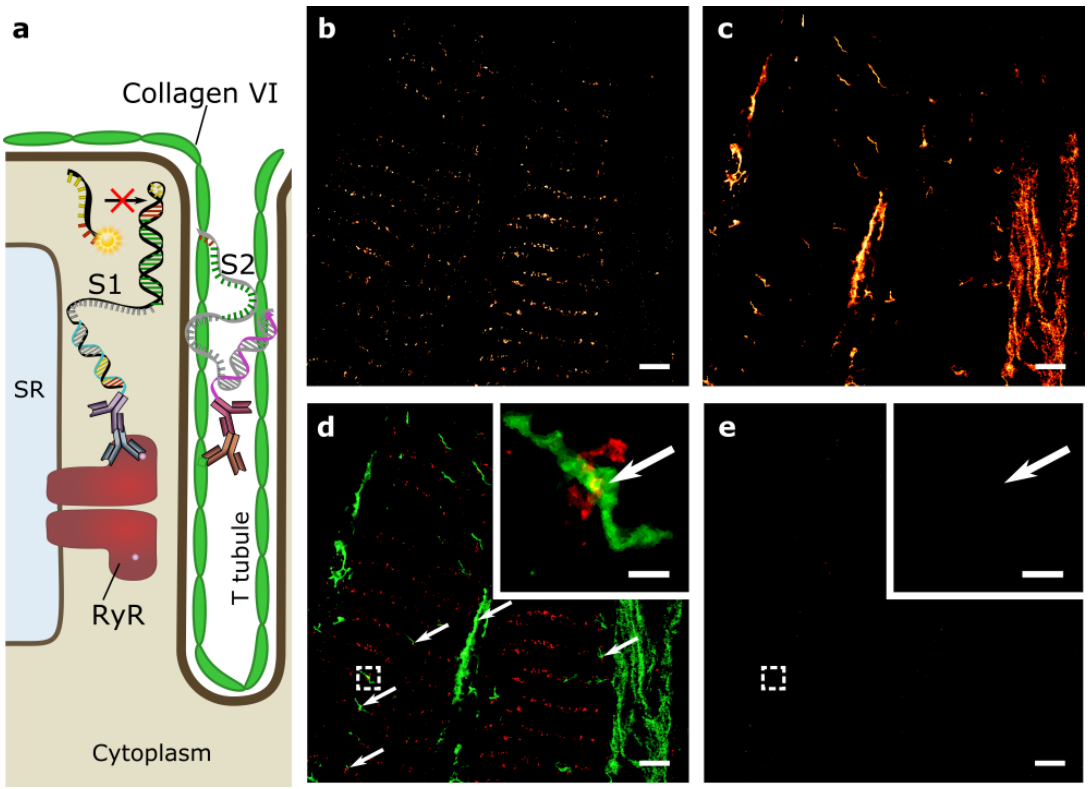

Figure 6.8: Negative control experiment. **(a)** Schematic of locations of RyR and Collagen VI (ColVI) [127], including invaginations of the cell membrane referred to as T tubules. The RyR is a membrane protein of the sarcoplasmic reticulum (SR), located inside the cell, **(b)** RyR DNA-PAINT image (using imager P1), **(c)** Collagen-VI DNA-PAINT image (using imager P5), **(d)** RyR – ColVI overlay. Some regions suggest apparent colocalisation (e.g. see arrows pointing at overlaps of green and red regions). **(e)** S1 attached to RyR antibodies, S2 to ColVI antibodies. The distance between RyR and Collagen VI is too large to give any PD-PAINT signal, suggesting the apparent colocalisation seen in the RyR and COLVI signal overlay (d) does not reflect molecular proximity. Scale bars: 2 µm, insets 250 nm.

The steep dependency of PD-PAINT signals on the proximity of S1 and S2 is further demonstrated in an experiment that serves as a negative control (figure 6.8). For this experiment, collagen type VI (ColVI) and RyR were labelled with primary and secondary antibodies to host D1/S1 and D5/S2 constructs, respectively (figure 6.8 a). RyR and ColVI have a broadly similar distribution pattern in cardiomyocytes but are separated by the cell membrane and thus not in direct molecular contact. When the two antibody populations were individually imaged using conventional DNA-PAINT targeted towards the D1 and D5 docking strands (figure 6.8 b,c), the resulting two-colour DNA-PAINT image exhibited overlap in some areas, an occurrence that would be interpreted as molecular colocalisation (figure 6.8 d). When the same areas were imaged using PD-PAINT targeting S1 and S2 now tethered to D1 and D5, no PD-PAINT signal was detected above background levels (figure 6.8 e). This suggests that the areas of overlap observed in the two-colour DNA-PAINT image are false positives and that no epitopes of ColVI and RyR are located within close proximity to each other. This is consistent with the expected distribution of collagen and RyRs - although relative distances can often be as small as ~100 nm, ColVI and RyR would be expected to be separated by 30 nm or more based on myocyte ultrastructure determined by electron microscopy [181]. Note that the probability of S1-S2 dimerisation predicted by MC simulations at such separations is, consistently, negligibly small (figure 6.2), even if taking into account a possibly reduced distance of the proximity probes due to the length of anchoring double strand D1 and the spatial extent of antibody labels (which can account for up to ~20 nm).

6.5 Quantitative imaging by PD-PAINT

Exploiting one of the advantages of DNA-PAINT, the possibility to quantitatively measure the number of accessible docking sites, and thus the number of protein pairs, from PD-PAINT data is shown. This is done by applying the qPAINT method, previously demonstrated for conventional DNA-PAINT [21]. Quantitative estimates of protein-pair numbers are critical, for example, in assays that test for changes in protein-protein signalling in response to experimental interventions. Some types of proximity detection have been shown to be prone to saturation which can preclude detecting changes in such experiments [116]. To validate quantitative PD-PAINT, biotin-binding sites on streptavidin-

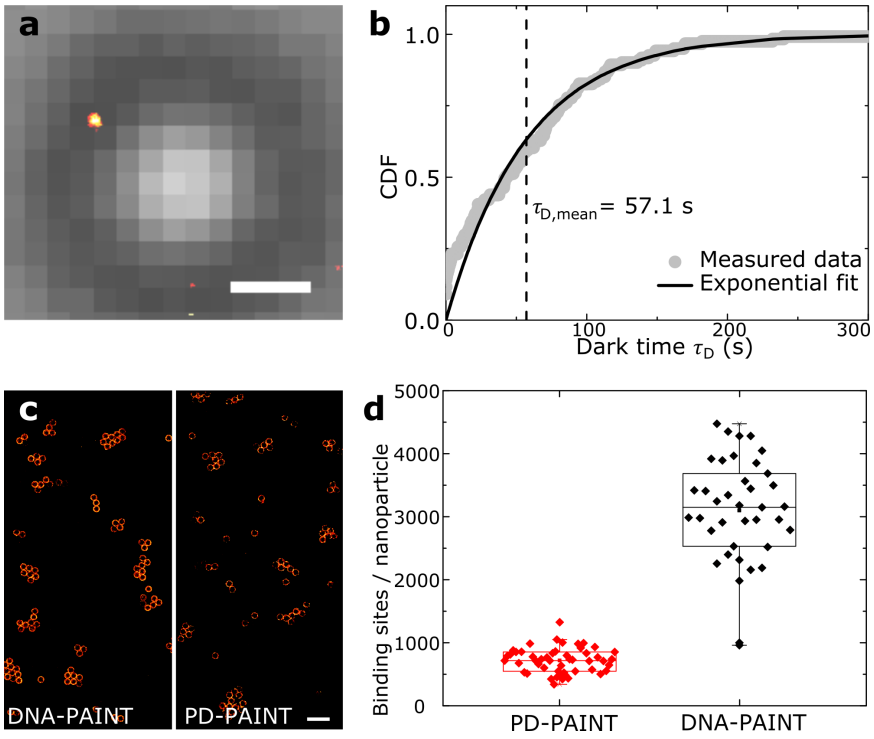

Figure 6.9: Quantitative imaging with PD-PAINT. **(a)** Widefield image of a streptavidin-coated particle (grey), with rendered DNA-PAINT image of a single biotinylated docking strand (yellow), used for qPAINT calibration. **(b)** Mean dark times $\tau_{D,mean}^{single}$ calculated by fitting an exponential to the cumulative dark time distribution of the calibration site shown in a, for a single conventional DNA-PAINT docking site. **(c)** Colloidal particles coated with conventional P1 docking strands (left) and PD-PAINT strands S1 and S2. **(d)** Using the calibrations obtained in b, the number of accessible docking sites for PD-PAINT (red) and conventional DNA-PAINT (black) per particle is calculated. A reduction of available sites in PD-PAINT compared to conventional DNA-PAINT is expected, due to the stochastic distribution of S1/S2 pairs. Scale bars: 250 nm (a), 2 µm(c).

coated particles were imaged as discussed above (figure 6.3). In qPAINT, the number of available binding sites within an area of interest is estimated from the kinetics of imager-docking binding events recorded within the area as $N_{\text{bind}} = (k_{\text{on}} \times c_i \times \tau_{\text{D,mean}})^{-1}$, where k_{on} is the imager-docking association rate constant, c_i is the imager concentration and $\tau_{\text{D,mean}}$ is the average time between consecutive binding events, or "mean dark time", determined as discussed in chapter 3.3.1. Here, k_{on} is estimated from a calibration measurement performed on a bead featuring a single binding site as $k_{\text{on}} = (\tau_{\text{D,mean}}^{\text{single}} \times c_i)^{-1}$ (figure 6.9) [21]. Binding of a single docking strand on a particle was achieved by functionalising the particles with a very dilute solution of docking strands (0.5 nM, see also Delcanale et al. [151]). Using $c_i = 5\,\text{nM}$, a mean dark time $\tau_{\text{D,mean}}^{\text{single}} = 57.1\,\text{s}$ (figure 6.9 b, see Methods in chapter 3.3.1) and $k_{\text{on}} = 3.5 \times 10^6\,\text{M}^{-1}\text{s}^{-1}$ were obtained for conventional DNA-PAINT, in broad agreement with previously reported values [18, 151].

qPAINT was first applied to a conventional DNA-PAINT experiment performed on beads simply decorated with the P1 docking sequence (black points in figure 6.9 d). For PD-PAINT, the experiment was repeated with beads featuring S1 and S2 as described above (red points in figure 6.9 d). A reduction of detected PD-PAINT sites as compared to the maximal capacity of biotin binding sites as measured by conventional DNA-PAINT was observed. Such a decrease is expected due to at least three factors:

(1) two biotin-binding sites, one occupied by S1 and the other by S2 are required to produce a single docking strand, resulting in a 50% decrease,

(2) among the pairs of binding sites the stochastic distribution of strands S1 and S2 reduces the number of S1-S2 pairs as compared to S1-S1 and S2-S2 to ~50 – 63% [182] of the total, corresponding to between 2 to 4 adjacent biotin binding sites being available for S1/S2 binding on a single streptavidin molecule.

(3) Finally, it has to be considered that ~50% of proximal S1-S2 pairs are dimerised when separated by ~2 nm.

Cumulatively, this would reduce the available imager binding sites to ~13% – 16% of those observed with conventional DNA-PAINT. Here, ~23 ± 9% was measured, in broad agreement with these considerations.

The considerations above show that when combining qPAINT with PD-PAINT, the estimation of the number of all proximal S1-S2 pairs is subject to the knowledge of the distance-dependent P1-P2 dimerisation probability. The most precise estimates can thus be obtained in cases where the distance between target epitopes is uniform throughout the sample or approximately known a priori, as for the case of biotin binding sites on streptavidin or proteins clustering in specific morphologies. In cases in which a broad distribution of epitope-distances is expected, as for example, in the case of nonspecific and random aggregates, our technique can provide a lower bound to the number of pairs, assuming a peak S1-S2 dimerisation probability of 60% (figure 6.2 a).

6.6 Multiplexed imaging by PD-PAINT

As a final application, it is shown that using the vast combinatorial space of DNA-sequence design, it is possible to design orthogonal imaging probes that, analogously to S1 and S2, expose different docking strands when in close proximity. Figure 6.10 demonstrates the use of spectral and temporal multiplexing to detect two different proximity-pair populations in the same sample. Based on this principle, a virtually unlimited number of distinct protein pairs can be detected within a single sample.

6.7 Increased nonspecific binding in biological samples

As shown in section 6.4 for PD-PAINT on biological samples, the signal, i.e. the number of binding events, detected from the proximity assay is typically considerably smaller than the typical signal detected in conventional DNA-PAINT. This is due to the limited probability of $\leq$60% open S1 loops in case of high S1/S2 proximity and additionally due to the number of S1/S2 complexes being limited by the labelling density of both S1 and S2 strands. Consequently, the number of nonspecific binding events, which is independent of the labelling density, can be of increased importance. Figure 6.11 shows the difference in nonspecific binding for different imager sequences in tissue sections. Qualitatively, differences in nonspecific binding with different imagers are already apparent in images of sections in which RyRs were labelled with docking strands. Aside from the expected localisations at z lines where RyR clusters are located, a more

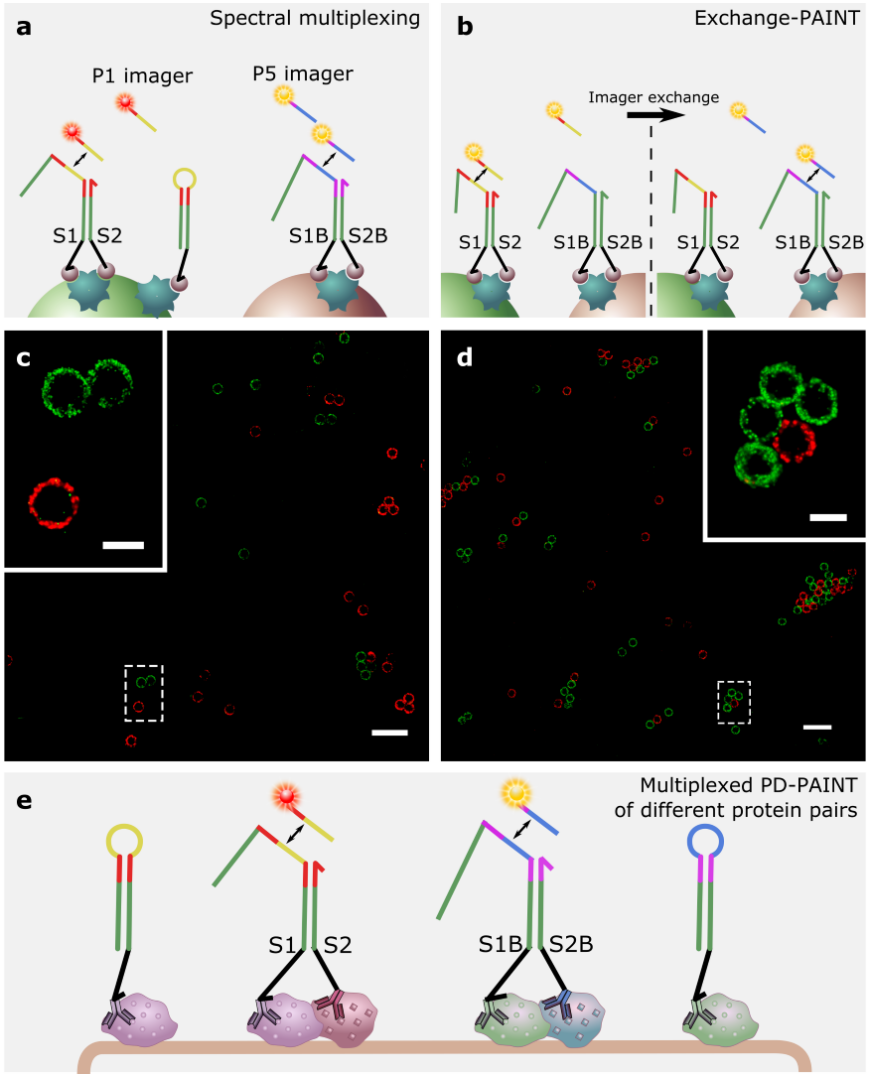

Figure 6.10: Multichannel PD-PAINT imaging of two populations of streptavidin-coated microparticles. Bead population 1 was labelled with biotinylated PD-PAINT strands S1 and S2 containing a P1 docking sequence (green), population 2 with S1B and S2B containing a P5 docking sequence (red). **(a)** Simultaneous imaging by spectral multiplexing, i.e. different imager sequences are labelled with dyes of different emission spectra. They are simultaneously excited by a single laser source but the detection path is spectrally split. For details on the optical setup see chapter 3.2 and Baddeley et al. [53]. Atto 655 is conjugated to imager P1, Atto 700 to imager P5. **(b)** Temporal multiplexing ("Exchange-PAINT"), both imagers are labelled with Atto 655 and imaged sequentially, for details see Jungmann et al. [20]. **(c)** Rendered image of PD-PAINT by spectral multiplexing. **(d)** Rendered image of PD-PAINT by Exchange-PAINT. **(e)** Proposed use of multiplexed PD-PAINT for imaging of different populations of protein pairs in the same sample. Scale bars: 2 µm, insets: 500 nm.

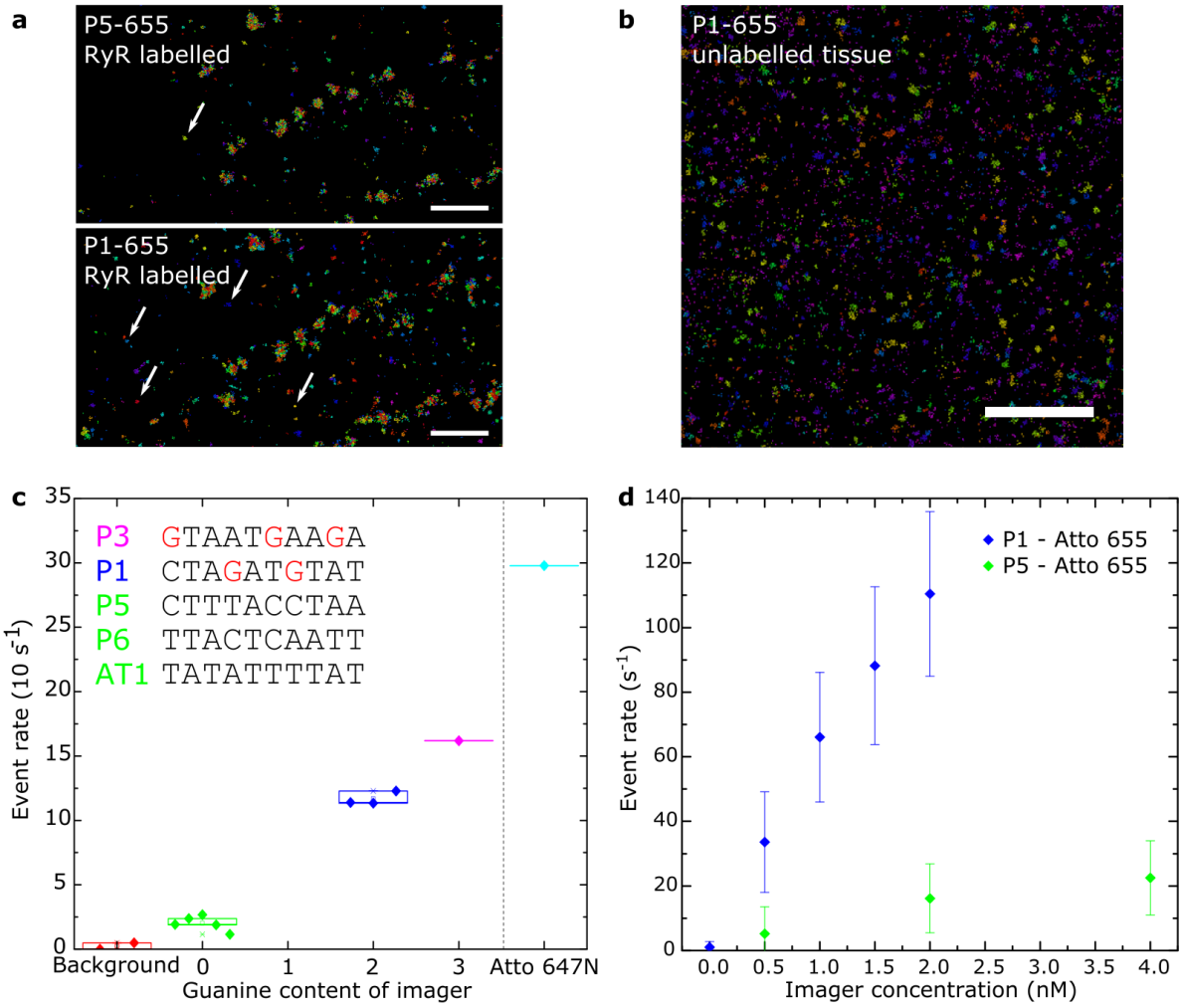

Figure 6.11: Increased nonspecific imager binding in biological samples. **(a)** Ryanodine receptor imaged in a cardiac tissue section, using imager sequence P5 (top) and P1 (bottom). Slightly increased background levels are observed for imager P1. Arrows pointing at a subset of suspected nonspecific binding events. **(b)** Localisation data in unlabelled, fixed porcine cardiac tissue section using imager sequence P1, modified with fluorophore Atto 655. **(c)** Rates of nonspecific imager binding events for imager sequences with different guanine content, and using a different dye modification (Atto 647N instead of Atto 655). **(d)** Nonspecific binding rates of P1 and P5 imager with Atto 655 in dependence of the imager concentration. As in c, higher nonspecific binding was observed for P1, but for both imagers the binding rate is roughly proportional to the imager concentration. Error bars showing standard deviation of number of binding events per second. Scale bars: 2 µm.

random pattern was observed across the whole image (figure 6.11 a). The relative prominence of the random pattern was more pronounced when using imager P1 vs imager P5.

In order to study purely nonspecific binding, a cardiac tissue section was treated in the same way as for immunolabelling, but without addition of the antibodies (see chapter 3.1.5). Localisation data which was recorded after addition of imager of sequence P1 is shown in figure 6.11 b. As may be expected, detected events were essentially homogeneously distributed, consistent with nonspecific imager binding. Figure 6.11 c shows the mean binding event rate in the absence of docking strands in tissue sections, using different imager sequences. In red, the detected event rate without addition of imagers is shown. Imager sequences were found to show similar event rates for equal content of guanine in the sequence. A lower guanine content (no guanine for P5, P6 and AT1, green) showed ~6× lower nonspecific binding compared to imager P1 (2 guanine), and ~8× lower than P3 (3 guanine), indicating a near linear relationship between guanine content of the imager and the level of nonspecific binding. Apart from guanine, using fluorophore Atto 647N instead of Atto 655 increased nonspecific binding considerably. In figure 6.11 d, the nonspecific binding for imager sequences P1 (blue) and P5 (green), both modified with Atto 655, was measured for different imager concentrations. It was found that the rate of nonspecific binding interactions scales proportionally with the imager concentration, similarly to the concentration dependence of specific imager-docking binding interactions as shown in chapter 4, figure 4.7. The effect described here was not observed with a microsphere test sample, which indicates that imagers with increased guanine content show an increased affinity to structures present only in the biological sample, e.g. any nonspecifically, single stranded DNA-binding proteins [183].

6.8 Discussion

In this chapter, Proximity-Dependent PAINT is presented, a technique which allows imaging of the distribution of protein pairs, or other biological targets in close proximity, with nanoscale resolution. As opposed to conventional multi-channel-imaging colocalisation techniques, proximity detection is decoupled from the imaging resolution, which is especially important in biological cell and tissue samples where the achievable resolution can vary greatly due to refractive index inhomogeneities and related optical challenges. Indeed, with PD-PAINT

the proximity range can be smaller than the imaging resolution which is a distinct advantage. A similar decoupling from imaging resolution can be achieved by a FRET-based assay, a fluorescent method that is distance sensitive in the nanometre range [184]. However, in contrast to FRET, PD-PAINT does not require specific dye pairs, eliminates the need for a more complex excitation and detection setup, and does not suffer from the effects of specific molecular orientations which can complicate the interpretation of FRET experiments. In addition, PD-PAINT can be efficiently multiplexed, a more challenging task with FRET based approaches.

It is shown that PD-PAINT is compatible with the complexities of biological environments by imaging different epitopes of primary antibodies and different epitopes of the ryanodine receptor, a large protein, in fixed cardiac tissue sections. Owing to the modularity of the DNA nanostructures used, PD-PAINT can be implemented relatively easily and with little penalty as an additional step in any Exchange-PAINT experiment [20]. With modern sensitive and affordable cameras (Exchange-) PD-PAINT is straightforward to implement on a conventional fluorescence microscope, the equipment required can be assembled from components with a relatively modest budget [185]. Additionally, the technique can be adapted to various marker types by conjugating the proximity-detection strands S1 and S2 directly to secondary antibodies, primary antibodies, aptamers and related emerging marker technologies.

Guided by quantitative numerical calculations, one could foresee design changes to the basic PD-PAINT machinery aimed at optimizing its performance in specific experimental settings. For example, one could fine tune the range of proximity-detectability. The PD-PAINT system could also be modified to sense the proximity of more than two targets, similarly to what has been previously shown for PLA [186].

Increasing the affinity between the imager and the S1 docking domain, e.g. by adjusting the CG/AT ratio or by extending the number of bases in the stem loop, in combination with an adjusted imager concentration, would enable a near-permanent labelling of open S1-loop structures with single imagers. In this configuration, the PD-PAINT machinery can be exploited to render other super-resolution imaging modalities proximity sensitive, such as STED, SIM, (d)STORM, (f)PALM, or even wide-field and confocal microscopy [13, 14, 32, 33, 36].

Finally, differences in nonspecific imager binding with dependence on base sequence and fluorophores were demonstrated, which is of particular interest for samples with potentially sparse labelling, such as PD-PAINT. In further implementations, the background in PD-PAINT could be reduced by integrating only docking sequences into the S1 loop which show minimised nonspecific binding of the respective imager. Additionally, the signal-to-background ratio and thus the imaging quality could be improved by schemes which reduce the background in DNA-PAINT, e.g. one which is explored in the following chapter. A moderate repetition of docking domains on a docking strand, such as the opened S1/S2 complex, increases the number of imager binding events without the need to increase the imager concentration. Thus, it equally increases the ratio of specific to nonspecific binding events.

7. Amplification of DNA-PAINT Signals

The quality of the data that can be obtained with DNA-PAINT and other single-molecule super-resolution techniques depends on several factors, such as the localisation precision of single emitters, compensation of sample drift and the labelling density [44, 187]. The localisation precision, in turn, depends on the signal-to-noise level, that is on the number of detected photons and on background levels, as shown in equation 2.5 [16]. The diffuse background originating from imager strands in solution, which is specific for DNA-PAINT, is typically reduced by imaging in total internal reflection fluorescence (TIRF) or near-TIRF (HILO) modes [3, 22, 63, 65].

Other methods for background reduction in DNA-PAINT have been published, e.g. by moderate levels of imager self-quenching if guanine is incorporated into the imager strand sequence [18] or by using Förster resonance energy transfer (FRET) [70, 188]. Additionally, the use of fluorescence quenchers has been proposed [168]. However, a quencher-based approach has not yet been successfully demonstrated and instead, in chapter 5 it is shown that the use of simple fluorescence quencher-based strands does not increase the single-to-noise ratio. While background reduction by FRET was demonstrated on DNA origami and in fixed cells, resolution was not shown to improve beyond results achieved by regular DNA-PAINT and considerably more complex optical and chemical systems are required [70, 188].

Here, more straightforward approaches for increased localisation precision by increasing the signal-to-noise ratio in DNA-PAINT are discussed. The signal, that is the photon number detected from a single binding event, can be increased with additional fluorophore-modifications on the imager. However, in this case

self-quenching of the fluorophores and guanine quenching can become more critical. The noise originating from fluorescence background, which is proportional to the imager concentration, can be reduced by using a docking strand which shows controlled, moderate repetition of single docking domains. This enables the use of lower imager concentrations without reducing the binding rates, which in turn leads to reduced fluorescence background.

7.1 Imager with additional fluorophore-modification

A straightforward way of increasing the number of fluorophores per imager is by adding a fluorophore-modification on both the 3' and 5' end, while leaving the imager sequence unchanged (imager 2iP1, figure 7.1 a). Imagers 2iP1 and P1 – the imager with equivalent sequence but only one fluorophore-modification at the 3' end – were successively imaged by Exchange-PAINT [20]. Imager performance was compared using the streptavidin-functionalised polystyrene microsphere test sample (see chapter 4) labelled with biotinylated P1 docking strands, and in biological cell samples in which microtubules in isolated cells and ryanodine receptors (RyR) in cardiac tissue sections were immunolabelled with P1 docking strands. In figure 7.1 b, the ratio of the mean number of photons in binding events using the 2iP1 imager to the mean number of photons using the regular P1 imager is shown for imaging rounds in different samples. On average, no detectable increase in mean photon number was observed for 2iP1. In fluorescence raw data, consistent with the event analysis, no obvious increase in brightness was observed (figure 7.1 c).

Whereas no increase in photon numbers was observed, the mean duration of 2iP1 imager binding events was observed to be twice that for the regular P1 imager (figure 7.1 d). Two factors may contribute to the increase in binding time:

(1) the additional fluorophore might increase the affinity of the imager and docking strands. A similar effect has been previously observed for fluorophore Cy3, with a significant increase in affinity [167]. Note that different dye chemistries complicate the direct comparison between Atto 655 and Cy3,

(2) as discussed in section 2.2.2 and shown in figure 4.8, the observed event time τ_F can be reduced to values below the imager binding time τ_{ds} if

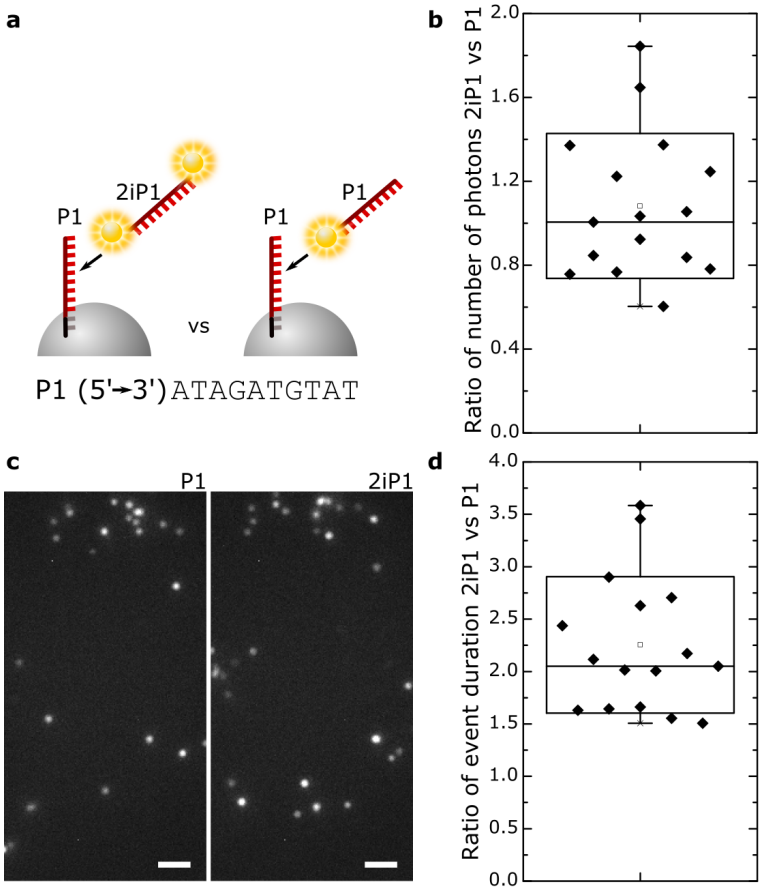

Figure 7.1: Comparison of imager with single to double fluorophore-modification. **(a)** Schematic drawing showing imagers 2iP1 and P1, sharing the same nucleotide sequence, but with an additional fluorophore attached to the 5' end for 2iP1. **(b)** Ratio of the mean number of photons for different experiments in biological samples and on microspheres, comparing the number of photons for 2iP1 with regular P1. **(c)** Example of raw data for P1 and 2iP1, showing little difference in intensity. **(d)** Comparison of the imager-docking binding event duration for experiments used in b. Ratio of event durations for 2iP1 vs P1. Scale bars: 2 µm.

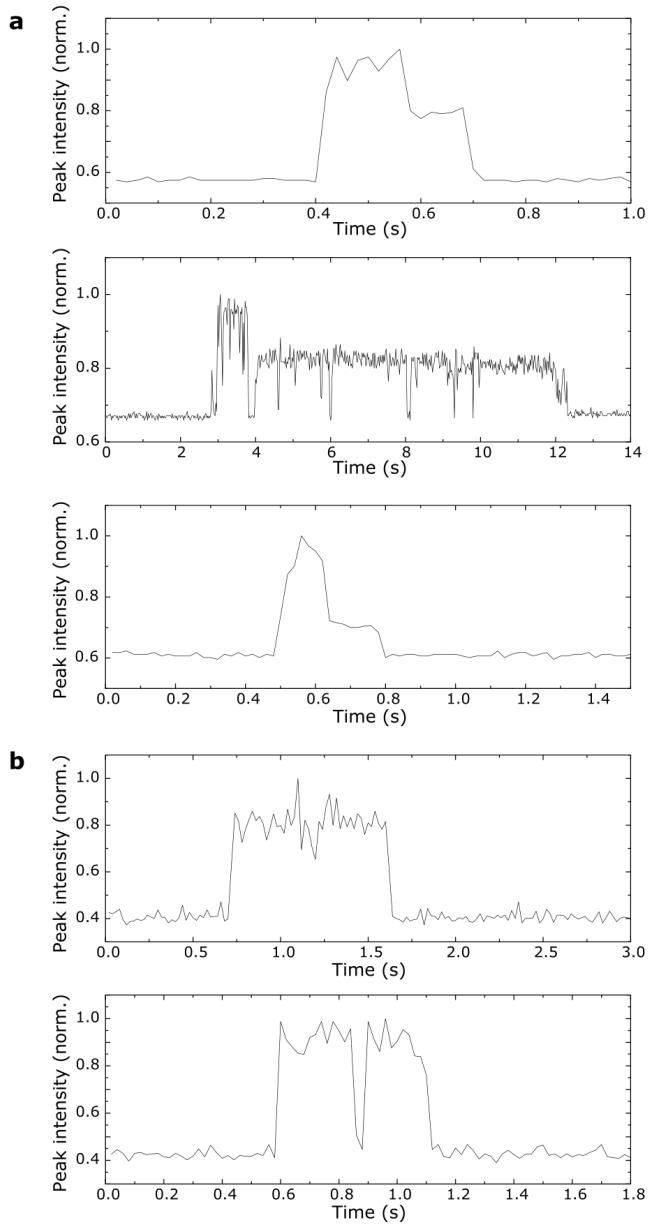

Figure 7.2: Examples of time traces of single imager binding showing step-like photobleaching of double-fluorophore imager. **(a)** Time traces of imager with two fluorophores 2iP1, showing stepwise photobleaching. **(b)** Regular single-fluorophore imager P1, no stepwise photobleaching was observed.

photobleaching times become sufficiently short. If it is assumed that photobleaching times are independently stochastically distributed for single fluorophores, then an imager with two fluorophores (2iP1) would exhibit an extended mean photobleaching time, leading to an extended observed event duration.

However, the samples were imaged at moderate illumination intensities, that is at ~30% of the maximum illumination intensity used in figure 4.9. Thus, it seems unlikely that factor 2, i.e. photobleaching, plays a significant role.

An indication that two fluorophores are present on 2iP1 can be obtained from analysis of individual intensity time traces. Shown in figure 7.2 a are several time traces using 2iP1 imager binding which show step-like decrease in intensity while bound. This can result from photobleaching of one of the two fluorophores, which would reduce the intensity to ~50%. While only a subset of blinking events show this behaviour, it was not observed for the regular P1 imager, which showed only characteristic on-off blinking behaviour (figure 7.2 b).

7.2 Intrinsic quenching of imager fluorescence in DNA-PAINT

The results described above for photon numbers of 2iP1 imager being lower than expected, raise the possibility of an increased fluorescence quenching effect in 2iP1. Guanine has been shown to lead to increased fluorescence quenching, and with Atto 655 being a strong electron acceptor it is specifically prone to quenching by the electron donor guanine [23, 189]. However, neither in the imager sequence directly, nor at the docking strand, is the additional 5'-modified fluorophore in higher proximity to guanine than the 3'-modified of the regular P1 imager.

A second effect which could result in reduced 2iP1 brightness are dye-dye interactions leading to self-quenching. Distance dependent studies on DNA origami have shown that self quenching becomes non-negligible for a range of Atto dyes at a distance of ~5 nm (not measured for Atto 655) [190, 191], for 2iP1 however, the dye-dye distance is only ~3 nm. Methods to reduce self-quenching at closer fluorophore proximity rely on strong electrostatic repulsion of fluorophores, improved by an asymmetric charge distribution [192, 193]. The use

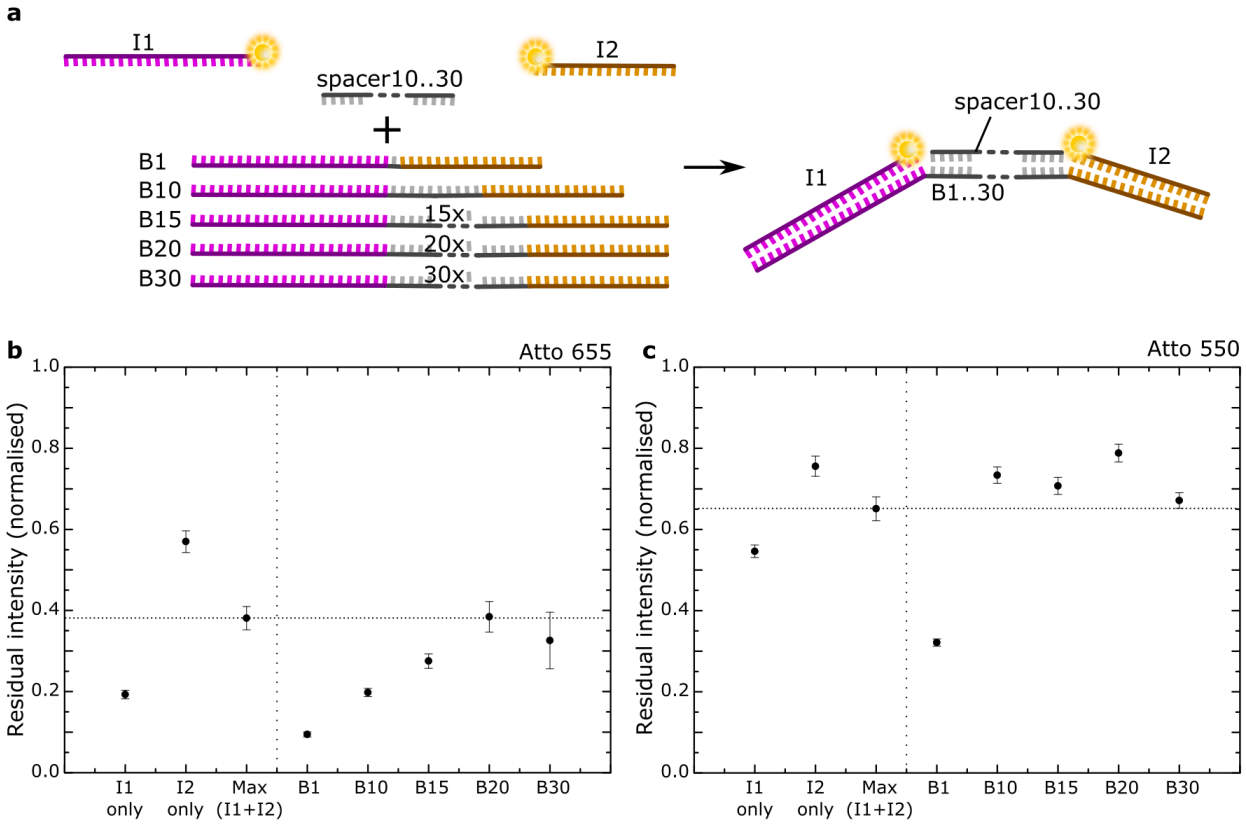

Figure 7.3: Quenching effects reducing imager brightness. **(a)** Schematic drawing, showing two orthogonal fluorophore-modified oligonucleotides (I1 pink, I2 orange) which are complementary to connecting connection strands B1,..., B30, with the number indicating the number of separating nucleotides (grey). The separation sequence can be stabilised by hybridisation of spacer strands. **(b),(c)** Fluorescence intensity ratio comparing intensity of strands B1...30 added stoichiometrically to I1 and I2 to intensity without added B1...30 for Atto 655 (b) and Atto 550 (c). The maximum expected value, given by the mean between I1 only and I2 only hybridising to the connection strands, is indicated as a dotted horizontal line. Error bars showing standard deviation between three repetitions of the experiment.

of those fluorophores for DNA-PAINT is problematic due to limited commercial availability and due to potentially increased nonspecific binding.

Quenching effects of Atto 655 and Atto 550 were studied as shown in figure 7.3 a. Two orthogonal oligonucleotides (I1, I2) were modified with the same fluorophore, on the 3' and 5' end, respectively. In solution, self-quenching should be negligible due to large mean distances between the dyes. The dye-dye distance can be controlled by adding a unmodified connection strand (B1...B30) to the solution stoichiometrically, ensuring that all I1 and I2 are permanently hybridised to a connector strand. For increased rigidity and thus a defined dye-dye distance, a spacer strand is added which hybridises to the domain between the I1 and I2 binding sites. Measurements were repeated three times, to reduce potential errors due to nonstochiometric mixing.

Figure 7.3 b shows the residual fluorescence intensity of Atto 655 in solution after addition of the connection strands, normalised to the intensity of single-stranded fluorophore-modified strands. If a connection strand is added to a solution containing only either I1 or I2, fluorescence is reduced by ~80% and ~45%, respectively, presumably due to the location of guanine in the connection strand directly next to the fluorophore (I1) and 1 nt away from the fluorophore (I2). This indicates that the presence of guanine in the docking strand sequence can affect the fluorophore brightness if it is positioned close to a dye molecule.

If strands I1, I2 and a connection strand are mixed stochiometrically and if I1 and I2 did not influence each other in terms of quenching, then a reduction of intensity by the mean value of individual I1 and I2 intensity reduction would be expected, indicated as Max(I1+I2) in figure 7.3. Any further intensity reduction can be attributed to an interaction between I1 and I2, e.g. to dye self-quenching. A total fluorescence reduction of 90% is observed when connection strand B1 is used, corresponding to a dye-dye distance of <1 nm, indicating that a strong self-quenching effect is present which reduces the intensity by ~75%. Increased fluorescence is observed for a distance of 10 nt (~3 nm) and 15 nt (~5 nm), with no fluorescence reduction observed at distances larger than 20 nt (~7 nm). In figure 7.3 c, equivalent measurements were done for Atto 550, with guanine quenching being significantly reduced compared to Atto 655, and self-quenching only observed at dye-dye distances of <1 nm.

In conclusion, the observed self-quenching effects for Atto 655 at dye-dye distances <7 nm could explain the lack of intensity increase observed for 2iP1 im-

ager, as shown above. Instead, an amplification of signal by using multiple fluorophores appears to be possible when using Atto 550, or if the dye-dye distance of Atto 655 can be increased to >7 nm.

7.3 Amplification of imager brightness

Increasing the dye-dye distance of a single imager with two fluorophore modifications is difficult due to the fixed overlap between imager and docking strand of 9 – 10 bp, resulting in a fixed length of the imager of approx. 3 nm. Adding non-interfering nucleotides to the imager would not increase the dye-dye distance to the necessary level, as the persistence length of single stranded DNA is more than an order of magnitude smaller than that of double stranded DNA which leads to formation of a tightly packed coil [194], and thus not to a controlled increase in dye-dye distance. Additional spacing of the imager which is stabilised by a double stranded region requires relatively long sequences for permanent binding of the stabiliser, as illustrated for a 3-fluorophore imager complex in figure 7.4 (design type I). Additionally, the fabrication of an oligonucleotide with multiple fluorophore modification is significantly more expensive than single fluorophore modifications.

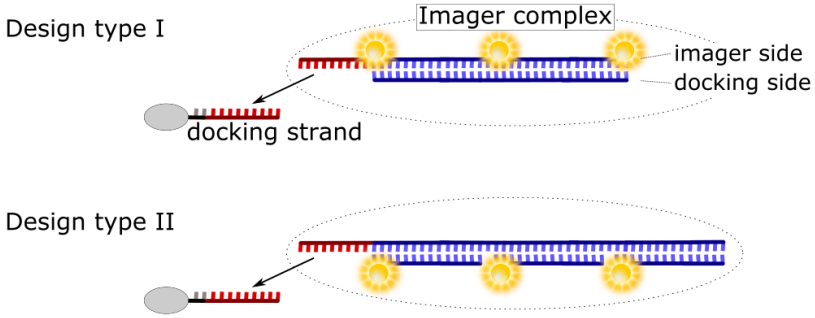

Figure 7.4: Designs for imager complexes with increased brightness by avoiding dye self-quenching. Design type I and type II are expected to yield equivalent brightness increase of the imager complex by a factor of 3, compared to a single-fluorophore imager. Type I is based on multiple internal dye-modification on a single strand (imager side), with spacing between dyes maintained by a stabilising strand (docking side). In type II, multiple dye-modified docking side strands permanently attach to the imager side of the imager complex.

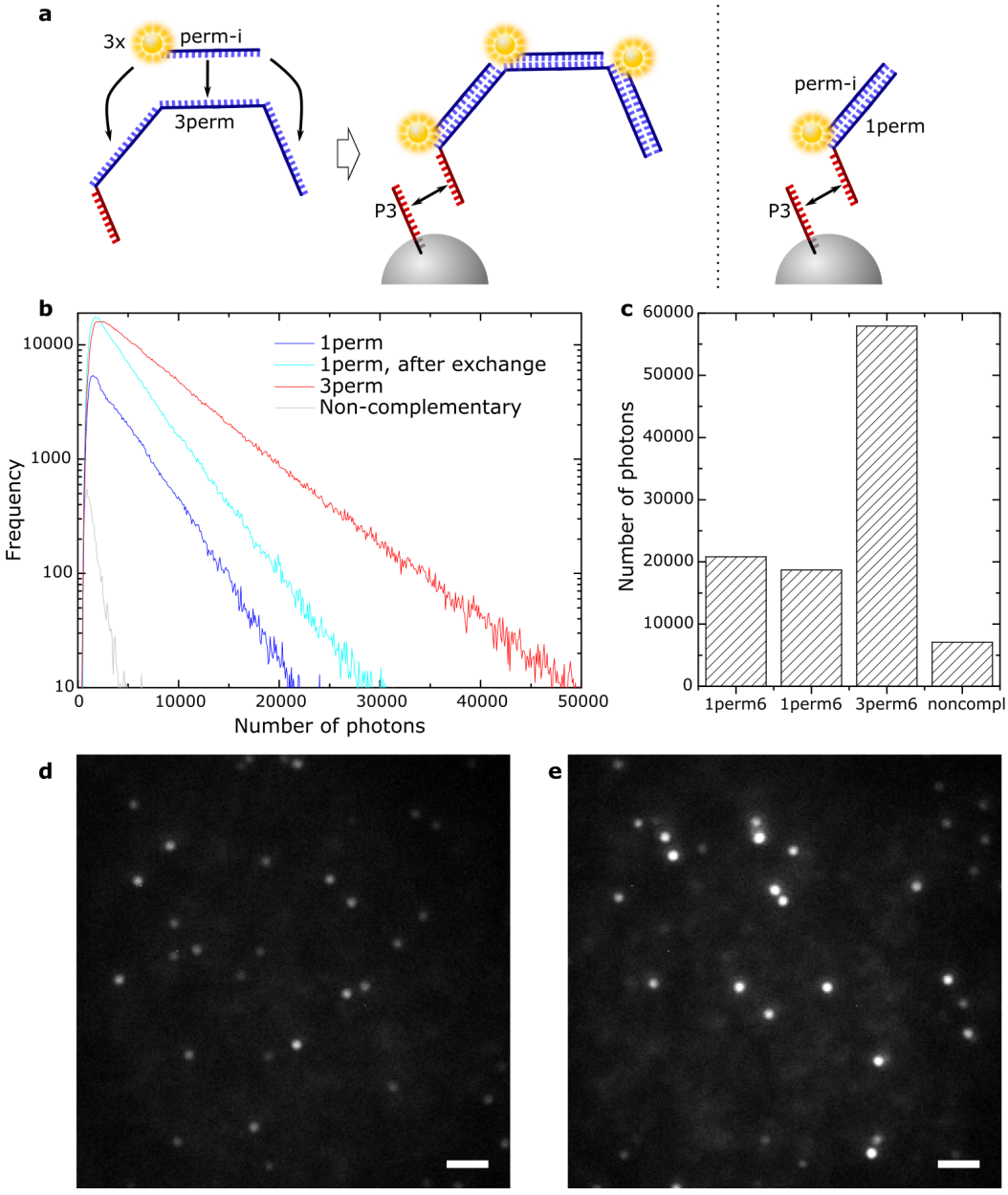

Figure 7.5: Increased photon number of three-fluorophore imager complex. **(a)** Schematic drawing showing an imager complex consisting of three fluorophore-modified strands (perm-i) near-permanently attached to a connecting strand (3perm), which contains a regular P3 imager domain for transient binding to a docking strand. The imager complex is compared to a second complex (perm-i and 1perm), containing a single fluorophore. **(b)** Distribution of number of photons per binding event for the 3 fluorophore complex (3perm) and two individual imaging rounds of the single-fluorophore complex (1perm). **(c)** Mean number of photons per binding event corresponding to b. **(d)** Raw fluorescence intensity data of 1perm binding events. **(e)** Raw data of 3perm binding events, using the same grey-scale as d. Scale bars 2 µm.

A more flexible design for an imager complex with multiple dyes is design type II (figure 7.4), its realisation when used with microspheres is shown in figure 7.5. A longer connecting strand (3perm) consists of three equal binding sites for a permanently binding fluorophore-modified strand (perm-i) and a single imager domain. With 17 nt, binding between 3perm and perm-i is effectively permanent. A Nupack analysis shows an equilibrium probability at relevant imager concentrations of >99.99% for a bound conformation of three perm-i to one 3perm connector. Strand perm-i was added at slight (1.5×) excess to ensure full hybridisation of all 3perm binding sites. The imager domain of 3perm is complementary to a 9 nt docking strand (P3), resulting in regular DNA-PAINT type binding of the imager complex to the docking strand. For comparison to a single-fluorophore imager with comparable imager-docking binding characteristics, an imager complex consisting of a connector strand with a single perm-i binding site (1perm) was used.

Figure 7.5 b shows the distribution of the number of photons per binding event, with mean photon numbers shown in figure 7.5 c. An amplification of photon numbers by a factor of ~3 can be observed for the 3perm imager complex (red) compared to the single-dye imager complex, with repeated imaging rounds separated by washing steps yield comparable photon numbers for the single-dye imager 1perm (blue, cyan). Binding events of both imager complexes show higher photon numbers than background blinking or from occasional nonspecific imager binding (here perm-i only) (grey). The increased photon numbers are visible directly in the raw fluorescence data, with figure 7.5 d showing a single frame using the 1perm complex and figure 7.5 e with the 3perm complex.

As shown in figure 4.7, the background fluorescence is proportional to the imager concentration, i.e. the concentration of fluorophores in solution. Therefore, additional fluorophores on imager complexes also increase the background fluorescence by the amplification factor A, if the same imager concentration is used, that is

$$\begin{aligned} N_{\text{ampl}} &= A \cdot N, \\ b^2_{\text{ampl}} &= A \cdot b^2, \end{aligned} \tag{7.1}$$

with the number of photons per event N and the number of background photons per pixel b^2 for single-fluorophore imagers, the subscript "ampl" denoting an amplified imager complex. Inserting equation 7.1 into equation 2.5 gives

an improvement of the amplified localisation precision Δx_{ampl} over the single-fluorophore localisation precision Δx of

$$\Delta x_{\text{ampl}} = \frac{1}{\sqrt{A}} \cdot \Delta x. \tag{7.2}$$

For a 3-dye imager complex, this would give a localisation precision which is ~58% of that of a single-dye imager. Here, the measured mean localisation error was reduced from 5.88 nm to 3.96 nm, corresponding to a localisation precision of 67% of the single-dye imager localisation precision. Thus, a clear improvement in localisation precision was observed; deviations from the expected value might be due to the localisation error's dependence on multiple different parameter estimates.

7.4 Amplification of imager-docking binding rate

Alternatively, or in addition to the amplification of fluorescence of a single imager, the signal-to-noise ratio of DNA-PAINT can be amplified by repetition of docking domains within a single docking strand. As shown in figure 7.6 a, microspheres were labelled with a regular docking strand P1, compared to microspheres labelled with docking strands 3xP1 and 6xP1, which consist of 3 or 6 repetitive P1 docking domains, respectively. As shown in previous chapters and publications for quantitative imaging, the imager binding rate scales linearly with the number of available docking sites. The number of docking sites on a microsphere can be measured by its qPAINT index [3, 21].

A qPAINT analysis comparing the amplified docking strands is shown in figure 7.6 b, with the qPAINT index being proportional to the inverse of the mean dark time $\tau_{D,mean}$ per microsphere, determined by fitting an exponential function to the dark time distribution (see chapters 3.3.2 and 4.3). Here, different populations of microspheres labelled with regular P1 (black), 3xP1 (red) and 6xP1 (blue) docking strands are imaged separately at equal imager concentration of 0.05 nM. The qPAINT index is approximately proportional to the number of binding sites, being ~3× higher for 3xP1 and ~6× higher for 6xP1 compared to P1. Additionally, the imager concentrations for 3xP1 and 6xP1 were reduced by a factor of 3 (0.016 nM) and 6 (0.0083 nM), respectively, and a qPAINT index comparable to the one obtained with the regular P1 at 0.05 nM imager concentration was measured. A sample containing a mixture of microsphere

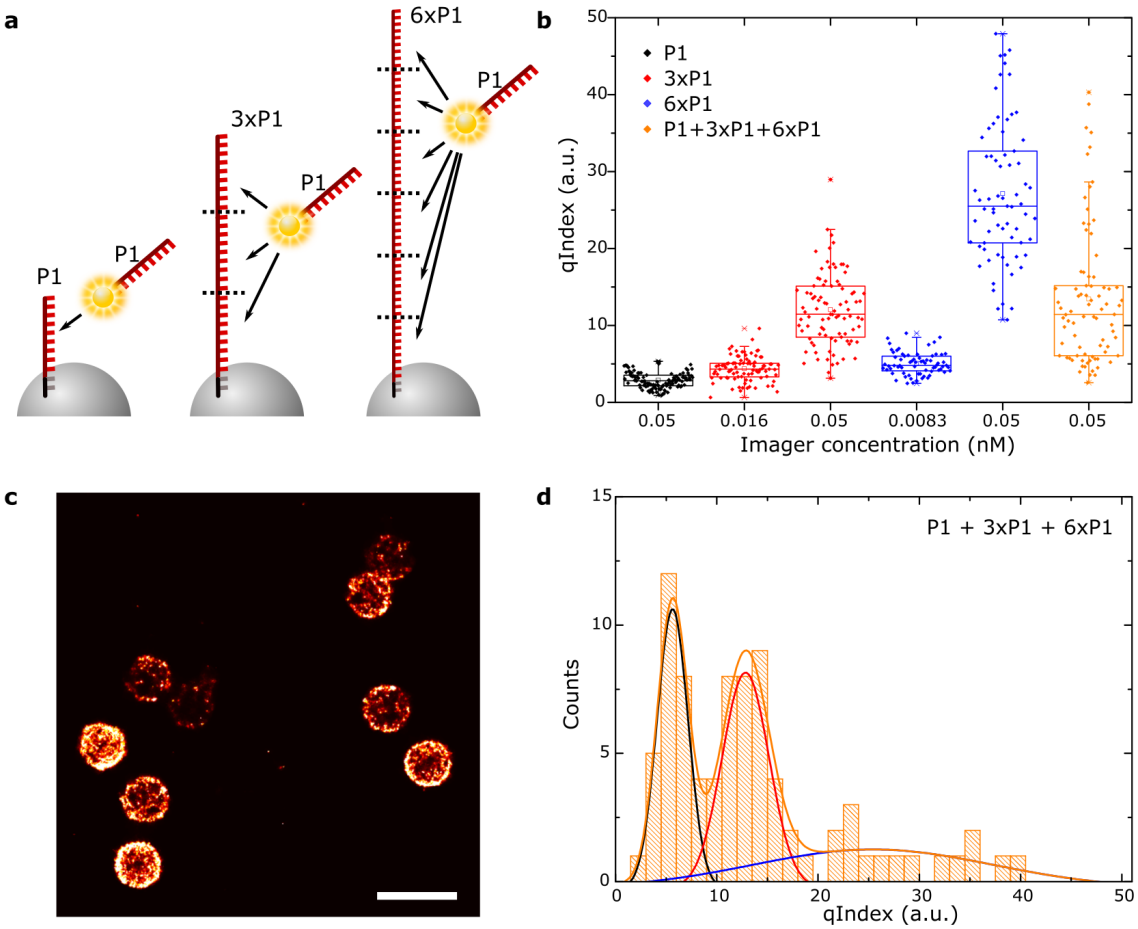

Figure 7.6: Increased binding event rate by docking strands with repeated docking domains. **(a)** Schematic drawing showing docking strands P1, 3xP1 and 6xP1 with 1, 3 and 6 equal docking domains. The same imager (P1) is used in all three cases, imaging microspheres. **(b)** qPAINT index of qPAINT anaylsis for docking strands P1 (black), 3xP1 (red), 6xP1 (blue) and a sample with a mixture of microspheres labelled with P1, 3xP1 and 6xP1 each (orange). **(c)** Rendered super-resolution image of local event density of microsphere mixture (b, orange), showing different populations of microspheres with different numbers of binding events. **(d)** Histogram of qPAINT index data shown in b, orange. Gaussian fits to three expected populations of microspheres. Scale bar: 1 µm.

populations labelled with the three docking strands and imaged using an imager concentration of 0.05 nM showed a distribution covering all previously observed qPAINT indices (orange). Figure 7.6 c shows the rendered image of the fluorescence event density, showing a broad range of event densities per microsphere, resulting from labelling with different docking strands P1, 3xP1 and 6xP1.

Consequently, the repetition of docking domains allows for an equal event density at concentrations which are reduced by the binding domain repeat factor (here 3 and 6) as compared to the reference concentration used with a single docking region per docking strand. The reduced imager concentrations directly reduce the background intensity and increase the signal-to-noise ratio, enabling a higher localisation precision. Additionally, the labelling with different binding domain repeat factors allows for multiplexed, simultaneous imaging using a single imager, as shown in figure 7.6 d. Here, a histogram of the qPAINT index distribution in figure 7.6 c (orange) shows multiple distinct peaks. The mean qPAINT index of the individual docking strands were determined from the individual distributions in figure 7.6 c, which allows for fitting of the three expected microsphere populations. Depending on the measured qPAINT index of a microsphere, it can be assigned to one of the three groups. A similar approach was very recently published by Wade et al. [163]. However, this method for multiplexing will fail if the number of docking sites in one cluster of binding events are not known a priori (here assumed to be constant for all microspheres), as a variation in the number of docking strands cannot be distinguished from a single docking strand with multiple docking domain repeats.

7.5 Discussion

In this chapter, different possibilities to increase the signal-to-noise ratio and with it the localisation precision in DNA-PAINT are discussed. A straightforward approach to increase the signal, i.e. the photon flux of binding events, by adding a second fluorophore-modification to a regular imager strand is shown to not be advantageous largely due to fluorescence quenching. Quenching effects are characterised for two commonly used fluorophores in DNA-PAINT, Atto 655 and Atto 550, indicating a strong guanine quenching if guanine is in high proximity to the dye. Similar effects have been described for a wide range of fluorophores [18, 189]. Additionally, a dye-dye distance for Atto 655 of up to ~5 nm reduces fluorescence emission noticeably due to significant self-quenching,

as has been shown previously for similar dyes [191]. Instead, the imager brightness, and thus the localisation precision, can be increased by assembly of an imager complex which consists of an imager domain for DNA-PAINT binding and of multiple domains for permanent binding of fluorophore-modified strands. Here, an amplification by a factor of three is shown.

The signal-to-noise ratio can further be increased by reducing the diffuse fluorescence background originating from unbound imager strands in solution. As discussed in chapters 4 and 5, the background is proportional to the imager concentration, however, a reduction in concentration equally reduces the imager binding rate and thus the detected signal. Here, it is shown that the binding rate can be maintained at reduced imager concentrations ($3-6\times$), if the sample is labelled with an extended docking strand consisting of $3-6$ repeated docking domains. Similarly, the use of a 3-fold repeated docking domain has been recently published for simultaneous multiplexed imaging [163], confirming the qPAINT anaylsis shown here. While these results seem to contradict similar experiments using extended docking strands shown in figure 4.15, chapter 4, the differences in base sequences have to be taken into account, with a P5 docking site potentially forming secondary structures and showing an inherently reduced imager binding rate.

In future experiments, it should be tested whether the extended docking strand leads to an increased blurring of detected imager binding events which could lead to reduced localisation precision. The length of a 6-fold repeated P1 domain docking strand is ~16 nm. However, due to single stranded DNA forming a tightly packed random coil [194], the effective mean distance of imager binding events to the target is presumably multiple times lower. In either case, these values fall below typically observed imaging resolutions and are consequently expected to be negligible for the localisation precision.

Furthermore, the ideas tested here on the microsphere assay are expected to be useful in biological samples. As shown in figure 6.11 d in the previous chapter, nonspecific binding is proportional to the imager concentration. Especially in sparsely labelled samples, e.g. in PD-PAINT, the binding rate amplification by docking domain repetition could increase the ratio of specific to nonspecific binding events considerably. Multiplexed imaging using repeated docking domains is also expected to be straightforward to implement, however, unwanted secondary structures of new docking strand designs should be excluded.

8. Conclusion and Outlook

Choosing from the wide range of imaging methods for a biomedical question requires careful consideration of the method's advantages and limitations. With sizes of most intracellular structures being far below the diffraction limit, optical super-resolution imaging has become increasingly popular for imaging biomolecule distributions within cells. One such technique, DNA-PAINT, is based on targets being labelled with oligonucleotides, which are then imaged via fluorescently labelled complementary strands. Typically, this limits DNA-PAINT to fixed, permeabilised samples which allow for (immuno-)labelling and for free diffusion of the fluorescent imager strands to the target. Additionally, detection of data points for sufficient sampling requires imaging over tens of minutes, further reducing its use for approaches such as live-cell imaging [59, 195].

However, compared to other super-resolution imaging techniques, DNA-PAINT has multiple advantages, namely the high specificity, freedom in the choice of fluorophore, straightforward implementation on a conventional fluorescence microscope without the need for complex optical setups, and most importantly the possibility to achieve high resolution through high photon yields [22]. Additionally, the flexibility in DNA design and independence from fluorophore characteristics allows for multiple modifications and variations of DNA-PAINT, such as straightforward multiplexed imaging (Exchange-PAINT) or quantitative imaging (qPAINT) [20, 21].

Recent publications related to DNA-PAINT often introduce new variations of imaging schemes [163, 196], but increasingly focus on its application for biological problems [3, 170, 197]. Consequently, there is the need to simplify the implementation for new users and introduce efficient methods for quality control, e.g. by developing test samples. This thesis is focused on the development and assessment of methods which make DNA-PAINT more accessible for new users and more straightforward to use, e.g. by introducing a new test assay

and a new process for time-multiplexed imaging, and on the optimisation of DNA-PAINT to achieve higher precision measurements, e.g. with the introduction of proximity-dependent PAINT for protein pairs and by increasing the signal-to-noise ratio of DNA-PAINT.

In chapter 4, DNA origami as a commonly used test sample is compared to a new approach based on functionalised microspheres. While DNA origami allow for DNA-PAINT docking strands to be placed with single nanometre precision, the samples require a relatively complex and expensive fabrication procedure and show only limited stability. Instead, fabrication of microsphere samples is straightforward, yet still shows highly mono-disperse structures for DNA-PAINT imaging and highly specific imager-docking binding. It is shown that multiple DNA-PAINT parameters can be optimised, such as the imager concentration, buffer conditions or illumination intensity. Additionally, limitations of the assay are described when comparing to biological applications and the microsphere assay is used for comparison of drift correction methods.

Using the microspheres, issues related to the estimation quality of the mean dark time used in qPAINT, which so far have only been vaguely described in literature [21, 83], are explored. It is shown, that a general solution which applies to all cases of DNA-PAINT is not feasible and that the quality of the exponential fit to the cumulative dark time distribution could be used to characterise the quality of the dark time approximation. In future implementations, methods to quantify the fit quality should be compared, possibly while even comparing in which cases a fit of the on-rates or a fit of the dark time density distribution yields more reliable results. With qPAINT measurements, particularly of sparsely labelled samples, requiring very long acquisition times (several hours for mean dark times of tens of seconds or higher), it might be recommended to use computer models of qPAINT characteristics for different cases as described in section 4.3. Further potential for advances of qPAINT lies in the exploration of labelling methods which allow for stoichiometric labelling, as this improves the comparison of the number of detected docking strands to the number of targets. All points mentioned in chapter 4 are vital for the characterisation of new DNA-PAINT modifications described in later chapters.

The microsphere assay is used for comparison of different approaches of optimised Exchange-PAINT imaging (chapter 5). Several methods for solution exchange are compared; pipetting in open-top chambers, the use of a fluidic handling system in combination with 3D printed imaging chambers and the

implementation of a fluorescence quencher-based competition resulting in suppression of imager-docking binding. This method, called Quencher-Exchange-PAINT is shown to allow rapid, low-crosstalk imager exchange in microsphere assays, as well as biological samples, with considerably decreased imaging times in samples with limited imager diffusion, e.g. thick tissue sections.

Equally demonstrated first on the microsphere assay and confirmed in biological samples, is a variation of DNA-PAINT which enables the super-resolution imaging of protein-protein pairs and other biological targets in high proximity (chapter 6). The technique, called Proximity-Dependent PAINT (PD-PAINT) is first characterised with extensive computational modelling, showing a strong distance-dependency of the DNA-PAINT signal on sub-10 nm proximity of the labels. Biotin-binding sites of streptavidin on the microsphere assay are imaged, as well as pairs of high-proximity secondary and primary antibodies. False positives are excluded by imaging of targets at larger distances and quantitative imaging is demonstrated, using the optimised qPAINT protocol as described above.

When characterising the role of quencher-modified strands in DNA-PAINT, as done in chapter 5, it becomes obvious that reduction of fluorescence background and thus an increase in localisation precision cannot be achieved by simple imager-quenching in solution. A proposed method of using FRET for reduced background suffers from a considerably more complex DNA interaction system which prevents the use of qPAINT [70, 195]. Alternative advanced approaches for increased signal-to-noise ratio are described in chapter 7. Using imagers with additional fluorophores is shown to be complicated by both dye self-quenching as well as guanine-quenching, but an increase in imager brightness can be achieved by use of larger imager complexes with multiple fluorophore modifications. An alternative option for the increase in signal-to-noise ratio is described, based on the moderate repetition of docking domains, enabling the use of lower imager concentrations while maintaining the imager-docking binding rate.

Both proposed ideas for an increased SNR should be validated in biological samples in future implementations. For imager strand complexes with multiple dyes, the increased size with rigid double-stranded components might suffer from limited diffusion in samples such as cardiac tissue sections, an effect which would not have been observed with the microsphere assay. To avoid a complex size increasing proportionally with the number of dyes, new designs for multi-dye imager complexes could be developed, e.g. a dye arrangement in tetrahedral or

star shape. The size of the extended docking strand structure with repeated docking domains is expected to be less critical, due to a single strand having a very short persistence length and the likely formation of a densely packed random coil. This expectation would ideally be confirmed in a sample allowing for high resolution measurements such as DNA origami. Additionally, an approach to quantify the effect of docking repeats in biological samples has to be developed, e.g. by labelling a sample with a certain repeat factor, then removing the repeat docking strand by toehold-mediated strand displacement [108] and subsequently re-labelling with a docking strand of a different repeat factor.

While the advances presented in this thesis should facilitate the implementation of DNA-PAINT and should make it of interest for new applications, there is still potential for considerable further improvement. An increasingly important challenge with improving resolution is the size of the labels used for DNA-PAINT. While antibodies used in this thesis provide high specificity, the use of a primary-secondary system extends to tens of nanometres, within the range of imaging resolution. Particularly for the highly distance-sensitive PD-PAINT, antibodies might limit the specificity of the technique. As a first step, PD-PAINT should be demonstrated with strands S1 and S2 directly conjugated to the primary antibodies. Preferably, smaller labels should be used for PD-PAINT and DNA-PAINT in future implementations, such as recently developed SOMAmers [59] if they provide the required affinity. In general, DNA-PAINT would greatly benefit from the development of labels which are smaller, more specific and allow for stoichiometric and efficient labelling.

In addition to the use with smaller labels, PD-PAINT may be considerably improved by combination with the schemes for higher signal-to-background ratio. Furthermore, the kinetic behaviour of the S1-S2 interaction should be better characterised and the scheme could be adjusted to allow for higher affinity of S1-S2 when in close proximity. This could possibly be achieved by introducing an additional "protection" strand, which prevents S1-S2 interaction during labelling steps, but can be removed once the strands are fixed in place in the sample. This way, a steep transition of interaction efficiency would even allow a tuning of the interaction distance and thus enable resolution-independent distance measurements on single-nanometre scale.

Even with the described methods for increased signal-to-noise ratio, the high fluorescence background is expected to still pose a major limitation of the technique. Apart from methods involving complex FRET interactions [70, 188], dy-

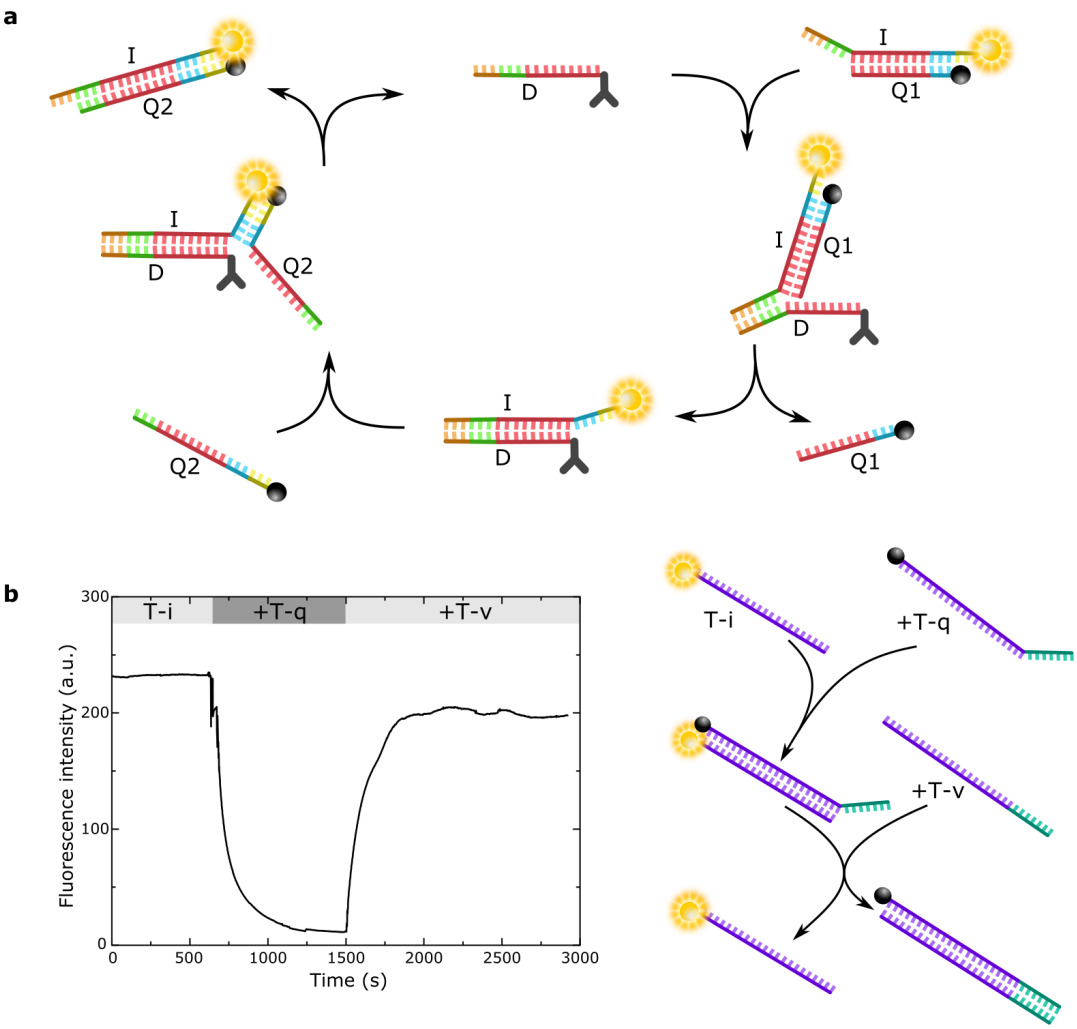

Figure 8.1: Advanced oligonucleotide interaction scheme for further background reduction of DNA-PAINT. **(a)** Schematic drawing showing an docking strand-cycling principle. The docking strand acts as a catalyst similarly described by Zhang et al. [198]. Imager strand I in solution is always hybridised to quencher strands Q1 and Q2, but can hybridise to and dissociate from the docking strand by toehold-mediated strand displacement. **(b)** Proof-of-principle experiment showing toehold-mediated strand replacement in solutions, similar to Zhang and Winfree [108]. Fluorescence remains constant if only fluorophore-modified strand T-i is in solution, but gets rapidly quenched upon addition of quencher-modified T-q. T-q has an additional toehold domain (green), which acts as an anchor for invading strand T-v, leading to dissociation of T-i and T-q by toehold-mediated strand replacement, detected as restored fluorescence after addition of T-v.

namic DNA interactions could be used for background-free DNA-PAINT. One potential implementation is shown in figure 8.1 a, based on a DNA catalysed reaction cycle published by Zhang et al. [198]. Here, the imager strand I in solution is hybridised to a quencher strand Q1, which reduces background. Via toehold-mediated strand replacement [108], the docking strand D binds to I and removes Q1. Subsequently, a second quencher strand Q2 can bind to I and remove it from D, making the docking strand available for repeated binding to new imager strands. Assuming the effective concentration of D is lower than that of the other strands, the on- and off-rates should depend on the concentrations of I and Q2. A proof-of-principle experiment showing the rates involved in toehold-mediated strand displacement is shown in figure 8.1 b. Here, a fluorophore-modified strand T-i is quenched by complementary strand T-q and fluorescence can be restored via toehold-mediated strand displacement using an invading strand T-v. The full scheme has not been tested yet and could potentially lead to leakages by direct replacement of Q1 by Q2. In that case, multiple other DNA interaction schemes could be used instead, e.g. catalytic hairpin assembly shown by Li et al. [199].

As shown previously, the concept of Exchange-PAINT, allowing for temporally multiplexed imaging with a change of labels during image acquisition, can be generalised to other imaging modalities such as STED, SIM or confocal imaging [74, 75]. Consequently, the techniques and methods presented in this thesis, in particular Quencher-Exchange-PAINT, PD-PAINT and the repeat of docking domains, could be easily applied to other imaging methods as well. Presumably, this would only require slight variations of the protocols, e.g. simulating permanent labelling with an increased imager affinity, the use of different strand concentrations or the use of washing buffers as proposed by Schueder et al. [75]. With the flexibility and possibilities of DNA nanotechnology offering potentially many more modifications of DNA-PAINT than presented in this thesis and above, and with the technique already achieving some of the highest resolutions in optical microscopy, the future is certainly bright for DNA-PAINT.

Bibliography

(1) Lutz, T.; Clowsley, A. H.; Lin, R.; Pagliara, S.; Michele, L. D.; Soeller, C. *Nano Res.* **2018**, 1–14.

(2) Lutz, T.; Kaufhold, W. T.; Clowsley, A. H.; Meletiou, A.; Michele, L. D.; Soeller, C. *bioRxiv* **2019**, 591081.

(3) Jayasinghe, I.; Clowsley, A. H.; Lin, R.; Lutz, T.; Harrison, C.; Green, E.; Baddeley, D.; Michele, L. D.; Soeller, C. *Cell Reports* **2018**, *22*, 557–567.

(4) Lin, R.; Clowsley, A. H.; Lutz, T.; Baddeley, D.; Soeller, C. *Methods* **2019**, DOI: `10.1016/j.ymeth.2019.05.018`.

(5) The Nobel Prize in Chemistry 2014. `https://www.nobelprize.org/prizes/chemistry/2014/summary/` (accessed 02/05/2019).

(6) Abbe, E. *Archiv f. mikrosk. Anatomie* **1873**, *9*, 413–418.

(7) Takayanagi, K.; Kim, S.; Lee, S.; Oshima, Y.; Tanaka, T.; Tanishiro, Y.; Sawada, H.; Hosokawa, F.; Tomita, T.; Kaneyama, T.; Kondo, Y. *J Electron Microsc (Tokyo)* **2011**, *60 Suppl 1*, S239–244.

(8) Cosslett, V. E.; Nixon, W. C., *X-Ray Microscopy*; Cambridge University Press: 2014; 455 pp.

(9) Pawley, J. B., *Handbook of Biological Confocal Microscopy*, 3rd; Springer Science+Business Media: New York, 2006.

(10) Gustafsson, M. G. L. *Journal of Microscopy* **2000**, *198*, 82–87.

(11) Hell, S.; Stelzer, E. H. *JOSA A* **1992**, *9*, 2159–2166.

(12) Gustafsson, M. G. L. *Proceedings of the National Academy of Sciences of the United States of America* **2005**, *102*, 13081.

(13) Hell, S. W.; Wichmann, J. *Optics letters* **1994**, *19*, 780–782.

(14) Betzig, E.; Patterson, G. H.; Sougrat, R.; Lindwasser, O. W.; Olenych, S.; Bonifacino, J. S.; Davidson, M. W.; Lippincott-Schwartz, J.; Hess, H. F. *Science* **2006**, *313*, 1642–1645.

(15) Rust, M. J.; Bates, M.; Zhuang, X. *Nature Methods* **2006**, *3*, 793–796.

(16) Mortensen, K. I.; Churchman, L. S.; Spudich, J. A.; Flyvbjerg, H. *Nature Methods* **2010**, *7*, 377–381.

(17) Sharonov, A.; Hochstrasser, R. M. *Proc Natl Acad Sci U S A* **2006**, *103*, 18911–18916.

(18) Jungmann, R.; Steinhauer, C.; Scheible, M.; Kuzyk, A.; Tinnefeld, P.; Simmel, F. C. *Nano Lett.* **2010**, *10*, 4756–4761.

(19) Rothemund, P. W. K. *Nature* **2006**, *440*, 297–302.

(20) Jungmann, R.; Avendaño, M. S.; Woehrstein, J. B.; Dai, M.; Shih, W. M.; Yin, P. *Nat Meth* **2014**, *11*, 313–318.

(21) Jungmann, R.; Avendaño, M. S.; Dai, M.; Woehrstein, J. B.; Agasti, S. S.; Feiger, Z.; Rodal, A.; Yin, P. *Nat Meth* **2016**, *13*, 439–442.

(22) Schnitzbauer, J.; Strauss, M. T.; Schlichthaerle, T.; Schueder, F.; Jungmann, R. *Nat. Protocols* **2017**, *12*, 1198–1228.

(23) ATTO-TEC GmbH - ATTO 655. `https://www.atto-tec.com/` (accessed 02/07/2019).

(24) Johnson, I. D., *Molecular Probes Handbook: A Guide to Fluorescent Probes and Labeling Technologies*; Life Technologies Corporation: 2010; 1060 pp.

(25) Zhao, Q.; Young, I. T.; de Jong, J. G. S. *JBO* **2011**, *16*, 086007.

(26) Pendry, J. B. *Phys. Rev. Lett.* **2000**, *85*, 3966–3969.

(27) Rayleigh, L. *The London, Edinburgh, and Dublin Philosophical Magazine and Journal of Science* **1879**, *8*, 261–274.

(28) Ash, E. A.; Nicholls, G. *Nature* **1972**, *237*, 510–512.

(29) Weisenburger, S.; Boening, D.; Schomburg, B.; Giller, K.; Becker, S.; Griesinger, C.; Sandoghdar, V. *Nature Methods* **2017**, *14*, 141–144.

(30) Hell, S. W. *Nature Methods* **2009**, *6*, 24–32.

(31) Eggeling, C.; Willig, K. I.; Sahl, S. J.; Hell, S. W. *Quarterly Reviews of Biophysics* **2015**, *48*, 178–243.

(32) Heilemann, M.; van de Linde, S.; Schüttpelz, M.; Kasper, R.; Seefeldt, B.; Mukherjee, A.; Tinnefeld, P.; Sauer, M. *Angewandte Chemie International Edition* **2008**, *47*, 6172–6176.

(33) Hess, S. T.; Girirajan, T. P. K.; Mason, M. D. *Biophysical Journal* **2006**, *91*, 4258–4272.

(34) Hofmann, M.; Eggeling, C.; Jakobs, S.; Hell, S. W. *PNAS* **2005**, *102*, 17565–17569.

(35) Hell, S. W. *Nat Biotech* **2003**, *21*, 1347–1355.

(36) Bailey, B.; Farkas, D. L.; Taylor, D. L.; Lanni, F. *Nature* **1993**, *366*, 44–48.

(37) Huang, B. *Current Opinion in Chemical Biology* **2010**, *14*, 10–14.

(38) Tortarolo, G.; Sun, Y.; Teng, K.-W.; Ishitsuka, Y.; Lanzanó, L.; Selvin, P. R.; Barbieri, B.; Diaspro, A.; Vicidomini, G. *bioRxiv* **2018**, 408286.

(39) Sage, D.; Kirshner, H.; Pengo, T.; Stuurman, N.; Min, J.; Manley, S.; Unser, M. *Nature Methods* **2015**, *12*, 717–724.

(40) Baddeley, D.; Jayasinghe, I. D.; Cremer, C.; Cannell, M. B.; Soeller, C. *Biophysical Journal* **2009**, *96*, L22–L24.

(41) Fölling, J.; Bossi, M.; Bock, H.; Medda, R.; Wurm, C. A.; Hein, B.; Jakobs, S.; Eggeling, C.; Hell, S. W. *Nature Methods* **2008**, *5*, 943–945.

(42) Berning, S.; Willig, K. I.; Steffens, H.; Dibaj, P.; Hell, S. W. *Science* **2012**, *335*, 551–551.

(43) Rittweger, E.; Han, K. Y.; Irvine, S. E.; Eggeling, C.; Hell, S. W. *Nature Photonics* **2009**, *3*, 144–147.

(44) Legant, W. R.; Shao, L.; Grimm, J. B.; Brown, T. A.; Milkie, D. E.; Avants, B. B.; Lavis, L. D.; Betzig, E. *Nat Meth* **2016**, *13*, 359–365.

(45) Banterle, N.; Bui, K. H.; Lemke, E. A.; Beck, M. *Journal of Structural Biology* **2013**, *183*, 363–367.

(46) Fox-Roberts, P.; Marsh, R.; Pfisterer, K.; Jayo, A.; Parsons, M.; Cox, S. *Nature Communications* **2017**, *8*, 13558.

(47) Balzarotti, F.; Eilers, Y.; Gwosch, K. C.; Gynnå, A. H.; Westphal, V.; Stefani, F. D.; Elf, J.; Hell, S. W. *Science* **2017**, *355*, 606–612.

(48) Huang, B.; Wang, W.; Bates, M.; Zhuang, X. *Science* **2008**, *319*, 810–813.

(49) Lee, H.-l. D.; Sahl, S. J.; Lew, M. D.; Moerner, W. E. *Applied Physics Letters* **2012**, *100*, 153701.

(50) Baddeley, D.; Cannell, M. B.; Soeller, C. *Nano Res.* **2011**, *4*, 589–598.

(51) Juette, M. F.; Gould, T. J.; Lessard, M. D.; Mlodzianoski, M. J.; Nagpure, B. S.; Bennett, B. T.; Hess, S. T.; Bewersdorf, J. *Nat Meth* **2008**, *5*, 527–529.

(52) Bates, M.; Huang, B.; Dempsey, G. T.; Zhuang, X. *Science* **2007**, *317*, 1749–1753.

(53) Baddeley, D.; Crossman, D.; Rossberger, S.; Cheyne, J. E.; Montgomery, J. M.; Jayasinghe, I. D.; Cremer, C.; Cannell, M. B.; Soeller, C. *PLOS ONE* **2011**, *6*, e20645.

(54) Hell, S. W. et al. *J. Phys. D: Appl. Phys.* **2015**, *48*, 443001.

(55) Giannone, G.; Hosy, E.; Levet, F.; Constals, A.; Schulze, K.; Sobolevsky, A. I.; Rosconi, M. P.; Gouaux, E.; Tampé, R.; Choquet, D.; Cognet, L. *Biophysical Journal* **2010**, *99*, 1303–1310.

(56) Kiuchi, T.; Higuchi, M.; Takamura, A.; Maruoka, M.; Watanabe, N. *Nature Methods* **2015**, *12*, 743–746.

(57) Chen, J.; Bremauntz, A.; Kisley, L.; Shuang, B.; Landes, C. F. *ACS Appl. Mater. Interfaces* **2013**, *5*, 9338–9343.

(58) Beliveau, B. J. et al. *Nat Commun* **2015**, *6*, 7147.

(59) Strauss, S.; Nickels, P. C.; Strauss, M. T.; Sabinina, V. J.; Ellenberg, J.; Carter, J. D.; Gupta, S.; Janjic, N.; Jungmann, R. *Nature Methods* **2018**, *15*, 685–688.

(60) Raab, M.; Schmied, J. J.; Jusuk, I.; Forthmann, C.; Tinnefeld, P. *ChemPhysChem* **2014**, *15*, 2431–2435.

(61) Lukacs, G. L.; Haggie, P.; Seksek, O.; Lechardeur, D.; Freedman, N.; Verkman, A. S. *J. Biol. Chem.* **2000**, *275*, 1625–1629.

(62) Kuriyan, J.; Konforti, B.; Wemmer, D., *The Molecules of Life: Physical and Chemical Principles: Physical Principles and Cellular Dynamics*, 1 edition; Garland Science: New York, NY, 2012; 512 pp.

(63) Axelrod, D. *The Journal of Cell Biology* **1981**, *89*, 141–145.

(64) Fish, K. N. *Current Protocols in Cytometry* **2009**, *50*, 12.18.1–12.18.13.

(65) Tokunaga, M.; Imamoto, N.; Sakata-Sogawa, K. *Nature Methods* **2008**, *5*, 159–161.

(66) Sanderson, M. J.; Smith, I.; Parker, I.; Bootman, M. D. *Cold Spring Harb Protoc* **2014**, *2014*, 071795.

(67) Mücksch, J.; Blumhardt, P.; Strauss, M. T.; Petrov, E. P.; Jungmann, R.; Schwille, P. *Nano Lett.* **2018**, *18*, 3185–3192.

(68) Iinuma, R.; Ke, Y.; Jungmann, R.; Schlichthaerle, T.; Woehrstein, J. B.; Yin, P. *Science* **2014**, *344*, 65–69.

(69) Schueder, F.; Lara-Gutiérrez, J.; Beliveau, B. J.; Saka, S. K.; Sasaki, H. M.; Woehrstein, J. B.; Strauss, M. T.; Grabmayr, H.; Yin, P.; Jungmann, R. *Nature Communications* **2017**, *8*, 2090.

(70) Auer, A.; Strauss, M. T.; Schlichthaerle, T.; Jungmann, R. *Nano Lett.* **2017**, *17*, 6428–6434.

(71) Johnson-Buck, A.; Nangreave, J.; Kim, D.-N.; Bathe, M.; Yan, H.; Walter, N. G. *Nano Lett.* **2013**, *13*, 728–733.

(72) Tam, J.; Cordier, G. A.; Borbely, J. S.; Álvarez, Á. S.; Lakadamyali, M. *PLOS ONE* **2014**, *9*, e101772.

(73) Annibale, P.; Scarselli, M.; Greco, M.; Radenovic, A. *Optical Nanoscopy* **2012**, *1*, 9.

(74) Beater, S.; Holzmeister, P.; Lalkens, B.; Tinnefeld, P. *Opt. Express, OE* **2015**, *23*, 8630–8638.

(75) Schueder, F.; Strauss, M. T.; Hoerl, D.; Schnitzbauer, J.; Schlichthaerle, T.; Strauss, S.; Yin, P.; Harz, H.; Leonhardt, H.; Jungmann, R. *Angew. Chem. Int. Ed.* **2017**, *56*, 4052–4055.

(76) Cattoni, D. I.; Fiche, J.-B.; Valeri, A.; Mignot, T.; Nöllmann, M. *PLoS One* **2013**, *8*, e76268.

(77) Sograte-Idrissi, S.; Oleksiievets, N.; Isbaner, S.; Eggert-Martinez, M.; Enderlein, J.; Tsukanov, R.; Opazo, F. *Cells* **2019**, *8*, 48.

(78) Lu, C.-H.; Pégard, N. C.; Fleischer, J. W. *Applied Physics Letters* **2013**, *102*, 161115.

(79) Tam, J.; Cordier, G. A.; Bálint, Š.; Sandoval Álvarez, Á.; Borbely, J. S.; Lakadamyali, M. *PLoS ONE* **2014**, *9*, e115512.

(80) Bell, L.; Seshia, A.; Lando, D.; Laue, E.; Palayret, M.; Lee, S. F.; Klenerman, D. *Sensors and Actuators B: Chemical* **2014**, *192*, 36–41.

(81) Dempsey, G. T.; Vaughan, J. C.; Chen, K. H.; Bates, M.; Zhuang, X. *Nat Meth* **2011**, *8*, 1027–1036.

(82) Nieuwenhuizen, R. P. J.; Bates, M.; Szymborska, A.; Lidke, K. A.; Rieger, B.; Stallinga, S. *PLOS ONE* **20-May-2015**, *10*, e0127989.

(83) Baker, M.; Nieves, D. J.; Hilzenrat, G.; Berengut, J. F.; Gaus, K.; Lee, L. K. *bioRxiv* **2019**, 525345.

(84) Blumhardt, P.; Stein, J.; Mücksch, J.; Stehr, F.; Bauer, J.; Jungmann, R.; Schwille, P. *Molecules* **2018**, *23*, 3165.

(85) Fricke, F.; Beaudouin, J.; Eils, R.; Heilemann, M. *Scientific Reports* **2015**, *5*, 14072.

(86) Alberts, B.; Johnson, A.; Lewis, J.; Raff, M.; Roberts, K.; Walter, P., *Molecular Biology of the Cell*, 4th; Garland Science: 2002.

(87) In *Wikipedia*, Page Version ID: 884526381, 2019.

(88) Richmond, T. J.; Davey, C. A. *Nature* **2003**, *423*, 145–150.

(89) Drew, H. R.; Wing, R. M.; Takano, T.; Broka, C.; Tanaka, S.; Itakura, K.; Dickerson, R. E. *Proc.Natl.Acad.Sci.USA* **1981**, *78*, 2179–2183.

(90) Watson, J. D.; Crick, F. H. *Nature* **1953**, *171*, 737–738.

(91) Yakovchuk, P.; Protozanova, E.; Frank-Kamenetskii, M. D. *Nucleic Acids Res* **2006**, *34*, 564–574.

(92) Opazo, F.; Rizzoli, S.; Schauen, M. **2013**.

(93) Wong, K.-Y.; Pettitt, B. M. *Biophys J* **2008**, *95*, 5618–5626.

(94) SantaLucia, J.; Hicks, D. *Annual Review of Biophysics and Biomolecular Structure* **2004**, *33*, 415–440.

(95) Marmur, J.; Doty, P. *Journal of Molecular Biology* **1962**, *5*, 109–118.

(96) Breslauer, K. J.; Frank, R.; Blöcker, H.; Marky, L. A. *PNAS* **1986**, *83*, 3746–3750.

(97) Oligo Analyzer. `https://www.idtdna.com/calc/analyzer` (accessed 02/16/2019).

(98) Madsen, M.; Gothelf, K. V. *Chem. Rev.* **2019**, *119*, 6384–6458.

(99) Seeman, N. C. *Journal of Theoretical Biology* **1982**, *99*, 237–247.

(100) Holliday, R. *Genetics Research* **1964**, *5*, 282–304.

(101) Seeman, N. C.; Sleiman, H. F. *Nature Reviews Materials* **2018**, *3*, 17068.

(102) Douglas, S. M.; Marblestone, A. H.; Teerapittayanon, S.; Vazquez, A.; Church, G. M.; Shih, W. M. *Nucleic Acids Res* **2009**, *37*, 5001–5006.

(103) Knudsen, J. B. et al. *Nat Nano* **2015**, *10*, 892–898.

(104) Simmel, F. C.; Yurke, B.; Singh, H. R. *Chem. Rev.* **2019**, *119*, 6326–6369.

(105) Reynaldo, L. P.; Vologodskii, A. V.; Neri, B. P.; Lyamichev, V. I. *Journal of Molecular Biology* **2000**, *297*, 511–520.

(106) Srinivas, N.; Ouldridge, T. E.; Šulc, P.; Schaeffer, J. M.; Yurke, B.; Louis, A. A.; Doye, J. P. K.; Winfree, E. *Nucleic Acids Res* **2013**, *41*, 10641–10658.

(107) Li, F.; Tang, Y.; Traynor, S. M.; Li, X.-F.; Le, X. C. *Anal. Chem.* **2016**, *88*, 8152–8157.

(108) Zhang, D. Y.; Winfree, E. *J. Am. Chem. Soc.* **2009**, *131*, 17303–17314.

(109) Ouldridge, T. E.; Šulc, P.; Romano, F.; Doye, J. P. K.; Louis, A. A. *Nucleic Acids Res* **2013**, *41*, 8886–8895.

(110) Fredriksson, S.; Gullberg, M.; Jarvius, J.; Olsson, C.; Pietras, K.; Gústafsdóttir, S. M.; Östman, A.; Landegren, U. *Nature Biotechnology* **2002**, *20*, 473–477.

(111) Gullberg, M.; Gústafsdóttir, S. M.; Schallmeiner, E.; Jarvius, J.; Bjarnegård, M.; Betsholtz, C.; Landegren, U.; Fredriksson, S. *PNAS* **2004**, *101*, 8420–8424.

(112) Söderberg, O.; Gullberg, M.; Jarvius, M.; Ridderstråle, K.; Leuchowius, K.-J.; Jarvius, J.; Wester, K.; Hydbring, P.; Bahram, F.; Larsson, L.-G.; Landegren, U. *Nature Methods* **2006**, *3*, 995–1000.

(113) Koos, B. et al. *Nature Communications* **2015**, *6*, 7294.

(114) Jones, S.; Thornton, J. M. *PNAS* **1996**, *93*, 13–20.

(115) Söderberg, O.; Leuchowius, K.-J.; Gullberg, M.; Jarvius, M.; Weibrecht, I.; Larsson, L.-G.; Landegren, U. *Methods* **2008**, *45*, 227–232.

(116) Mocanu, M.-M.; Váradi, T.; Szöllősi, J.; Nagy, P. *PROTEOMICS* **2011**, *11*, 2063–2070.

(117) Dirks, R. M.; Pierce, N. A. *PNAS* **2004**, *101*, 15275–15278.

(118) Ikbal, J.; Lim, G. S.; Gao, Z. *TrAC Trends in Analytical Chemistry* **2015**, *64*, 86–99.

(119) Koos, B.; Andersson, L.; Clausson, C.-M.; Grannas, K.; Klaesson, A.; Cane, G.; Söderberg, O. In *High-Dimensional Single Cell Analysis: Mass Cytometry, Multi-Parametric Flow Cytometry and Bioinformatic Techniques*, Fienberg, H. G., Nolan, G. P., Eds.; Current Topics in Microbiology and Immunology; Springer Berlin Heidelberg: Berlin, Heidelberg, 2014, pp 111–126.

(120) Agasti, S. S.; Wang, Y.; Schueder, F.; Sukumar, A.; Jungmann, R.; Yin, P. *Chem. Sci.* **2017**, *8*, 3080–3091.

(121) Vicidomini, G.; Schönle, A.; Ta, H.; Han, K. Y.; Moneron, G.; Eggeling, C.; Hell, S. W. *PLoS ONE* **2013**, *8*, ed. by Chirico, G., e54421.

(122) Zhuang, X. *Nat Photonics* **2009**, *3*, 365–367.

(123) Frost, N. A.; Shroff, H.; Kong, H.; Betzig, E.; Blanpied, T. A. *Neuron* **2010**, *67*, 86–99.

(124) Xu, K.; Babcock, H. P.; Zhuang, X. *Nature Methods* **2012**, *9*, 185–188.

(125) Vaughan, J. C.; Jia, S.; Zhuang, X. *Nature Methods* **2012**, *9*, 1181–1184.

(126) Schlichthaerle, T.; Ganji, M.; Auer, A.; Wade, O. K.; Jungmann, R. *ChemBioChem* **2018**, *20*, 1032–1038.

(127) Crossman, D. J.; Shen, X.; Jüllig, M.; Munro, M.; Hou, Y.; Middleditch, M.; Shrestha, D.; Li, A.; Lal, S.; dos Remedios, C. G.; Baddeley, D.; Ruygrok, P. N.; Soeller, C. *Cardiovasc Res* **2017**, *113*, 879–891.

(128) Wagner, E. et al. *Circulation Research* **2012**, *111*, 402–414.

(129) Jayasinghe, I. D.; Clowsley, A. H.; Munro, M.; Hou, Y.; Crossman, D. J.; Soeller, C. *Eur J Transl Myol* **2014**, *25*, 15–26.

(130) Hou, Y.; Crossman, D. J.; Rajagopal, V.; Baddeley, D.; Jayasinghe, I.; Soeller, C. *Progress in Biophysics and Molecular Biology* **2014**, *115*, 328–339.

(131) Crossman, D. J.; Ruygrok, P. N.; Hou, Y. F.; Soeller, C. *Heart Fail Rev* **2015**, *20*, 203–214.

(132) Munro, M. L.; Jayasinghe, I. D.; Wang, Q.; Quick, A.; Wang, W.; Baddeley, D.; Wehrens, X. H. T.; Soeller, C. *J. Cell. Sci.* **2016**, *129*, 4388–4398.

(133) Kimlicka, L.; Van Petegem, F. *Sci. China Life Sci.* **2011**, *54*, 712–724.

(134) *J Cell Biol* **1984**, *99*, 875–885.

(135) Jorgensen A O; Broderick R; Somlyo A P; Somlyo A V *Circulation Research* **1988**, *63*, 1060–1069.

(136) Beard, N. A.; Laver, D. R.; Dulhunty, A. F. *Prog. Biophys. Mol. Biol.* **2004**, *85*, 33–69.

(137) Baddeley, D.; Jayasinghe, I. D.; Lam, L.; Rossberger, S.; Cannell, M. B.; Soeller, C. *PNAS* **2009**, *106*, 22275–22280.

(138) DINAMelt — Mfold.Rit.Albany.Edu. `http://unafold.rna.albany.edu/?q=DINAMelt/` (accessed 10/01/2017).

(139) Markham, N. R.; Zuker, M. *Nucleic Acids Res.* **2005**, *33*, W577–581.

(140) Markham, N. R.; Zuker, M. *Methods Mol. Biol.* **2008**, *453*, 3–31.

(141) NUPACK: Nucleic Acid Package. `http://www.nupack.org/` (accessed 01/09/2018).

(142) Zadeh, J. N.; Steenberg, C. D.; Bois, J. S.; Wolfe, B. R.; Pierce, M. B.; Khan, A. R.; Dirks, R. M.; Pierce, N. A. *Journal of Computational Chemistry* **2011**, *32*, 170–173.

(143) SantaLucia, J. *PNAS* **1998**, *95*, 1460–1465.

(144) Routh, E. D.; Creacy, S. D.; Beerbower, P. E.; Akman, S. A.; Vaughn, J. P.; Smaldino, P. J. *J Vis Exp* **2017**, *121*, e55496.

(145) Crossman, D. J.; Hou, Y.; Jayasinghe, I.; Baddeley, D.; Soeller, C. *Methods* **2015**, *88*, 98–108.

(146) Ooi, Y.; Hanasaki, I.; Mizumura, D.; Matsuda, Y. *Sci Technol Adv Mater* **2017**, *18*, 316–324.

(147) McGorty, R.; Kamiyama, D.; Huang, B. *Opt Nano* **2013**, *2*, 3.

(148) Baddeley, D.; Cannell, M. B.; Soeller, C. *Microscopy and Microanalysis* **2010**, *16*, 64–72.

(149) Lin, R.; Clowsley, A. H.; Jayasinghe, I. D.; Baddeley, D.; Soeller, C. *Opt. Express, OE* **2017**, *25*, 11701–11716.

(150) Balinovic, A.; Albrecht, D.; Endesfelder, U. *J. Phys. D: Appl. Phys.* **2019**, *52*, 204002.

(151) Delcanale, P.; Miret-Ontiveros, B.; Arista-Romero, M.; Pujals, S.; Albertazzi, L. *ACS Nano* **2018**, *12*, 7629–7637.

(152) Steinhauer, C.; Jungmann, R.; Sobey, T. L.; Simmel, F. C.; Tinnefeld, P. *Angewandte Chemie International Edition* **2009**, *48*, 8870–8873.

(153) Schmied, J. J.; Forthmann, C.; Pibiri, E.; Lalkens, B.; Nickels, P.; Liedl, T.; Tinnefeld, P. *Nano Lett.* **2013**, *13*, 781–785.

(154) Raab, M.; Jusuk, I.; Molle, J.; Buhr, E.; Bodermann, B.; Bergmann, D.; Bosse, H.; Tinnefeld, P. *Scientific Reports* **2018**, *8*, 1780.

(155) Chada, N.; Sigdel, K. P.; Gari, R. R. S.; Matin, T. R.; Randall, L. L.; King, G. M. *Scientific Reports* **2015**, *5*, 12550.

(156) Auer, A.; Schlichthaerle, T.; Woehrstein, J. B.; Schueder, F.; Strauss, M. T.; Grabmayr, H.; Jungmann, R. *ChemPhysChem* **2018**, *19*, 3024–3034.

(157) Properties. `https://microparticles.de/en/properties.html` (accessed 03/30/2019).

(158) Tan, Z.-J.; Chen, S.-J. *Biophys J* **2006**, *90*, 1175–1190.

(159) Aitken, C. E.; Marshall, R. A.; Puglisi, J. D. *Biophysical Journal* **2008**, *94*, 1826–1835.

(160) Su, X.; Li, L.; Wang, S.; Hao, D.; Wang, L.; Yu, C. *Scientific Reports* **2017**, *7*, 43824.

(161) Yagi, S.; Inoue, H. *Chemical Engineering Science* **1962**, *17*, 411–421.

(162) Hartwich, T. M.; Chung, K. K.; Schroeder, L.; Bewersdorf, J.; Soeller, C.; Baddeley, D. *bioRxiv* **2018**, 465492.

(163) Wade, O. K.; Woehrstein, J. B.; Nickels, P. C.; Strauss, S.; Stehr, F.; Stein, J.; Schueder, F.; Strauss, M. T.; Ganji, M.; Schnitzbauer, J.; Grabmayr, H.; Yin, P.; Schwille, P.; Jungmann, R. *Nano Lett.* **2019**, *19*, 2641–2646.

(164) Thevathasan, J. V.; Matti, U.; Kahnwald, M.; Kumar Peneti, S.; Nijmeijer, B.; Kueblbeck, M.; Ellenberg, J.; Ries, J. *Biophysical Journal* **2019**, *116*, 137a.

(165) Salas, D.; Le Gall, A.; Fiche, J.-B.; Valeri, A.; Ke, Y.; Bron, P.; Bellot, G.; Nollmann, M. *Proc Natl Acad Sci U S A* **2017**, *114*, 9273–9278.

(166) Thompson, R. E.; Larson, D. R.; Webb, W. W. *Biophysical Journal* **2002**, *82*, 2775–2783.

(167) Peterson, E. M.; Manhart, M. W.; Harris, J. M. *Anal. Chem.* **2016**, *88*, 6410–6417.

(168) Molle, J.; Raab, M.; Holzmeister, S.; Schmitt-Monreal, D.; Grohmann, D.; He, Z.; Tinnefeld, P. *Current Opinion in Biotechnology* **2016**, *39*, 8–16.

(169) Almada, P.; Pereira, P.; Culley, S.; Caillol, G.; Boroni-Rueda, F.; Dix, C. L.; Laine, R. F.; Charras, G.; Baum, B.; Leterrier, C.; Henriques, R. *bioRxiv* **2018**, 320416.

(170) Wang, Y. et al. *Nano Lett.* **2017**, *17*, 6131–6139.

(171) Phizicky, E. M.; Fields, S. *Microbiol Rev* **1995**, *59*, 94–123.

(172) Fields, S.; Song, O.-k. *Nature* **1989**, *340*, 245–246.

(173) Dai, M.; Jungmann, R.; Yin, P. *Nature Nanotechnology* **2016**, *11*, 798–807.

(174) Genot, A. J.; Zhang, D. Y.; Bath, J.; Turberfield, A. J. *J. Am. Chem. Soc.* **2011**, *133*, 2177–2182.

(175) Ouldridge, T. E.; Louis, A. A.; Doye, J. P. K. *Phys. Rev. Lett.* **2010**, *104*, 178101.

(176) Ouldridge, T. E.; Louis, A. A.; Doye, J. P. K. *J. Chem. Phys.* **2011**, *134*, 085101.

(177) Pettersen, E. F.; Goddard, T. D.; Huang, C. C.; Couch, G. S.; Greenblatt, D. M.; Meng, E. C.; Ferrin, T. E. *J Comput Chem* **2004**, *25*, 1605–1612.

(178) Mognetti, B. M.; Leunissen, M. E.; Frenkel, D. *Soft Matter* **2012**, *8*, 2213–2221.

(179) Parolini, L.; Mognetti, B. M.; Kotar, J.; Eiser, E.; Cicuta, P.; Di Michele, L. *Nat Commun* **2015**, *6*, 5948.

(180) Hendrickson, W. A.; Pähler, A.; Smith, J. L.; Satow, Y.; Merritt, E. A.; Phizackerley, R. P. *Proc Natl Acad Sci U S A* **1989**, *86*, 2190–2194.

(181) Morita, T.; Shimada, T.; Kitamura, H.; Nakamura, M. *Arch. Histol. Cytol.* **1991**, *54*, 539–550.

(182) Li, F.; Zhang, H.; Wang, Z.; Li, X.; Li, X.-F.; Le, X. C. *J. Am. Chem. Soc.* **2013**, *135*, 2443–2446.

(183) Travers, A., *DNA-Protein Interactions*; Springer Netherlands: 1993.

(184) Truong, K.; Ikura, M. *Current Opinion in Structural Biology* **2001**, *11*, 573–578.

(185) Ma, H.; Fu, R.; Xu, J.; Liu, Y. *Scientific Reports* **2017**, *7*, 1542.

(186) Schallmeiner, E.; Oksanen, E.; Ericsson, O.; Spångberg, L.; Eriksson, S.; Stenman, U.-H.; Pettersson, K.; Landegren, U. *Nature Methods* **2007**, *4*, 135–137.

(187) Demmerle, J.; Wegel, E.; Schermelleh, L.; Dobbie, I. M. *Methods* **2015**, *88*, 3–10.

(188) Lee, J.; Park, S.; Kang, W.; Hohng, S. *Molecular Brain* **2017**, *10*, 63.

(189) Nazarenko, I.; Pires, R.; Lowe, B.; Obaidy, M.; Rashtchian, A. *Nucleic Acids Res.* **2002**, *30*, 2089–2195.

(190) Woehrstein, J. B.; Strauss, M. T.; Ong, L. L.; Wei, B.; Zhang, D. Y.; Jungmann, R.; Yin, P. *Science Advances* **2017**, *3*, e1602128.

(191) Schröder, T.; Scheible, M. B.; Steiner, F.; Vogelsang, J.; Tinnefeld, P. *Nano Lett.* **2019**, *19*, 1275–1281.

(192) Mujumdar, S. R.; Mujumdar, R. B.; Grant, C. M.; Waggoner, A. S. *Bioconjugate Chem.* **1996**, *7*, 356–362.

(193) Zhegalova, N. G.; He, S.; Zhou, H.; Kim, D. M.; Berezin, M. Y. *Contrast Media Mol Imaging* **2014**, *9*, 355–362.

(194) Chi, Q.; Wang, G.; Jiang, J. *Physica A: Statistical Mechanics and its Applications* **2013**, *392*, 1072–1079.

(195) Nieves, D. J.; Gaus, K.; Baker, M. A. B. *Genes* **2018**, *9*, 621.

(196) Deußner-Helfmann, N. S.; Auer, A.; Strauss, M. T.; Malkusch, S.; Dietz, M. S.; Barth, H.-D.; Jungmann, R.; Heilemann, M. *Nano Lett.* **2018**, DOI: 10.1021/acs.nanolett.8b02185.

(197) Werbin, J. L.; Avendaño, M. S.; Becker, V.; Jungmann, R.; Yin, P.; Danuser, G.; Sorger, P. K. *Scientific Reports* **2017**, *7*, 12150.

(198) Zhang, D. Y.; Turberfield, A. J.; Yurke, B.; Winfree, E. *Science* **2007**, *318*, 1121–1125.

(199) Li, B.; Ellington, A. D.; Chen, X. *Nucleic Acids Res* **2011**, *39*, e110.

(200) Shi, Z.; Castro, C. E.; Arya, G. *ACS Nano* **2017**, *11*, 4617–4630.

(201) Torrie, G. M.; Valleau, J. P. *Journal of Computational Physics* **1977**, *23*, 187–199.

(202) Whitelam, S.; Geissler, P. L. *The Journal of Chemical Physics* **2007**, *127*, 154101.

(203) Kumar, S.; Rosenberg, J. M.; Bouzida, D.; Swendsen, R. H.; Kollman, P. A. *Journal of Computational Chemistry* **1992**, *13*, 1011–1021.

(204) Jong, D. H. D.; Schäfer, L. V.; Vries, A. H. D.; Marrink, S. J.; Berendsen, H. J. C.; Grubmüller, H. *Journal of Computational Chemistry* **2011**, *32*, 1919–1928.

(205) Snodin, B. E. K.; Randisi, F.; Mosayebi, M.; Šulc, P.; Schreck, J. S.; Romano, F.; Ouldridge, T. E.; Tsukanov, R.; Nir, E.; Louis, A. A.; Doye, J. P. K. *J. Chem. Phys.* **2015**, *142*, 234901.

Appendix

A Modelling of PD-PAINT properties

The following methods describing simulation of PD-PAINT characteristics are the work of William T. Kaufhold and Lorenzo Di Michele and given here for completeness as published in Lutz et al. [2].

A.1 Coarse-grained model

We used the coarse grained model oxDNA to estimate the free energies of S1-S2 hybridization (Fig. 6.2 a, main text) and of the imager interacting with the binding site on S1 (Fig. 6.2 b, main text) [175, 176]. The oxDNA representation has been developed for studying DNA nanostructure reconfiguration in the context of strand displacement reactions [106, 175] but is remarkably versatile, accurately modelling the configurational freedom of large origami nanostructures [200]. Each nucleotide is modelled as three beads, representing the phosphate backbone, the stacking site, and the hydrogen bonding site. Nucleotides interact with each other via potentials encoding excluded volume, nucleotide stacking, cross-stacking, and backbone connectivity. Coulomb repulsion between the negatively-charged backbone sites is modelled through the Debye Hückel approximation. The model has been parameterized top down to match a diverse range of thermodynamic and structural features observed in experiments.

A.2 S1-S2 dimerization free energy

Following previous studies on the hybridization of DNA constructs tethered to solid or fluid substrates, we express the dimerization free energy of S1 and S2 while anchored at a distance x from each other as [178, 179]

$$\Delta G_{\mathrm{tet}}(x) = \Delta G^{0}_{\mathrm{sol}} - \phi^{0}(x) \tag{S1}$$

In Eq. S1 $\Delta G^{0}_{\mathrm{sol}}$ is the standard hybridization free energy of the nanostructures free in solution, which we extract based on the DNA sequences used in experiments with the nearest-neighbour thermodynamic parameters as implemented in the software suite NUPACK [142, 143].

The contribution $\phi^{0}(x)$ encodes for the steric and electrostatic interactions between the nanostructures and the entropy of the ssDNA spacers anchoring the binding domains to the substrate (Fig. 6.1, main text). Given the relative complexities of the system we did not assume any closed functional form for $\phi^{0}(x)$ but estimated it via MC simulations using oxDNA. This was done implicitly, by first extracting a numerical estimate of the tethered-construct dimerization free energy $\Delta G^{\mathrm{MC}}_{\mathrm{tet}}(x)$ for a range of x values, and then subtracting off an analogous estimate $\Delta G^{0,\mathrm{MC}}_{\mathrm{sol}}$ for free constructs

$$\phi^{0}(x) = \Delta G^{\mathrm{MC}}_{\mathrm{tet}}(x) - \Delta G^{0,\mathrm{MC}}_{\mathrm{sol}}. \tag{S2}$$

Our approach thus decouples evaluation of $\phi^{0}(x)$ from that of $\Delta G^{0}_{\mathrm{sol}}$, with the former being dependent on the construct geometry only and the latter on the base-sequence of the interacting domains.

This implies that once $\phi^{0}(x)$ has been estimated via MC, one can rapidly explore the performance of a range of nanostructures that share the same geometry but differ for base sequence by simply computing the corresponding $\Delta G^{0}_{\mathrm{sol}}$ with the nearest neighbour rules and using Eq. S1 to extract $\Delta G_{\mathrm{tet}}(x)$,without the need for computationally expensive simulations.

For these simulations we used the original oxDNA model which has been parameterized for a monovalent salt concentration of 0.5 M, similar to experimental values. This choice was made to improve computational efficiency. Since as discussed above these simulations were aimed at quantifying the effects of configurational entropy, excluded volume and electrostatics, we used sequence averaged interaction potentials.

Tethering of S1 and S2 constructs has been simulated implicitly though stiff harmonic bonds of the nucleotides that in experiments are immobilized to the substrates (Fig. 6.2 a, main text). For all these calculations, the concentration of DNA nanostructures in the box was set as 2.7 μM, using a cubic box of length 85 nm with periodic boundary conditions.

A.3 Sampling

The free energy difference between the dimerized and un-dimerized states of the S1-S2 system, for both the tethered and un-tethered case, was acquired via umbrella sampling [201]. Each window was sampled using Virtual Move Monte Carlo (VMMC), a method which is especially suited to the sampling of stiff polymers which otherwise suffer from low acceptance probabilities [202]. We defined a four dimensional reaction coordinate $\vec{q} = (b_1, b_2, d_1, d_2)$, where b_1 corresponds to the number of bonds between S1 and itself, b_2 to the number of bonds between S1 and S2, d_1 to a discrete measure of the distance between hybridizing domains A-B and their complementary A*-B* on S1. d_2 is an analogous measure of the distance between hybridizing domains A-B on S1 and complementary domains A*-B* on S2. To evaluate the discrete measure of distance, $d_i (i = 1, 2)$, first we calculated the minimum distance m_i between complementary nucleotides between the domains of interest which are expected to bind in the final stable state. Subsequently, m_i was identified with an interface in the ordered list $\{m_i \leq \lambda_0, \lambda_0 < m_i \leq \lambda_1, \lambda_1 < m_i \leq \lambda_2 \ldots \lambda_n < m_i\}$, whose index is d. The chosen values of $\lambda_j (j = 1 \ldots n)$ were $2, 4, 6, 8, 10, 15, 25$, expressed in oxDNA distance units of 0.85 nm.

While in reality the opening process of the hairpin on S1 would almost certainly proceed along a branch migration trajectory in line with previously well studied strand displacement reactions [106], such a trajectory is difficult to sample adequately. Instead, we sampled along an unphysical path where the S1 stem loop opens completely before any of the S1-S2 bonds are formed. The reaction coordinates for the thermodynamic windows we used to sample this pathway are shown in Table A.1. Sampling within each of the windows was run initially with biases chosen from experience, and later optimized to ensure flat histogram sampling.

Table A.1: Umbrella sampling windows expressed in terms of the four components of the chosen reaction coordinate.

Window	b_1	b_2	d_1	d_2
A_0	$20 \leq b_1 \leq 14$	0	0	-
A_1	$15 \leq b_1 \leq 9$	0	0	-
A_2	$10 \leq b_1 \leq 4$	0	0	-
A_3	$5 \leq b_1 \leq 1$	0	0	-
A_4	$3 \leq b_1 \leq 0$	0	0	-
W_0	0	0	-	$0 \leq d_2 \leq 2$
W_1	0	0	-	$1 \leq d_2 \leq 3$
W_2	0	0	-	$2 \leq d_2 \leq 4$
W_3	0	0	-	$3 \leq d_2 \leq 5$
W_4	0	0	-	$4 \leq d_2 \leq 6$
W_5	0	0	-	$5 \leq d_2 \leq 7$
B_4	0	$20 \leq b_2 \leq 14$	-	$d_2 \leq 1$
B_3	0	$15 \leq b_2 \leq 9$	-	0
B_2	0	$10 \leq b_2 \leq 4$	-	0
B_1	0	$5 \leq b_2 \leq 1$	-	0
B_0	0	$3 \leq b_2 \leq 0$	-	0

To improve sampling we disallow misbonded configurations, where Watson-Crick bonds are present between nucleotides whose domains are not entirely complementary.

The Weighted Histogram Analysis Method (WHAM) [203], as implemented in Python, was used to combine the probability distributions of different windows. To improve computational efficiency for this step, the four dimensional order parameter was converted by an injective map to a two dimensional order parameter, given by $(d_{\max} - d_1 + b_1, d_{\max} - d_2 + b_2)$. Such a map is injective as $d_i = 0$ whenever $b_i > 0$. Here, $d_{\max}$ is the value of the maximum interface of d_i, so that each dimension of the 2D order parameter varies monotonically from a minimum value of 0 to a maximum value of 28, when all bonds have been formed correctly.

We ran simulations of the 16 thermodynamic windows using between 4 and 8 independent repeats. For each independent repeat, we used WHAM to make an estimate of the 2D free energy profile along the transition path. In the following, all uncertainties are given from the standard error in evaluating the quantity of interest for each of these independent repeats.

Subsequently, we evaluated the probability that the system is in the hybridized state $p_{\mathrm{dim}}^{\mathrm{MC}}(x)$, which we define as to have at least 17 of the 20 S1-S2 bonds formed. We then evaluate the free energy in accordance with standard methods [204]

$$\Delta G_{\mathrm{tet}}^{\mathrm{MC}}(x) = -k_{\mathrm{B}}T \log\left[\frac{p_{\mathrm{dim}}^{\mathrm{MC}}(x)}{1 - p_{\mathrm{dim}}^{\mathrm{MC}}(x)}\right]. \tag{S3}$$

Note that $\Delta G_{\mathrm{tet}}^{\mathrm{MC}}$ and $p_{\mathrm{dim}}^{\mathrm{MC}}(x)$ calculated at this stage and appearing in Eqs. S2 and S3 do not correspond to the analogous quantities in Eq. S1 and discussed in the main text, as for the latter the free energy contribution deriving from the S1-S2 base pairing is computed using the nearest-neighbor rules, and MC is only used to derive the entropic contribution $\phi^0(x)$.

To estimate $\Delta G_{\mathrm{sol}}^{\mathrm{MC}}$ we then perform an analogous simulation without stiff restraints, with concentrations of S1 and S2 set at $c = 2.7\,\mu\mathrm{M}$, for which we obtain $p_{\mathrm{dim}}^{\mathrm{MC}} = (3.3 \pm 0.7) \times 10^{-5}$. Using the reference concentration $\rho_0 = 1\,\mathrm{M}$ we then acquire the standard bulk dimerization free energy of the simulated system as

$$\Delta G_{\mathrm{sol}}^{0,\mathrm{MC}} = -k_{\mathrm{B}}T \log\left[\frac{p_{\mathrm{dim,sol}}^{\mathrm{MC}}}{1 - p_{\mathrm{dim,sol}}^{\mathrm{MC}}}\frac{\rho_0}{c}\right] = -2.4 \pm 0.6 k_{\mathrm{B}}T. \tag{S4}$$

Subsequently we used Eq. S2 to evaluate $\phi^0(x)$ from $\Delta G_{\mathrm{tet}}^{\mathrm{MC}}(x)$ (Eq. S3) and $\Delta G_{\mathrm{sol}}^{0,\mathrm{MC}}$ (Eq. S4). Following Eq. S1 we then combined $\phi^0(x)$ with $\Delta G_{\mathrm{sol}}^{0}$ acquired from NUPACK [142], which we find to be $\Delta G_{\mathrm{sol}}^{0} = -7.00 k_{\mathrm{B}}T$, to derive values of $\Delta G_{\mathrm{tet}}(x)$ discussed in the main text. The dimerization probability discussed in the main text and shown in Fig. 6.2 a was derived as

$$p_{\mathrm{dim}}(x) = \frac{\exp\left(-\Delta G_{\mathrm{tet}}(x)/k_{\mathrm{B}}T\right)}{1 + \exp\left(-\Delta G_{\mathrm{tet}}(x)/k_{\mathrm{B}}T\right)} \tag{S5}$$

A.4 S1-imager dimerization free energy

For the study of imager hybridization to the docking site, we use the updated oxDNA2 force field, which features tunable cation concentration and various other improvements [205]. In this case, as the observables we extract are sequence-specific free energies and bond lifetimes, we use sequence-dependent interaction potentials.

Table A.2: Umbrella sampling windows expressed in terms of the 2 reaction coordinates. * Indicates that this window was only used for the case of the closed S1 loop, with a bias to accentuate probability of observing binding events.

Window	b	d
B	$0 \leq b \leq 2$	$0 \leq d \leq 1$
F	$1 \leq b \leq 9$	0
S	0	$0 \leq d \leq 4$
I	0	$4 \leq d \leq 7$
L*	$1 \leq b \leq 9$	0

Simulations were run to evaluate the free energy ΔG_{S1-P1} of imager P1 binding to the docking domain on S1 in three cases, as discussed in the main text (Fig. 6.2 b):

(1) Closed S1 loop, where the stem of the hairpin on S1 is allowed to close

(2) Open S1 loop, where the S1-S2 dimer is forced open using a potential which requires that at least 17 of the 20 S1-S2 bonds are formed

(3) Classical DNA-PAINT configuration, using a sequence S1' where loop formation is prevented by using a different base sequence

We follow a simulation protocol analogous to what was done for the S1-S2 interaction free energy. Specifically, we perform umbrella sampling using a set of windows defined in terms of a two-dimensional reaction coordinate $\vec{q} = (b, d)$, where b is the number of P1-S1 bonds and d is a discrete measure of distance between P1 and its complementary domain on S1, defined as explained above for the S1-S2 case. The chosen windows are here listed in Table A.2. Sampling within each window is performed using the VMMC algorithm [202] and the probability distributions from each window stitched together using WHAM [203]. As done above, we simulated our system in a periodic box of length 85 nm, corresponding to an effective concentration of $c = 2.7\,\mu\text{M}$ for each of the strands.

By defining as $p(b)$ the probability of P1 forming b bonds with S1, we extract

$$\Delta G_{S1-P1}(b) = \begin{cases} -k_{\text{B}}T \log\left[\frac{p(b)}{1-p(b)}\right] & \text{for } b = 0 \\ -k_B T \log\left[\frac{p(b)}{1-p(b)} \frac{c\ \exp}{c}\right] & \text{for } b > 0 \end{cases} \tag{S6}$$

Table A.3: Expected half-lives for the dissociation of the imager (P1), to the docking region on S1. Uncertainties shown here were calculated considering only the uncertainty in the hybridization equilibrium constant K evaluated from simulation. (*) This estimate is an approximate lower bound, as here, the on-rate k_{on} used in the calculation of the half life from the equilibrium constant K (obtained from the simulations) is that of simple hybridizing strands, whereas the loop will limit the rate of encounter between the binding sites.

System	Estimated Half Life
S1 closed loop	$1.4 \pm 0.3^*\,\mu\text{s}$
S1 open loop	$0.19 \pm 0.05\,\text{s}$
P1 docking (classical DNA-PAINT)	$0.13 \pm 0.02\,\text{s}$

where the correction applied for $b > 0$ accounts for the different imager concentration C_{exp} used in experiments, where $C_{\text{exp}} = 0.05\,\text{nM}$.

To extract the half-life for the dissociation of the imager we evaluated the probability of P1 and S1 having at least one base-pairing bond, $p_{\text{bound}} = \sum_{b=1}^{9} p(b)$. Then, the equilibrium constant was computed as

$$K = \frac{p_{\text{bound}}}{1 - p_{\text{bound}}} \frac{\rho_0}{c}. \tag{S7}$$

ρ_0 is a reference concentration, here, 1 M. The P1-S1 off rate can then be estimated as $k_{\text{off}} = k_{\text{on}}/K$. Here we used the rough estimate $k_{\text{on}} = 10^6\,\text{M}^{-1}\text{s}^{-1}$, a value often reported in the literature, and thought to be accurate for sufficiently short oligonucleotides at sufficiently high ionic strengths, conditions that should be fulfilled in our experimental system. The P1-S1 binding lifetimes shown in Table A.3 are then extracted as $\tau_{\text{bound}} = \log(2)/k_{\text{off}}$.

B Cover figure for Nano Research 11/12

Figure B.2: Figure designed and used as cover figure for Nano Research 11/12, illustrating the principle of Quencher-Exchange-PAINT [1]